



Vrije
Universiteit
Brussel



VRIJE UNIVERSITEIT BRUSSEL

Faculteit Wetenschappen en Bio-ingenieurswetenschappen
Vakgroep Fysica - Interuniversity Institute for High Energies

A Search for Dark Matter in the Center of the Earth with the ICECUBE Neutrino Detector

Jan Kunnen

Proefschrift ingediend met het oog op het behalen van
de academische graad van Doctor in de Wetenschappen.

Promotoren: **Prof. Dr. Catherine De Clercq,**
Prof. Dr. Nick van Eijndhoven

Oktober 2015

Doctoral Examination Committee

Chair: Prof. Dr. S. Lowette (VUB)

Promotor: Prof. Dr. C. De Clercq (VUB)

Promotor: Prof. Dr. N. van Eijndhoven (VUB)

Secretary: Prof. Dr. L. Lopez Honorez (VUB)

Prof. Dr. P. Claeys (VUB)

Prof. Dr. C. Pérez de los Heros (Uppsala University, Sweden)

Prof. Dr. M. Gustafsson (Georg-August University Göttingen, Germany)

To Leyla, my soulmate, my love, my life

Abstract

Understanding the nature of dark matter is one of the major challenges in modern physics. Many effects caused by this mysterious matter have been seen, but until today, there is no clear idea on what this dark matter is made of. The current best model to describe our Universe, the Lambda Cold Dark Matter model, incorporates a dark matter component, which makes up about 27% of all the energy in the Universe and roughly 80% of all the matter.

In the most popular models, the dark matter consists of particles which are stable, slowly moving (cold), heavy and only interact weakly and gravitationally with ordinary baryonic matter. These particles are therefore called Weakly Interacting Massive Particles (WIMPs). An excellent candidate for the WIMP is the hypothetical neutralino, the Lightest Supersymmetric Particle (LSP), arising in supersymmetric theories beyond the Standard Model of particle physics.

Heavy celestial bodies, such as the Earth, could capture these WIMPs and accumulate them. Over time the WIMPs will self-annihilate and may produce standard model particles, including neutrinos. The dark matter annihilation rate in the center of the Earth, and thus the resulting neutrino flux depend on the local Dark Matter density and the mass of the Dark Matter particle. The neutrino flux could be within reach of a large scale neutrino telescope like the cubic kilometer ICECUBE Neutrino Observatory located at the South Pole. ICECUBE would indirectly observe the presence of Earth WIMPs as an excess of neutrinos from the center of the Earth.

In this thesis, the first search for Earth WIMPs with the ICECUBE detector is presented. No significant excess from the direction of the center of the Earth has been found in one year of ICECUBE data. As a result, upper-limits have been set on the annihilation rate of the WIMPs, the muon flux caused by Earth WIMP-induced neutrinos and the spin-independent component of the WIMP-nucleon cross-section. The obtained upper-limits are the current best limits on the annihilation rate of Earth WIMPs and on the muon flux caused by Earth WIMP-induced neutrinos.

*Writers make national literature, while translators
make universal literature.*

José Saramago

Samenvatting

Uit verscheidene experimenten blijkt dat ons heelal doordrongen moet zijn van een onbekende soort materie. Deze zogenaamde *donkere materie* is één van de grote mysteries in de moderne fysica. Volgens recente waarnemingen zou de donkere materie zorgen voor maar liefst 27% van de totale energie-dichtheid in ons Universum, terwijl de zichtbare materie slechts ongeveer 5% bijdraagt. Een tot nog toe onbekend deeltje, met de eigenschappen dat het massief en zwak interagerend is, het zogeheten WIMP, zou een mogelijke oplossing bieden voor dit mysterie.

De Minimale Supersymmetrische uitbreiding van het Standaard Model (MSSM) is een hypothetische theorie waarin elk deeltje uit het Standaard Model een supersymmetrische partner heeft. Deze theorie postuleert dus verscheidene nieuwe (tot vandaag ongeobserveerde) deeltjes, waaronder het neutralino. Dit neutralino, χ , is één van de meest populaire WIMP kandidaten op dit ogenblik.

Als deze WIMPs bestaan, zullen zij gravitationeel aangetrokken worden door massieve objecten, zoals de aarde. Hierdoor zal een ophoping aan WIMPs ontstaan in de kern van de aarde. Eens de dichtheid van deze WIMPs groot genoeg is, zullen zij paarsgewijs annihileren en Standaard Model deeltjes produceren. Deze Standaard Model deeltjes kunnen in hun verval onder andere neutrino's produceren. Aangezien neutrino's heel zwak interagerende deeltjes zijn, zullen de geproduceerde neutrino's ontsnappen uit de kern van de aarde. Heel af en toe zal één van de neutrino's toch interageren, en kan het dus gedetecteerd worden door een neutrinotelescoop zoals bijvoorbeeld ICECUBE.

IceCube is een detector met een volume van één kubieke kilometer en ligt begraven op de geografische Zuidpool onder anderhalve km ijs. IceCube heeft een hexagonale vorm en bestaat uit 5160 optische sensoren die verspreid zijn over 86 kabels. Wanneer een neutrino interageert in de omgeving van de detector, ontstaat het bijhorende geladen lepton van het neutrino (e, μ, τ), hetgeen een lichtspoor achterlaat in het ijs. Dit lichtspoor wordt dan gedetecteerd door de optische sensoren en via deze detectie kan het originele neutrino vervolgens geanalyseerd worden.

De meeste deeltjes die ICECUBE meet, zijn echter atmosferische muonen en neutrino's. Deze zijn geproduceerd na de interactie van kosmische deeltjes in de atmosfeer. ICECUBE detecteert ongeveer 4000 van deze *atmosferische* deeltjes per seconde ($\mathcal{O}(10^{11})$ /jaar), terwijl de meest optimistische modellen slechts een WIMP-annihilatieflux van enkele

μHz ($\mathcal{O}(10^3)/\text{km}^2/\text{jaar}$) voorspellen in ICECUBE. De atmosferische achtergrond moet dus sterk onderdrukt (of *gefilterd*) worden, zonder dat hierbij teveel signaal verloren gaat. Een heel groot deel van het beschreven werk in deze thesis, bestaat uit het ontwikkelen van een *filter* die specifiek deeltjes selecteert met de verwachte eigenschappen van neutrino's die geproduceerd zijn ten gevolge van de annihilatie van WIMPs in de aarde. Aan het einde van deze specifieke selectie, is het aantal deeltjes verminderd met zowat zeven grootteordes naar $\mathcal{O}(10^4)/\text{jaar}$, terwijl ongeveer 15% van de mogelijke signaal overblijft.

In deze finale dataset, die voornamelijk bestaat uit atmosferische neutrino's, wordt dan gezocht naar een mogelijke bijdrage van de neutrino's die afkomstig zijn van de WIMPs in de aarde. Dit gebeurt aan de hand van een statistische analyse, waarbij er nagegaan wordt of de experimentele data al dan niet overeenkomen met de gesimuleerde, atmosferische achtergrond neutrino's en -muonen. In het geval dat deze niet overeenkomen, is er mogelijk een bijdrage van signaalneutrino's, hetgeen een sterke indicatie zou zijn van de aanwezigheid van WIMPs in het centrum van de aarde. In het andere geval, wanneer de data wél overeenkomen met de achtergrond simulatie, kan er besloten worden dat indien er een signaal zou zijn, dit niet sterk genoeg is om zichtbaar te zijn in de experimentele data. In dit laatste geval kunnen dus limieten gezet worden op de mogelijke neutrinoflux die de WIMPs veroorzaken, en kunnen er dus theoretische modellen uitgesloten worden.

In de analyse die beschreven wordt in deze thesis hebben we één jaar van de data, gemeten door ICECUBE geanalyseerd. Uit onze analyse blijkt dat deze gemeten data volledig overeenkomen met de verwachte, atmosferische achtergrondflux. Aan de hand van deze niet-observatie van neutrino's die gecreëerd zijn na de annihilatie van WIMPs, hebben we met deze analyse de tot dusver beste limieten gezet op de mogelijke neutrinoflux veroorzaakt door WIMPs in het centrum van de aarde.

*Have no mean hours, but be grateful for every hour,
and accept what it brings. The reality will make any
sincere record respectable.*

Henry David Thoreau

Acknowledgements

Although this is one of the first pages in the thesis, this was actually the very last part I wrote. Doing this, I saved the best for the last, as it is a pleasure to thank everyone for the support during the last four or more years.

First of all, I would like to thank the Interuniversity Institute for High Energies (ULB-VUB). This institute has been my work environment for the last 5 years, and I really enjoyed working here both during the research of my Masters thesis as well as during the four years of PhD research.

A special thanks goes to the administrative and computing staff, for making my life so much easier. Bedankt Marleen voor alles! Niet alleen zorg jij ervoor dat de administratie binnen het IIHE loopt als een gesmeerde machine, maar daarboven zorgt jouw aanwezigheid steeds voor veel warmte en genegenheid. Merci Samir, Abdelhakim et Abdelhak pour toute l'aide informatique. Ces dernières années j'ai souvent voulu balancer mon ordinateur par la fenêtre, mais grâce à vous, le laptop est toujours en vie. Merci!

Of course, I can not thank my supervisors Catherine De Clercq and Nick van Eijndhoven enough for all the help, support, discussion, trust, ... over the past years. Thanks for giving me the opportunity to really taste scientific research. Thanks for sending me to conferences, workshops, seminars and (collaboration) meetings. Both of you have been great supervisors, I was very lucky to work for such great bosses, both from the personal as well as the professional point of view. Bedankt Catherine and Nick!

The IIHE is such a great institute, because its members are wonderful people. I wish to thank everyone connected to the IIHE during the last five years for contributing to the nice atmosphere in the lab. More specifically I would like to thank my colleagues within the Brussels IceCube group. We started off as colleagues, and ended as friends. Merci Lio et Martin pour tout les moments agréables, gourmands et décadents. Thanks to my office mates Giuliano (¡Muchas gracias Amigo!), Isabelle, Sabrina and Mathieu. A special thanks to the people with whom I have worked closely, and who have put lots of efforts in reading and correcting this thesis, Jan, Krijn, Gwen, Jon and Erik. Jan, it has been a pleasure to finish this analysis in close collaboration with you in the last year, vielen Dank! Krijn, bedankt voor het herlezen van de thesis in zulk een detail, alsook bedankt voor de fijne besprekingen tijdens één van onze vele fietstochten. Merci Gwen pour relire toute ma thèse, même à 5h00 du matin!

Thanks Debanjan for the joyful moments we shared. Gracias Geraldina for your guidance, help and warm presence. I really enjoyed your superb organizational skills! Grazie Elisa for always being available for a chat and for your smile. Stijn, David, Thomas, Mark, Alberto and Aongus, it was great to work, drink coffee and eat pizza with you guys!

Also thanks to the new members of the group, Chris, Simona, Kevin, Juanan. Welcome and good luck!

Of course I also want to thank the ICECUBE collaboration. Being part of this collaboration has been a great experience, which I would recommend to everyone interested in doing state of the art experimental physics in a dynamic group.

A special thanks to Dima and Katherine for reviewing and approving my analysis and to Carlos and Carsten for leading the “Beyond the Standard Model” working group. And of course thanks Queen Kim!

Finally I want to thank the members of the jury, Steven Lowette, Laura Lopez Honorez, Philippe Claeys, Carlos Pérez de los Heros and Michael Gustafsson.

Naast mijn collega's, wil ik ook graag vrienden en familie danken voor alle steun, fijne en minder fijne momenten.

Bedankt Annik om zulk een fijne klasgenoot, collega en vriendin te zijn.

Bedankt aan alle sparringspartners op de ju-jitsu en de tang soo do. Dankzij jullie allemaal kon ik mijn frustraties kwijt! Merci Jean en Oli!

Merci aan alle fietsvrienden voor de vele leuke en ontspannende, doch vuile en pijnlijke fietstochten. In het bijzonder een dikke merci aan Fourre en Krijn!

Ook veel dank aan (den) Daf, Leo en Z, voor alle fantastische momenten die al geweest zijn, en die nog moeten komen!

Mama en papa, bedankt voor jullie immer aanwezige steun en vertrouwen, alsook voor het warme nest waarin we zijn opgegroeid. Bedankt liever broers en zus om lieve broers en zus te zijn! Bedankt ook aan de schoonfamilie om zo een leuke schoonfamilie te zijn!

En dan, om af te sluiten met de belangrijkste persoon van allemaal, ook ongelooflijk veel bedankingen aan het adres van Leyla, mijn Liefje, mijn (bijna) vrouw, mijn beste vriendin, kortom mijn alles. Ik heb ongelooflijk hard genoten van de voorbije 9 jaren, en kijk al heel hard uit naar alles wat ons nog, samen, te wachten staat. Bedankt voor alles Liefje!

Contents

1	An indirect search for dark matter in the center of the Earth with ICECUBE	1
2	A brief introduction to dark matter	7
2.1	Introduction	8
2.2	The Lambda Cold Dark Matter model	9
2.3	Candidates	12
2.4	Dark matter distribution in the Universe	14
2.5	Experiments	16
2.5.1	Direct detection	17
2.5.2	Indirect detection	21
2.5.3	Collider experiments	22
2.6	WIMPs in the center of the Earth	23
3	Neutrinos as a probe for Earth WIMPs	29
3.1	Neutrinos from WIMP annihilations in the center of the Earth	31
3.2	Neutrinos and their interactions with matter	33
3.3	Neutrino Oscillations	34
3.4	Neutrino Detection in Ice	40
3.4.1	Muon energy losses	40
3.4.2	Cherenkov radiation	42
4	The ICECUBE Detector	47
4.1	Introduction	49
4.2	The South Pole ice	52
4.3	Digital Optical Modules	54
4.4	Neutrino signatures in ICECUBE	57
4.5	Physical processes measured by ICECUBE	58
4.6	The ICECUBE data acquisition	61
4.6.1	Triggering	62
4.6.2	Online filtering	63
5	Hit Cleanings and Event Reconstructions	71
5.1	Hit Processing and Cleaning	72
5.1.1	Waveform Calibration and Fitting	72

5.1.2	Hit Cleaning and splitting	73
5.2	Event Reconstruction	75
5.2.1	LINEFIT	76
5.2.2	Likelihood Fit	77
5.2.3	Reconstruction of the interaction vertex and the length	78
5.2.4	MuEX reconstruction	80
5.3	Removing Noise Clusters	81
6	The Analyzed ICECUBE Datasets	83
6.1	Experimental Data	84
6.2	Simulated Data	86
6.2.1	Generation of events	87
6.2.2	Propagators	91
6.2.3	Detector simulation	91
7	Event Processing and Selection	93
7.1	Overview	95
7.2	Signal and background	96
7.2.1	The signal definition	96
7.2.2	Estimation of the background	98
7.3	Online filter selection	99
7.4	Removing Noise Clusters	99
7.5	Reducing the data rate to a few Hz	101
7.5.1	The LEVEL 3 cut variables	102
7.5.2	Selecting the cut values.	106
7.6	Splitting the data sample	108
7.7	The low energy optimization	113
7.7.1	HIVESPLIT Cleaning	114
7.7.2	Introducing Boosted Decision Trees	117
7.7.3	Cuts prior to the BDT	121
7.7.4	Moving towards a neutrino pure sample: the BDT	127
7.7.5	Rates, efficiencies and angular resolution of the FINAL LOWE sample	135
7.8	The high energy optimization	141
7.8.1	Selecting up-going tracks	141
7.8.2	Pull-Validation	141
8	Estimation of the Sensitivities	147
8.1	Probability densities	148
8.2	Shape analysis	152
8.3	Sensitivity	156

9 Measurement of the WIMP annihilation rate and related physical quantities	163
9.1 Systematic Uncertainties	164
9.2 The Unblinded Zenith Angle Distributions	171
9.3 Flux Limits	176
9.3.1 Upper-Limit on the Volumetric Flux	176
9.3.2 Upper-Limit on the Annihilation Rate	176
9.3.3 Upper-Limit on the Muon Flux	178
9.3.4 Upper-Limit on the Spin-Independent cross-section	182
10 Summary and Outlook	187
10.1 Summary	187
10.2 Outlook	190
Appendices	193
A Distributions of the Variables used in the BDT	195
B The effect of coincident events on the neutrino flux	205

CONTENTS

Before you start some work, always ask yourself three questions - Why am I doing it, What the results might be and Will I be successful. Only when you think deeply and find satisfactory answers to these questions, go ahead.

Chanakya

1

An indirect search for dark matter in the center of the Earth with ICECUBE

In 1933 the astronomer Fritz Zwicky estimated the mass of the Coma cluster of galaxies. His calculation was based on the motions of galaxies near its edge. After this first calculation, he compared the estimated mass to the mass based on the number of galaxies and total brightness of the cluster. The amount of mass he estimated was much higher than the visually observable mass. Zwicky concluded that there should be matter that is not observable by its electromagnetic radiation, so-called *dark matter*. Today, more than 80 years later, there is much more, indisputable, evidence for the presence of this dark matter. Nevertheless it remains unknown what this dark matter is made of, making this dark component of the Universe one of the great experimental and theoretical challenges in modern physics.

There are many possible candidates to describe the dark matter, for example axions and particles arising in models with universal extra dimensions, but the most popular candidate is the Weakly Interacting Massive Particle (WIMP). An excellent candidate for the WIMP is the hypothetical neutralino, the Lightest Supersymmetric Particle (LSP), arising in supersymmetric theories beyond the Standard Model of particle physics.

The current best model to describe our Universe, the *Lambda Cold Dark Matter* (Λ CDM) model, naturally incorporates a dark matter component. According to the best fit of this model to the latest Planck data, dark matter makes up about 27% of all the energy in the Universe and roughly 80% of all the matter.

The distribution of dark matter in the Universe, is estimated by observations and simulations. From simulations it follows that dark matter is not completely homogeneously

distributed in the Universe. Instead there are voids, walls and filaments in the dark matter distributions, which seems to be in agreement with the large scale distribution of galaxies.

The general view on the distribution of dark matter particles in galaxies (e.g. the Milky Way) is that they form a fairly smooth spherical halo around an embedded baryonic component like e.g. a central bulge and a spiral disk. In this Standard Halo Model (SHM), the dark matter velocities follow a Maxwell-Boltzmann distribution. Some simulations also show the possible existence of a thick disc of dark matter. In the simulations, this dark disc has kinematics similar to the thick disc of stars. The dark disc is formed as the baryonic disc of the galaxy draws satellites closer to the disc plane by dynamical friction, where they are disrupted by the gravitational potential of the galaxy. In case of the existence of such a co-rotating dark disc, the dark matter velocity distribution gets an additional component with relatively low velocities.

A dense WIMP population is expected in the center of heavy celestial bodies such as the Sun or the Earth. This population arises when dark matter particles from the galactic halo become bound in the gravitational potential of the solar system as it passes through the Milky Way. These particles may then scatter weakly on nuclei in the Sun or Earth and loose energy, after which they get trapped. Over time, this leads to an accumulation of dark matter in the center of the celestial body. If the accumulated dark matter density reaches a high enough value, it may self-annihilate, generating a flux of Standard Model particles which is spectrally dependent on the annihilation channel and WIMP mass. The presence of a thick dark disc in the Milky Way would enhance the WIMP capture in the Earth, which would lead to a higher neutrino flux than expected, as discussed further in this thesis.

Only neutrino telescopes are able to look for these signals, as neutrinos are the only Standard Model particles which can escape the celestial bodies. While many searches for a flux of high-energy neutrinos coming from the self-annihilation of Solar WIMPs have already been done, only few experiments searched for an excess of neutrinos from WIMP annihilations in the center of the Earth. The most recent (yet unpublished) limit comes from the ANTARES neutrino telescope located in the Mediterranean Sea. Prior to this result, one has to go back to the Earth WIMP results of the predecessor of ICECUBE, the AMANDA neutrino telescope, located at the South Pole.

The indication of the possible existence of a dark disc, which would lead to an increased neutrino flux, together with the fact that no Earth WIMP search has been done yet with ICECUBE, were the main motivations to perform the first search for Earth WIMP-induced neutrinos with the ICECUBE neutrino detector. ICECUBE is a cubic kilometer detector buried deep in the South Pole ice, which, just as AMANDA and ANTARES, records the Cherenkov emission of high energy charged particles that cross the detector volume.

In this thesis, the first Earth WIMP search with ICECUBE will be presented. This

Structure of the thesis

Chapter 2: The aim of this chapter is to give a brief overview of the status of the dark matter problem, both on theoretical, as well as the experimental side. First the Lambda Cold Dark Matter model, which naturally incorporates a dark matter component into cosmology, is introduced. Next, it is discussed that the hypothetical neutralino, arising from supersymmetric theories beyond the Standard Model, is an excellent candidate for the Weakly Interacting Massive Particle (WIMP). After describing this particle, its distribution in the Universe, and in galaxies, such as our Milky Way, is discussed. Furthermore, an overview of the different detection methods is given, along with the current experimental status. At the end of the chapter, the physics behind WIMP capture and annihilation in the Earth, is discussed.

Chapter 3: In this chapter, the underlying physics related to indirect detection of dark matter from the center of the Earth using muon neutrinos is discussed. First, it is explained how neutrinos are created in the decay of standard model particles, which are produced during the WIMP annihilation. Next, the neutrino-nucleon interaction is discussed. Also a brief discussion on neutrino oscillations is given, as, considering the energy scales which are relevant in this analysis, this is an important feature. Finally, an overview on how the daughter neutrino induced muons lose their energy in ice, and how they can be detected via Cherenkov radiation, is given.

Chapter 4: In this chapter, an overview is presented of the technical aspects of the ICECUBE Neutrino Detector. The overview starts with a discussion on the ice properties and the sensors that are used, and goes up to the low level data treatment at the South Pole.

Chapter 5: In this chapter, the basics of the ICECUBE data processing are described. These basics consist of hit calibration and cleaning on one hand, and reconstruction of the direction, starting and stopping points and energy of the events on the other hand. A description is given of all the cleaning and reconstruction algorithms that will be used in the present analysis.

Chapter 6: The analysis presented in this thesis is based on data recorded by ICECUBE during its first year after completion. The experimental and simulated data which are used in the present analysis, are described in this chapter.

Chapter 7: In this chapter an overview is given of the selection methods and filters which were used in this analysis. These methods and filters were applied to remove the noise and atmospheric particles that trigger the detector, but at the same time keep as much of the triggered signal events as possible. ICECUBE triggers at a rate of roughly 4 kHz ($\mathcal{O}(10^{11})/\text{year}$), while the expected WIMP-induced muon flux is at most at the order of a few μHz ($\mathcal{O}(10^3)/\text{km}^2/\text{year}$). A dedicated event selection will

thus be needed, as the expected signal is hidden in the overwhelming background. To make the Earth WIMP analysis efficient for both low and high WIMP masses, the analysis will be split in 2 parts, based on reconstructed energy. Both data samples will then be further filtered, until the rate in both samples is reduced to the mHz level ($\mathcal{O}(10^4)$ /year).

This chapter is one of the core chapters of this thesis, as most of the effort of the present analysis went into the development of a dedicated and sophisticated event selection.

Chapter 8: In this chapter, the sensitivity of the present analysis will be calculated. The reconstructed zenith angle distributions of the signal and background will be used as Probability Density Functions to test hypotheses with μ_s signal events in the final dataset. The sensitivity will then be calculated for different WIMP masses in the range 10 GeV-10 TeV, by testing the background-only hypothesis ($\mu_s = 0$), based on background simulations.

This chapter is, together with the previous chapter, one of the key chapters in the thesis, as the results of the analysis depend crucially on the event selection as well as the statistical method.

Chapter 9: In this chapter, the zenith distribution of the complete IC86-I dataset will be analyzed to see if there is a neutrino excess from the direction of the center of the Earth. This analysis will be done on the final samples from Chapter 7, using the statistical method presented in Chapter 8. Before comparing the experimental data with the background simulation, the uncertainties on the latter distributions will be studied. The results will then be compared to the results of other experiments. Presenting the final results, this becomes the most important chapter of the thesis.

Chapter 10: Finally, a summary of the work described in this thesis will be given, putting forward the most interesting parts of the analysis. Also an overview of the possible improvements for future analyses will be presented.

Final note: in this thesis, we will use natural units adopted in particle physics, hence $c = 1$.

CHAPTER 1. AN INDIRECT SEARCH FOR DARK MATTER IN THE CENTER
OF THE EARTH WITH ICECUBE

There are known knowns. These are things we know that we know. There are known unknowns. That is to say, there are things that we know we don't know. But there are also unknown unknowns. There are things we don't know we don't know.

Donald H. Rumsfeld

2

A brief introduction to dark matter

The aim of this chapter is to give a brief overview of the status of the dark matter problem, which is one of the great experimental and theoretical challenges in modern physics, and has been a problem for over 80 years (Section 2.1). According to the latest measurements, dark matter makes up about 27% of all the energy in the Universe and roughly 80% of all the matter, as presented in Section 2.2.

There are many theoretical candidates which could describe this dark matter, but the most popular one is the Weakly Interacting Massive Particle (WIMP), which is, as its name suggests, a particle which only interacts weakly and probably has a mass of the order GeV-TeV. The hypothetical neutralino, the Lightest Supersymmetric Particle (LSP), is an excellent candidate for the WIMP, as explained in Section 2.3.

Thanks to simulations on the one hand and observations of e.g. radial velocities of stars on the other hand, a more detailed view of the distribution of dark matter in galaxies, such as our Milky Way has been provided. This will be discussed in Section 2.4.

Many experiments are looking for a signal from either a WIMP, or other dark matter candidates, but so far no compelling evidence has been found. As discussed in Section 2.5, these experiments can be divided in three classes, direct, indirect and collider experiments.

As the aim of the work presented in this thesis is to look for a neutrino signal from WIMP annihilations in the center of the Earth, it is important to understand the physics behind WIMP capture and annihilation in the Earth. This will be discussed in Section 2.6.

2.1 Introduction

The astrophysicist Zwicky was the first to notice the presence of so-called dark matter. In 1933 Zwicky estimated the mass of the Coma Cluster of galaxies by observing the motions of galaxies near the edge of the cluster on the one hand, and by estimating the brightness in the cluster by counting the number of galaxies on the other hand [1]. He found that the brightness was much smaller than he expected for the amount of mass that was present, and hence there had to be a large amount of non-luminous, dark, matter.

Today, more than 80 years later, much more evidence exists for the presence of this dark matter. The most convincing and direct evidence comes from the observations of orbital velocities of stars versus their distance from the center of spiral galaxies. From these observations, we learn that most of the luminous matter in spiral galaxies is concentrated in the center, so the radial velocity v_{rad} is expected to behave as

$$v_{rad} = \sqrt{\frac{GM(r)}{r}}, \quad (2.1)$$

where G is Newtons constant, $M(r)$ is the mass density profile and r is the distance to the center of the galaxy. Fig. 2.1 shows the expected and the measured rotation curves. A possible explanation for the discrepancy between the observed rotation curve (solid line) and the expected rotation curve from the centered luminous matter (dashed line) and the gas (dotted line) is provided by including a halo of dark matter (dashed-dotted line).

This dark matter is one of the great experimental and theoretical challenges in modern physics, as although it has a big contribution to the energy density of the Universe, only very little is known about this energy component.

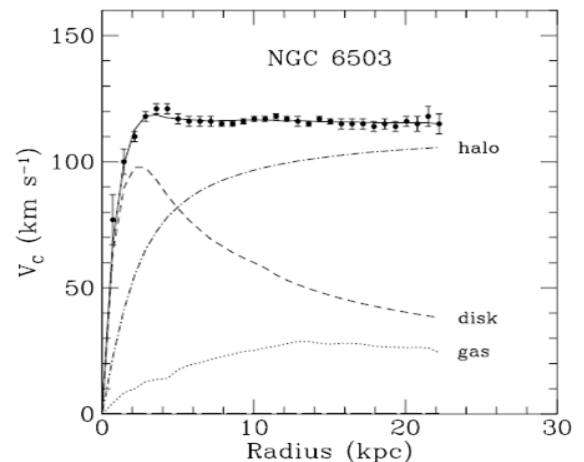


Figure 2.1: Rotation curve of NGC 6503. The dotted, dashed and dash-dotted lines are the contributions of gas, disk and dark matter, respectively. Figure from [2].

2.2 The Lambda Cold Dark Matter model

The most generally accepted model of the Universe in which the observed dark matter is incorporated is the *Lambda Cold Dark Matter* (Λ CDM) model. This Λ CDM model, referred to as the *standard cosmological model* [3], is based on the so-called *Big Bang* scenario. According to this scenario, the universe expanded from a hot and highly compressed state to the form it has today, in about 10^{10} years. This Big Bang model finds its roots in Hubble's law, which states that the observed recession velocity, v , of an astrophysical object is directly proportional to the distance of the object, d , to the observer [4]

$$v = H_0 \cdot d, \quad (2.2)$$

where $H_0 = (67.8 \pm 0.9) \text{ km s}^{-1} \text{ Mpc}^{-1}$ is the present value of the Hubble parameter $H(t)$ [5]. From Eq. (2.2) it follows that the larger the distance between two objects, the faster they move away from each other. This is nicely explained by an expanding universe, as is the case in the Big Bang model.

If we assume that the Universe is isotropic and homogeneous, its metric is given by the *Friedmann-Lemaître-Robertson-Walker metric* [6]. The solutions of the *Einstein Field Equations* [6] for this metric lead to the *Friedmann Equations*

$$\left(\frac{\dot{a}}{a}\right)^2 \equiv H(t)^2 = \frac{8\pi G}{3}\rho - \frac{\kappa}{a^2} \quad (2.3)$$

$$\frac{\ddot{a}}{a} = -\frac{4\pi G}{3}(\rho + 3p), \quad (2.4)$$

where $a(t)$ is a dimensionless scale factor, which represents the size of the Universe, G is the gravitational constant, κ is a constant describing the *curvature* of the universe, ρ is the total average energy density and p is the pressure. $H(t) = \dot{a}/a$ is the Hubble parameter at time t , and is equal to H_0 at present.

Different components (matter, radiation and vacuum energy, see below) contribute to the total energy density in the Universe, each with their energy density ρ_i . The abundance Ω_i of each of these components is written as

$$\Omega_i \equiv \frac{\rho_i}{\rho_c}, \quad (2.5)$$

where ρ_c is the total average density in the case of a flat Universe ($\kappa = 0$), often referred to as the *critical density*

$$\rho_c = \frac{3H(t)^2}{8\pi G}. \quad (2.6)$$

The total abundance Ω is given by the sum of the individual abundance Ω_i of each

component

$$\begin{aligned}
 \Omega &= \sum_i \Omega_i = \sum_i \frac{\rho_i}{\rho_c} \\
 &= \frac{\rho_i}{\rho_c} = \frac{8\pi G}{3H(t)^2} \rho \\
 &= \frac{\kappa}{H(t)a^2} + 1.
 \end{aligned} \tag{2.7}$$

The sign of κ thus determines if Ω is greater than, equal or less than one, and whether the Universe is open, flat or closed

$$\begin{array}{llllll}
 \rho < \rho_c & \leftrightarrow & \Omega < 1 & \leftrightarrow & \kappa < 0 & \leftrightarrow & \text{open Universe} \\
 \rho = \rho_c & \leftrightarrow & \Omega = 1 & \leftrightarrow & \kappa = 0 & \leftrightarrow & \text{flat Universe} \\
 \rho > \rho_c & \leftrightarrow & \Omega > 1 & \leftrightarrow & \kappa > 0 & \leftrightarrow & \text{closed Universe}
 \end{array}$$

The six parameter Λ CDM model is built by using the above mentioned Einstein Field Equations. According to this Λ CDM, the Universe is made up of radiation, ordinary matter, cold (slow) dark matter and vacuum energy Λ , where Λ , also referred to as the *Cosmological Constant*, is linked with a repulsive energy that is responsible for the accelerated expansion of the Universe. An overview of the six fundamental parameters which describe the Λ CDM model, together with their most recent values [5] is given in Table 2.1¹. Note that $h = H_0/(100\text{km s}^{-1}\text{Mpc}^{-1})$ is a dimensionless parameter.

Table 2.1: Overview of the fundamental parameters in the Λ CDM model. The indicated values, are the most recent results of the fit of the Λ CDM model to the Planck data [5], with their one standard deviation uncertainty.

parameter	brief explanation	current value
$\Omega_b h^2$	The physical baryon density	0.02230 ± 0.00014
$\Omega_c h^2$	The physical dark matter density	0.1188 ± 0.0010
t_0	The age of the Universe	(13.799 ± 0.021) Gyr
n_s	The scalar spectral index	0.9667 ± 0.0040
Δ_R^2	The curvature fluctuation amplitude	$2.441_{-0.092}^{+0.088} \times 10^{-9}$
τ	Reionization optical depth	0.066 ± 0.012

The values of the six parameters, and their derived parameters, are calculated by modeling the temperature power spectrum of the Cosmic Microwave Background (CMB). The variations in the CMB temperature reflect the situation of the Universe at the time the CMB radiation decoupled from matter, an epoch referred to as *recombination*. Recombination occurred roughly 380.000 years after the Big Bang [7]. Studying these variations

¹The reader is referred to [5] for a detailed description of all the involved parameters.

gives insight to the composition of the Universe. The most recent measurements of the temperature variations of the CMB come from the Planck satellite [5], which measures the various angular scales of these temperature inhomogeneities. Extraction of the temperature inhomogeneities in a multipole expansion allows a detailed study of the temperature angular power spectrum of the primary CMB. In Fig. 2.2 the temperature angular power spectrum of the primary CMB data measured by Planck is shown, together with the fitted six-parameter Λ CDM model.

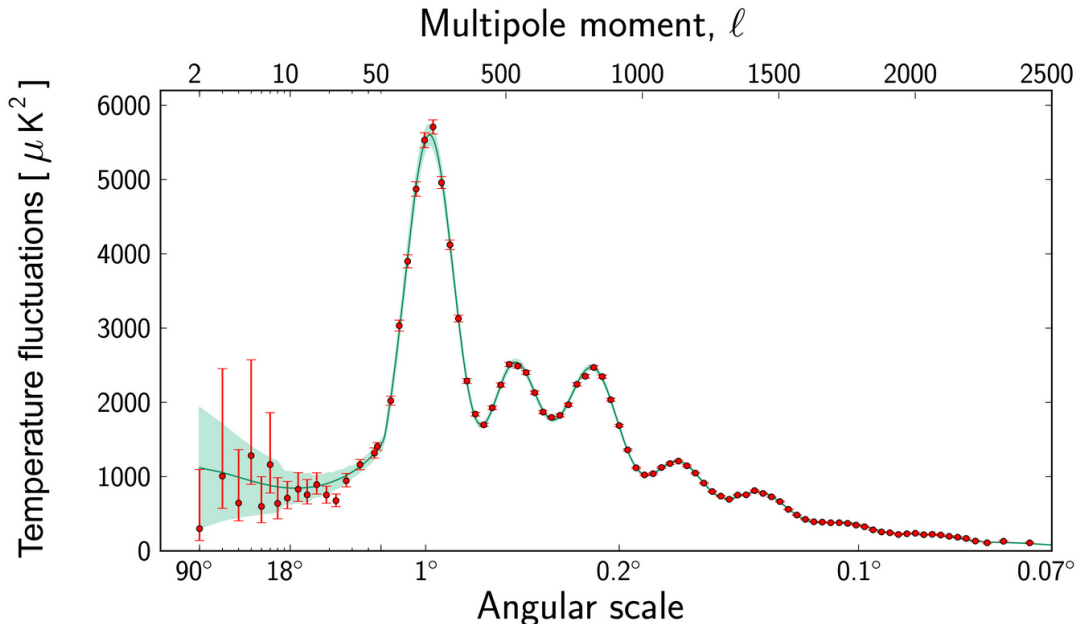


Figure 2.2: The temperature angular power spectrum of the primary CMB data measured by Planck (red dots with errorbars), together with the fitted six-parameter Λ CDM model (blue line). Figure from [5].

The best-fit model indicates an expanding Universe which is spatially-flat ($\kappa = 0$) and is isotropic and homogeneous on large scales. It follows that $\Omega = \sum_i \Omega_i = 1$ (see Eq. (2.7)). According to the Λ CDM, three different components make up the energy content of the Universe, each with their own abundances Ω_i [5],

1. radiation, $\Omega_R \sim 10^{-4}$,
2. matter, $\Omega_M \sim 0.31$,
3. vacuum energy, $\Omega_\Lambda \sim 0.69$.

Hence, roughly one third of the energy density in our current universe consists of matter, which is made up of a combination of known (referred to as *baryonic*) matter and cold dark matter, with physical densities [5] $\Omega_b h^2 = 0.02230 \pm 0.00014$ and $\Omega_c h^2 = 0.1188 \pm 0.0010$

respectively, as mentioned in Table 2.1. Ordinary baryonic matter thus makes up roughly 20% of the matter in the universe, while the other 80% is made up of dark matter.

Even though there are many observational evidences for the presence of dark matter², like e.g. the rotation curves of stars (see Section 2.1), gravitational lensing [8], the velocity dispersion of stars in dwarf spheroidal galaxies [9] and the CMB (as discussed above), it remains unknown what the dark matter is actually made of. Several theoretical candidates arise from yet unobserved theories like the supersymmetric extension of the Standard Model [10, 11] or models with extra space dimensions [12]. To be in agreement with the Λ CDM model, these candidates should have an abundance

$$\Omega_c = \Omega_M - \Omega_b \sim 0.27. \quad (2.8)$$

Note that this number (Ω_c) can be the sum of many different kind of particles. The Standard Model neutrinos for example have a small contribution, but the experimental upper-limit on their relic density is only [13]

$$\Omega_\nu h^2 \lesssim 0.009, \quad (2.9)$$

Neutrinos are thus not abundant enough to be the dominant component of the dark matter. The relic density (like e.g. $\Omega_\nu h^2$) for a generic stable and annihilating CDM particle species X can be approximated by [2]

$$\Omega_X h^2 \approx \frac{3 \times 10^{-27} \text{cm}^3 \text{s}^{-1}}{\langle \sigma_{Av} \rangle}, \quad (2.10)$$

where $\langle \sigma_{Av} \rangle$ is the velocity-averaged self-annihilation cross-section. If $\langle \sigma_{Av} \rangle$ is known for a generic particle species X , its thermal abundance can be calculated.

2.3 Candidates

It was already mentioned that there are several theoretical candidates for the dark matter particles and that the Standard Model neutrinos have a small contribution to the dark matter. In this section, the focus lies on today's most promising candidate: *the neutralino*. There are many more candidates which are not discussed here like for example axions [14] and universal extra dimensions [15]. For an overview of these candidates, the reader is referred to [2].

The neutralino is a particle that arises from Supersymmetry (SUSY), which is a theory that goes beyond the Standard Model [11]. Supersymmetry is a symmetry between fermions and bosons, hence generators are introduced which change fermions into bosons and vice versa

$$Q|\text{fermion}\rangle = |\text{boson}\rangle; \quad Q|\text{boson}\rangle = |\text{fermion}\rangle. \quad (2.11)$$

²see [2] for an overview of the most important observational evidences.

According to Supersymmetry, each Standard Model (SM) particle thus has a supersymmetric partner with a half integer spin difference. Supersymmetry provides a natural solution to the *hierarchy problem* and unifies the gauge coupling scales at $M_U \sim 2 \cdot 10^{16}$ GeV, which has been taken as a strong hint in favor of Grand Unified Theories [10, 11].

The *minimal* extension of the Standard Model of particle physics is described by the Minimal Supersymmetric Standard Model (MSSM). The MSSM contains the smallest possible field content necessary to give rise to all the fields of the Standard Model (an overview is given in Table 2.2). The fact that the MSSM is such an interesting theory in the search for dark matter, is because one of its basic elements is *R-parity conservation*. R-parity is a multiplicative quantum number, defined as

$$R \equiv (-1)^{3B+L+2s}, \quad (2.12)$$

where B is the baryon number, L the lepton number and s the spin of the particle. It thus follows that

$$\begin{cases} R = +1 & \text{for SM particles,} \\ R = -1 & \text{for SUSY particles.} \end{cases} \quad (2.13)$$

Conservation of R-parity implies that SUSY particles can only decay into an odd number of SUSY particles (plus SM particles), from which it can be concluded that there should be a Lightest Supersymmetric Particle (LSP) if the theory is correct. This LSP is an excellent dark matter candidate, since it is stable and can only be destroyed via pair annihilation. This LSP is electrically neutral and colorless [11]. The MSSM contains 4 of these electrically neutral and colorless particles, namely the *neutralinos* $\tilde{\chi}_1^0$, $\tilde{\chi}_2^0$, $\tilde{\chi}_3^0$ & $\tilde{\chi}_4^0$ (see table 2.2), which are a combination of gauginos and Higgsinos. In this thesis, we will focus on the lightest neutralino namely $\tilde{\chi}_1^0$, from now on simply noted as χ .

Assuming that χ is the dominant component of dark matter, $\Omega_\chi h^2$ should be

$$\Omega_\chi h^2 \approx \frac{3 \cdot 10^{-27} \text{cm}^3 \text{s}^{-1}}{\langle \sigma_{Av} \rangle} \sim \mathcal{O}(0.1), \quad (2.14)$$

according to the latest Planck results for $\Omega_c h^2$. The above equation is satisfied if $\langle \sigma_{Av} \rangle$ is of the order of a picobarn to a femtobarn, which is the typical size for a weak process. So the dark matter particles should be massive and weakly interacting, which is why they are often referred to as Weakly Interacting Massive Particles (WIMPs). Neutralinos satisfy these conditions and are thus a good WIMP candidate.

The analysis described in this thesis will be optimized to search for WIMPs. In the remainder of this thesis, the symbol χ will be used to refer to these (generic) WIMPs.

Table 2.2: SM particles and their superpartners in the MSSM (adapted from [11]).

Standard Model particles and fields		Supersymmetric partners			
Symbol	Name	Interaction eigenstates Symbol	Name	Mass eigenstates Symbol	Name
$q = d, c, b, u, s, t$	quark	\tilde{q}_L, \tilde{q}_R	squark	\tilde{q}_1, \tilde{q}_2	squark
$l = e, \mu, \tau$	lepton	\tilde{l}_L, \tilde{l}_R	slepton	\tilde{l}_1, \tilde{l}_2	slepton
$\nu = \nu_e, \nu_\mu, \nu_\tau$	neutrino	$\tilde{\nu}$	sneutrino	$\tilde{\nu}$	sneutrino
g	gluon	\tilde{g}	gluino	\tilde{g}	gluino
W^\pm	W -boson	\tilde{W}^\pm	wino	} $\tilde{\chi}_{1,2}^\pm$	chargino
H^-	Higgs boson	\tilde{H}_1^-	higgsino		
H^+	Higgs boson	\tilde{H}_2^+	higgsino		
B	B -field	\tilde{B}	bino	} $\tilde{\chi}_{1,2,3,4}^0$	neutralino
W^3	W^3 -field	\tilde{W}^3	wino		
H_1^0	Higgs boson	\tilde{H}_1^0	higgsino		
H_2^0	Higgs boson	\tilde{H}_2^0	higgsino		
H_3^0	Higgs boson				

2.4 Dark matter distribution in the Universe

While it remains unknown what the dark matter actually is made up of, the understanding of its distribution in the Universe keeps on improving.

At the largest scales, the dark matter distribution can be modeled by CPU intensive N-body simulations [16]. In these simulations, only dark matter and dark energy are assumed, as it is too complex and CPU intensive to include baryonic matter at these scales. From these simulations it seems that dark matter is not completely homogeneously distributed in the Universe, but that there are voids, walls and filaments in the dark matter distributions, which seems to be in agreement with the large scale distribution of galaxies [16, 17].

The distribution of dark matter inside galaxies can be modeled thanks to measurements of e.g. the radial velocities of stars [1, 18] and weak lensing [19] on the one hand and numerical N-body simulations [20] on the other hand. The general view on the distribution of dark matter particles in galaxies is that they form a fairly smooth spherical halo around an embedded baryonic component like e.g. a central bulge and a spiral disk. In particular, there is a quite good consensus on the dark matter density, ρ_{DM} , and distribution in the Milky Way, which are inferred from the rotational kinematics of the baryons [21]. The two density profiles which are mainly considered are the Navarro-Frenk-White NFW [22], and the Burkert [23] model. Fig. 2.3 shows the dark matter density in the Milky way as a function of the distance to the center for some fits of these models based on simulations [24] or observational data [25]. Note that the NFW model

is *cuspy*, i.e. it gives rise to a rapidly increasing dark matter density towards the center, whereas the dark matter density is more constant in the center in the Burkert, *core*, model.

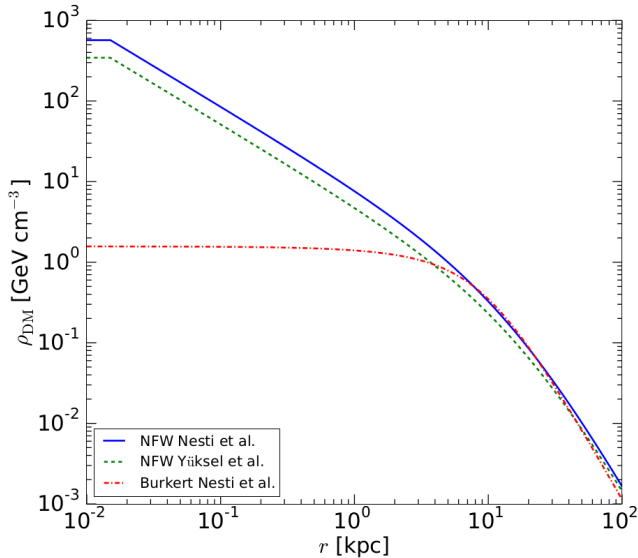


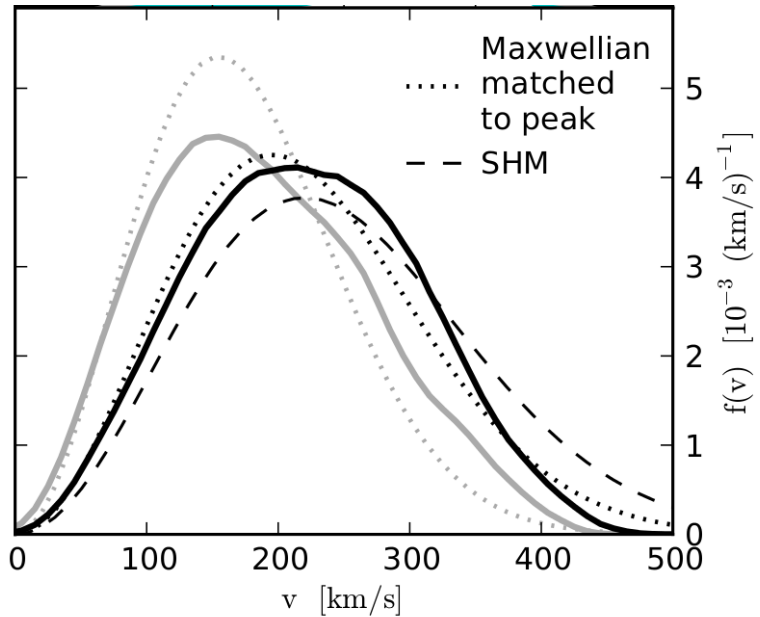
Figure 2.3: Dark matter mass density profile in the galactic halo as a function of the distance from the GC for the DM halo models listed. Figure from [26].

Besides studying the distribution of the dark matter, one can also study its velocity distribution inside galaxies, and more precisely in the Milky way. The velocity distribution of the dark matter particles is very sensitive to theoretical assumptions, as different models for the halo lead to different dark matter velocity distributions. The most popular halo model is the Standard Halo Model (SHM), in which the dark matter velocities follow a Maxwell-Boltzmann distribution. This is modeled as a smooth, spherically symmetric density component with a non-rotating Gaussian velocity distribution. In this model, the average velocity of the Earth with respect to the dark matter halo of the Milky way is believed to be $v_0 = 220$ km/s and the velocity dispersion of the dark matter particles at the location of the Earth is in general considered to $v_{\text{rms}} = 270$ km/s [27, 28].

Galaxy formation simulations including baryons indicate that the dark matter velocity distributions deviate from this SHM, possibly leading to lower dark matter velocities at the location of the Earth [20]. This is shown in Fig. 2.4, in which the dark matter velocity distributions in the Milky Way are shown for dark matter simulations with (gray) and without (black) baryons. The solid lines in this plot indicate the distributions found by the ERIS simulation [20], the dotted lines indicate the Maxwellian fit and the dashed line indicates the SHM with the parameters indicated above.

Some simulations also show the possible existence of a thick disc of dark matter, with the kinematics similar to the thick disc of stars, which is formed as the baryonic disc of the Milky Way draws satellites closer to the disc plane by dynamical friction, where they are disrupted by the gravitational potential of the Milky Way [29]. According to

Figure 2.4: Dark matter velocity distribution in the Milky Way for dark matter simulations (ERIS [20]) with (solid gray) and without (solid black) baryons. The Maxwellian fit to the data is indicated by the dotted lines and the dashed line indicates the SHM. Figure from [20].



e.g. the simulations discussed in [30, 31], this disk has a mid-plane density $\rho_{DM,d}$ in the range between 0.25 – 1.5 times the dark halo density at the location of the Solar System, $\rho_{DM,H,local}$.

In case of the existence of a co-rotating dark disc, the dark matter velocity distribution gets an additional component at low velocities, as indicated in Fig. 2.5, where the contributions of dark discs with different dark matter densities are shown on top of the Standard Halo Model (SHM, referred to as SMH in the plot). Note also that the contribution of this dark disc depends on the dark matter density in this disc $\rho_{DM,d}$ compared to the density in the halo $\rho_{DM,H}$.

The latest constraints (from observations and simulations) on the local dark matter density give values for $\rho_{DM,local}$ in the range between 0.20-0.56 GeV/cm^3 [21]. These measurements indicate that the dark matter is distributed in a spherical halo, with little or no halo flattening in the disc plane, suggesting that there is no dark disc. The results are not conclusive yet, as the current measurements all have large (systematic) uncertainties.

2.5 Experiments

Many experimental efforts to search for a dark matter signal exist, and many more are planned for the future. Typically, these detectors are searching for WIMP signals, but also other types of dark matter particles can be probed. The experiments can be divided in three main classes. A first class of experiments, *direct detection* experiments, search for

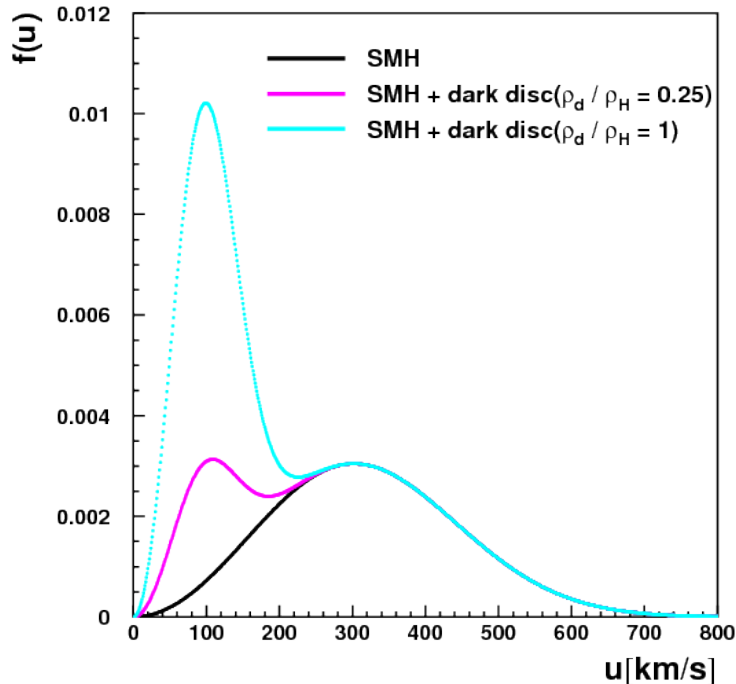


Figure 2.5: Expected dark matter velocity distribution in the Milky Way for the Standard Halo Model (black), as well as for two examples of a contribution of a co-rotating dark disc, with relative densities $\rho_{d,DM}/\rho_{H,DM} = 0.25$ (pink) and $\rho_{d,DM}/\rho_{H,DM} = 1$ (light blue). Figure from [32].

the recoil energy of a WIMP particle scattering on an atom inside the detector volume. A second class of experiments are *indirect detection* experiments. These search for the radiation that is produced in either dark matter self-annihilation or dark-matter decay. The last class, *collider experiments*, try to find dark matter through its production in particle collisions. A summary of the WIMP-SM-particle processes in each of these classes of searches is given in Fig. 2.6.

So far, no clear signal for dark matter has been found in any of these search channels. Some observations hint at a possible dark matter signal. Nevertheless, these hints/claims are still inconclusive, as there are other possible physical explanations for these, and the signals have not yet been confirmed by other experiments. In most cases, an observation in at least two independent experiments would be needed to confirm a signal.

2.5.1 Direct detection

Direct detection experiments try to measure the recoil energy Q of a WIMP-particle scattering on an atom in a lattice. The differential recoil energy spectrum dR/dQ (where R is the rate, expressed in (event/kg/day)) of such an interaction between a WIMP of mass m_χ and a nucleus of mass m_N depends on the masses of the WIMP and the nucleus, the elastic scattering cross-section between the WIMP and nucleus $\sigma_{\chi-N}$, the local WIMP density $\rho_{DM,local}$ and velocity v_0 and the nuclear form factor $F(Q)$ in the

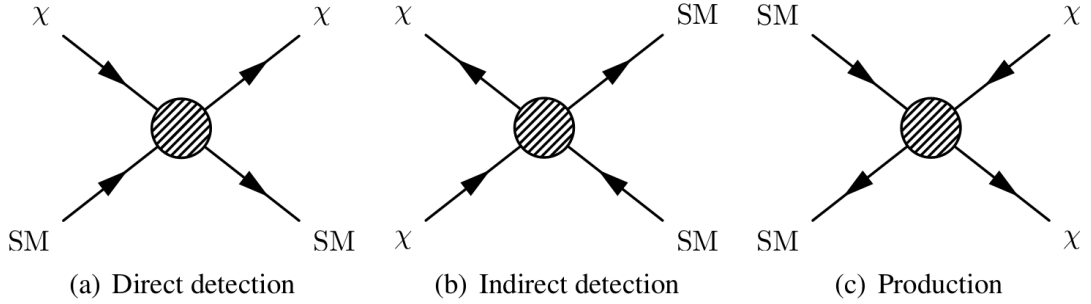


Figure 2.6: Simplified Feynman diagrams showing the three different dark matter detection channels described in the text. In these diagrams, time goes from left to right, so the two particles on the left hand side interact and produce the particles on the right hand side. The direct detection experiments look for the recoil of a WIMP, χ , on a Standard Model particle, SM, in the detector, as shown in (a). Indirect detection experiments either look for the Standard Model annihilation products of WIMPs (b) or the decay products of a WIMP (not illustrated in this figure). Collider experiments look for the creation of WIMPs in Standard Model particle collisions (c). Figure from [33].

following way [34]

$$\frac{dR}{dQ} = \frac{\sigma_{\chi-N} \rho_{DM,local}}{\sqrt{\pi} v_0 m_\chi m_r^2} F^2(Q) T(Q), \quad (2.15)$$

where $T(Q)$ is a dimensionless integral over the local WIMP velocity distribution and $m_r = \left(\frac{m_\chi m_N}{m_\chi + m_N} \right)$ is the WIMP-nucleus reduced mass. The WIMP-nucleon cross-section $\sigma_{\chi-N}$ is a combination of the spin-independent component $\sigma_{\chi-N}^{SI}$ and spin-dependent component $\sigma_{\chi-N}^{SD}$ of the interaction cross-section, which are responsible for scalar interactions and axial-vector interactions respectively. In the case of spin-independent scattering $\sigma_{\chi-N} \approx A^2 \sigma_{\chi-p}$, meaning that heavier atoms will enhance the WIMP interactions in the detector. For spin-dependent scattering, the dependence on the nuclear properties of the target is proportional to the total spin J .

Different techniques are used to detect these nuclear recoils from dark matter interactions and distinguish them from events caused by background. These techniques can be separated in three major classes, as indicated in Fig. 2.7, namely the detection of a given deposited energy caused by scintillation, ionization, or phonon signals. Experiments use one of these techniques or a combination of multiple techniques. A large part of the effort goes in discriminating the WIMP signal from recoils caused by background events. By placing these detectors deep under ground, the background coming from cosmic rays is reduced, but there still remains a background from radioactive materials and photons. A complementary approach is provided by superheated liquid detectors, which operate like bubble chambers.

Some experiments try to remove all the background, by e.g. discriminating the events

based on their relative scintillation, ionization, or phonon signals, which are different for WIMPs than for background events, see e.g. [35, 36, 37, 38]. Other experiments look for seasonal or annual modulations of the event rate, which would be caused by the revolution of the Earth around the Sun [39]. Future experiments are planned to also look for directional variation of the recoiling nucleus. One expects to measure the effect of the motion of the solar system through the WIMP halo, especially in the case of non-rotating WIMP halo [40]. A correlation between the direction of the recoiling nucleus and the motion of the Solar System, would thus indicate a signal, as this effect is not expected for background events.

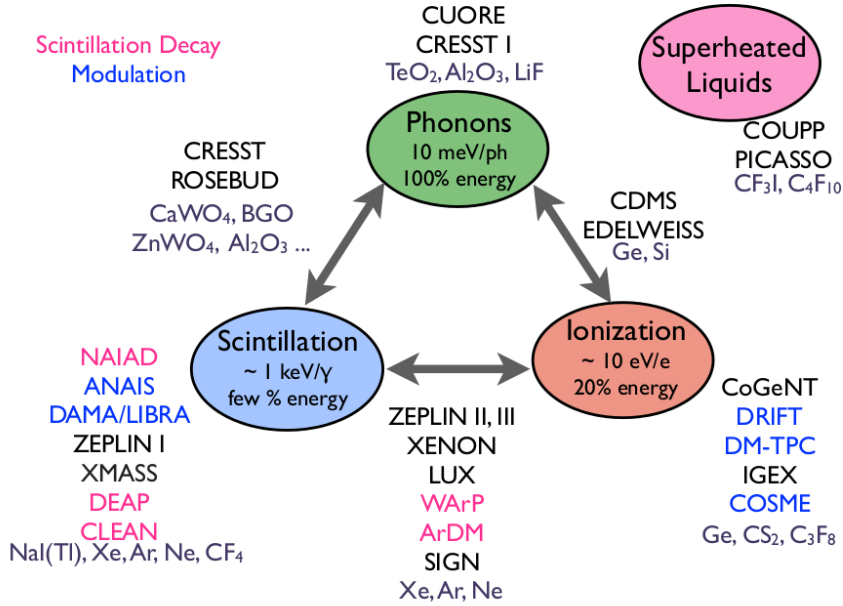


Figure 2.7: Overview of the different direct dark matter detectors, categorized according to the way they try to detect the dark matter particles. Figure from [34].

The DAMA/LIBRA experiment claims to have detected dark matter, as they see an annual modulation of the event rate which is not expected for background [41]. This result is controversial though, as it is in conflict with the non-observation of WIMP signal events in other dark matter experiments with similar or better sensitivity.

An overview of the current best 90% Confidence Level (CL) upper-limits of direct dark matter experiments on the spin-independent WIMP-nucleon cross-section $\sigma_{\chi-N}^{SI}$ is shown in Fig. 2.8. The green and pink regions show the phase space which has been excluded by the non-observation of signal events in the CDMSlite [42] (and more recently also CRESST [38], but this limit is not included in the figure) and LUX [36] detectors, which respectively have the best sensitivity in the 1-10 GeV and 10-10⁴ GeV WIMP

mass range. Other colored areas like e.g. the brown area indicate the phase space in which WIMPs would exist if the observation of DAMA/LIBRA [39] is really due to a WIMP signal. In the considered WIMP framework, the WIMP explanation of the DAMA/LIBRA observation is thus ruled out by LUX. Note that also other direct detection experiments (CRESST [43], CoGeNT [44], CDMS Si [45]) have indications of a signal, but all of these have been ruled out by the recent data from LUX [36] and CDMSlite [42].

The yellow dashed-line at the bottom of the plot indicates the *neutrino floor* [46, 47]. Detectors with a sensitivity below this curve, will measure an irreducible neutrino background. These neutrinos are dominated by solar neutrinos in the WIMP mass region below $m_\chi < 10$ GeV, and for the higher masses the dominating neutrino background comes from atmospheric neutrinos and neutrinos from Diffuse Supernova Neutrino Background (DSNB) [46]. A possible way to overcome this problem, is by using direction-sensitive detectors, as explained above.

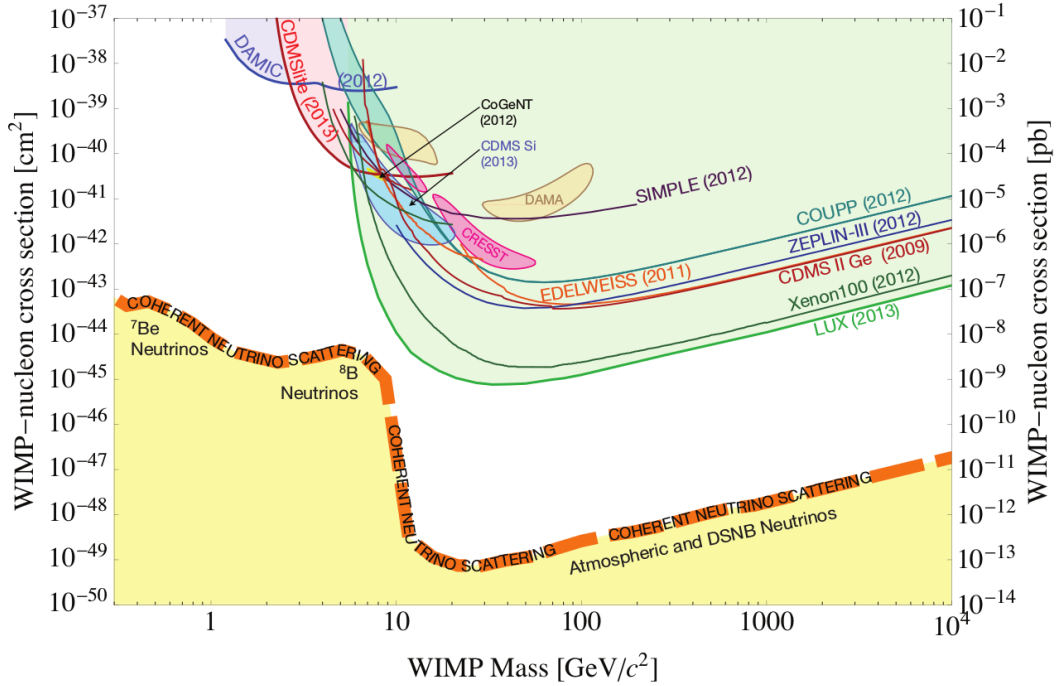


Figure 2.8: Upper limits at 90% CL (solid lines) of current direct dark matter experiments on the spin-independent WIMP-nucleon cross-section $\sigma_{\chi-N}^{SI}$. The green and pink regions show the phase space which has been excluded by the non-observation of signal events in the CDMSlite [42] and LUX [36] detectors. Other colored areas like e.g. the brown area indicate the phase space in which WIMPs would exist if the observation of DAMA/LIBRA [39] is really caused by a WIMP signal. The yellow dashed-line at the bottom of the plot indicates the *neutrino floor* [46, 47]. Figure from [46].

2.5.2 Indirect detection

Indirect detection experiments look for the radiation that is produced in either dark matter self-annihilation or dark-matter decay. These searches typically look for a signal from a region in which a high dark matter population is expected. Examples are e.g. Dwarf Galaxies or the center of the Milky Way. Different experiments look for an excess of particles (in a certain energy range) from these directions. Experiments such as the Fermi Large Area Telescope [48], HESS [49], MAGIC [50] and VERITAS [51] look for gamma rays produced by WIMP annihilations. Other experiments, like PAMELA [52] and AMS [53], look for a signal in the anti-proton or positron channel. Neutrino telescopes such as ICECUBE [54, 55], ANTARES [56] and Baikal [57] look for an excess of neutrinos from the direction of these locations with high dark matter densities.

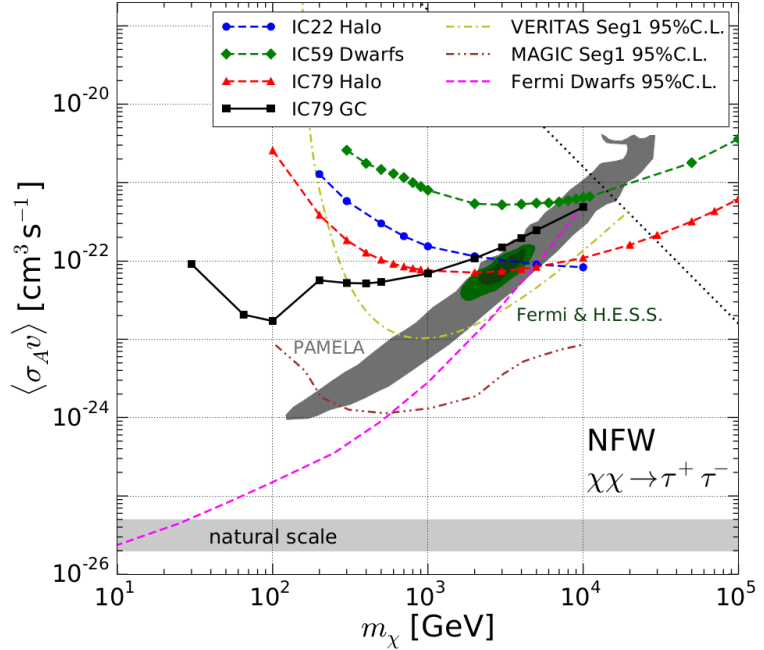
Recently, there has been a lot of discussion on the *Galactic Center GeV excess*, a clear excess in the Fermi-LAT gamma ray data, from the inner Galaxy, around energies of a few GeV. This excess could be explained by the annihilation of WIMPs in the center of the galaxy [58, 59, 60], but it could also be caused by millisecond pulsars [61]. PAMELA, Fermi and AMS reported an increased positron flux at high energies above expected background, which could be explained by a signal from WIMPs in the TeV range [62], but also in this case, pulsars and remnants of nearby supernovae provide a more standard astrophysical explanation [63, 64, 65].

Indirect searches which look in the direction of the center of the galaxy, or at galaxy clusters or dwarf galaxies, typically probe the WIMP self-annihilation cross-section times relative velocity $\langle\sigma_{Av}\rangle$. Upper limits have thus been placed on this quantity, as shown in Fig. 2.9, which shows the 90% CL upper-limits of several analyses as a function of the WIMP mass. The shaded areas indicate the regions of the phase space, in which the WIMPs would exist if the PAMELA excess (gray) or Fermi and HESS excess (green) would be caused by WIMPs. Note that the latest Fermi-LAT excess is not indicated in this plot.

A dense WIMP population is also expected in the center of heavy celestial bodies such as the Sun or the Earth. Dark matter particles from the galactic halo become bound in the gravitational potential of the solar system as it passes through the galaxy. These particles may then scatter weakly on nuclei in the Sun or Earth and loose energy, after which they get trapped. Over time, this leads to an accumulation of dark matter in the center of the celestial body. If the accumulated dark matter density reaches a high enough value, it may self-annihilate, generating a flux of Standard Model particles which is spectrally dependent on the annihilation channel and WIMP mass.

Only neutrino telescopes are able to look for these signals, as neutrinos are the only Standard Model particles which can escape the celestial bodies. In general, the Sun is a more promising source than the Earth, for the search of a flux of high-energy neutrinos coming from the self-annihilation of WIMPs. This is because the gravitational well of

Figure 2.9: Upper limits at 90% CL on the WIMP self-annihilation cross-section times relative velocity $\langle\sigma_A v\rangle$ as a function of the WIMP mass. The limits of several experiments are shown. The colored areas indicate the phase space in which the WIMPs would exist if the observation of the PAMELA excess (gray) or Fermi and HESS excess (green) is really caused by a WIMP signal. Figure from [55].



the Sun is orders of magnitude stronger than that of the Earth, leading to a much higher WIMP population in the Sun than in the Earth. Many searches for a flux of high-energy neutrinos coming from the self-annihilation of Solar WIMPs have already been done [66, 67, 68], and the current best limits on the spin-dependent WIMP-nucleon cross-section $\sigma_{\chi-N}^{SD}$ in WIMP mass range of 100 GeV-10 TeV range are set by these searches, as indicated in Fig. 2.10.

Only few experiments have looked for an excess of neutrinos from WIMP annihilations in the center of the Earth, which is the work described in this thesis. The most recent (yet unpublished) limit comes from ANTARES [70], and prior to this result, one has to go back to the AMANDA analysis [71].

A thick dark disc in the Milky Way would enhance the WIMP capture in the Earth, which would lead to a higher neutrino flux than expected, as discussed further in this thesis. The indication of the possible existence of a dark disc was one of the motivations to search for Earth WIMP-induced neutrinos with the ICECUBE neutrino detector.

2.5.3 Collider experiments

The interest in searching for dark matter signatures in data from colliders such as the Large Hadron Collider has gained a lot of interest in the past years [72]. These searches are generally looking for collisions with an energy or momentum imbalance in the final state. This imbalance could arise in two different ways, either by the creation of stable

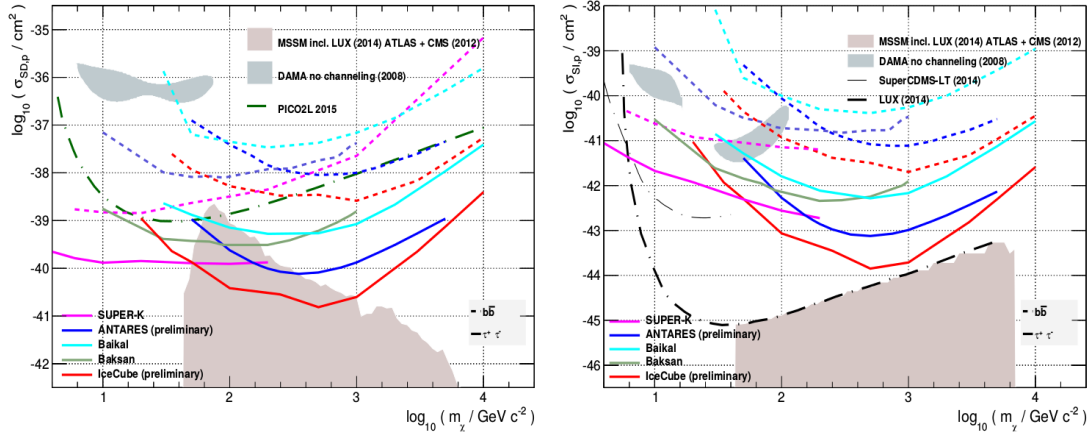


Figure 2.10: Upper limits of several experiments at 90% CL on the spin-dependent (left) and spin-independent (right) WIMP-proton cross-section as a function of WIMP mass. The limits on the $\tau^+\tau^-$ and $b\bar{b}$ annihilation channel are respectively represented by the solid and dashed lines. The blue colored regions indicate the phase space in which WIMPs would exist if the observation of DAMA is really caused by a WIMP signal, and the brown region shows the allowed parameter space in the 25-parameter MSSM. Figure from [69].

dark matter particles in the decay process of other particles or by creating a pair of dark matter particles through some *off-shell mediator*.

In the first case, the stable dark matter particles could e.g. be created at the end of the decay chain of other heavier new states. This would e.g. be the case if the dark matter particle is the supersymmetric neutralino, and R -parity is conserved.

The second case, direct off-shell creation of dark matter particles, could also happen in supersymmetric theories which conserve R -parity. To make this channel detectable, initial state radiation (ISR) gluons or photons should be emitted, such that one can search for monojet, monophoton or monolepton events.

These searches give the best upper-limits on the spin-independent $\sigma_{\chi-N}^{SI}$ and spin-dependent $\sigma_{\chi-N}^{SD}$ WIMP-nucleon cross-section for low WIMP masses with respectively $m_\chi < 3$ GeV and $m_\chi < 200$ GeV. This can be seen in Fig. 2.11, in which the results of several CMS searches [73] are shown for $\sigma_{\chi-N}^{SI}$ and $\sigma_{\chi-N}^{SD}$ as a function of the WIMP masses. As a comparison, the current best limits of direct and indirect searches are also shown on these plots, although it is very complicated to directly compare the results of different type of experiments, as assumptions have to be made before they can be compared in this way.

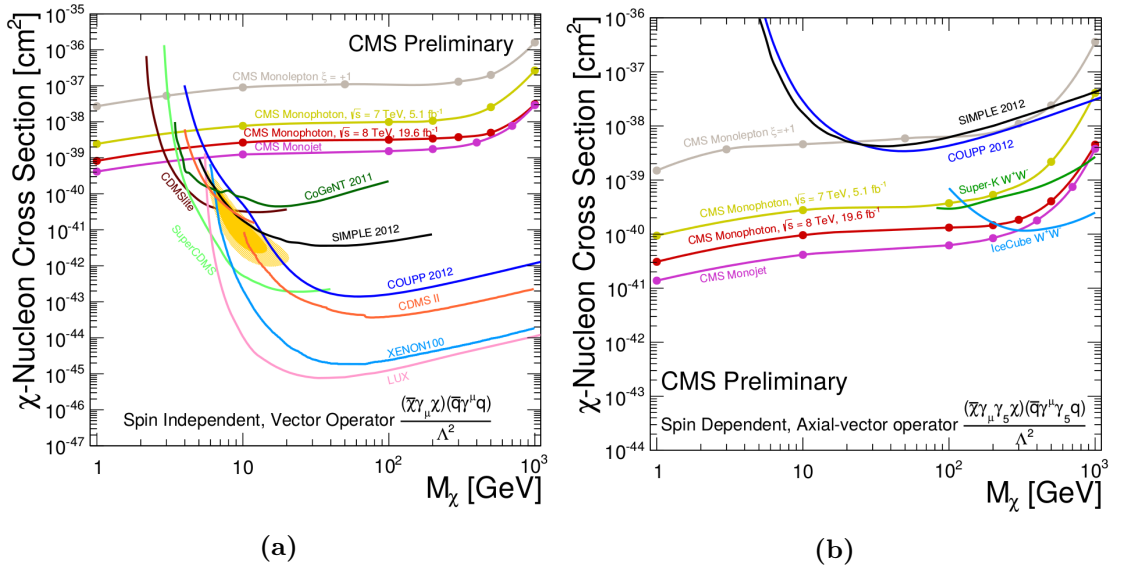


Figure 2.11: Upper limits of monojet, monophoton, and monolepton CMS searches at 90% CL on the spin-dependent (left) and spin-independent (right) WIMP-proton cross-section as a function of WIMP mass. As a comparison, 90% CL upper-limits of other direct and indirect experiments are shown. Figures from [73].

2.6 WIMPs in the center of the Earth

WIMPs accumulated in the center of the Earth will produce a unique signature in neutrino detectors such as ICECUBE, as vertically up-going muons.

The number of WIMPs, N , in a celestial body, as e.g. the Earth, depends on the capture (C_C), annihilation (C_A) and evaporation (C_E) of WIMPs in that body in the following way

$$\frac{dN}{dt} = C_C - C_A N^2 + C_E N, . \quad (2.16)$$

The evaporation (C_E) of WIMPs is a phenomenon in which WIMPs are ejected from the celestial body by hard elastic scattering from nuclei. This effect is negligible for WIMP masses above 10 GeV [28], and will thus be ignored in this work.

The capture (C_C) of WIMPs mainly depends on the WIMP-nucleon cross-section $\sigma_{\chi-N}$, the WIMP mass m_χ and the mass and distribution of the elements in the Earth. For capture in the Earth, the main contribution will thus come from the spin-independent component $\sigma_{\chi-N}^{SI}$ which is quadratically proportional to the atomic mass of the elements in the Earth, i.e. to A^2 .

The annihilation of the WIMPs (C_A) depends on the WIMP annihilation cross-section σ_A and the distribution of the WIMPs in the Earth, which is related to the WIMP mass [28]

$$C_A = \frac{\langle \sigma_A v \rangle \cdot (m_\chi / (10 \text{ GeV}))^{3/2}}{2\sqrt{8} \cdot 10^{25} \text{ cm}^3}, \quad (2.17)$$

where $\langle \sigma_A v \rangle$ is the velocity-averaged self-annihilation cross-section. The total annihilation rate, Γ_A , depends on σ_A and on the number of WIMPs, N ,

$$\Gamma_A = \frac{1}{2} C_A N^2. \quad (2.18)$$

The number of WIMPs N in a celestial body at a time t is calculated by solving Eq. 2.16 for N ,

$$\Gamma_A(t) = \frac{1}{2} C_C \tanh^2 \left(\frac{t}{\tau} \right), \quad (2.19)$$

where $\tau = (C_C C_A)^{-1/2}$ is the equilibrium time τ , which is defined by the time it takes for the annihilation rate and the capture rate to be in equilibrium. For the Earth, this equilibrium time is of the order of 10^{11} years if the spin-independent WIMP-proton cross-section is $\sigma_p^{SI} \sim 10^{-43} \text{ cm}^2$ [28]. Since the age of the solar system is $t_\oplus \approx 4.5 \text{ Gyr}$, $t_\oplus/\tau \ll 1$, so there is no equilibrium between the annihilation rate and the capture rate in the Earth, contrary to the Sun, in which most WIMP models predict $t_\odot/\tau \gg 1$. Even if equilibrium is not achieved, $\Gamma_A \propto C_C^2$, i.e. the higher the capture rate, the higher the annihilation rate and thus the neutrino-induced muon flux in neutrino detectors.

The rate at which WIMPs are captured in the Earth depends on the mass and the velocity of the WIMPs. If the WIMP mass is nearly identical to that of one of the

nuclear species in the Earth, the capture rate will increase considerably, as is shown in Fig. 7.2. It should be noted that recent direct detection limits [36] exclude cross-sections larger than $\sigma_p^{SI} = 10^{-43} \text{ cm}^2$ over a wide range of WIMP masses. This implies that the normalization in Fig. 2.12 will be about an order of magnitude lower, as the cross-section that is assumed in the calculation for the capture rate equals $\sigma = 10^{-42} \text{ cm}^2$ [74].

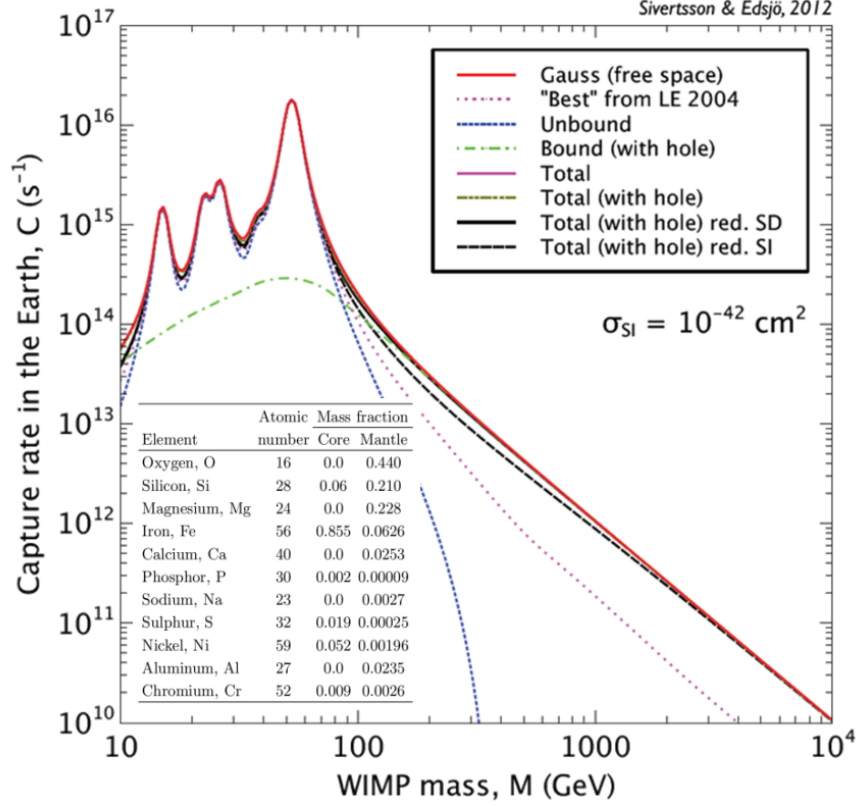


Figure 2.12: This figure shows the rate at which dark matter particles are captured to the interior of the Earth, for a scattering cross-section of $\sigma = 10^{-42} \text{ cm}^2$. The peaks correspond to resonant capture on the most abundant elements (listed in the table, abundances are given in weight %) considered in the Earth model [75], ^{16}O , ^{24}Mg , ^{28}Si and ^{56}Fe and their isotopes. A dark matter halo density of $\rho_X = 0.3 \text{ GeV cm}^{-3}$ is assumed [74]. Figure from [74].

The capture rate could be higher if the WIMPs have a low velocity with respect to the Earth. This is because the escape velocity v_{esc} of WIMPs inside the Earth is low. It varies from $v_{esc} \sim 11 \text{ km/s}$ at the mantle to $v_{esc} \sim 15 \text{ km/s}$ at the center. Thus, the higher speed WIMPs will only be captured at the center where the escape velocity is the highest, whereas the lowest speed WIMPs may be captured anywhere in the Earth. In Section 2.4, it was discussed that the WIMP velocity distribution at the location of the Earth is usually described by the Standard Halo Model (SHM), but that there are large uncertainties on this distribution. Furthermore, the possible existence of a dark disc was

discussed, in which the WIMPs have a lower relative velocity w.r.t. the Earth compared to the SHM. Therefore, less scattering is needed for the particles in the dark disc to become gravitationally captured. So the dark disc hypothesis leads to a higher capture rate and thus a higher neutrino-induced muon flux at detectors such as the ICECUBE neutrino telescope [76].

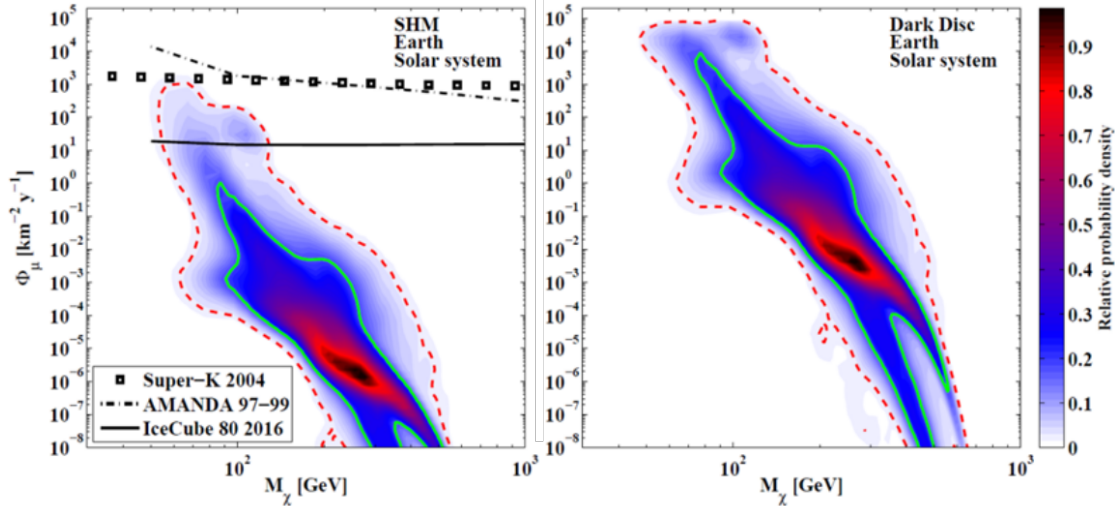


Figure 2.13: Expected muon flux at the surface of the Earth as a function of the WIMP mass for the SHM (left) and a dark disc model (right). The closed contours show 95% (red/dashed) and 68% (green/solid) of the probability density of CMSSM models consistent with both astrophysical and collider constraints at the time of the publication of reference [76]. The colour-bar gives the relative probability density. The lines on the left plot indicate the upper-limits on the muon flux from Super-Kamiokande and AMANDA, along with the estimated sensitivity of five years of ICECUBE data. This estimated ICECUBE sensitivity was based on the work presented in [77]. This estimation was performed before the construction of ICECUBE was started. It does not include the DeepCore array and, lacking a precise simulation of the hardware, is based on a simplified simulation of the detector response. Figure from [76].

Fig. 2.13 shows the expected [76] muon flux (Φ_μ) for $E_\mu > 1$ GeV at the Earth's surface as a function of the WIMP mass from neutrinos originating from WIMP annihilations in the center of the Earth. Compared to the flux from the SHM given in the left panel, the flux from the dark disc (right panel) is boosted by two to three orders of magnitude, depending on the specific model. A feature like this dark disc, might thus really enhance the neutrino-induced muon flux in neutrino detectors such as ICECUBE, making it interesting to look for neutrinos from Earth WIMPs.

Summary

Understanding the nature of dark matter is one of the major challenges in modern physics. Many effects caused by this mysterious matter have been seen, but until today, there is no clear idea on what this dark matter is made of.

The current best model to describe our Universe, the *Lambda Cold Dark Matter*(Λ CDM) model, naturally incorporates a dark matter component. According to the best fit of this six-parameter model to the latest Planck data, dark matter makes up about 27% of all the energy in the Universe and roughly 80% of all the matter.

It was discussed that there are many possible candidates to describe the dark matter, but that the most popular candidate is the Weakly Interacting Massive Particle (WIMP). An excellent candidate for the WIMP is the hypothetical neutralino, the Lightest Supersymmetric Particle (LSP), arising in supersymmetric theories beyond the Standard Model of particle physics.

The current models of the distribution of dark matter in the Universe were described. The dark matter velocity distribution in our Milky Way was discussed in more detail, as this has a direct impact on the capture rate of the dark matter particles in the Earth. It is possible that the low velocity part of the distribution is enhanced by the existence of a co-rotating dark disk, which would lead to a higher capture of WIMPs in the Earth, and thus to a higher flux of WIMP-induced neutrinos.

An overview of the principles of direct detection, indirect detection and collider detection was given. So far, no undisputed dark matter signal has been observed in any of these classes, but more efforts are on the way, as there is indisputable cosmological evidence for the presence of dark matter in the Universe. A signal in at least two of the three detection classes will probably be needed to be conclusive.

In the final part of this chapter, an overview was given of the physics behind WIMP capture and annihilation in the Earth, which is important for the understanding of the work described in this thesis. In the next chapter, the particle physics involved in this research is explained. This starts with the annihilation of WIMPs in the center of the Earth into Standard Model particles, which in turn decay and in this way produce neutrinos.

I have done a terrible thing, I have postulated a particle that cannot be detected.

Wolfgang Pauli

3

Neutrinos as a probe for Earth WIMPs

In this chapter, the underlying physics related to indirect detection of dark matter from the center of the Earth using muon neutrinos is discussed. As explained in the previous chapter, WIMPs accumulated in the center of the Earth, might annihilate and produce Standard Model particles. While traveling through the Earth, these standard model particles will decay and in the decay process, neutrinos will be created. Unlike the other Standard Model particles, neutrinos are capable of traveling through the Earth (almost) without interacting and are thus the perfect particles to indirectly look for Earth WIMPs.

WIMPs could annihilate into many different particles, and the neutrino spectrum in the detector will heavily depend on the annihilation channel, as explained in Section 3.1. The neutrinos are not directly detectable, but the particles that are created when a neutrino interacts with a nucleon, are. The interaction between a neutrino and a nucleon is discussed in Section 3.2. In the work presented in this thesis, the main focus lies on the detection of muon neutrinos, or more precisely the produced muon, in ice. An overview on how the daughter muons of the muon neutrinos lose their energy in ice, and how they can be detected via Cherenkov radiation is given in Section 3.4. A brief discussion on neutrino oscillations is given in Section 3.3, which is an important feature, considering the energy scales which are relevant in this analysis.

Neutrino detectors, such as IceCube, can then be used to detect this Cherenkov radiation and thus the neutrinos, as explained in the Chapter 4.

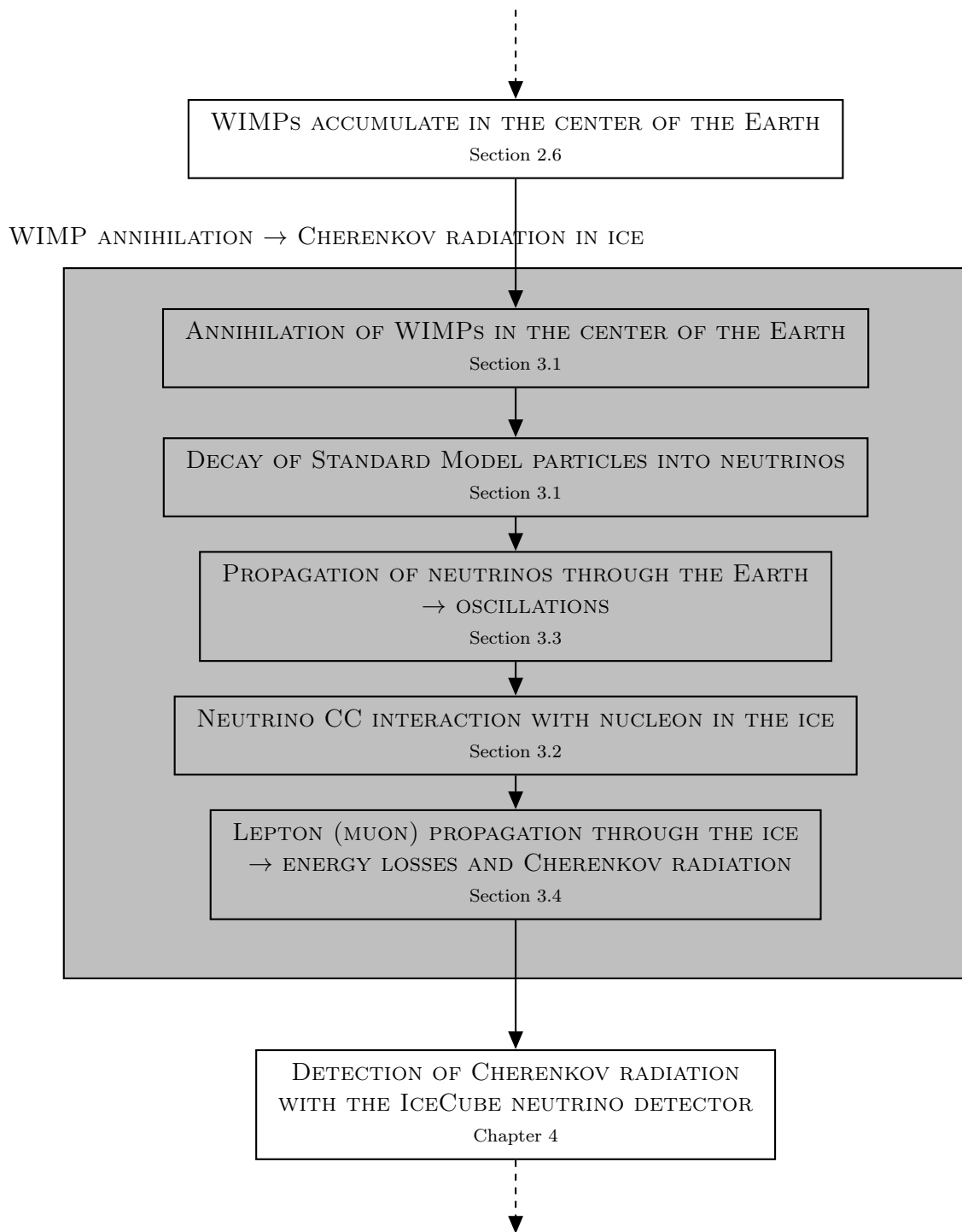


Figure 3.1: Overview of the described processes in this chapter.

3.1 Neutrinos from WIMP annihilations in the center of the Earth

As discussed in the previous chapter, WIMPs might have accumulated in the center of the Earth for about $t_{\oplus} \approx 4.5$ Gyr (age of the solar system). These WIMPs could then self-annihilate at a rate Γ_A , producing a differential neutrino flux at the surface of the Earth, given by

$$\frac{d\Phi}{dE_\nu} = \frac{\Gamma_A}{4\pi R_{\oplus}^2} \left(\frac{dN_\nu}{dE_\nu} \right), \quad (3.1)$$

where R_{\oplus} is the radius of the Earth and dN_ν/dE_ν is the total neutrino spectrum, which depends on the branching ratio of annihilation channel X and its differential neutrino spectrum $\left(\frac{dN}{dE_\nu} \right)_X$

$$\left(\frac{dN_\nu}{dE_\nu} \right) = \sum_X B_X \left(\frac{dN}{dE_\nu} \right)_X. \quad (3.2)$$

This spectrum depends on the WIMP mass and composition, which are still unknown. Therefore choices have to be made for these quantities. The mass range which is scanned is 10 GeV-10 TeV, as this is where the analyses described in this work have sensitivity.

Because of the tiny neutrino mass, the annihilation channel $\chi\chi \rightarrow \nu\nu$ is strongly suppressed in the MSSM, so the neutrinos will come from decays of other annihilation products. The less energetic neutrino spectrum, often referred to as softest spectrum, is in general given by 100% annihilation into $b\bar{b}$ and the most energetic (hardest) spectrum is given by 100% annihilation into $\tau^+\tau^-$ or W^+W^- , but this of course depends on the event selection. In the work presented in this analysis 100% annihilation into W^+W^- is considered as the hard channel if $m_\chi > m_W$ and 100% annihilation into $\tau^+\tau^-$ otherwise. This is to compare with other analyses, in which these annihilation channels were chosen for historical reasons.

The neutrino spectra at the surface of the Earth, at generation level (generated with WimpSim [78]) are shown in Figs. 3.2 and 3.3 for 50 GeV WIMPs annihilating into respectively $b\bar{b}$ (channel 5) and $\tau^+\tau^-$ (channel 11). In these plots the differential fluxes of the neutrino (left panels) and anti-neutrino (right panels) are shown as a function of the neutrino energy E_ν divided by the WIMP mass m_χ , for the different neutrino species, each indicated with a different color. Note that the spectrum in the case of $\chi\chi \rightarrow b\bar{b}$ is indeed much softer than the spectrum of $\chi\chi \rightarrow \tau^+\tau^-$.

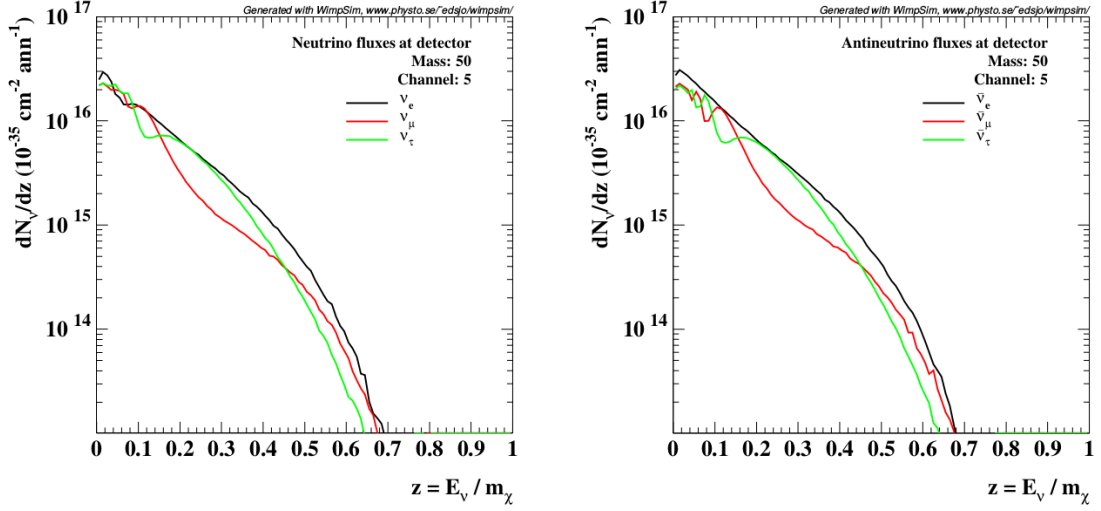


Figure 3.2: The differential fluxes of the neutrino (left panel) and anti-neutrino (right panel) as a function of the neutrino energy E_ν divided by the WIMP mass m_χ , at the surface of the Earth, at generation level (generated with WimpSim [78]) for 50 GeV WIMPs annihilating into $b\bar{b}$ (channel 5). The spectra of ν_e , ν_μ and ν_τ are represented by the black line, red line and green line respectively.

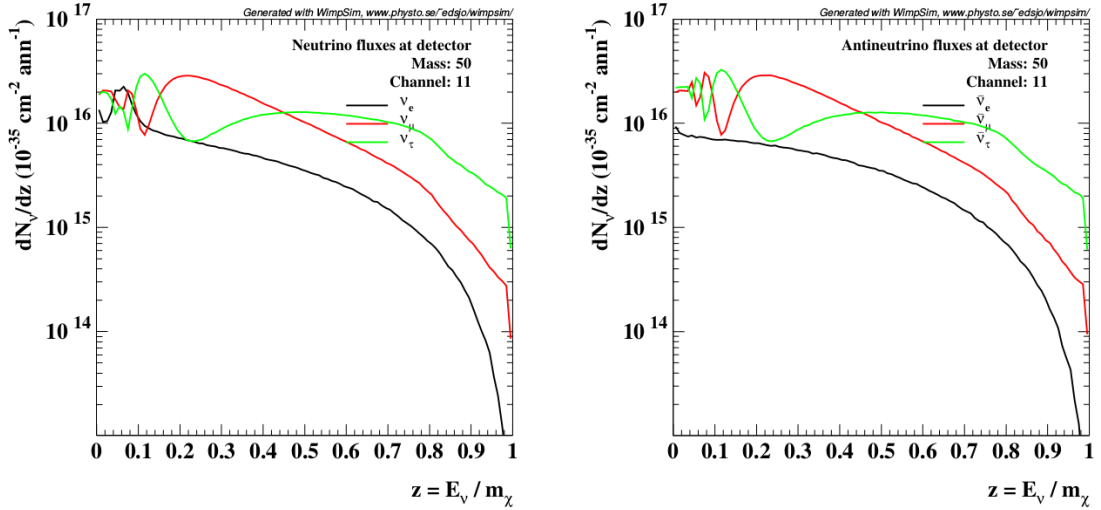


Figure 3.3: The differential fluxes of the neutrino (left panel) and anti-neutrino (right panel) as a function of the neutrino energy E_ν divided by the WIMP mass m_χ , at the surface of the Earth, at generation level (generated with WimpSim [78]) for 50 GeV WIMPs annihilating into $\tau^+\tau^-$ (channel 11). The spectra of ν_e , ν_μ and ν_τ are represented by the black line, red line and green line respectively.

3.2 Neutrinos and their interactions with matter

Neutrinos are part of the Standard Model of Particle Physics, which is a relativistic quantum field theory that describes the interactions between elementary particles¹. Neutrinos are electrically neutral spin $\frac{1}{2}$ fermions. They come in three different flavor states, ν_e , ν_μ and ν_τ and interact weakly.

There are two ways in which a neutrino can weakly interact with a nucleon N : either through a Charged Current (CC) interaction or a Neutral Current (NC) interaction.

1. In the case of a CC interaction, the neutrino couples to its accompanying charged lepton via a W^\pm exchange, allowing the identification of the neutrino flavor by detecting the produced charged lepton ℓ^\pm (Fig. 3.4a):

$$\nu_\ell(\bar{\nu}_\ell) + N \rightarrow \ell^-(\ell^+) + X \quad (3.3)$$

2. This identification is not possible in the case of a NC interaction, which occurs through the exchange of a Z^0 boson (Fig. 3.4b):

$$\nu_\ell(\bar{\nu}_\ell) + N \rightarrow \nu_\ell(\bar{\nu}_\ell) + X. \quad (3.4)$$

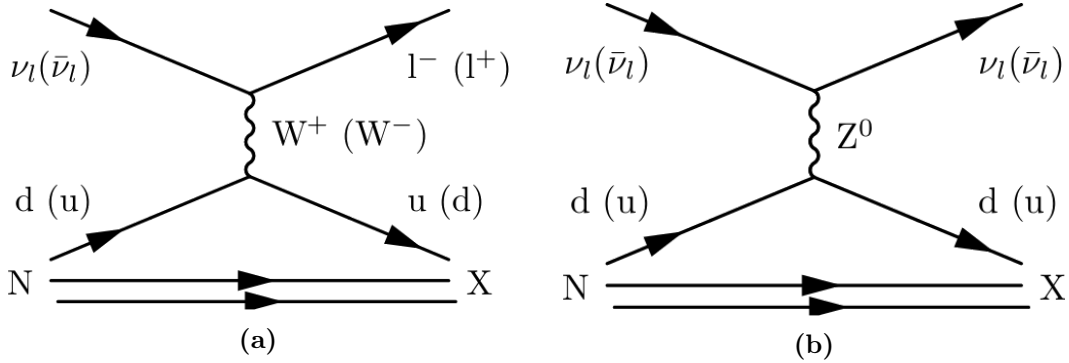


Figure 3.4: Feynman diagrams contributing to the neutrino interaction with nuclei: the CC interaction (a) and the NC interaction (b). l indicates the lepton flavor, N the initial nucleon and X the resulting hadronic cascade.

As will be discussed in Section 3.4, this analysis will search for muons produced during CC interactions of muon neutrinos ν_μ :

$$\nu_\mu(\bar{\nu}_\mu) + N \rightarrow \mu^-(\mu^+) + X. \quad (3.5)$$

The main reason for this is that muons travel a longer distance through ice (the detection medium) than electrons or taus, allowing for a better angular resolution in the detector.

¹This model is nicely described in many textbooks, such as [79].

The differential cross-section of the process in Eq. (3.5) can be written as

$$\frac{d^2\sigma}{dx dy} = \frac{2G_F^2 M E_\nu}{\pi} \left(\frac{M_W^2}{Q^2 + M_W^2} \right)^2 \left[xq(x, Q^2) + x\bar{q}(x, Q^2) (1-y)^2 \right], \quad (3.6)$$

where $-Q^2$ is the invariant squared four-momentum transfer between the incident neutrino and the outgoing muon, M and M_W are the nucleon and intermediate W boson masses, $q(x, Q^2)$ and $\bar{q}(x, Q^2)$ are the parton density functions of the nucleons, G_F is the Fermi constant, and x and y are the Bjorken scaling variables, which determine the degree of inelasticity of the interaction [80]

$$x = \frac{Q^2}{2M(E_\nu - E_\mu)} \quad (3.7)$$

= fraction of the momentum of the nucleon carried by the quark,

$$y = 1 - \frac{E_\mu}{E_\nu} \quad (3.8)$$

= fraction of neutrino energy transferred to this quark.

As can be seen in Fig. 3.5, the inclusive cross-section approaches a linear dependence on neutrino energy, especially in the domain $10 \text{ GeV} \leq E_\nu \leq 400 \text{ GeV}$, which is the region of interest for low mass WIMP models and will thus be the probed space for both WIMP-induced signal neutrinos and atmospheric background neutrinos. Fig. 3.5 also shows that the neutrino cross-section for scattering on nuclei is roughly two times larger for the neutrino than for the anti-neutrino. This is due to helicity suppression of the CC interaction of the anti-neutrino by a factor $(1-y)^2$ for energies below $\sim 10 \text{ TeV}$ [81]. At energies above $\sim 10 \text{ TeV}$, the $(1-y)^2$ suppression is much less pronounced, and the neutrino and anti-neutrino cross-sections become nearly identical, as the cross-section is no longer dominated by valence quarks but by sea quarks, which are $q - \bar{q}$ symmetric.

In the presented analysis, the interactions of the type given in Eq. (3.5) are simulated using parameterizations of the parton density functions according to CTEQ6 [83].

3.3 Neutrino Oscillations

The analysis described in this thesis is focusing on CC interacting muon neutrinos in the energy range $\mathcal{O}(\text{GeV-TeV})$. Neutrinos with energies $E_\nu \lesssim 100 \text{ GeV}$, which travel through the Earth, will undergo oscillations, which are transitions in flight between the different flavor neutrinos ν_e, ν_μ and ν_τ (anti-neutrinos $\bar{\nu}_e, \bar{\nu}_\mu$ and $\bar{\nu}_\tau$), caused by nonzero neutrino masses and neutrino mixing [84]. These oscillations will occur for both the WIMP-induced signal neutrinos and the atmospheric background neutrinos, as they travel through the Earth.

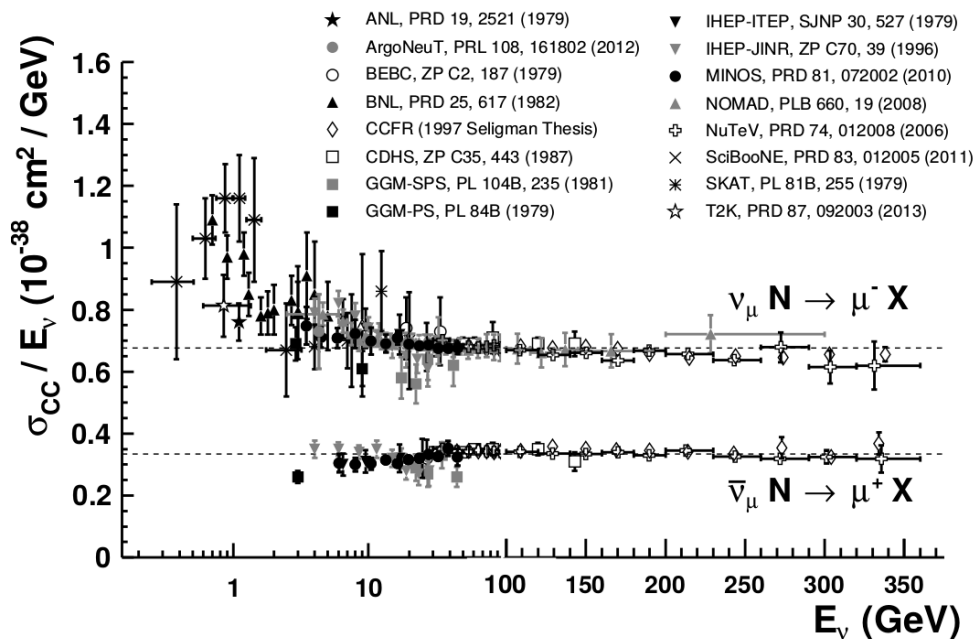


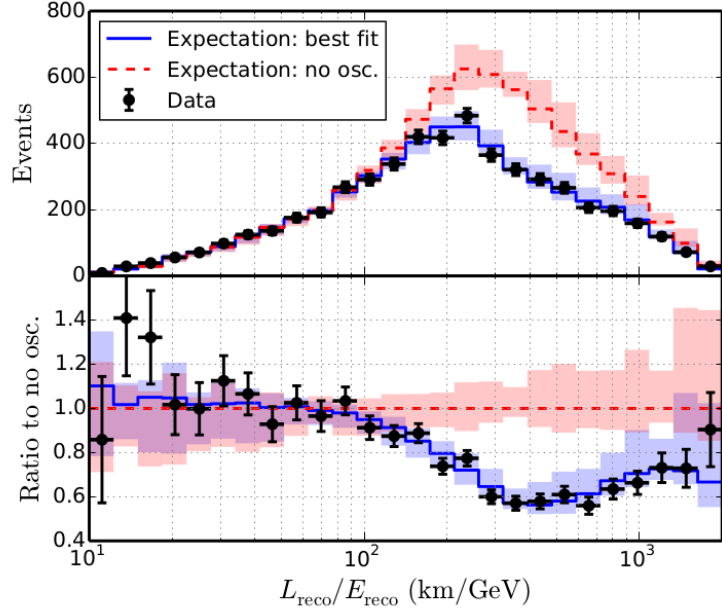
Figure 3.5: Measurements of ν_μ and $\bar{\nu}_\mu$ CC inclusive scattering cross-sections divided by neutrino energy as a function of neutrino energy. Note the transition between logarithmic and linear scales occurring at 100 GeV. Neutrino cross-sections are typically twice as large as their corresponding anti-neutrino counterparts, although this difference can be larger at lower energies. NC cross-sections (not shown) are generally smaller but non-negligible compared to the CC scattering case. Figure from [82].

Several experiments with solar [85], atmospheric [86, 87, 88], reactor [89] and accelerator [90] neutrinos have provided compelling evidences for the existence of these neutrino oscillations. The existence of flavor neutrino oscillations implies that if a neutrino of a given flavor, say ν_μ , with energy E is produced in some weak interaction process, at a sufficiently large distance L from the ν_μ source the probability to find a neutrino of a different flavor, say ν_τ , $P(\nu_\mu \rightarrow \nu_\tau; E, L)$, is non-zero. This means that the “ ν_μ survival probability” $P(\nu_\mu \rightarrow \nu_\mu; E, L)$ will be smaller than one, so a “disappearance” of muon neutrinos from their source to the detectors is expected.

This muon neutrino disappearance has already been measured by several experiments, such as Super-Kamiokande [86] and IceCube/DeepCore [88]. In these searches, a disappearance of atmospheric muon neutrinos is observed, as shown in Fig. 3.6, where the number of events is shown as a function of reconstructed baseline (distance traveled through the Earth) over energy.

As mentioned before, the flavor eigenstate of a neutrino $\nu_{\ell=e,\mu,\tau}$ is defined by the flavor of the charged lepton ℓ to which it couples during its interaction. As opposed to charged leptons, this flavor eigenstate does not necessarily represent a well-defined mass

Figure 3.6: Distribution of events as a function of reconstructed L/E . Data (black dots with error-bars) are compared to the best fit and to the expectation with no oscillations (red dashed line), and the ratio of data and best fit to the expectation without oscillations (blue solid line). Bands indicate estimated systematic uncertainties. Figure from [88].



eigenstate of the neutrino [81]. This is due to the fact that neutrinos are only indirectly detectable. The flavor eigenstate ν_ℓ of a neutrino can be written as a superposition of mass eigenstates $\nu_{i=1,2,3}$,

$$\begin{pmatrix} \nu_e \\ \nu_\mu \\ \nu_\tau \end{pmatrix} = U \begin{pmatrix} \nu_1 \\ \nu_2 \\ \nu_3 \end{pmatrix}, \quad (3.9)$$

where U is the 3×3 unitary Pontecorvo, Maki, Nakagawa and Sakata (*PMNS*) mixing matrix [91]. This matrix can be expressed by six parameters: three mixing angles $\theta_{12}, \theta_{13}, \theta_{23}$, and three complex phases δ, ρ_1 and ρ_2 . The latter two parameters ρ_1 and ρ_2 only appear if the neutrino is of Majorana type. A convenient way to parameterize the *PMNS* matrix is:

$$U = \begin{pmatrix} 1 & 0 & 0 \\ 0 & c_{23} & s_{23} \\ 0 & -s_{23} & c_{23} \end{pmatrix} \begin{pmatrix} c_{13} & 0 & s_{13}e^{i\delta} \\ 0 & 1 & 0 \\ -s_{13}e^{-i\delta} & 0 & c_{13} \end{pmatrix} \begin{pmatrix} c_{12} & s_{12} & 0 \\ -s_{12} & c_{12} & 0 \\ 0 & 0 & 1 \end{pmatrix} \begin{pmatrix} e^{-i\rho_1} & 0 & 0 \\ 0 & e^{-i\rho_2} & 0 \\ 0 & 0 & 1 \end{pmatrix}, \quad (3.10)$$

where $c_{jk} = \cos(\theta_{jk})$ and $s_{jk} = \sin(\theta_{jk})$. To fully describe the neutrino oscillations, also the squared mass differences of the mass eigenstates $\Delta m_{jk}^2 = m_{\nu_j}^2 - m_{\nu_k}^2$ are needed. As there are 3 neutrinos in the standard model, there are only two independent neutrino mass squared differences, say $\Delta m_{21}^2 \neq 0$ and $\Delta m_{31}^2 \neq 0$. The numbering of massive neutrinos ν_j is arbitrary, but is most often chosen in such a way that $m_{\nu_1} < m_{\nu_2}$, so that $\Delta m_{21}^2 > 0$.

Table 3.1: The best-fit values and 1σ (standard deviations) allowed ranges of the 3-neutrino oscillation parameters, derived from a global fit of the current neutrino oscillation data (from [95]). The results shown are obtained with reactor $\bar{\nu}_e$ fluxes [96]. The values (values in brackets) correspond to *normal* (*inverted*) hierarchy. The definition of $\Delta m^2 = m_{\nu_3}^2 - (m_{\nu_2}^2 + m_{\nu_1}^2)/2$

Parameter	best-fit $\pm 1\sigma$	Experimental channel
$\Delta m_{21}^2 [10^{-5} \text{eV}^2]$	$7.54^{+0.26}_{-0.22}$	$L/E \sim 16 \text{km/MeV}$
$ \Delta m^2 [10^{-3} \text{eV}^2]$	$2.43^{+0.06}_{-0.10}$ ($2.42^{+0.07}_{-0.11}$)	$L/E \sim 500 \text{km/GeV}$
$\sin^2 \theta_{12}$	$0.307^{+0.018}_{-0.016}$	$\nu_e \rightarrow \nu_\alpha$ (solar), $\bar{\nu}_e \rightarrow \bar{\nu}_e$ (reactor)
$\sin^2 \theta_{23}$	$0.386^{+0.024}_{-0.012}$ ($0.392^{+0.039}_{-0.022}$)	$\nu_\mu \rightarrow \nu_\mu$ ($\nu_\mu \rightarrow \nu_\mu$) (atmospheric, beam)
$\sin^2 \theta_{13}$	0.0241 ± 0.0025 ($0.0244^{+0.0023}_{-0.0025}$)	$\bar{\nu}_e \rightarrow \bar{\nu}_e$ (reactor), $\nu_\mu \rightarrow \nu_e$ (beam)

With these choices made, there are two possibilities:

1. *normal hierarchy*: $m_{\nu_1} < m_{\nu_2} < m_{\nu_3}$,
2. *inverted hierarchy*: $m_{\nu_3} < m_{\nu_1} < m_{\nu_2}$.

As the sign of Δm_{32}^2 is still unknown, both the normal and the inverted mass hierarchy are still possible. This is the so-called *mass hierarchy problem*. However, the absolute values of the squared mass differences $|\Delta m_{jk}^2| = |m_{\nu_j}^2 - m_{\nu_k}^2|$ have been determined by several experiments [89, 92, 93, 94]. The values of all the above parameters are summarized in Table 3.1.

Using these parameters, the probability of a neutrino to change from flavor α to β in vacuum can be calculated as

$$P(\nu_\alpha \rightarrow \nu_\beta; E, L) = \sum_{kj} U_{\alpha k}^* U_{\beta k} U_{\alpha j} U_{\beta j}^* e^{-i \frac{\Delta m_{kj}^2 L}{2E}} \quad (3.11)$$

Eq. (3.11), can be understood easily when considering the two-neutrino scheme. In this case, U is a 2×2 matrix which only depends on a single mixing angle θ :

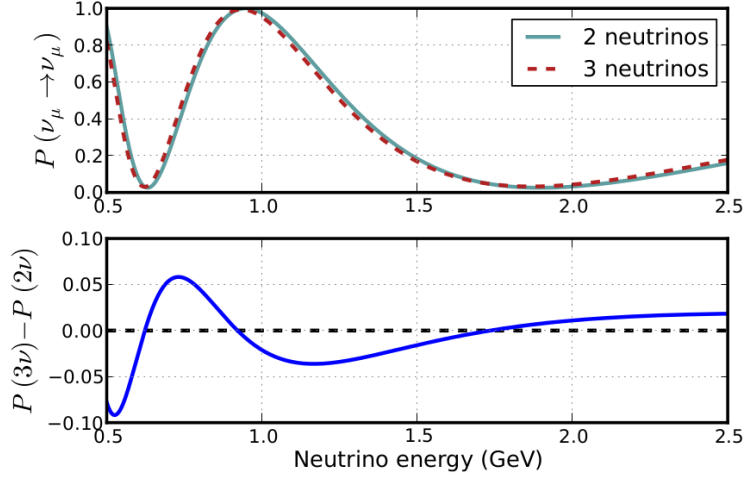
$$U = \begin{pmatrix} \cos \theta & \sin \theta \\ -\sin \theta & \cos \theta \end{pmatrix} \quad (3.12)$$

Combining Eqs. (3.11) and (3.12) results in [97]

$$P^{2\nu}(\nu_\alpha \rightarrow \nu_\beta; E, L) = \sin^2(2\theta) \sin^2\left(\frac{\Delta m^2 L}{4E}\right). \quad (3.13)$$

Eq. (3.13) has the advantage that it is quite straightforward to interpret and can still be rather precise. This latter statement is shown in Fig. 3.7, where the survival probability for an electron neutrino after a propagation distance of 1000 km is shown for the two- and three-neutrino schemes. From this plot, it is clear that in this case the probability differences of the two- and three-neutrino schemes are smaller than 0.05 for most of the energies in Fig. 3.7.

Figure 3.7: Survival probability for ν_μ after traveling 1000 km in vacuum as a function of the neutrino energy. Calculated in the two- and three-neutrino formalisms for the case of *normal hierarchy*. Using the oscillation parameters from Table 3.1. Figure from [97].



In all of the above, neutrino propagation in vacuum was considered, so no matter effects were taken into account. As this analysis will look for neutrinos that (partially) pass through the Earth, it is important to take their interactions with matter into account. Wolfenstein found that neutrinos are coherently forward scattered off the electrons, protons and neutrons in matter which can be described by an effective potential V_{eff} [98],

$$V_{\text{eff}} = \begin{cases} \sqrt{2}G_F n_e & \text{if } \nu = \nu_e \\ -\sqrt{2}G_F n_e & \text{if } \nu = \bar{\nu}_e \end{cases}, \quad (3.14)$$

where n_e is the electron number density along the path. When considering oscillations in the Earth (or more generally in matter), the effective potential for electron neutrinos (Eq. 3.14) is highly dominant over the potential of muon and tau neutrinos. It can be shown [97] that neutrino flavor transitions due to oscillations in matter can become maximal, regardless of how small they are in vacuum, due to the effect of the coherent forward scattering. This is known as the *MSW effect*, named after Mikheev, Smirnov and Wolfenstein, who first discovered this effect [99].

The strongest flux modification that will be important in this analysis, is experienced by $\nu_\mu^{(-)}$, which oscillate mainly into $\bar{\nu}_\tau^{(-)}$. In the energy range of interest ($E_\nu \geq 10$ GeV), this muon disappearance can be approximated by the two-neutrino formalism in vacuum [97],

$$P(\nu_\mu \rightarrow \nu_\mu; E, L) = 1 - \sin^2(2\theta_{23}) \sin^2\left(\frac{\Delta m_{32}^2 L}{4E}\right). \quad (3.15)$$

Note the dependence on L/E , which explains the muon neutrino disappearance in Fig. 3.6. In Fig. 3.8, the expected survival probability for (atmospheric) ν_μ crossing the Earth is shown as a function of neutrino energy and arrival zenith angle (left). The zenith angle is correlated to the distance L a neutrino travels through the Earth before reaching the detector. Note that in these plots (as well as in the rest of this thesis) $\cos(\theta)=1$

corresponds to down-going neutrinos ($L = 0$) and $\cos(\theta)=-1$ corresponds to up-going neutrinos ($L = 2R_\oplus$), as indicated in Fig. 3.9. The calculation was done in the two-neutrino formalism for the *normal hierarchy* case in vacuum and using the oscillation parameters from Table 3.1. From this figure, it is clear that neutrino oscillations have to be taken into account when studying muon neutrinos in the energy range $10 \text{ GeV} \leq E_{\nu_\mu} \leq 100 \text{ GeV}$ that (partially) cross the Earth. These effects will thus be included in the simulations.

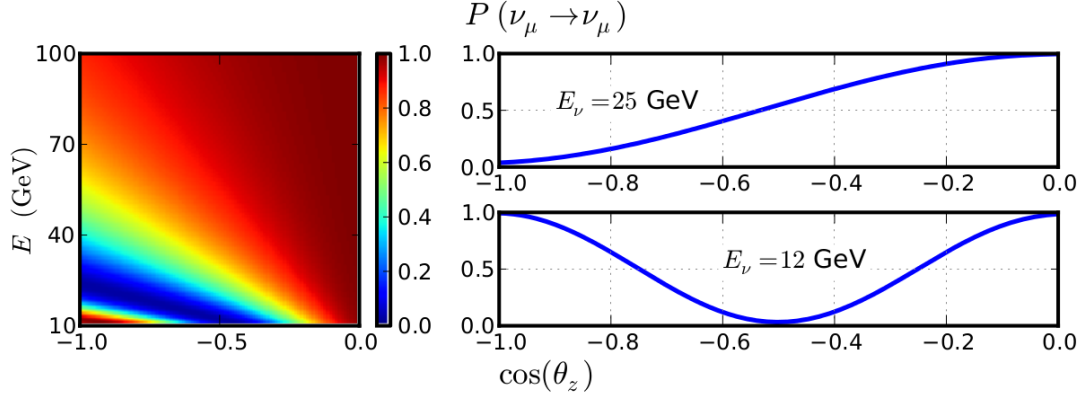


Figure 3.8: Survival probability for muon neutrinos crossing the Earth, calculated in the two-neutrino formalism for the case of *normal hierarchy* in vacuum and using the oscillation parameters from Table 3.1. The left plot shows the survival probability as a function of neutrino energy and arrival zenith angle, and in the right plot two energy slices are shown. Figure from [97].

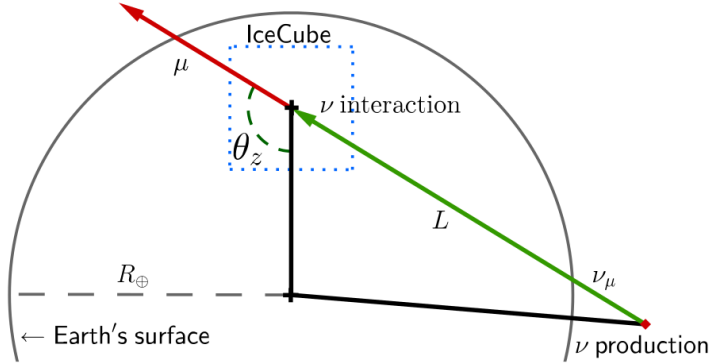


Figure 3.9: Diagram showing the relation between the zenith angle θ_z and propagation distance L for atmospheric neutrinos detected in the ICECUBE detector. Figure from [97].

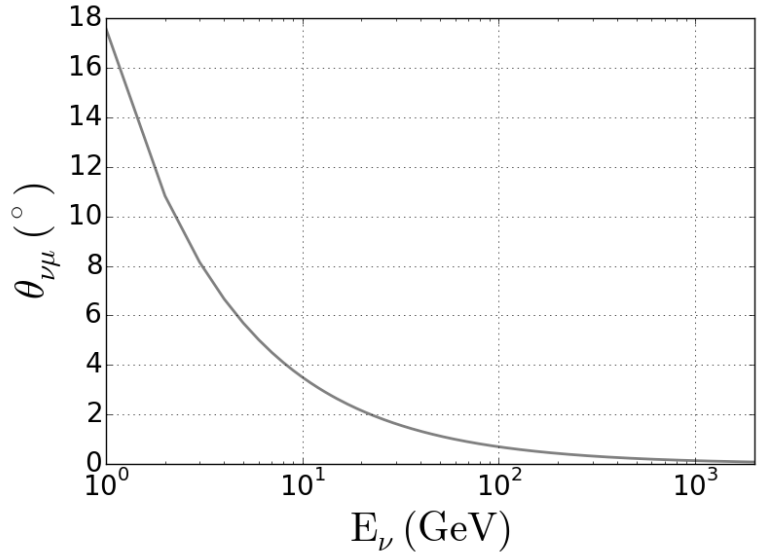
3.4 Neutrino Detection in Ice

The analysis described in this thesis is looking for an excess of neutrinos from the direction of the center of the Earth on top of the irreducible background of atmospheric neutrinos. It is thus important to have the best possible angular resolution. At the neutrino energies of interest in this analysis (GeV-TeV), only muon track events created in CC interactions yield enough information to adequately infer the initial neutrino direction. This is because only the muon propagates far enough through the ICECUBE Neutrino Detector before losing all its energy through interactions with the ice, or before decaying. The mean opening angle between the muon μ and its parent neutrino ν_μ can be approximated by [100],

$$\langle \theta_{\nu\mu} \rangle \approx \frac{0.7^\circ}{(E_\nu/\text{TeV})^{0.7}}, \quad (3.16)$$

from which it follows that this angle is less than 1° for $E_\nu \gtrsim 0.6$ TeV. This can be seen from Fig. 3.10, where the mean scattering angle between initial neutrino and created muon is shown as a function of E_ν .

Figure 3.10: The mean scattering angle between initial neutrino and created muon as a function of E_ν .



3.4.1 Muon energy losses

When a muon travels through a transparent medium like ice, it mainly loses energy through four different processes: ionization, bremsstrahlung, e^+e^- pair production, and inelastic photo-nuclear interactions.

Ionization occurs when a muon scatters elastically off the atomic electrons in a surrounding medium and knocks them out of their orbit. This type of energy loss, described by the Bethe-Bloch formula [101], is nearly energy independent at GeV range

and above, and occurs continuously along the trajectory of the muon, while the other three types are stochastic in nature and dE/dx in their case should only be taken as some average energy loss given large enough dx . Ionization is the dominant channel for muon energies below ~ 1 TeV.

Bremsstrahlung (braking radiation) takes place when a muon is suddenly decelerated and hereby emits high energy photons. A possible process is shown in Fig. 3.11a. In ice, this deceleration is caused by electromagnetic interactions with the surrounding atoms. The muon Bremsstrahlung effects and cross-sections are described by Kelner, Kokoulin en Petrukhin in [102].

e^+e^- **pair production** may happen when a muon passes close to an atom and transfers a small fraction of its energy and momentum to the nucleus or the atomic electron. A possible process is shown in Fig. 3.11b. This effect is the dominant energy loss process for muons with energies greater than ~ 1 TeV. The cross-sections formulae for these processes are derived in [103].

Photo-nuclear interactions are processes in which a muon interacts via a real or virtual photon with a hadron in the surrounding medium as shown in Fig. 3.11c. Bezrukov and Bugaev [104] parametrized the differential cross-section for these processes.

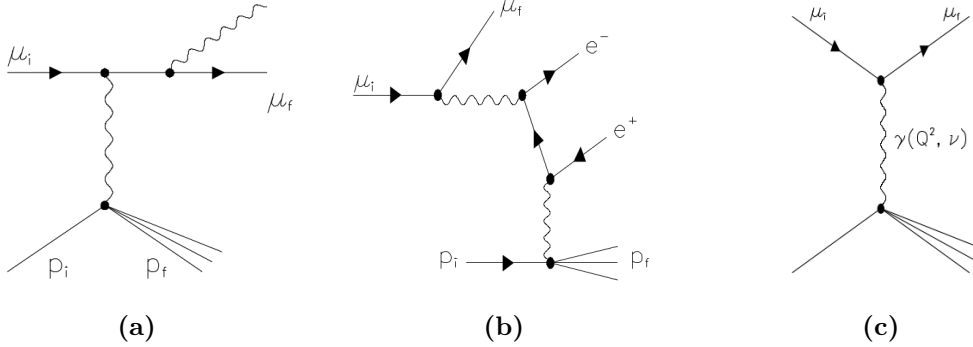


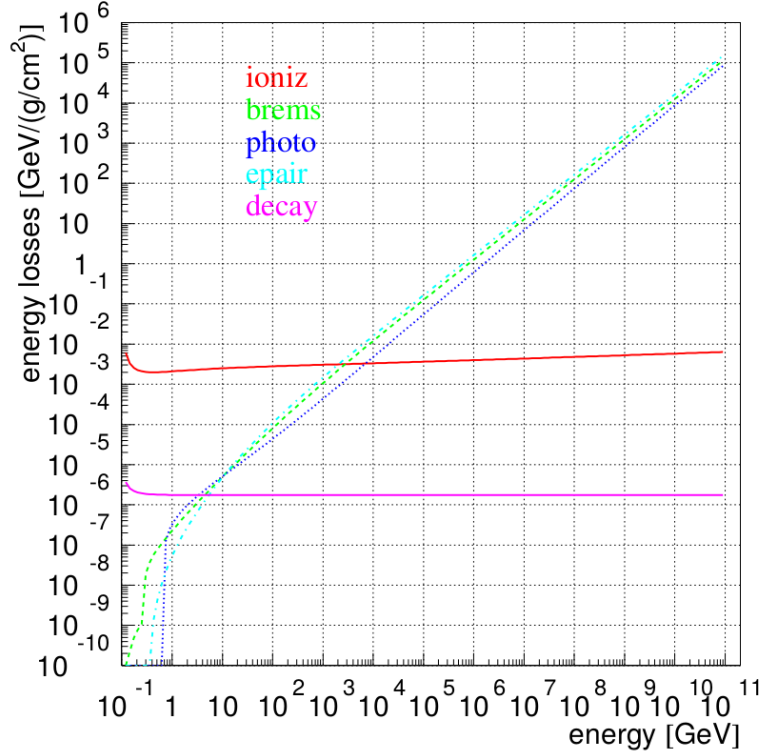
Figure 3.11: Feynman diagrams of the main stochastic energy losses for a muon transversing through ice. For each process one example is shown.

The individual contributions for all of the above processes on the average energy loss of a muon in ice are shown in Fig. 3.12. Also the decay energy loss is shown. This is calculated by multiplying the probability of decay by the energy of the particle.

From Fig. 3.12, it can be seen that the average muon energy loss rate can be approximated as

$$-\left\langle \frac{dE}{dx} \right\rangle = a(E) + b(E)E_\mu, \quad (3.17)$$

Figure 3.12: Ionization (upper solid curve), bremsstrahlung (dashed), photo-nuclear (dotted), pair production (dashed-dotted) and decay (lower solid curve) losses of a muon traversing through ice. Figure from [105].



with $a(E)$ the ionization energy loss and $b(E)$ the sum of the other (radiative) processes. As the coefficients a and b only have a weak energy dependence, useful constant approximations for these parameters can be made for typical values of ice: $a \simeq 2.6 \cdot 10^{-3} \text{ GeV cm}^{-1}$ and $b \simeq 4.3 \cdot 10^{-5} \text{ cm}^{-1}$ [105]. Under these approximations, the mean range R_μ of a muon with initial energy E_μ is given by

$$R_\mu \simeq \frac{1}{b} \ln \left(1 + \frac{E_\mu}{E_{\mu\text{crit}}} \right), \quad (3.18)$$

where $E_{\mu\text{crit}} = a/b$ is the muon critical energy, i.e. the energy at which ionization and radiative losses are equal. Fig. 3.13 shows the mean muon range R_μ in ice as a function of E_μ as given by Eq. 3.18.

3.4.2 Cherenkov radiation

Cherenkov radiation, is electromagnetic radiation emitted when a charged particle passes through a dielectric medium at a speed that exceeds the phase velocity of light in that medium (c_{vac}/n). When the charged particle traverses the medium, the local electromagnetic (EM) field in the medium is disrupted. The atoms of the medium become polarized because of the EM field. Once the EM field has passed, the electrons of the polarized atoms restore themselves to equilibrium and emit photons while doing this. These photons will interfere constructively and form a shock wave at a certain angle θ_c if

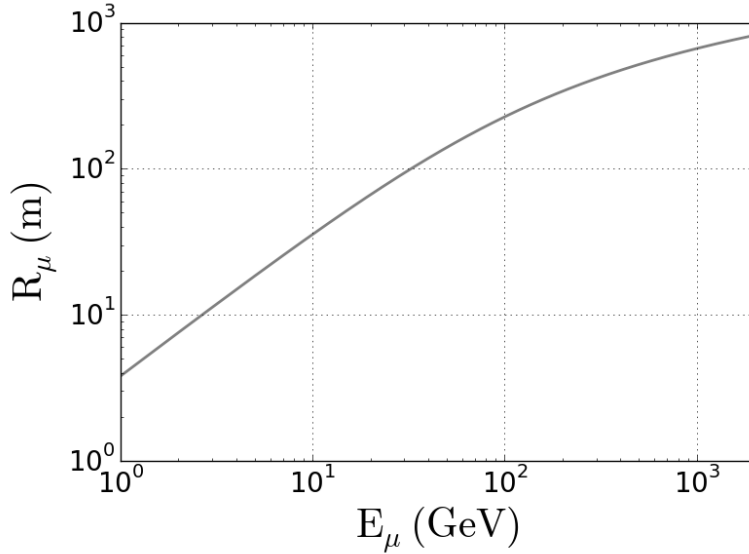


Figure 3.13: Mean muon range R_μ in ice as a function of E_μ as given by Eq. 3.18.

the speed of the disruption exceeds the light speed in the medium. This process, which is leading to the so-called Cherenkov radiation, is shown in Fig. 3.14. For this to happen for a muon (mass m_μ) that passes through the ice (refractive index n_{ice}), a minimum muon energy E_μ is needed

$$E_\mu^{\min}(\lambda) = \frac{m_\mu}{\sqrt{1 - n_{ice}(\lambda)^{-2}}}, \quad (3.19)$$

where λ is the wavelength of the emitted Cherenkov photons.

The number of Cherenkov photons emitted per unit path length is given by the Frank-Tamm expression [106]

$$\frac{dN}{dx} = 2\pi\alpha \int \left(1 - \frac{1}{n^2\beta^2}\right) \frac{d\lambda}{\lambda^2}, \quad (3.20)$$

where α is the fine structure constant, λ the wavelength of the emitted photon and $\beta = v/c_{vac}$ is the velocity of the charged particle divided by the speed of light in vacuum. The maximum number of Cherenkov photons per unit path are emitted in the visible spectrum $300 \text{ nm} < \lambda < 600 \text{ nm}$. In this range of wavelengths $n_{ice} \approx 1.33$, so using Eq. 3.19 one finds that $E_\mu^{\min} \approx 160 \text{ MeV}$ is the minimum energy for Cherenkov emissions by muons in ice. From integration of Eq. (3.20), it can be found that for wavelengths in this range, which is also the domain in which the Digital Optical Modules of the ICECUBE detector are sensitive, approximately 32000 photons are emitted by a muon in one meter of ice. The energy loss due to this type of radiation is about 86 keV/m, which is negligible compared to the energy losses described in Section 3.4.1.

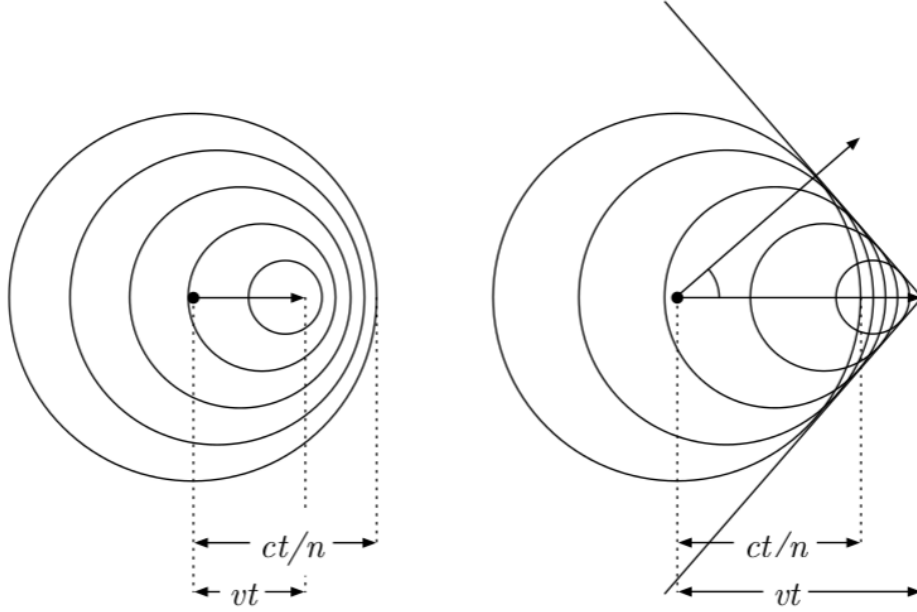


Figure 3.14: Illustration of the Cherenkov effect by Huygens' construction [107]. When a charged particle travels at $\beta = 0.5$, the spherical wave fronts are only slightly concentrated along the direction of travel (left figure). At $\beta = 1$ with $n = 1.33$, however, the wave fronts interfere constructively to produce a cone of light at an angle of 41° to the direction of the charged particle (right).

The angle under which the photons are emitted, called the Cherenkov angle θ_c , is given by

$$\cos \theta_c = \frac{1}{n(\lambda)\beta}, \quad (3.21a)$$

$$\Rightarrow \theta_c \approx 41^\circ, \quad (3.21b)$$

where $\beta = v/c_{vac} \equiv 1$ for the muon energy range that is important in this analysis, and $n_{ice} \approx 1.33$ as mentioned before. These Cherenkov photons then travel through the ice, where they are scattered and absorbed, but where they can also be recorded by Digital Optical Modules in the ICECUBE detector, as explained in the next chapter.

Summary

In this chapter, an overview of the underlying physics related to indirect detection of dark matter from the center of the Earth using muon neutrinos was given.

In the first part of the chapter, it was discussed that neutrinos might be produced in the decay of the annihilation products of WIMPs in the center of the Earth, and that their spectrum depends on the annihilation channel of the WIMPs. It was mentioned that in the work presented in this analysis 100% annihilation into $b\bar{b}$ is considered as the soft channel and 100% annihilation into W^+W^- is considered as the hard channel if $m_\chi > m_W$ and 100% annihilation into $\tau^+\tau^-$ otherwise. This is to compare to other analyses, in which these annihilation channels were chosen for historical reasons.

Next, an overview of the neutrino-nucleon interactions and the neutrino propagation through the Earth, in the energy range of interest, i.e. $\mathcal{O}(\text{GeV-TeV})$, was given. As the analysis described in this thesis will search for muons produced in Charged Current (CC) interactions of muon neutrinos in ice, the main focus in the discussion lied on muon neutrinos. It was discussed that an important feature of neutrinos with energies below approximately 100 GeV is that they will oscillate while traveling through the Earth, resulting in a so-called muon disappearance at the detector, which applies for both WIMP-induced signal neutrinos and atmospheric background neutrinos.

Finally, a discussion on the energy losses and Cherenkov radiation of the neutrino-induced muons in the ice was given.

In the next chapter, it is explained how neutrino detectors, such as IceCube, can be used to detect this Cherenkov radiation and thus the neutrinos.

Each time we find another way to make a picture of the sky - using gamma rays, X-rays, radio waves - you have always been able to see things you never saw before.

Francis Halzen

4

The ICECUBE Detector

The data used in this analysis, are recorded by the ICECUBE Neutrino Detector. ICECUBE is a cubic kilometer detector located at the geographical South Pole, which records the Cherenkov emission (described in the previous chapter) of high-energy charged particles that cross the detector volume.

The aim of this chapter is to give an overview of the technical aspects of ICECUBE, going from the ice properties (Section 4.2) over the sensors that are used (Section 4.3) to the low level data treatment at the South Pole (Section 4.6).

The low level data treatment starts by digitizing the hits which are recorded by the sensors (Section 4.3), followed by a local coincidence check, to remove single noise hits. Next, trigger algorithms are used to further reduce the noise rate of the digitized data, as described in Section 4.6.1. Data which trigger the detector, i.e. pass the trigger conditions of at least one trigger algorithm, are then further analyzed. These *events* are calibrated, cleaned and reconstructed, as described in Chapter 5, and the rate is further reduced by applying online filter algorithms. Each online filter is optimized for a certain class of signal events, of which a general overview is given in Section 4.4, and the aim of these online filters is to remove background atmospheric events, presented in Section 4.5, as well as detector noise. The online filter algorithms which are used in this analysis are presented in Section 4.6.2.

The low level treatment is needed to reduce the data rate before sending it to the data warehouse in Madison over satellite, after which they can further be processed and analyzed for a specific analysis, as e.g. the Earth WIMP analysis presented in this thesis.

An overview of this processing chain is given in Fig. 4.2.

DETECTION AND ONLINE PROCESSING WITH ICECUBE

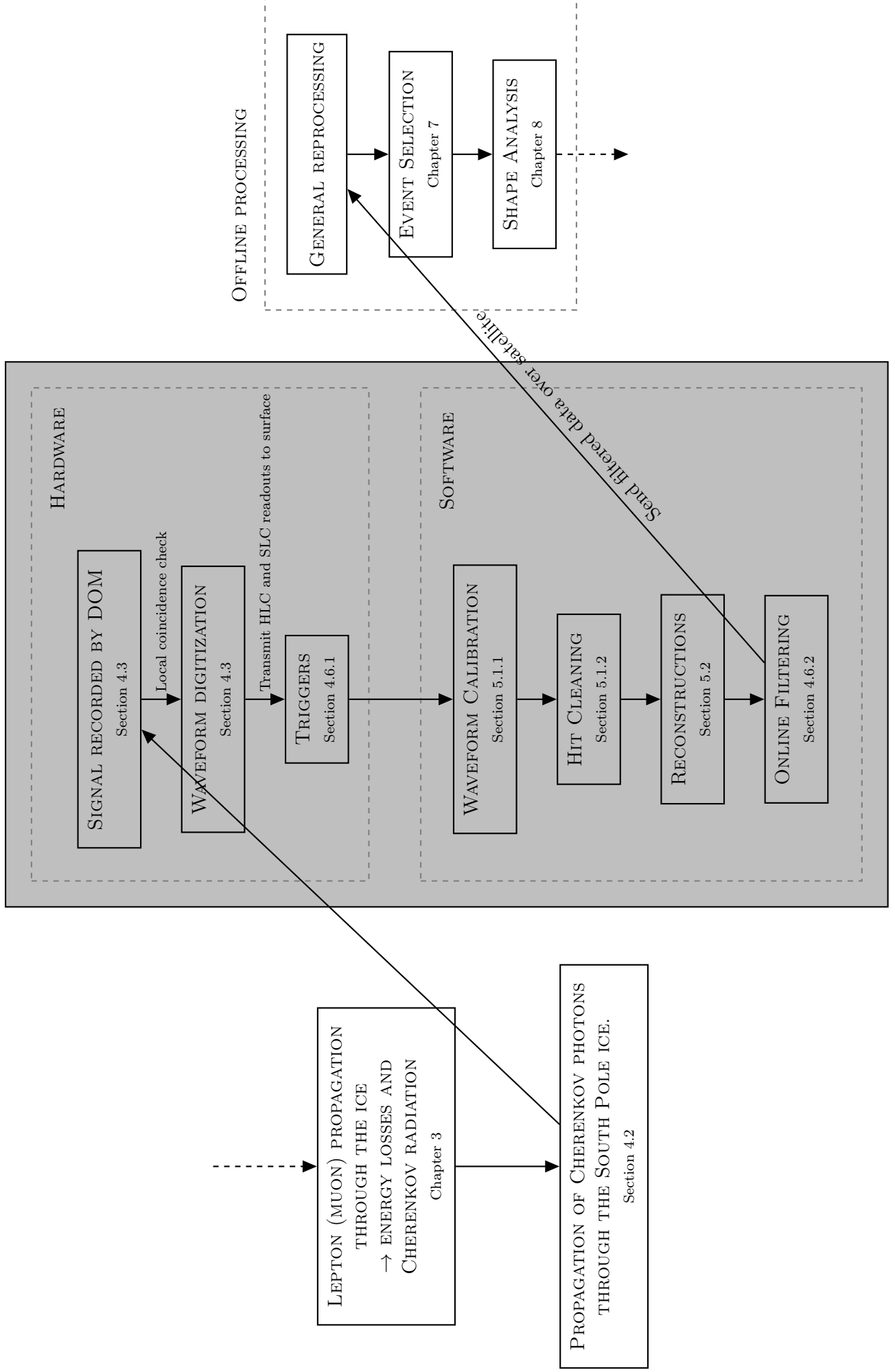


Figure 4.1: Overview of the described processes in this chapter.

4.1 Introduction

ICECUBE is a cubic kilometer neutrino detector located at the geographical South Pole. It consists of 78 kilometer-length strings, each instrumented with 60 Digital Optical Modules (DOMs, Section 4.3) vertically spaced by 17 m each. Each DOM houses a Photo Multiplier Tube (PMT). The strings are lowered into the Antarctic ice at depths between 1450 meters to 2450 meters. The detector is placed at this depth for two reasons, namely because the ice at this depth has a high transparency for visible light and because the upper ice sheet serves as a natural filter against low energy cosmic rays. The strings are arranged at the apexes of equilateral triangles 125 m on a side (Fig. 4.2b). This part of the detector is able to detect neutrinos with energies $E_\nu \geq 100$ GeV. The string- and DOM spacings have been optimized for the primary scientific goal of ICECUBE, namely the detection of high-energy extra-solar neutrinos [108, 109].

In the center of the ICECUBE detector there is a denser infill array called DEEPCORE. This subdetector consists of eight strings with 60 DOMs of higher quantum efficiency [110]. The eight DEEPCORE strings have a horizontal spacing of 72 m and the vertical DOM spacing in this subdetector is 7 m, with a large gap between the positions of the 10th and 11th DOM, as indicated in Fig. 4.2b. This gap is introduced due to the presence of *the dust layer*, which is a region in which the ice is less transparent, as discussed in Section 4.2. Note that the DOMs in DEEPCORE only start at a depth of 1.75 km. DEEPCORE can measure neutrinos with energies down to $E_\nu \sim 10$ GeV, and is thus of great importance for analyses using low energy neutrinos, such as neutrino oscillation analyses [111, 88] and searches for neutrinos from Dark Matter annihilations [66, 55] which are expected to occur at relatively low energies.

A particle detector called ICETOP is located on top of the ICECUBE detector [112]. This air shower array consists of 81 stations, each hosting two frozen water tanks instrumented with two DOMs each. The aim of this array is to measure cosmic rays in the range of about 300 TeV to 1 EeV and reveal their composition and characteristics [113]. The ICETOP data will not be used in this analysis.

An overview of the detector with its different components is given in Fig. 4.2a. Fig. 4.2b shows a top and side view of the detector, as well as the dust concentration in the ice as a function of the depth. This is discussed in more detail in Section 4.2.

The detector was built over a time span of several years. Each year (during the South Pole summer), more strings were added to the detector. The deployment started in 2005, when the first string was lowered in the ice, and the detector was completed in December 2010. There have been many analyses for each detector configuration, as the detector started taking data once the first string was deployed. The “Search for Dark Matter Annihilations in the Sun with the 79-String ICECUBE Detector” [66] for example used data recorded with 79 strings.

The convention that is used within the ICECUBE collaboration and in this thesis, is that particles which travel downwards (upwards) in the detector have a zenith angle $\theta = 0^\circ$ ($\theta = 180^\circ$), as indicated in Fig. 4.3.

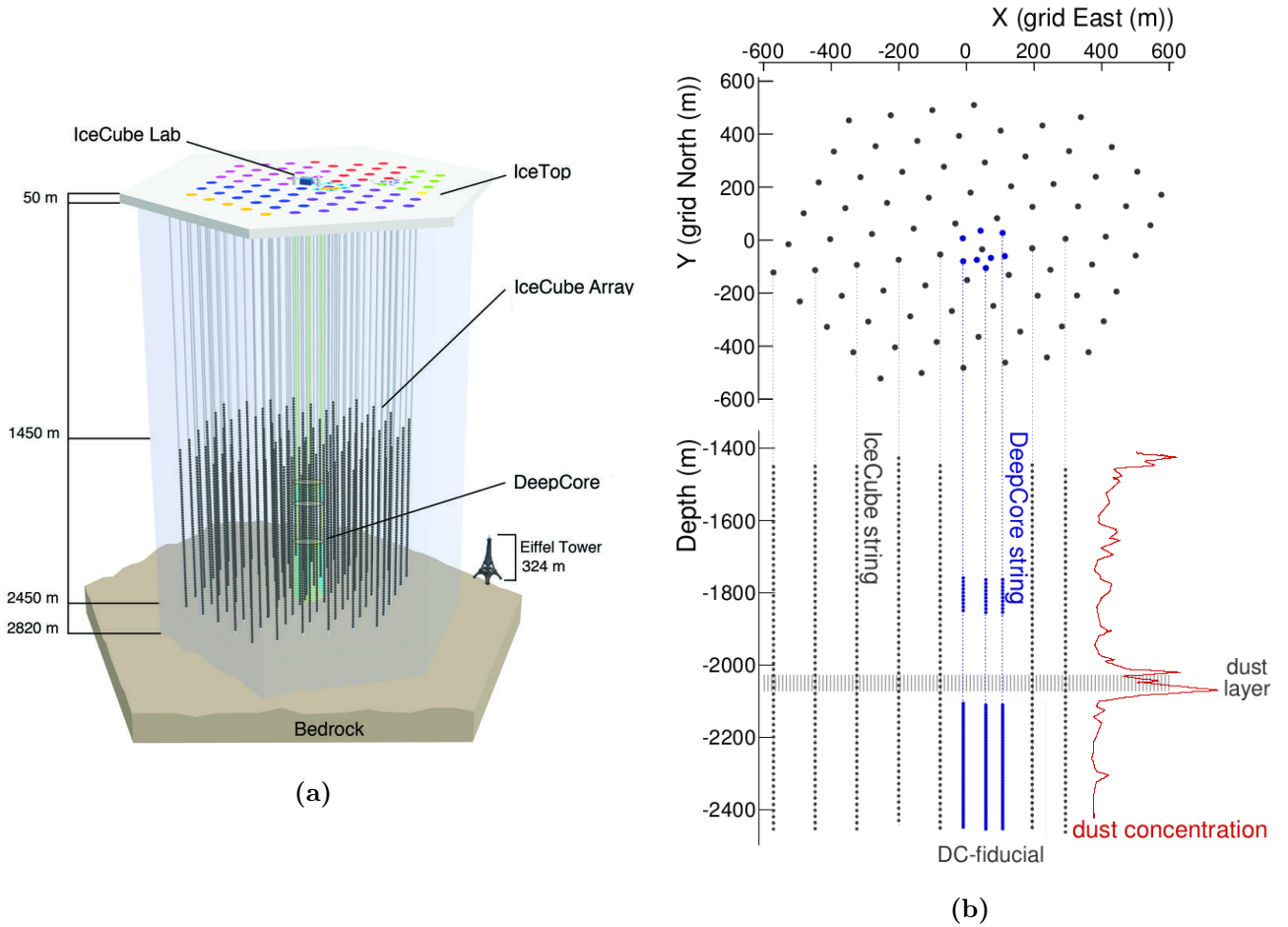


Figure 4.2: Overview of the ICECUBE detector. A schematic view of the ICECUBE detector with its components DEEPCORE and ICETOP is shown in (a). In (b) a top and side view of the detector, as well as the dust concentration in the ice as a function of the depth are shown. Figures (a) and (b) are from <http://icecube.wisc.edu> and [33] respectively.

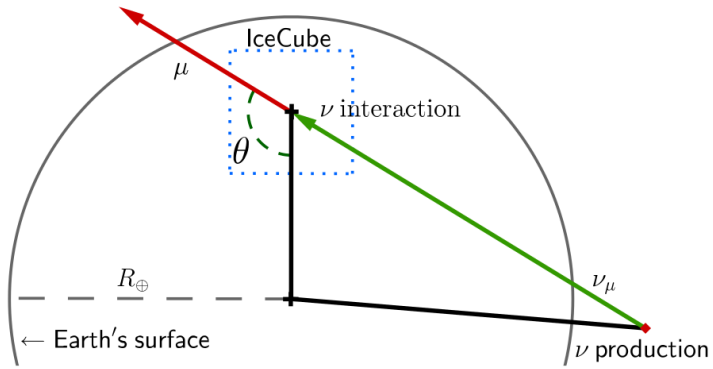


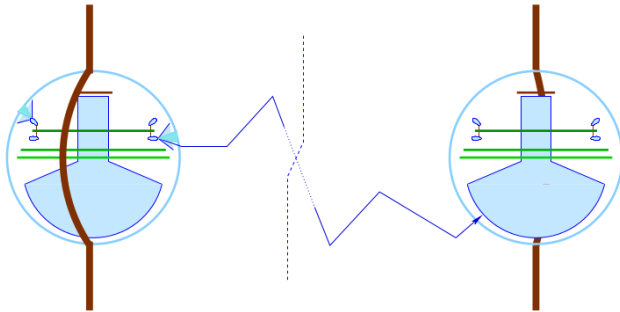
Figure 4.3: Diagram showing the definition of the zenith angle θ in the ICECUBE detector. Figure from [97].

4.2 The South Pole ice

ICECUBE indirectly measures neutrinos, by detecting the Cherenkov light from the daughter lepton that is produced when the parent neutrino ν_ℓ interacts with nucleons in the detector volume. The lepton and thus neutrino direction is reconstructed by measuring the photon arrival times in different PMTs and linking these to the lepton. It is thus crucial to understand and describe the propagation of these Cherenkov photons from their point of emission to the receiving sensor, and hereby take into account the scattering and absorption effects due to the ice.

It is crucial to understand the propagation effects of photons in both simulation and reconstruction of ICECUBE data, hence the scattering and absorption effects should be modeled carefully. The three main parameters that need to be taken into account in the modeling are the average absorption distance, the average distance between successive scatters of photons, and the angular distribution of the photon at each given scattering point. These parameters have been determined by using *flasher run data*, in which photons are emitted by the LEDs in DOMs and recorded by other DOMs, as sketched in Fig. 4.4.

Figure 4.4: The flasher run datasets are generated by sending out photons from the LED in one DOM and recording these with other DOMs. Figure from [114].



The flasher run data are used to construct the ice model. The most commonly used model in ICECUBE (and baseline model for this work) is SPICE-MIE [114], a six-parameter model including a detailed parametrization of Mie scattering [115]. This model describes the ice by a table of depth-dependent parameters $b_e(400)$ and $a(400)$ related to scattering and absorption at a wavelength of 400 nm, by the depth-dependent relative temperature $\delta\tau$ and by six global parameters that are fitted to the flasher run data, as described in detail in [114]. A wavelength of 400 nm is picked, as this is the wavelength for which the ICECUBE sensors have the highest sensitivity.

Recently a slight azimuthal dependence of the light propagation properties has been observed. This effect could be caused by the preferential alignment of the ice crystals, possibly resulting in the preferential alignment of the embedded dust particles [116]. This azimuthal dependence is included in the SPICE-LEA simulation, which is the most recent ice model used in ICECUBE simulations, and will only be included for the studies

of systematic uncertainties in this analysis. Including this azimuthal dependence has a small effect, as can be seen in Fig. 4.5, by comparing the grey (SPICE-MIE) and purple (SPICE-LEA) distributions for the absorption coefficient $b_e(400)$ and scattering coefficient $a(400)$.

Fig. 4.5 shows the scattering and absorption of photons in the ICECUBE detector as a function of depth, for both the SPICE-MIE and SPICE-LEA ice models. These plots show that the ice gets clearer to the bottom of the detector and that there is a layered structure, causing peaks in the absorption and scattering coefficients between different layers. The layered structure arises from the fact that the ice of the Antarctic glacier was formed from snow after it was compacted under its own weight in a very slow process. Because of the pressure, the air bubble content decreases with depth and at depths below ~ 1300 m all bubbles have converted to non-scattering air hydrates [117]. This is the main reason why the ICECUBE sensors are deployed at depths of 1500 to 2000 m below the ice sheet. It should be noted that there is a peak in these distributions at depths between 1950 m and 2100 m, where the scattering and absorption are approximately a factor 4 stronger than average. This peak arises from an extra dusty layer, often referred to as *the dust layer*, that is very likely indicating the presence of layers of volcanic ash [118].

Fig. 4.5 also shows that the average scattering length λ_s is about 20 m and the average absorption length λ_a is roughly 125 m. For this reason, the horizontal spacing of the strings in ICECUBE was decided to be 125 m.

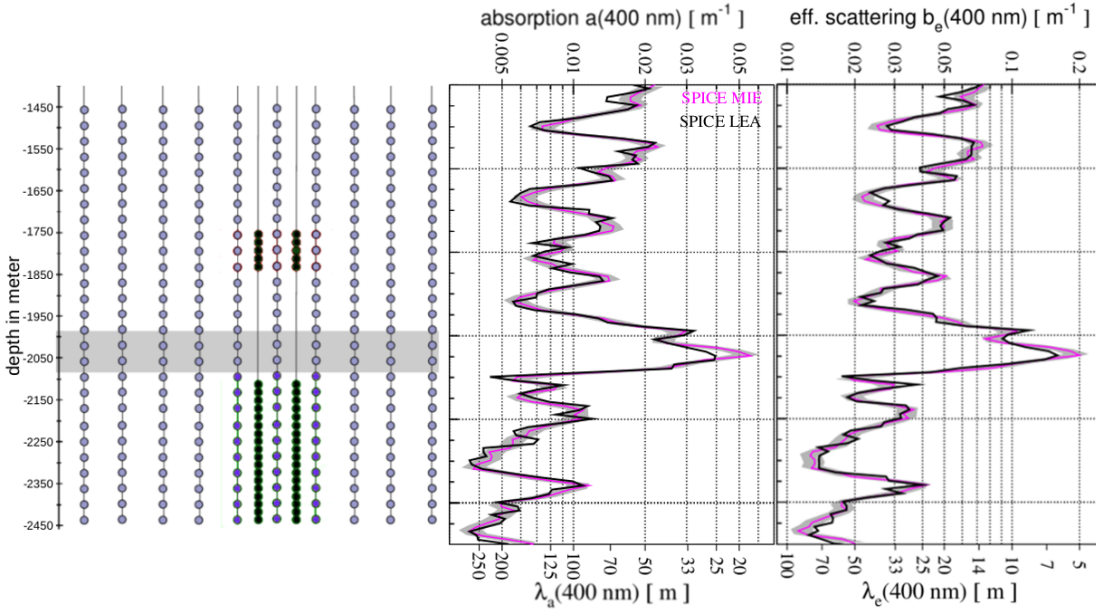
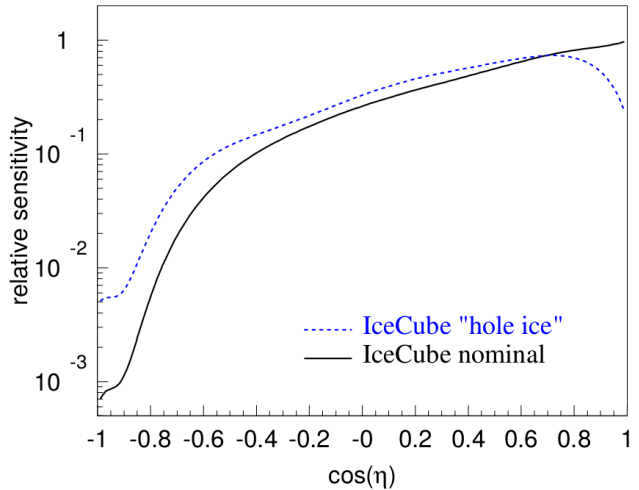


Figure 4.5: The absorption and scattering coefficients, a and b_e respectively (top axis) and absorption and scattering lengths, λ_a and λ_e respectively (bottom axis) of the South Pole ice as a function of the depth for the SPICE-MIE (magenta) and SPICE-LEA (black) ice models [116].

One final property to account for is the so-called *hole ice* effect [119]. To deploy the ICECUBE strings in the ice, 2500 m deep holes are drilled, by melting the ice in columns of about 60 cm radius with a hot-water drill. When the water refreezes, it is not as pure as the surrounding ice. The increased amount of scattering due to this impure ice is taken into account by empirically modifying the effective angular sensitivity curve of the receiving DOM, as shown in Fig. 4.6. The best fit for the scattering length in these holes is about 50 cm, which is about a factor of 10 smaller than the scattering length in the dust layer.

Figure 4.6: Angular sensitivity of an ICECUBE DOM where η is the photon arrival angle with respect to the PMT axis. The nominal model, based on a lab measurement, is normalized to 1.0 at $\cos \eta = 1$. The area under both curves is the same. Figure taken from [114].



4.3 Digital Optical Modules

The Cherenkov photons emitted by high-energy charged particles that cross ICECUBE, are recorded by Digital Optical Modules (DOMs), making these DOMs the centerpieces of the ICECUBE detector. Each DOM contains a downwards oriented 10 inch Photomultiplier Tube (PMT) to record the photons, along with a DOM Mainboard (DOM MB) to further process and digitize the signal. The PMT and the DOM MB are powered by a 2 kV high voltage power supply and is housed in a 13 mm thick glass sphere, capable of withstanding pressures to 70 MPa [120]. There is also a LED flasher board, that is used for *flasher runs* as described in Section 4.2.

The PMT is in contact with the glass via a transparent silicone gel and is surrounded by a mu-metal grid to shield it from the terrestrial magnetic field and improve its performance. A photon is detected in the following way [120]: first it reaches the DOM and crosses the glass sphere and the silicon gel to arrive at the PMT, where it can then be absorbed by the photo-cathode. After absorption, a photo-electron (PE) is emitted, which is amplified by a factor 10^7 as it passes 10 dynodes. This amplified signal is read out as a change in voltage of the anode in the PMT and is passed to the DOM MB for further processing. Further processing is triggered whenever there is a *hit*, i.e. whenever

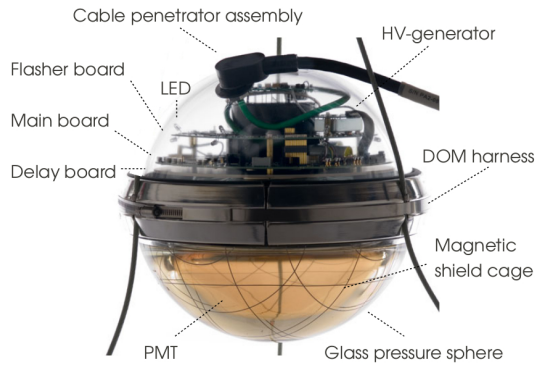


Figure 4.7: Schematic view of a Digital Optical Module (DOM) with its main hardware components.

the anode voltage exceeds 0.25 PE, where 1 PE is defined as the anode voltage level that a single photo electron holds after being amplified through all diode stages in the PMT. The probability that an incident photon produces a PE, called the quantum efficiency (QE) of a PMT, reaches a maximal value of 25% for light with a wavelength of 420 nm. ICECUBE PMTs are sensitive to photons with wavelengths from 300 nm to 675 nm.

Hits get tagged as Hard Local Coincidence (HLC) if 2 or more neighboring and/or next-to-neighboring DOMs (see Fig. 4.8) record a hit within a time window of $\pm 1 \mu\text{s}$. If no local coincidence is found, the solitaire hit is tagged as Soft Local Coincidence (SLC). This check is performed by an on-board CPU that communicates with the other electronics via a Field-Programmable Gate Array (FPGA).

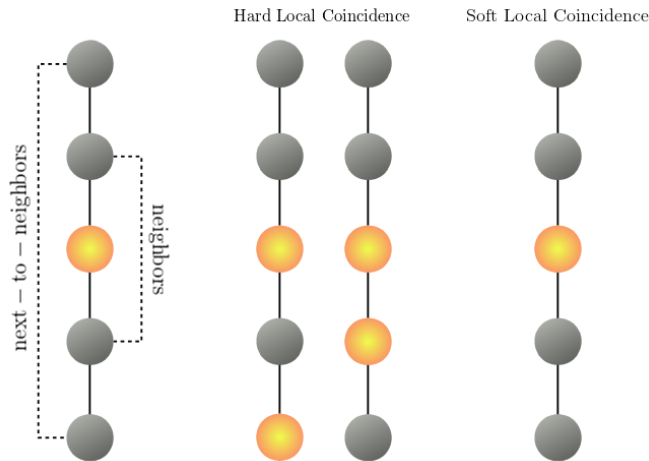


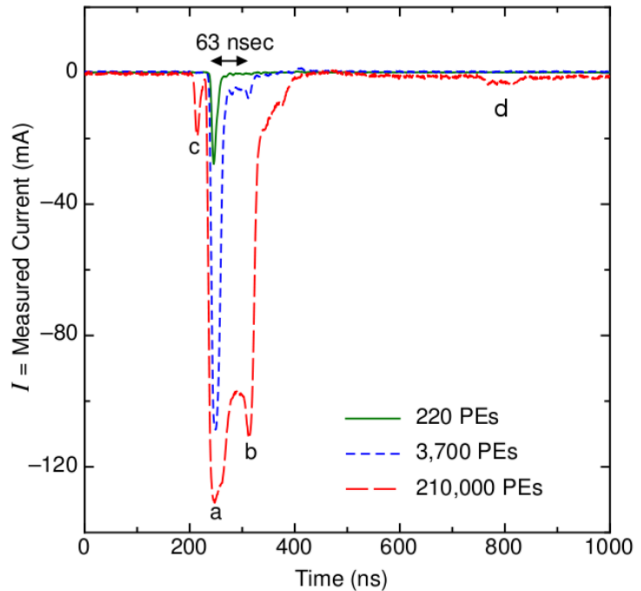
Figure 4.8: If ≥ 2 neighboring or next-to-neighboring DOMs are hit within $1 \mu\text{s}$, they are flagged as Hard Local Coincidence (HLC). Hits that don't satisfy this condition are called Soft Local Coincidence (SLC) hits.

The hits are read out in either high or low resolution mode, depending on the length of the PMT hit and on the local coincidence [120]. The hits are digitized by a Fast Analog to Digital Converter (fADC) that samples the PMT waveforms at a rate of 40 MHz. In case of SLC hits, only 3 samples (the highest amplitude bin and its two neighbors) of the first 25 samples of the fADC channel are read out. For HLC hits, a high resolution

digitizer, the Analog Transient Waveform Digitizer (ATWD), is read out on top of the full fADC channel. This digitizer has a sampling rate of 300 MHz, but can only sample for 422 ns, so longer signals are read out through the fADC. As the ATWD needs $29 \mu\text{s}$ to digitize and clear, two ATWDs are used in alternation to reduce the dead time.

The digitized signals are consequently sent to the surface electronics, where they are used for further analysis.

Figure 4.9: Average waveforms observed in a PMT as observed for 3 ns laser light pulses with progressively higher intensity. (a) Main peak; (b) secondary peak due to unusual electron trajectories, such as inelastic scattering on dynodes (late pulses); (c) pre-pulse; and (d) after-pulse. Figure from [120].



A typical PMT waveform is shown in Fig. 4.9, where the measured current in the anode is plotted as a function of time. This is shown for 3 ns laser light pulses with progressively higher intensity. While the low intensity pulse (220 PEs, solid green curve) only has one peak, being the main peak, the higher intensity curves clearly show more peaks. First a pre-pulse (c) is observed, which is coming from PEs that are ejected from the first dynode on their way in the amplification phase and thus causing a pulse prior to the main, amplified signal. The second peak (a) is the main peak, which is the actual physical hit. Directly after this main peak, a secondary peak (b) is observed, which is believed to be caused by electrons being scattered back from the first dynode to the photo-cathode, after which they turn around again, initiating a pulse. The final feature, called an after-pulse (d), is caused by ionization of residual gases by electrons accelerated in the space between dynodes. The ions can travel to the photo-cathode, where they can be absorbed, causing the emission of an electron that is then amplified and produces a signal. These after-pulses are observed in the range of 300 ns to $11 \mu\text{s}$, after the physical signal.

Another effect that is observed in the DOMs is the *Dark Rate*. This dark current is recorded by the PMT in absence of light. Although no consensus yet exists on the source, it is believed to come from a combination of electronics noise, radioactive decays in the

glass of both the PMT and pressure sphere and low-quality scintillation and Cherenkov light production in the glass. This dark noise rate is on average 560 Hz for standard DOMs with normal quantum efficiency PMTs, and 780 Hz for the DEEPCORE high Quantum Efficiency (QE) DOMs.

4.4 Neutrino signatures in ICECUBE

To identify whether hits belong to physical events rather than to the dark noise, it is necessary to understand how the expected physical events look like. ICECUBE is a neutrino observatory, and is able to detect neutrinos with energies ranging from 10 GeV to several PeV. The topology of the event in the detector will depend on the type of interaction, i.e. whether it is a charged current (CC) interaction or a neutral current (NC) interaction and in the case of CC interaction it will also depend on the flavor of the charged lepton and thus its parent neutrino. Remind that the interactions between neutrinos and nucleons were discussed in Section 3.2. The event topologies can be categorized in two main classes, *tracks* and *cascades*.

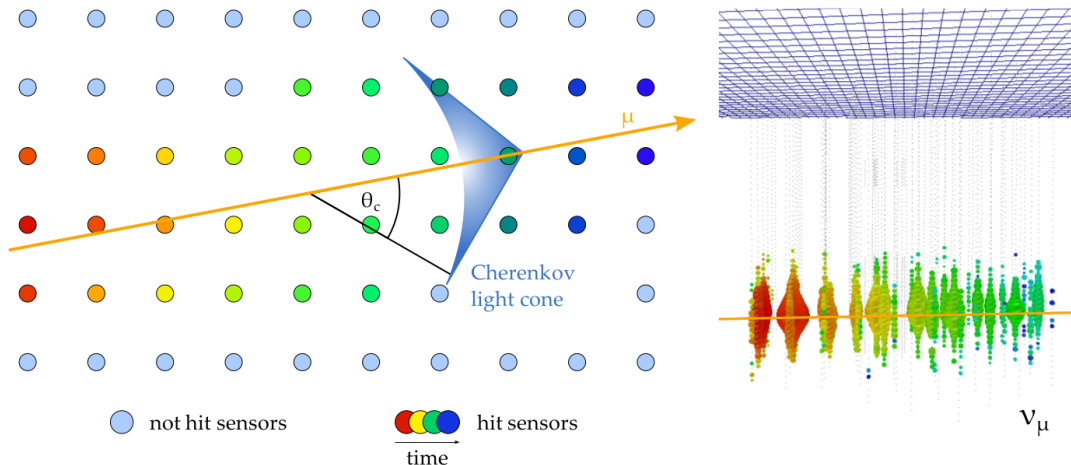


Figure 4.10: A sketch of a high-energy muon track in ICECUBE. Picture from [121].

Track-like events are produced in CC interactions with muon neutrinos: $\nu_\mu + N \rightarrow \mu + X$. As the muon has a long lifetime and limited energy loss, it travels for a significant distance in the detector before it decays, hereby producing Cherenkov photons, as is illustrated in Fig. 4.10. Thanks to the long lever arm of the muon track, its direction can be reconstructed with a precision that is inversely proportional with its energy. The angular resolution for TeV muons is better than 1° . This precision is increasing with the length of the track and thus the energy of the muon, hence the angular resolution degrades with decreasing energies. The energy resolution of muons is less precise, as they are often not fully contained in the detector and thus only deposit part of their energy inside the detector volume.

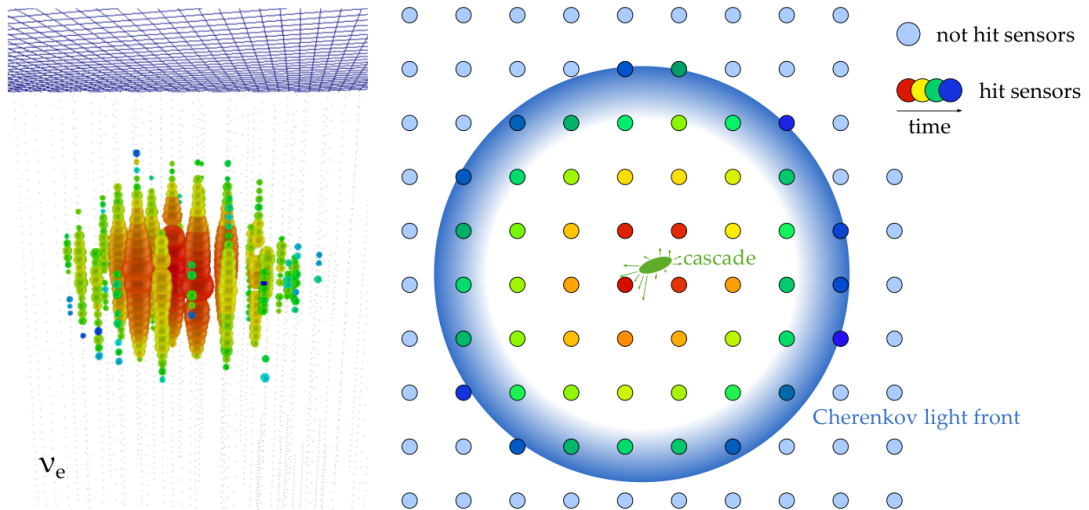


Figure 4.11: A sketch of a high-energy cascade in ICECUBE. Picture from [121].

Cascades can be of hadronic or electromagnetic type. Hadronic cascades are formed at the interaction vertex, in all types of interactions (NC, CC and all neutrino flavors), while electromagnetic cascades come from the interaction of an electron produced in the CC interaction $\nu_e + N \rightarrow e + X$. The spherical shape of these events (shown in Fig. 4.11) makes the direction reconstruction much harder, leading to a worse angular resolution than for the tracks. On the other hand it is more probable that events are fully contained, making it easier to reconstruct the energy.

A third CC event type is a tau neutrino interaction $\nu_\tau + N \rightarrow \tau + X$. The topology of these events depends on the energy and on the location of the interaction relative to the detector. For neutrinos in the GeV-TeV range, these events will look like electron cascades, as the tau lepton will immediately decay. As the higher energy taus are not of interest in this analysis, they are not discussed here and the interested reader is referred to [122].

4.5 Physical processes measured by ICECUBE

The analysis described in this thesis is looking for muon neutrinos ν_μ coming from the center of the Earth, where they originate from the decay of annihilation products of WIMPs. Whenever these neutrinos interact with a nucleon in the detector volume or the underlying bedrock via the CC interaction, the produced muon can be detected. The expected event rate of these signal neutrinos is at most at the order of a few μHz ($\mathcal{O}(10^3)/\text{km}^2/\text{year}$), as higher rates have been excluded by previous analyses.

However, most of the muons that ICECUBE is detecting, are produced in *cosmic ray air showers*. The *primary cosmic rays* are charged particles that are accelerated by astrophysical sources. When these particles reach the Earth and collide with nuclei in the atmosphere, jets of hadrons like pions and kaons are produced, which in turn decay into secondary particles like muons and neutrinos. A typical interaction chain is

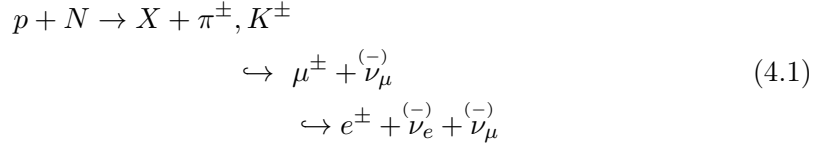


Fig. 4.12 schematically shows the evolution of a cosmic ray air shower.

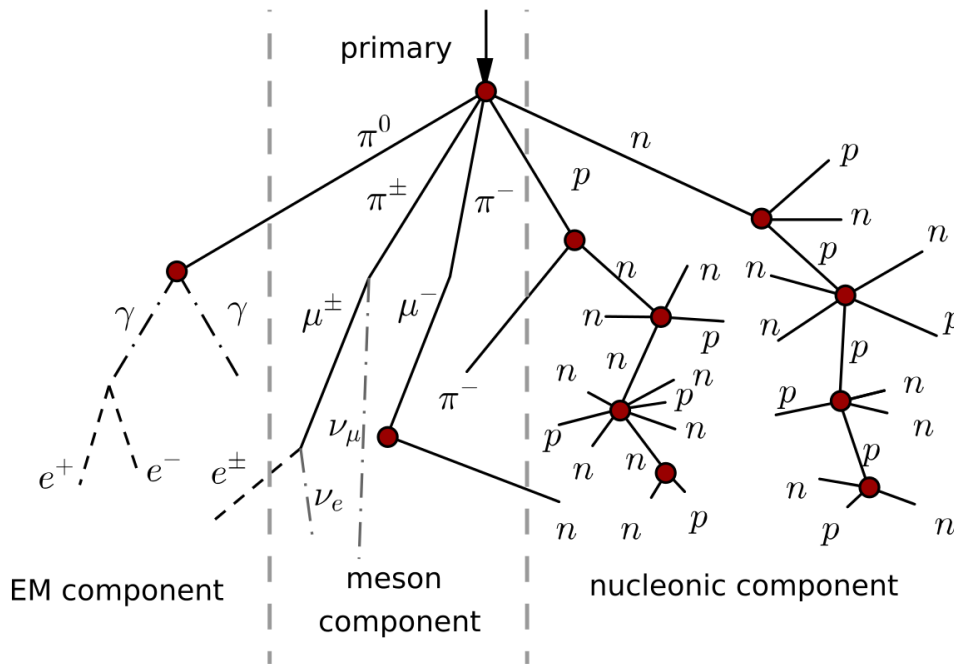


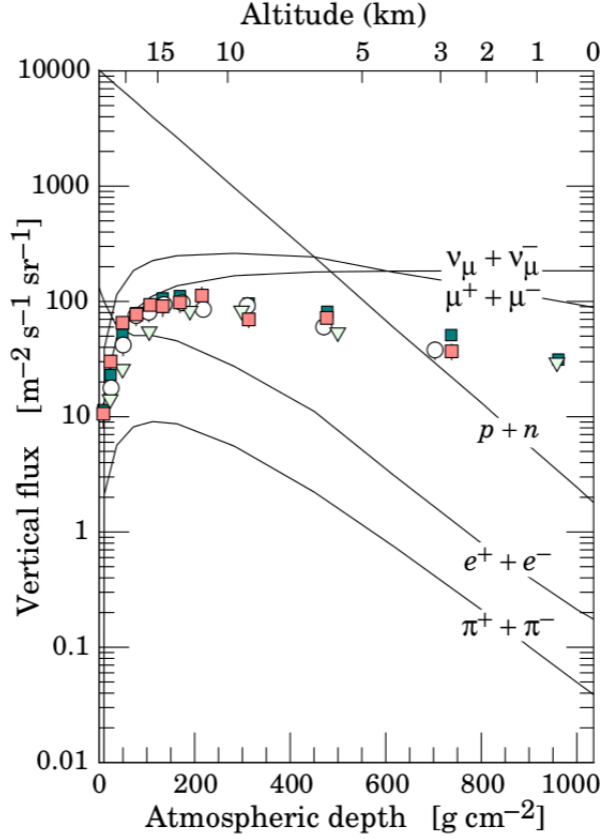
Figure 4.12: Schematic example of the evolution of a cosmic ray air shower. An extraterrestrial particle (e.g. proton) enters the atmosphere and collides with a nucleus in the atmosphere (e.g. Nitrogen). After this collision jets of hadrons, like pions and kaons, are produced, which in turn decay into secondary particles like muons and neutrinos.

Most of the particles in this shower interact in the atmosphere such that at sea level, the remaining particles of the shower are dominantly neutrinos and muons, as illustrated in Fig. 4.13¹. The flux of the atmospheric muons is strongly reduced once they reach the surface of the Earth and start to travel through it, but these particles are still the main background in the ICECUBE detector, which detects these atmospheric muons at

¹Note that the South Pole surface is at 3300 m altitude, so the top DOMs of ICECUBE are at about 1800 m altitude.

a rate of roughly 4 kHz. The higher the zenith angle, the lower the atmospheric muon flux, since more matter should be passed before the detector is reached. This means that up-going and horizontal muons cannot be atmospheric muons, but have to come from CC neutrino interactions close to the detector.

Figure 4.13: Vertical fluxes of cosmic rays in the atmosphere as a function of depth, for cosmic rays with $E > 1$ GeV. The points show the measurements of atmospheric μ^- , with $E_\mu > 1$ GeV. The solid lines show the expected spectra for different particles, where these spectra are derived from the measured muon flux. Figure from [82].



Since neutrinos only interact weakly with ordinary matter, they are able to travel across the Earth and could interact close to the detector via a CC interaction to produce up-going and horizontal muons. The up-going and horizontal muons are mainly produced by CC interactions of atmospheric muon neutrinos, which are also products of the cosmic ray showers. ICECUBE is measuring $\mathcal{O}(10^3)$ of these events per day. Fig. 4.14 shows the atmospheric neutrino energy spectrum measured by different experiments, as well as several theoretical predictions. As the present analysis is searching for GeV-TeV neutrinos coming from the direction of the center of the Earth, the atmospheric neutrinos will represent an irreducible background.

An overview of the different kinds of events detected in ICECUBE is given in Fig. 4.15. It shows how the down-going events are dominated by atmospheric muons, while up-going events are atmospheric neutrinos and extraterrestrial neutrinos.

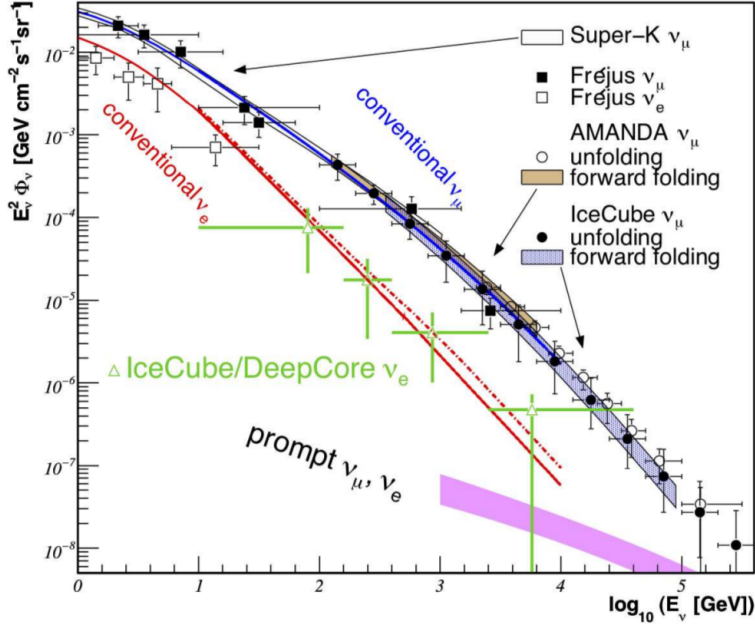


Figure 4.14: The atmospheric ν_μ and ν_e energy spectra measured by different experiments, as well as several theoretical predictions. The conventional ν_μ and ν_e from Honda are represented by the blue and red solid line respectively, and the ν_e spectrum according to Bartol is indicated by the red dashed-dotted line. The magenta band shows the charm-induced (prompt) neutrinos [123]. Previous measurements from Super-K [124], Fréjus [125], AMANDA [126, 126] and ICECUBE [127, 128, 129] are also shown. Figure from [129].

4.6 The ICECUBE data acquisition

The data acquisition (DAQ) at the South Pole goes in three steps [130]. It starts with a local coincidence check (Fig. 4.8) to reduce the dark-noise rate to 5-25 Hz per DOM for HLC hits. For the HLC hits all information is kept, while for the SLC hits only the time stamp and the waveform information around the peak is kept. In a second step these DOM hits are sent to the surface computers, where trigger algorithms check for a certain multiplicity of these hits within a given time window to reduce the noise rate even further (Section 4.6.1). The waveform data and non-HLC hit information of triggered events are then collected into events that are reconstructed and filtered, reducing the 1 TB/day raw data stream to approximately 100 GB/day. This first, low level data reduction is referred to as LEVEL 1.

After this LEVEL 1 filtering, the data are sent to the data warehouse at the University of Wisconsin (UW) Madison via satellite, where they can be accessed for further processing and analysis. At this processing stage, often referred to as LEVEL 2 processing, more sophisticated reconstructions and variables are calculated for each event. Specific event selections, such as the analysis presented in this thesis, start after this stage.

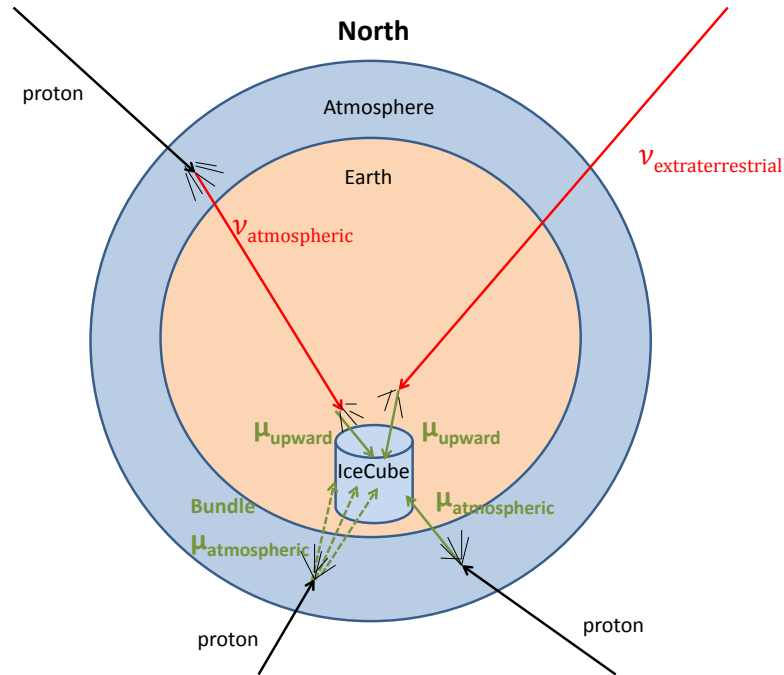


Figure 4.15: Schematic view of the different kind of events measured by ICECUBE. The down-going events (South to North) are dominated by atmospheric muons, while up-going events (North to South) will mainly be atmospheric neutrinos. For the analysis described in this thesis, these atmospheric muons and neutrinos are background.

4.6.1 Triggering

Trigger algorithms check for a certain multiplicity of HLC hits within a time window that is set according to the relevant light travel time in the ice and is slightly extended to allow early and late hits. The three trigger algorithms that are important for this analysis are

1. **The Simple Multiplicity Trigger** (SMT, also referred to as the simple majority trigger) is the workhorse trigger for ICECUBE. It looks for a multiplicity of N or more HLC hits within a sliding time window of several μs , without requiring any topology in the hit patterns. The trigger window is extended as long as the multiplicity condition is satisfied. The required multiplicity and the length of the time window depend on the subdetector in which the hit was recorded, as ICECUBE, DEEPCORE, IN-ICE (=ICECUBE+DEEPCORE) and ICETOP have different DOM spacings. An overview of these values is given in Table 4.1.
2. **The Volume Trigger** looks for 4 HLC hits within a cylinder with a fixed size ($r=175\text{m}$, $h=75\text{m}$), as shown in the left panel of Fig. 4.16. This locality condition allows to lower the multiplicity threshold, and thus to look for low energy tracks and cascades.

3. **The String Trigger** requires five HLC hits in seven neighboring DOMs on a single string (right panel of Fig. 4.16). This trigger looks for low-energy muons that pass vertically through the detector, and will thus be of great importance in the search for low energy Earth WIMPs.

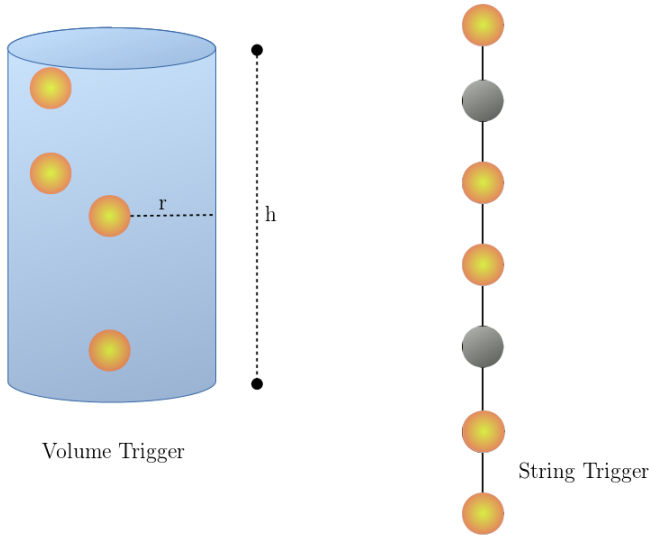


Figure 4.16: Schematic representations of the Volume Trigger that looks for four HLC hits in a cylindric volume (left) and the String Trigger that requires five HLC hits on a single string (right).

Table 4.1: ICECUBE trigger parameters (as of May 2013) and typical trigger rates of each algorithm (most rates have seasonal variations) [130].

Trigger	Subdetector	N HLC Hits	Window (μs)	Topology	Rate (Hz)
SMT	IN-ICE	8	5	/	2100
SMT	DEEPCORE	3	2.5	/	250
SMT	ICETOP	6	5	/	25
Volume	IN-ICE	4	1	Cylinder	3700
String	IN-ICE	5	1.5	7 neighboring DOMs on 1 string	2200

Other special-purpose triggers exist besides these three main triggers, but these are not explained here as they are not used in this analysis. The interested reader is referred to [130] for more information on these trigger algorithms.

4.6.2 Online filtering

The majority of the triggered events are due to atmospheric muons, which are a background for most of the analyses in ICECUBE. To reduce the rate of these events, special online filters have been developed. These filter algorithms are used to tag events which fulfill certain conditions on for example the energy, the direction and the topology of the event. Each filter has its own purpose and is designed to tag a certain type of events. Out of the 21 dedicated filters that ran online in the first season of the fully deployed ICECUBE detector (from now on referred to as IC86-I), which is the dataset used in

this analysis, four are of interest for this analysis and are explained below. One of these filters, the *Vertical Event Filter* (VEF) has been designed specifically for this analysis, and tags low energetic, vertically up-going events. Examples of the other filters are the Cascade Filter, which is dedicated to cascade events [131], the High Energy Starting Event (HESE) filter [108], the Extremely High Energy (EHE) filter [132].

Below, a brief description is given of the four online filters which are used in the analysis presented in this thesis. The efficiencies on the signal and experimental data, of the individual filters, as well as the combination of these filters, are presented in Fig. 4.19.

The reconstruction algorithms which are used in the filtering process, are described in detail in the next chapter.

Vertical Event Filter

The aim of the Vertical Event Filter (VEF) is to tag low energy, vertically up-going muon tracks, i.e. events of interest for oscillation analyses [88] and Earth WIMP searches. The IC86-I version of this filter, which is the one used in this analysis, is described in [133]. Events are tagged by the filter if they satisfy the following conditions:

1. The event is string triggered.
2. The event is successfully reconstructed by the low level LINEFIT reconstruction (see Section 5.2), and has a reconstructed zenith angle $\theta_{\text{LINEFIT}} > 70^\circ$.
3. The event is successfully reconstructed by the more sophisticated LLHFIT reconstruction (see Section 5.2), and has a reconstructed zenith angle $\theta_{\text{LLHFIT}} > 140^\circ$.
4. There are no hits in the top 5 DOM layer.
5. The clean TWSRT hits (see Section 5.1.2) are all on one single string.

Remind the zenith angle convention presented in Fig. 4.3.

After a study of data taken for this analysis, the filter has been further optimized for the next seasons as described in [134]. More precisely, the last condition, the single-string requirement, was removed. By removing this requirement, the efficiency of the filter increased for vertical events ($\theta_\nu > 170^\circ$) in the studied energy range $10 \text{ GeV} < E_\nu < 500 \text{ GeV}$, as indicated in Fig. 4.17.

As this change was only introduced from IC86-II (the second year of data taking of the complete ICECUBE detector), the work described here could not benefit from this increase in efficiency.

LowUp Filter

The LowUp-Filter is selecting low-energetic, up-going muon events. Contrary to VEF, it is not looking for vertically up-going events only, but broadens its search window to more horizontal events also. Thanks to this broad window, the filter is of interest for

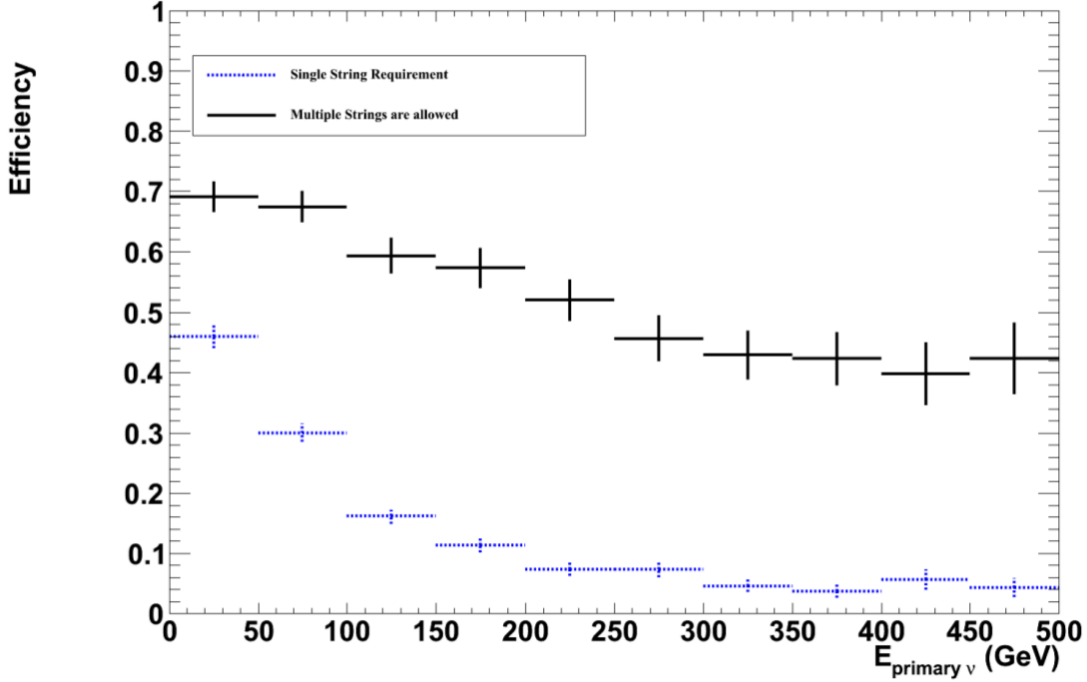


Figure 4.17: Signal ($\theta_\nu > 170^\circ$) efficiency of VEF with (blue dotted bars) and without (black solid bars) the single-string requirement. The efficiency is calculated w.r.t. string triggered events. Figure from [134].

many different types of analyses, and is mainly used in (Solar) WIMP searches. To be tagged by this filter, an event should satisfy the following conditions [135]:

1. It has to be triggered by at least one of the triggers in the list [SMT8, SMT3, String, Volume trigger] (see Table 4.1).
2. There should be at least 4 DOMs with clean TWSRT hits $N_{\text{Ch}} > 4$.
3. The event is successfully reconstructed by either the low level LINEFIT reconstruction or the more sophisticated LLHFIT reconstruction and the zenith of the reconstructed track should be $\theta_{\text{track}} > 80^\circ$, where track is the LLHFIT if this reconstruction succeeded, and LINEFIT otherwise.
4. The average drift of the n TWSRT hits in the vertical (z) direction $z_{\text{travel}} = \sum_{i=1}^n (z_i - \langle z_{\text{quartile},1} \rangle) / n$ should be greater than -10 m.
5. The event should have a duration $t_{\text{ext}} = t_{\text{max}} - t_{\text{min}}$ less than 4000 ns.
6. The extension in the vertical (z) direction $z_{\text{ext}} = |z_{\text{max}} - z_{\text{min}}|$ should be greater than 600 m.

7. The TWSRT hits should all have a z -coordinate below 440 m, hence $z_{\max} < 440$ m.

Muon Filter

The Muon Filter aims to provide a sample of muons useful for analyses over the whole sky. The conditions required by this filter, are based on the number of DOMs with clean TWSRT hits N_{Ch} , the zenith angles of the low level LINEFIT reconstruction θ_{LINEFIT} and the more sophisticated SPE1 reconstruction θ_{SPE1} , the total collected charge in the clean TWSRT hits Q_{tot} and the log-likelihood parameter of the SPE1 reconstruction \log_{SPE1} , which is a quality indicator of the track reconstruction. The filter checks events for the following conditions [136]:

1. The event is triggered by SMT8 trigger.
2. $N_{\text{Ch}} \geq 8$ and ($N_{\text{Ch}} \geq 10$ or $\theta_{\text{LINEFIT}} \geq 70^\circ$),
3. One of the following conditions also needs to be satisfied:
 - (a) $\theta_{\text{SPE1}} \leq 60^\circ$ and $\log(Q_{\text{tot}}) \geq 0.6 \cos(\theta_{\text{SPE1}}) + 2.6$
 - (b) $60^\circ < \theta_{\text{SPE1}} \leq 78.5^\circ$ and $\log(Q_{\text{tot}}) \geq 3.9 \cos(\theta_{\text{SPE1}}) + 2.6$
 - (c) $78.5^\circ < \theta_{\text{SPE1}}$ and $\log_{\text{SPE1}} / (N_{\text{Ch}} - 3) \leq 8.7$

To save computing time, the trigger check (1) and first base cut (2) are applied prior to the SPE1 maximum likelihood reconstruction.

DeepCore Filter

The aim of this filter is to select contained and partially contained neutrino-induced tracks and showers down to neutrino energies of 10 GeV. This filter algorithm applies a simple veto to the cosmic ray muon background events that dominate the low energy data set as is described in detail in [110]. The veto algorithm (sketched in Fig. 4.18) goes in 4 steps:

1. First the HLC hits within the DEEPCORE subdetector are selected.
2. Next the center of gravity (COG) of these selected hits is calculated.
3. After this, the algorithm loops over all HLC hits in the ICECUBE detector and calculates the speed v at which the particle would need to travel to reach the COG given the relative trigger times, as follows:

$$v = \frac{\vec{r}_{\text{HLC hit}} - \vec{r}_{\text{COG}}}{t_{\text{HLC hit}} - t_{\text{COG}}} \quad (4.2)$$

4. In the last step, events where this speed v is between 0.25 and 0.40 m/ns are removed.

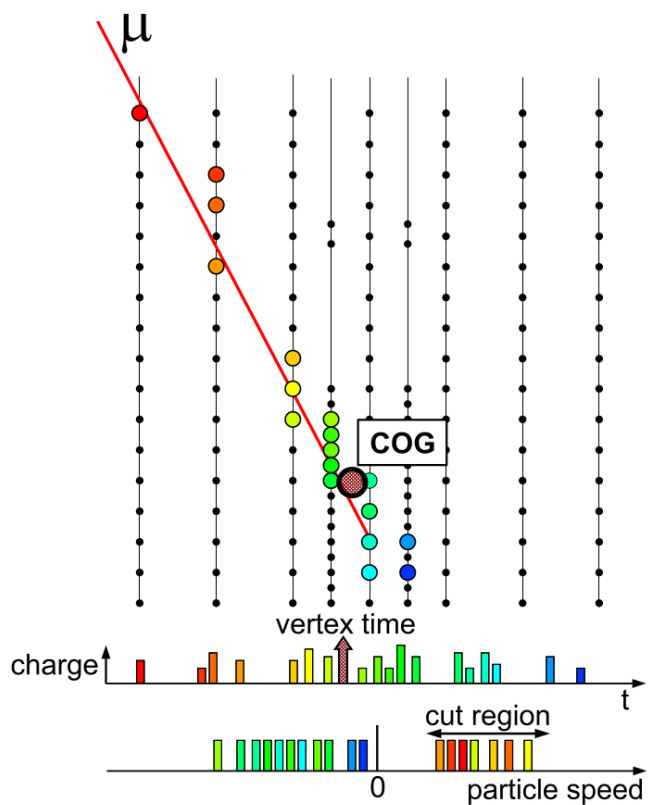


Figure 4.18: A conceptual diagram of DEEPCORE veto filter algorithm. Picture from [110]

The efficiencies of the individual filters, as well as the combination of the four filters are shown in Fig. 4.19 for two signal hypotheses and for the experimental data. These efficiencies are calculated w.r.t. LEVEL 1, i.e. all possible online filters.

All events passing at least one of the online filters are transferred via satellite to the data warehouse at the University of Wisconsin (UW) Madison, where they can be accessed for further processing and analysis. More sophisticated reconstructions and variables are then calculated for each event that is sent North. This step is often referred to as LEVEL 2 processing. Specific event selections, such as the analysis presented in this thesis, start with data that has been processed up to LEVEL 2 and further reduce the data rate. A detailed overview of the specific event selection of the analysis described in this thesis, is given in Chapter 7.

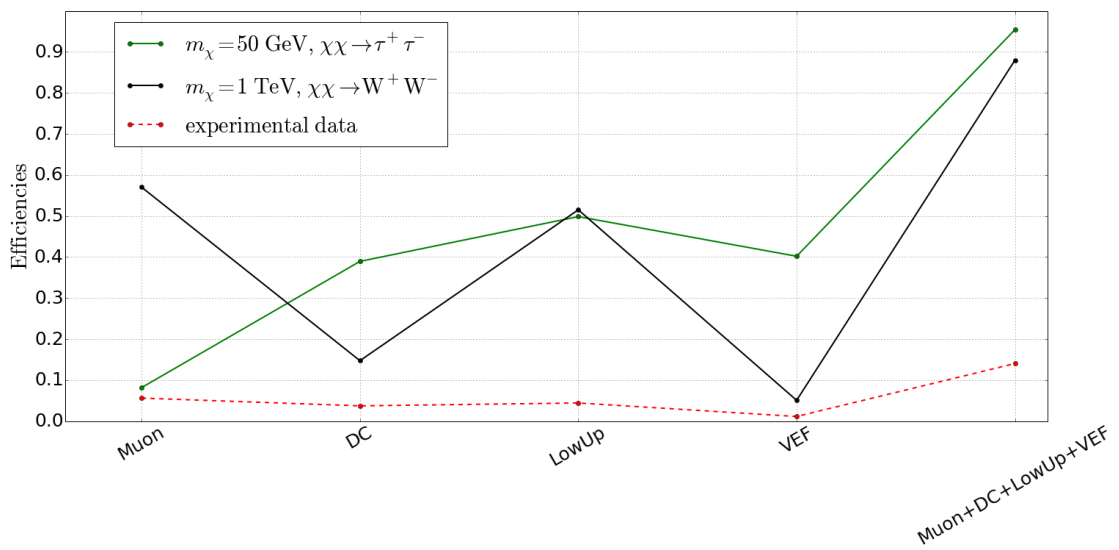


Figure 4.19: Efficiencies w.r.t. all online filters of the individual online filters considered for this analysis and the combination of these four filters. These efficiencies are shown for two different WIMP models: 50 GeV WIMPs annihilating into $\tau^+\tau^-$ (green solid line) and 1 TeV WIMPs annihilating into W^+W^- (black solid line), as well as for experimental data (red dashed line).

Summary

The ICECUBE neutrino detector is a cubic kilometer neutrino detector located at the geographical South Pole, 1.5 km beneath the ice surface. It consists of 5160 Digital Optical Modules, deployed on 86 strings, that record the Cherenkov photons of high-energy charged particles crossing the detector volume.

The DOMs digitize the triggered hits on board and send the digitized signals to the surface computers, where trigger algorithms check for a certain multiplicity of these hits within a given time window. The waveform data and non-HLC hit information of triggered events are then collected into events that are reconstructed and filtered, reducing the 1 TB/day raw data stream to approximately 100 GB/day. Amongst the online filters, four filters are used for the presented analysis and these filters were described in detail.

This reduced data stream is then sent to the data warehouse at the University of Wisconsin (UW) Madison via satellite, where they can be accessed for further processing and analysis.

If you do not change direction, you may end up where you are heading.

Lao Tzu

5

Hit Cleanings and Event Reconstructions

In this chapter, the basics of the event processing are described. These basics consist of hit calibration and cleaning on one hand, and reconstruction of the direction, starting and stopping points and energy of the events on the other hand. Some of the described cleaning and reconstruction algorithms were already used in the online filters, described in Chapter 4, and the other algorithms will be used in the event selection, which is discussed in detail in Chapter 7.

The recorded raw ICECUBE data have to be prepared before they can be used in analyses. This starts by calibrating the waveforms (Section 5.1.1), i.e. calculating how many photo-electrons belong to the waveform and at what time they arrived at the DOM. These calibrated waveforms are then split in individual pulses (Section 5.1.1), which are then cleaned (Section 5.1.2), such that most of the noise pulses are removed and they mainly consist of pulses caused by Cherenkov photons.

Some of the events, only consisting of noise pulses, are removed by a dedicated algorithm, as described in Section 5.3.

Consequently several reconstruction algorithms, discussed in Section 5.2, are used to reconstruct the direction, interaction vertex or length of the charged particle that emitted these Cherenkov photons.

5.1 Hit Processing and Cleaning

5.1.1 Waveform Calibration and Fitting

As described in Section 4.3, the Photo Multiplier Tubes (PMTs) in the Digital Optical Modules (DOMs) in ICECUBE are detecting Cherenkov radiation of charged particles which traverse the detector medium. The measured PMT charge pulses are sent to the surface electronics as digitized waveforms containing time stamps and number of ADC counts per digitizer bin. First the ADC counts are calibrated by performing a per DOM baseline subtraction and correcting for the droop that is caused by the transformer between the High Voltage supply and the PMT, which causes the tails of the waveform to undershoot. The calibrated ADC counts are translated into their voltage equivalent. In the next step the start times of the waveforms are calculated by correcting the contained time stamps for the time a pulse needs to be transmitted from the PMT to the readout chip.

Next the calibrated waveforms are unfolded into a series of reconstructed pulses by the WAVEDFORM [137] algorithm. This algorithm decomposes the waveforms into single photo-electron pulses with individual amplitudes and arrival times by searching for a set of pulses that combine linearly and provide a good fit to the fADC and the two ATWD channels simultaneously. An example result of this unfolding is shown in Fig. 5.1 for a waveform containing a single PE (Fig. 5.1a) and multiple PEs (Fig. 5.1b).

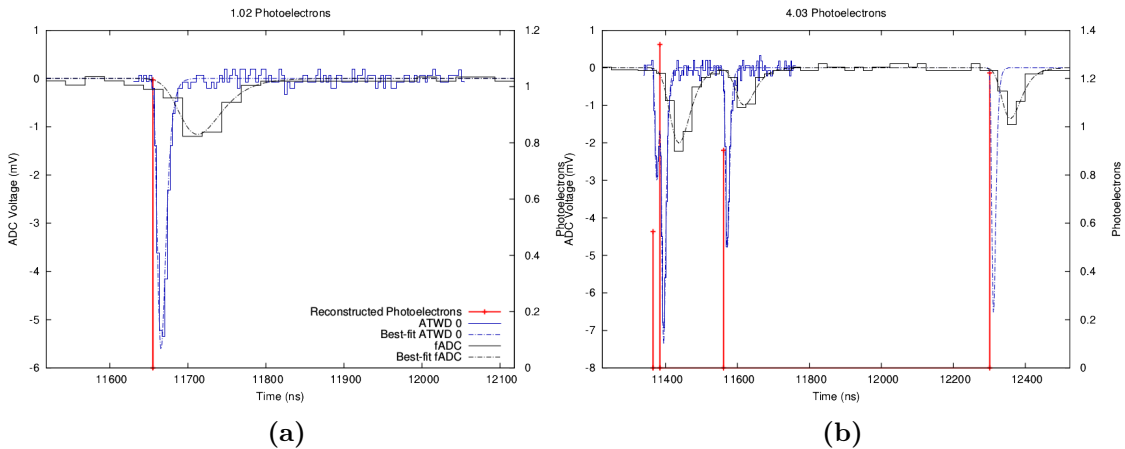


Figure 5.1: Examples of waveform unfolding for a waveform containing a single PE (a) and multiple PEs (b). The solid lines show the data in the ATWD and fADC channels and the dashed-dotted lines show the best fit through these data. The vertical red lines with crosses at the top represent the times and amplitudes of the unfolded pulses. Figure from [137].

An extracted single pulse with an associated extracted photon arrival time and integrated charge, is from now on referred to as *hit*.

5.1.2 Hit Cleaning and splitting

During the time window of a trigger, all HLC and SLC readouts are stored. While most of the HLC pulses will generally be associated to real physical events, most of the SLC pulses are caused by noise. Nevertheless, the SLC pulses caused by physics are of great importance in the direction reconstructions, mainly for low energy events with only few associated hits. Cleaning algorithms are used to remove irrelevant noise readouts from the pulse-series while keeping as many of the physics pulses as possible.

In this analysis two different cleaning algorithms are used, the TIME-WINDOW-SEEDED-RADIAL-TIME (TWSRT) cleaning and the more sophisticated HIVESPLIT cleaning.

TIME-WINDOW-SEEDED-RADIAL-TIME cleaning

This algorithm starts with a Radial-Time (R-T) cleaning of the HLC hits, i.e. by selecting all HLC hits that have another HLC hit a within 150 m and 1 μ s. These R-T-cleaned HLC hits are then used as a seed in the SRT algorithm, which looks in three iterations for HLC or SLC hits that satisfy the R-T condition with another hit that is already in the kept set at the start of the iteration and adds them to the set.

After the SRT cleaning, a static time-window cut is applied, which removes hits that occurred more than 4 μ s before or 10 μ s after the event triggering time.

The online filters used in this analysis are based on the TWSRT cleaned pulses, except for the DeepCore Filter which uses a dedicated veto technique as discussed in Section 4.6.2. Also the variables that are used for the first levels of the event selection are based on these cleaned pulses, as this information is available from the beginning of the processing.

HIVESPLIT cleaning

This cleaning algorithm takes into account that multiple events could be in the detector at the same time, i.e. during the same trigger time window. If these coincident events are not split correctly, they confuse the reconstruction algorithms, leading to wrong reconstructions. About ten percent of all triggered events in ICECUBE are coincident events, so it is important to split them into individual events or at least recognize that the event consists of multiple particle tracks.

In the HIVESPLIT algorithm [138, 139], all HLC and SLC hits get an individual active volume (IAV), which is a volume around the hit, as represented by the colored circles in Fig. 5.2. An overlap between at least 4 IAV (3 other IAV + the IAV of the hit itself) is required at the position of the hit, for the hit to be added to the set of cleaned pulses. This multiplicity requirement is sketched in Fig. 5.2, where the development of a particle track moving through the detector is shown. The particle starts in the left panel, where 5 hits are recorded. As the first hit does not overlap with the IAV of three other hits it is excluded, here marked as a hollow black circle. The other four hits satisfy the multiplicity requirement and are thus marked as clean hits, represented by a solid black circle. This

multiplicity check goes on for further hits, but as time evolves, the IAV of previous hits goes to zero as shown in the central and right panel of Fig. 5.2.

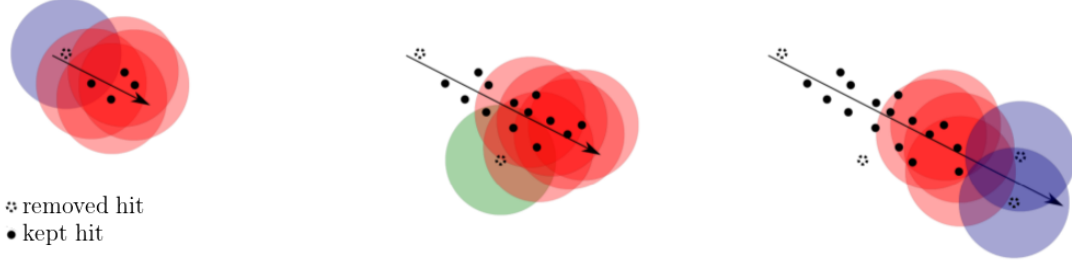


Figure 5.2: Overview of the HIVESPLIT cleaning principle. A hit is kept (marked with a solid black circle) whenever 4 IAV (colored circles) overlap at its location. If this multiplicity is not satisfied, hits are removed from the set (marked as a hollow black circle). Picture taken [139]

Unlike its representation in Fig. 5.2 the IAV of a hit is not a filled sphere, but rather a general mathematical object with a shell-thickness that corresponds to the allowed time residual, which is the difference between the propagation time of photons in absence of scattering and absorption, and the observed hit time

$$t_{\text{res}} = t_{\text{hit}} - t_{\text{geo}} = t_{\text{hit}} - \left(t_0 + r_{\text{geo}} \frac{n}{c} \right), \quad (5.1)$$

with r_{geo} the geometrical path of an unscattered photon. The mathematical object should be constructed such that two hits are connected if one of the following conditions is satisfied, as stated in [138]:

1. hits are located on different geometrical/topological sites of the same light-front (Cherenkov-cone), thus are spatially separated with no or little time separation,
2. hits are caused by photons of the same light-front traveling between DOMs, thus hits are connected by the speed of photon propagation,
3. hits are caused by light-emission at different positions along a muon-track, thus hits are connected by the speed of particle propagation.

These conditions are graphically represented in Fig. 5.3.

Each hit thus has three contributions to the IAV, each one with its own thickness, as different residual times have to be considered for all of the above listed processes. The size of the IAV also depends on the detector geometry and thus the location of the hit in the detector. Hits in DeepCore will have a smaller IAV, as the DOMs are closer together in this part of the detector. Optimizing this IAV is of great importance, as it will remove noise hits, which might wash out sharp event characteristics and topologies causing bad performance of the algorithm.

This algorithm is also used to separate coincident tracks, as is indicated in Fig. 5.4. In this figure the same hit cleaning is shown as in Fig. 5.2, but this time for two coincident particles.

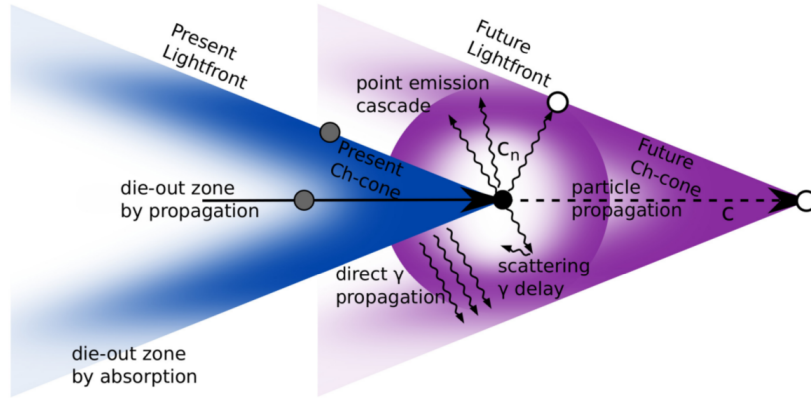


Figure 5.3: Possible light emission topologies for tracks and cascades at the present (blue) and future (pink) after photon-propagation for a particle (arrow) traversing the detector volume. Hits are registered on DOMs (circles); their relation is governed by the causal arguments of spatial separation, photon propagation and particle propagation. Picture from [138].

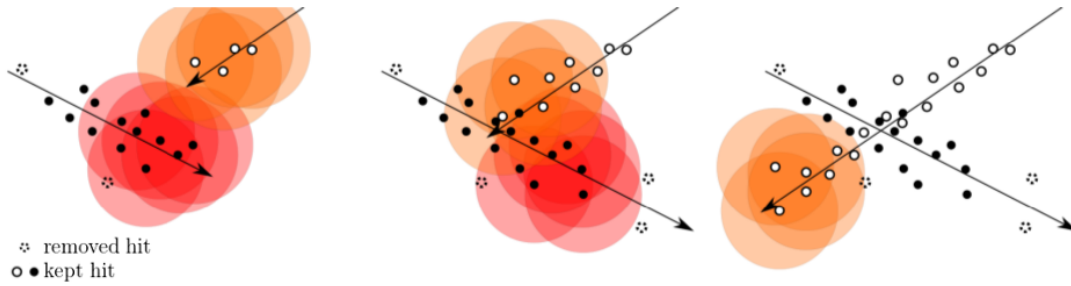


Figure 5.4: Illustration of how the HIVESPLIT Cleaning principle works for coincident tracks. Picture from [139].

The HIVESPLIT cleaned pulses are used in later stages of the analysis described in this thesis, as they are not available at low levels and the events thus have to be reprocessed. The splitting function of the algorithm is not used in this analysis directly, but the algorithm provides a parameter which indicates how many events were detected in coincidence, and this parameter is used.

5.2 Event Reconstruction

The cleaned pulses are used to reconstruct the direction, interaction vertex and track length of the particle to which they are associated. The reconstructions described below are all used at a certain point in the work described in this thesis.

5.2.1 LINEFIT

The first algorithm, LINEFIT, produces an initial track on the basis of the hit times with an optional amplitude weight. LINEFIT does not take into account the geometry of the Cherenkov cone, nor the optical properties of the medium. It assumes that the (reconstructed) particle travels through the detector with a velocity \vec{v} along a 1-dimensional path. DOMs that are located at positions \vec{r}_i and are hit at time t_i can be connected by a line [140]

$$\vec{r}_i \simeq \vec{r}_0 + \vec{v} \cdot t_i, \quad (5.2)$$

Using Eq. (5.2) a χ^2 can be defined that has to be minimized

$$\chi^2 = \sum_{i=1}^{N_{hit}} (\vec{r}_i - \vec{r}_0 - \vec{v} \cdot t_i)^2 \equiv \sum_{i=1}^{N_{hit}} \rho_i^2(\vec{r}_0, \vec{v}), \quad (5.3)$$

where N_{hit} is the number of hits. Eq. (5.3) is minimized by differentiation with respect to the free parameters \vec{r}_0 and \vec{v} . Solving this analytically, gives

$$\begin{cases} \vec{r}_0 &= \langle \vec{r}_i \rangle - \vec{v} \cdot \langle t_i \rangle, \\ \vec{v} &= \frac{\langle \vec{r}_i \cdot t_i \rangle - \langle \vec{r}_i \rangle \cdot \langle t_i \rangle}{\langle t_i^2 \rangle - \langle t_i \rangle^2}, \end{cases} \quad (5.4)$$

with $\langle x_i \rangle \equiv \frac{1}{N_{hit}} \sum_{i=1}^{N_{hit}} x_i$. The LINEFIT thus reconstructs

- a vertex point \vec{r}_0 ,
- a direction $\vec{e} = \vec{v}_{LF} / |\vec{v}_{LF}|$, and thus a zenith angle given by

$$\theta_{LF} = -\arccos(v_z / |\vec{v}_{LF}|), \quad (5.5)$$

where v_z is the z -component of the velocity vector \vec{v} .

- a speed $|\vec{v}_{LF}|$ which represents the mean speed of the particle propagating through the 1-dimensional detector projection. This speed can be used as a quality parameter for long muon tracks, as for these tracks the value of this speed factor will be close to c , while for cascade like or noisy events, the value will typically be lower.

Recently this model has been improved by giving outliers a linear weight instead of a quadratic weight [141]. This is done by replacing Eq. (5.3) by

$$\chi^2 \equiv \sum_{i=1}^{N_{hit}} \phi(\rho_i(\vec{r}_0, \vec{v})), \quad (5.6)$$

where $\phi(\rho)$ is the Huber penalty function, and is defined as

$$\phi(\rho) = \begin{cases} \rho^2 & \text{if } \rho < \mu \\ \mu(2\rho - \mu) & \text{if } \rho \geq \mu \end{cases}, \quad (5.7)$$

where $\rho_i(t_0, \vec{x}_0, \vec{v})$ is the same function as defined in Eq. (5.3) and μ is a constant that is optimized on the data. Using this function, hits in the near-hit regime ($\rho < \mu$) get a quadratic weight, while hits in the far-hit regime ($\rho \geq \mu$) get a linear weight. In this way the uncorrelated hits (probably noise) are penalized w.r.t. strongly correlated hits.

The simple, older version of LINEFIT, of which the χ^2 is given in Eq. (5.3) is used in the online filtering, as the improved version with the χ^2 given in Eq. (5.6) was not available yet at that time of online filtering in IC86-I. The improved version is used for all higher levels. The LINEFIT reconstruction is mainly used as a seed for more sophisticated reconstructions, such as the Likelihood Fit described in the next section.

5.2.2 Likelihood Fit

A more elaborate track reconstruction is obtained by using a Likelihood fit. In this reconstruction method, the parameters of the track are denoted by the set of values $\vec{a} = \{a_i\}$ and the measured quantities by $\vec{x} = \{x_i\}$. The likelihood that a set of quantities \mathbf{x} are measured, given the track parameters \vec{a} is given by

$$\mathcal{L}(\vec{x}|\vec{a}) = \prod_i p(x_i|\vec{a}), \quad (5.8)$$

where $p(x_i|\vec{a})$ is the probability density function (PDF) for observing the values $\{x_i\}$, given the hypothetical track parameters $\{a_i\}$.

The track parameters used in the likelihood are the vertex time, position and energy (t_0, \vec{r}_0, E_0) and a direction $\hat{p}_0 = (\theta, \phi)$ as shown in Fig. 5.5. The likelihood PDF can be

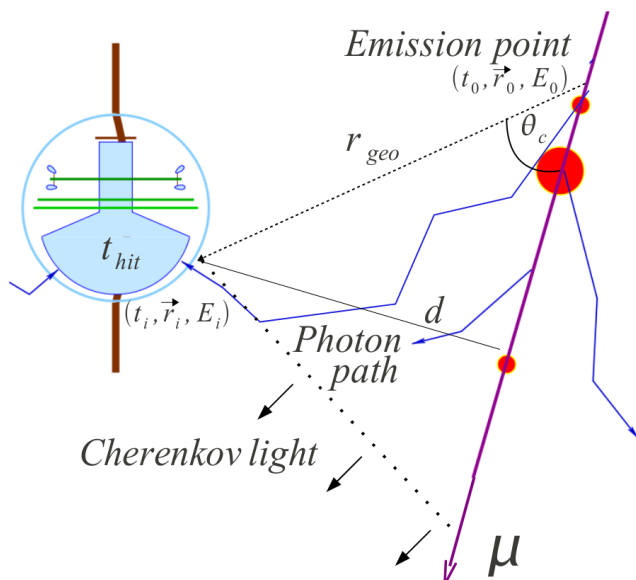


Figure 5.5: Schematic illustration of the parameters that are used to reconstruct a muon track. Figure from [33].

written in terms of time residuals t_{res} , which were defined in Eq. (5.1):

$$\mathcal{L} = \prod_i \mathcal{P}(t_{res,i}|\vec{a}), \quad (5.9)$$

where \mathcal{P} is the *Pandel function* [140], which is an analytic function that takes into account the absorption and scattering of the Cherenkov photons in the ice:

$$\mathcal{P}(t_{res,i}) = \frac{t_{res,i}^{d/\lambda-1}}{\Gamma(d/\lambda) \cdot \left(\frac{1}{\tau} + \frac{c_{\text{medium}}}{\lambda_a}\right)^{-d/\lambda}} \cdot \exp\left[-t_{res,i} \cdot \left(\frac{1}{\tau} + \frac{c_{\text{medium}}}{\lambda_a}\right)\right], \quad (5.10)$$

where d is the perpendicular distance between the track and the DOM, $\lambda_a = 98$ m is the average absorption length of the ice, c_{medium} is the speed of light in the ice and $\lambda = 33.3$ m and $\tau = 557$ ns are constants determined by simulation.

The Pandel function does not take into account the PMT jitter and the potential for negative time residuals from random noise in the detector, so it has to be convoluted with a Gaussian with a width σ_{jit} and a uniform function to account for the jitter and the noise respectively [142]. The convoluted function returns the probability of observing the measured hits at each PMT. Multiplying the likelihoods of all the PMTs yields a total likelihood \mathcal{L}_{tot} that can be maximized. The muon track that maximizes \mathcal{L}_{tot} or rather minimizes $-\mathcal{L}_{tot}$ is then the best guess hypothesis.

This reconstruction can either be done by only using the first pulse of each waveform, so doing a Single PE fit (SPEFIT), or by doing a Multiple PE fit (MPEFIT), i.e. using all the pulses in the event and thus correcting the PDF in each DOM according to the total charge n_{PE} observed by that DOM.

The likelihood based event reconstructions described above require a track vertex and direction as a seed to determine the initial values in the likelihood space. In the analysis presented here, the result of the LINEFIT reconstruction is used as a seed for the SPEFIT, which in its turn is used as a seed for the MPEFIT. The MPE tends to improve the reconstruction, especially when SPE provides a good seed.

These Likelihood-based reconstructions are used at all levels of the analysis.

5.2.3 Reconstruction of the interaction vertex and the length

The result of the previous reconstructions is a track with a reference point, a time and a direction, but still with an infinite length. Reconstruction of the starting and stopping point, and thus the length, of the track is done by the FINITERECO algorithm. This algorithm uses the direction of a previously reconstructed track, and calculates the starting and stopping point of the muon which travels along this track.

In a first step, the algorithm tries to find the range of the muon assuming no secondary processes along its path, such that only Cherenkov light emitted by the muon

is considered. This is done by only using DOMs within a certain radius (200 m in this analysis, indicated by yellow dashed lines in Fig. 5.6) around the reconstructed track, and neglecting hits that are further away. The starting point, from now on referred to as *reconstructed vertex*, and stopping point are found by projecting the selected hits onto the track under the Cherenkov angle, as illustrated in Fig. 5.6.

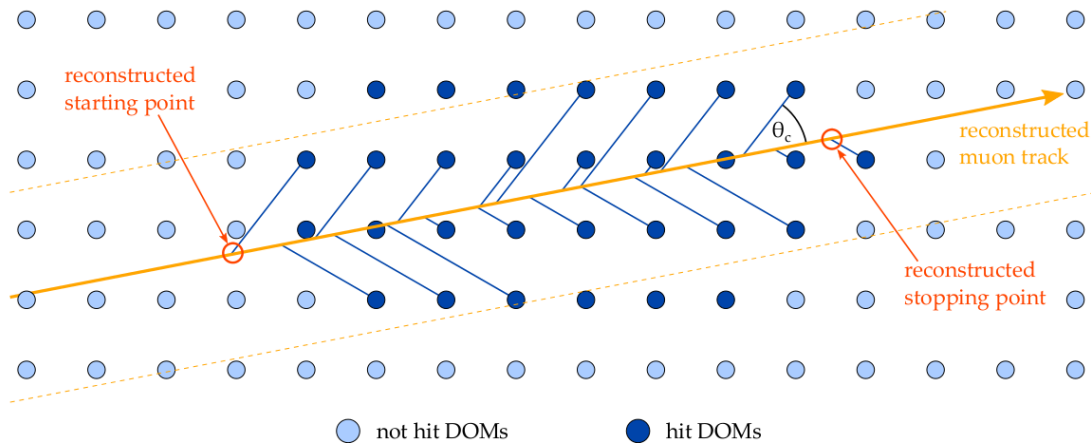


Figure 5.6: Schematic overview of the first step of the FINITERECO algorithm. All hits in a cylinder with a radius of 200 m around the track are projected onto the track under the Cherenkov angle. The reconstructed vertex and stopping point are defined by the outermost projected points. Picture from [121].

The reconstruction of the starting and stopping point is improved in a second step. This time it calculates the probability that a DOM in the direction of this seed track is not hit by taking all non-hit DOMs within a certain radius (200 m in this analysis, indicated in light blue in Fig. 5.7) and calculating the probability $P(\text{noHit}|\text{Track})$ of having such an amount of non-hit DOMs in the assumption of an infinite track. The next step is to calculate the probability $P(\text{noHit}|\text{noTrack})$ with the assumption that the track has a start and/or stop point within the detector volume. The starting and stopping points of the muon are then calculated by minimizing the likelihood ratio of the two calculated probabilities. This step is much more cpu intensive, not only because of the likelihood calculations, but also because the photon propagation properties in the ice are taken into account, using tables [119] that contain detailed simulations of the optical properties of the ice.

The vertex reconstruction of the simple version of this algorithm is used in the first part of the event selection. The more sophisticated reconstruction is used at a later stage, to reconstruct the length of the tracks. Both reconstructions use the MPE fit reconstruction as a seed for reconstructing the starting and stopping points.

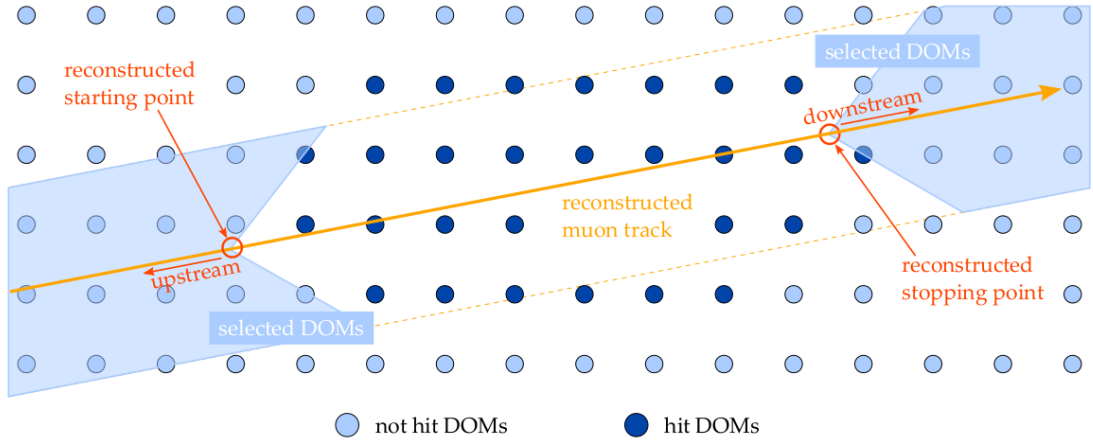


Figure 5.7: Overview of the second, improved step of the FINITERECO algorithm. In this step, the no-hit probability of all non-hit DOMs around the reconstructed track, $P(\text{noHit}|\text{Track})$, is calculated for the case of a infinite track and for the case of a finite track. The starting and stopping points of the muon are then calculated by minimizing the likelihood ratio of the two calculated probabilities. Picture from [121].

5.2.4 MUEX reconstruction

The MUEX reconstruction is a sophisticated and cpu intensive direction reconstruction, which is based on the Pandel distribution described in Eq. (5.10). Contrary to the other likelihood reconstructions, MUEX does not start from a seed provided by another reconstruction, but it creates its own seed. This initial seed is obtained by calculating a large number of possible tracks, all going through the center of gravity of the event, and picking the track which corresponds best to the measured data.

In a second step, the event is reconstructed using the Pandel distribution in the SPE or MPE likelihood (as described in Section 5.2.2), with the obtained seed. This step is repeated several times (four times in the present analysis), each time for a pulse series which is randomly resampled from the original pulse-series with the bootstrap method. Bootstrapping is the process of randomly resampling with replacement until the new sample has the same size of the original sample. Hence an element of the sample could occur multiple times in the new sample, while some other elements of the original sample do not occur in the new sample at all.

In the last step, the average of all the resulting reconstructions of the bootstrapped samples is used as a seed for the final reconstruction, which is again based on the original pulse-series.

The reconstruction which has the highest likelihood value out of all reconstructions that are performed, is then picked as the final result. The reconstruction not only provides a direction, but also an uncertainty parameter σ , which represents the spread between the iterations and is thus a quality parameter of the track, as a small value for this σ parameter corresponds to a stable track reconstruction and thus a clear, high quality

track.

Depending on the SPE or MPE likelihood is used, the reconstruction is respectively referred to as MuEx4SPE or MuEx4MPE. As this reconstruction is cpu intensive, it only enters the event selection at a high level, when the data rate is reduced to roughly 1 Hz.

5.3 Removing Noise Clusters

The previously described cleaning algorithms aim to remove random noise hits, which occur within the trigger time window of a physical event, from the hit series. Most noise hits occur randomly, but sometimes noise events come in sequences of short intervals. This phenomenon is referred to as *correlated noise hit clusters*. In [143] a study was performed to model these correlated noise clusters to search for their origin. Thanks to this study, the correlated noise can be simulated in an accurate way, but unfortunately a detailed understanding of the underlying physical processes is still missing. The author concluded that [143]:

The best candidate for the source of the entire process is luminescence triggered by radioactive decay of elements like Thorium and Uranium in the glass of the DOM.

As the signature in the detector of a noise cluster is very similar to that of a low energy charged particle, it is important to identify these noise events, such that they can be removed. This is especially important, as this type of noise is not included in all of the simulation that is used in this analysis. Not removing these noise clusters would thus lead to a bad agreement between data and simulations.

NOISEENGINE [144] is an algorithm dedicated to look for these correlated noise clusters. In this algorithm the direction of every possible hit pair is evaluated. The algorithm then checks for a preferred direction in all these hit pairs. If no preferred direction is found, the event is classified as a noise event. The algorithm is only performed if less than 30 hits are recorded, as these bright events are very unlikely to be caused by noise alone.

In this analysis this algorithm is only used for events passing the DeepCore filter, as this filter only requires four hits, and is thus very vulnerable for these noise clusters. This cleaning is done at the very beginning of the analysis.

Summary

In this chapter the basics of event processing were described.

Waveforms that are sent to the surface are first calibrated and decomposed into individual pulses from which the photon arrival times and intensities at the DOMs are calculated. These pulses are then cleaned, i.e. the noise pulses are removed, and the cleaned pulses are used to reconstruct the direction of the charged particle to which the pulses are associated. Correlated noise can fake real events, so a dedicated algorithm is used to remove these noise clusters.

War is ninety percent information.

Napoleon Bonaparte

6

The Analyzed ICECUBE Datasets

The analysis presented in this thesis is based on data recorded by ICECUBE during the first year after the detector was completed. The experimental data sample is presented in Section 6.1.

ICECUBE is recording events at a rate of about 4 kHz. Most of these events are atmospheric muons produced in cosmic ray air showers. Atmospheric neutrinos are recorded at a rate of about 5 orders of magnitude lower and are the second biggest contribution to the data. Both the atmospheric muons and atmospheric neutrinos compose the background in the present analysis. To find a signal, these background events should be understood and modeled as good as possible, to check to what extent their contributions are sufficient to describe the measured experimental data. Only then a potential additional signal contribution can be identified in the experimental data.

The signal contribution sought after in the data would come from neutrinos which are produced in the decay of annihilation products from Earth WIMPs. These would show up as a zenith dependent mismatch between data and the above mentioned background simulation.

The simulation of these signal and background events is described in Section 6.2.

6.1 Experimental Data

In the analysis described in this thesis, the first year of data of the full ICECUBE detector was analyzed. This period, also referred to as IC86-I, started on the 13th of May in 2011 and lasted until the 15th of May in 2012. The ICECUBE data is recorded in 8 hour samples, called *runs*.

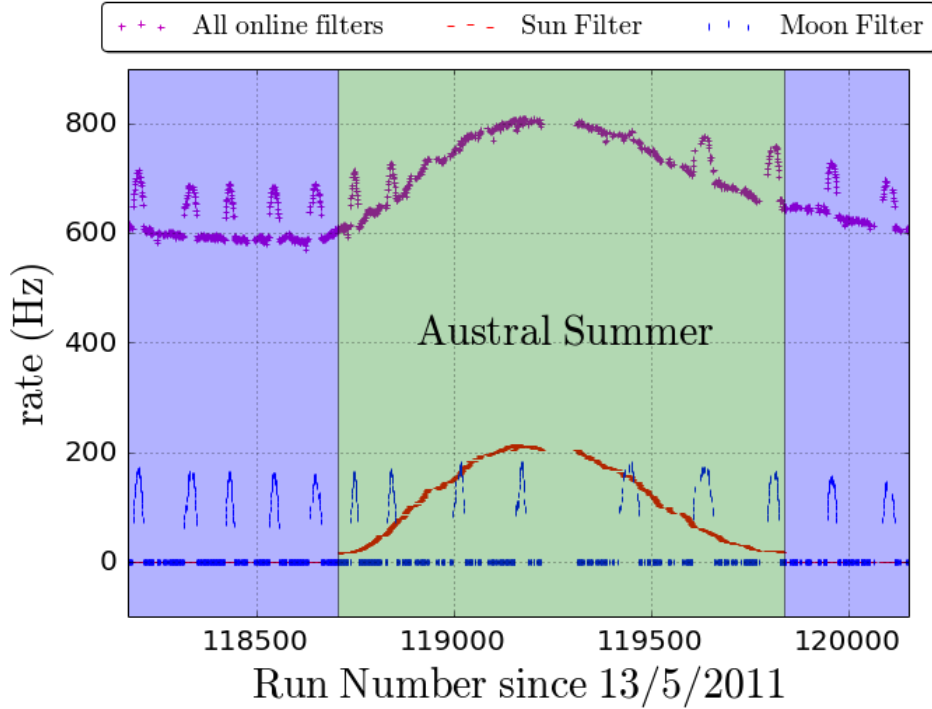
During the IC86-I period, the ICECUBE detector had clean uptime of roughly 90%, resulting in about 330 days of data which can be used for the present analysis. More precisely, the result of the analysis presented in this thesis is based on 28253988 s or 327 days of IC86-I clean data. These clean data are data from which bad runs, like e.g. test runs or runs with a high fraction of failing DOMs are removed. There is a list in IceCube, the *GoodRunList*, which keeps track of which runs can be used for analyses. The data used in this analysis uses the runs which are indicated as *good* indicated in this list.

The variation of the clean data rate of the total rate of all filtered data sent to Madison, and of the sum of the four online filters used in the present analysis (Vertical Event Filter, LowUp Filter, Muon Filter, DeepCore Filter, see Section 4.6.2) as a function of time is shown respectively in Fig. 6.1a and Fig. 6.1b. Each point in this figure is calculated with the first two minutes of a run.

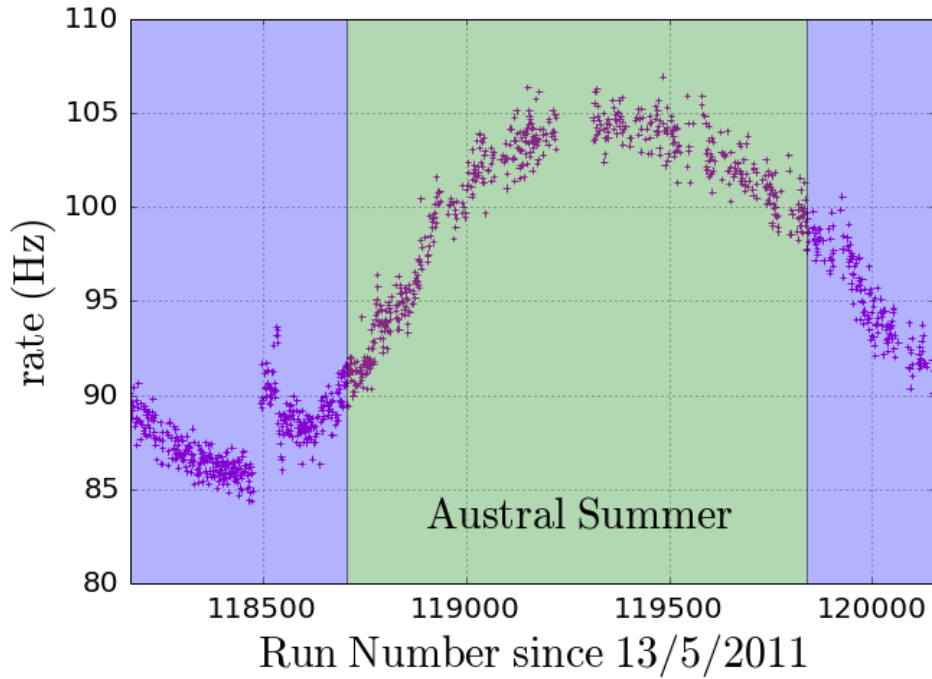
In Fig. 6.1, several features can be observed. The monthly rise in the rate distribution is caused by the *Moon Filter* [145], which is an online filter that only takes data when the Moon is above the horizon. The blue vertical stripes in Fig. 6.1a show the rates of this filter as a function of time. Another feature in Fig. 6.1a is the increase in rate during the Austral Summer, during which the Sun is above the horizon at the South Pole. In this period, the *Sun Filter* [145], an online filter that records data only when the Sun is above the horizon, is active. The rates of the Sun Filter are shown by the red horizontal stripes in Fig. 6.1a. The Sun and Moon Filter are used to study the shadow of the Sun and the Moon respectively in down-going muons. Measurements of the Moon shadow in TeV cosmic rays with ICECUBE set an upper limit on the absolute pointing accuracy of the detector of 0.2 degrees [146].

Note the raise in flux in the Austral Summer (green area), which is due to the fact that in summer the atmosphere is warmer and consequently less dense during the Austral Summer. As such the interaction length increases and a larger amount of particles will reach the detector [147].

The sudden raise at run 118495 (mainly visible in Fig. 6.1b) is due to a change in the used DOM software. As a result of that change, launch rates increased significantly for some days, until this was corrected for. The gap starting at around Run 119200 is because of detector upgrades and tests in the Summer season.



(a)



(b)

Figure 6.1: The event rate of all filtered data that is sent over to Madison (a), and of the data after selection of the four online filters used in the present analysis (b), as a function of time. The period during which the data were taken started on the 13th of May in 2011 and lasted until the 15th of May in 2012 (IC86-I). Each point in this histogram is calculated with the first two minutes of an eight hour run. The green area represents the Austral Summer, i.e. the period from 21st of September 2011 to 21st of March 2012, and the blue areas represent the Austral winter.

The work described in this thesis has been developed using only 10%, the so-called *burnsample*, of the full data set, to obey the blindness policy. This *blindness* policy is introduced to prevent a bias by the researcher. This policy is introduced to prevent that the researcher adapts his/her analysis unconsciously in such a way that the sought for result is obtained. Before *unblinding* the data one has to prove that the atmospheric background is well understood and under control.

The burnsample is used to verify if the simulation is describing the real data in a statistically correct way.

6.2 Simulated Data

At trigger level, the experimental data are highly dominated by atmospheric muons, which are recorded by ICECUBE at a rate of roughly 4 kHz ($\mathcal{O}(10^{11})$ /year). With a rate of the order of 25 mHz ($\mathcal{O}(10^5)$ /year), atmospheric neutrinos are the second largest contribution to the data. At high energies, there is also a non-negligible contribution from astrophysical neutrinos, but as this is outside the energy range of interest for the analysis described in this thesis, the contribution of these neutrinos will be neglected. The atmospheric muons and neutrinos are simulated and compared to the data, such that the contribution of these background particles can be checked at each level in the analysis.

The contribution sought after in the data is a possible signal due to neutrinos which are produced in the decay of annihilation products from Earth WIMPs, which are defined as the signal in the analysis described in this thesis. The signal would show up as a zenith dependent mismatch between data and the simulated atmospheric muons and atmospheric neutrinos, which make up the background for the present analysis. A good simulation of signal events is important, as the event selection will be optimized on these signal events. However, the WIMP model is just one possible explanation for the observed dark matter (Section 2.3). As a result the analysis described in this thesis will be optimized for this type of dark matter particles, but might thus be less optimal for other models.

Both the signal and the background simulation proceeds in several stages. In the first step the primary particles are *generated*, with their corresponding physical properties such as their flux, energy and direction. In the second step, these particles are *propagated* through various media until they reach the detector. This propagation takes into account energy losses and production of numerous secondaries, and it also tracks the Cherenkov photons emitted inside the generated detector volume. The last step consists of simulating the detector response.

6.2.1 Generation of events

Three different kind of events need to be considered in this thesis: atmospheric muons, atmospheric neutrinos and signal neutrinos, each with their own event generation.

Atmospheric Muons are simulated with the program *COsmic Ray Simulation for KAscades (CORSIKA)* [148], an extensive air shower generator, describing the shower development in the atmosphere. In ICECUBE, an internally released version of CORSIKA is used, which includes specific modifications. This version is called dCORSIKA and is developed by Dmitry Chirkin [149].

The primary cosmic ray particles are generated with a spectrum that is following the poly-gonato model by Hoerandel [150], which has a primary energy spectrum roughly proportional to $E^{-2.6}$. The showers are simulated with energies in the range 600 GeV- 10^{11} GeV. The particles are tracked through the atmosphere and ice until they undergo reactions with nuclei or decay. The simulation accounts for the fact that both single muons and muon showers containing multiple muons, reach the detector.

Atmospheric Neutrinos of all flavors are simulated with the programs *GENIE* [151] and *Neutrino-Generator (NuGen)*, which is based on *ANIS* [152]. The atmospheric neutrino flux is calculated using the parameterization of Honda [153] (recall the atmospheric neutrino energy spectrum shown in Fig. 4.14). As the neutrinos are propagated through the Earth, oscillation effects need to be taken into account. This is done by calculating the oscillation probabilities on an event basis, with the *NuCraft* open-source Python project [154]. The values for the oscillation parameters that were used for the simulations used in this thesis, are given in Table 6.1. These values date from 2013 [84], as the data used in the present analysis was simulated at that time. For this reason they differ from the values indicated in Table 3.1, which are based on more recent published oscillation parameters [82]. Note that the differences are very small, and will be accounted for as a systematic uncertainty in the final result.

Both the GENIE and NuGen event generators make use of the neutrino-nucleon cross-sections from CTEQ6 [155] to generate the interactions in the detector volume. As neutrinos only interact very rarely, the interactions are forced to happen within a certain distance to the detector and the event gets a weight which reflects the probability that this interaction actually took place. This is done to save computing time.

The GENIE event generator is valid for neutrinos with energies from MeV to a few hundred GeV [156, 157], while NuGen is only valid above approximately 100 GeV. There is a small discrepancy between the two generators, which is visible in Fig. 6.2a, where a comparison of the flux of the atmospheric muon neutrinos as a function of their energy (after online filter selection) is shown. Note that the energy range is chosen to cover the whole GENIE spectrum. The spectrum continues for NuGen. From this plot it is clear that the GENIE and NuGen simulations agree from about 100 GeV onwards,

and that GENIE only simulates neutrinos with energies up to 195 GeV. To take into account these effects, GENIE is used for neutrinos with energies below 190 GeV and NuGen for neutrinos with energies above 195 GeV. To have a continuous transition, a linear combination of the two generators is used for neutrinos with energies in the range 190-195 GeV, as is shown in Fig. 6.2b. The discrepancy arises from the fact that ANIS (and thus NuGen) only includes deep inelastic scattering cross-sections, which is not correct at lower energies, while GENIE uses a mixture of theoretical predictions and tuning to match the measured data. The atmospheric neutrino simulation used

Table 6.1: Neutrino oscillation parameters used in the simulations. These values come from the 2012 version of the Particle Data Group report about neutrino oscillations [84].

Parameter	value
$\Delta m_{21}^2 [10^{-5} \text{eV}^2]$	7.50
$\Delta m_{31}^2 [10^{-3} \text{eV}^2]$	2.32
$\sin^2(\theta_{12})$	0.311
$\sin^2(\theta_{23})$	0.388
$\sin^2(\theta_{13})$	0.0251

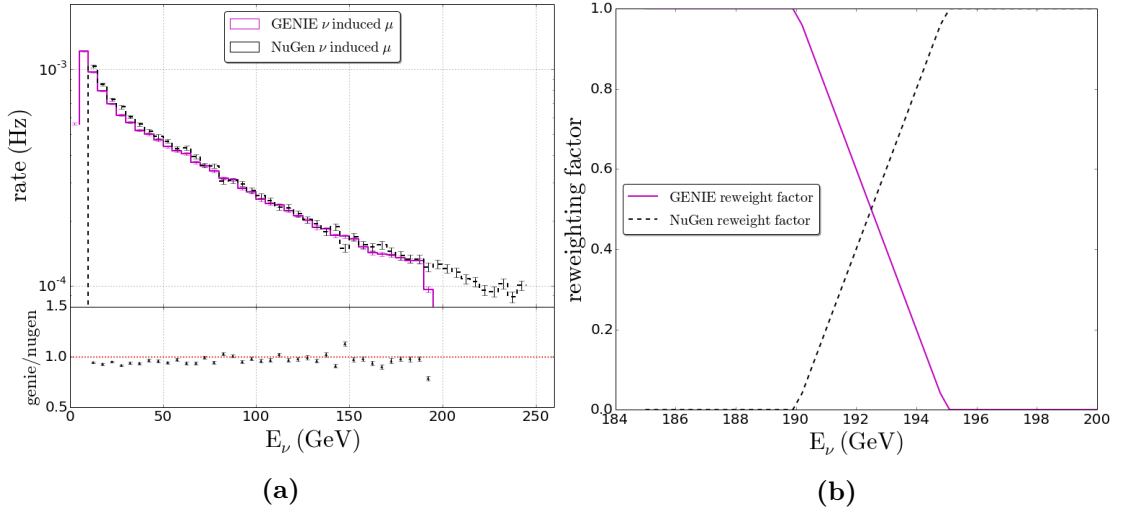


Figure 6.2: In the left panel the flux of the atmospheric neutrinos as a function of their energy is shown for GENIE (solid magenta bins) and NuGen (dashed black bins). For neutrinos with energies in the range 190-195 GeV a linear combination of the two generators is used, as shown in the right panel.

in the work presented in this analysis does not include coincident muon events, which occur about 10% of the time, as presented in Section 5.1.2. The effects of this will be discussed in more detail in Chapter 7, Chapter 9 and Appendix B.

Signal Neutrinos, i.e. neutrinos which are produced in the decay of annihilation products from Earth WIMPs, are simulated with the WimpSim simulation package [78], which is based on *DarkSusy* [158]. WimpSim is a code that describes the capture and annihilation of WIMPs inside the Sun or the Earth, collects all neutrinos that emerge after the consecutive decay and annihilation processes, and lets these propagate out of the Sun or the Earth to the detector. The code includes neutrino interactions and neutrino oscillations in a fully consistent three-flavour treatment, with the oscillation parameters given in Table 6.1. WimpSim provides physical events, with directional and energy information of the neutrino and the created lepton and hadronic cascade after interaction in the vicinity of the detector. In the present analysis, only muon neutrinos reaching the detector are considered.

The interaction vertices of the WimpSim simulated events are spread in a *generated volume* V_{gen} , which is different for every event and depends on the energy and direction of the neutrino, as described below. V_{gen} is defined as a box around the detector with a length L along the neutrino track and the projected area of the sensitive volume as cross-section, as shown in Fig. 6.3. The length L of the generated volume depends on the length over which the neutrino-induced lepton can emit Cherenkov-photons, and is thus energy dependent. In a second step, V_{gen} is projected onto the sensitive volume of the detector V_{sens} , in which ICECUBE is positioned (Fig. 6.3). From the generated volumes of the events, one can derive the effective volume V_{eff} , which is a measurement of the efficiency of the detector. It can be interpreted as the proper volume of a detector, which has an ideal efficiency ($\varepsilon \equiv 1$). The effective volume represents which events are selected out of the total amount of generated events in the generated volume

$$V_{\text{eff}} = \frac{N_{\text{sel}}}{N_{\text{gen}}} V_{\text{gen}} = \frac{\sum_{i=1}^{N_{\text{gen}}} w_i(E_\nu) \delta_i V_{\text{gen},i}(E_\nu, \theta_\nu)}{\sum_{i=1}^{N_{\text{gen}}} w_i(E_\nu)}, \quad (6.1)$$

where $w_i(E_\nu)$ is the weight of the event, δ_i is either 1 or 0 if the event respectively did or did not pass the selection criteria (like triggers, online filters, higher levels in the event selection presented in Chapter 7) and $V_{\text{gen},i}(E_\nu, \theta_\nu)$ is the generated volume of the event. The weight w_i of an event denotes the statistical importance of generated event i in the total simulated sample. Each generated event i thus corresponds to w_i physical events, where w_i is a combination of different weights w_χ , w_{abs} , w_σ and w_{vertex} [159], which are described below

- The physical distribution of the WIMP-induced neutrino energy spectrum at the surface of the Earth is given by $\frac{dN_\nu}{dE_\nu}$. This spectrum is however sampled from a spectrum given by $\frac{dN_\nu}{dE_\nu} \times E_\nu^\alpha$, where E_ν^α is chosen such that the low statistics regions are artificially populated¹. In order to correct for the unphysical E_ν^α factor, each event is weighted according to $E_\nu^{-\alpha} \equiv w_\chi$.

¹The cross-section increases almost linearly with neutrino energy, as shown in Fig. 3.5.

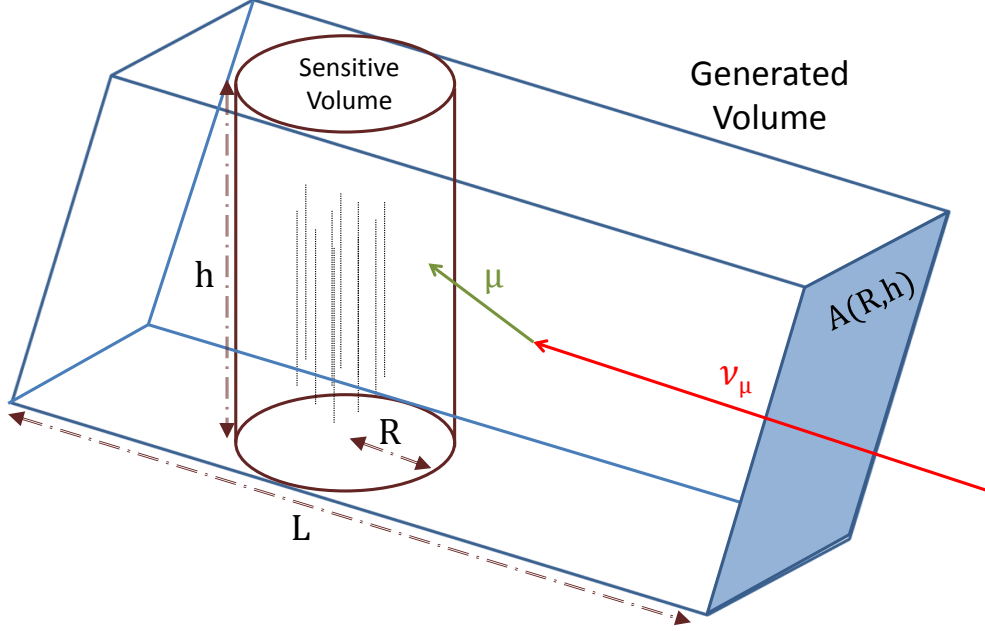


Figure 6.3: The generated volume V_{gen} for a WIMP neutrino is shown, together with the sensitive volume of the detector V_{sens} . This generated volume has a length L along the neutrino track and the projected area of the sensitive volume as cross-section.

- When a neutrino travels through the Earth, it is possible that it gets absorbed before it reaches the detector. To remove these absorbed neutrinos, a weight w_{abs} is introduced, which has a value in the range of $[0, 1]$ which reflects the survival probability.
- The interaction probability depends on the cross-section of the neutrino, so every event has a different weight w_σ , depending on this cross-section.
- As was already mentioned, the generated volume V_{gen} has to be projected onto the sensitive volume V_{sens} , leading to an additional weight w_{vertex} . Consider N_{gen} neutrino interactions in a generated volume V_{gen} , with interaction density $\rho = N_{\text{gen}}/V_{\text{gen}}$. In order to distribute these N_{gen} vertices in the sensitive volume V_{sens} , the interactions need to be weighted to recover the correct interaction density:

$N_{\text{gen}} \rightarrow N_{\text{sens}} = w_{\text{vertex}} \times N_{\text{gen}}$, with

$$\begin{aligned} \rho &= \rho' \\ \frac{N_{\text{gen}}}{V_{\text{gen}}} &= \frac{N_{\text{sens}}}{V_{\text{sens}}} \\ \Rightarrow w_{\text{vertex}} &\equiv \frac{N'_{\text{gen}}}{N_{\text{gen}}} = \frac{V_{\text{sens}}}{V_{\text{gen}}}. \end{aligned}$$

The total weight of an event is thus given by :

$$w_i = w_{\chi} \times w_{\text{abs}} \times w_{\sigma} \times w_{\text{vertex}}. \quad (6.2)$$

6.2.2 Propagators

To propagate the produced muons (atmospheric or coming from neutrino CC interactions) through the detector and its surrounding medium, the *Muon Monte Carlo (MMC)* [105] package is used. MMC takes both continuous and stochastic energy losses into account, which were described in Section 3.4.1.

The propagation of the produced Cherenkov photons in the ice is simulated with the software package *Photon Propagation Code (PPC)*, which is an ICECUBE-internal software package that takes into account the structure of the ice by varying scattering and absorption as a function of both wavelength and depth.

6.2.3 Detector simulation

The final step is to simulate the detector response (described in Chapter 4) on the simulated Cherenkov photons. The photon density at each DOM is retrieved from PPC and is used to generate a PMT waveform. A simulation of the DOM response is then performed and random noise hits are added. To add the correlated noise described in Section 5.3, a dedicated module, called VUVUZELA, is used. Unfortunately, this module was not available at the time when the IC86-I CORSIKA sets were simulated, so the atmospheric muon simulation used in the present analysis does not include the coincident noise events. As a consequence dedicated measures will have to be taken to account for this. If the simulated event is triggered, the information is read out and processed identically to experimental data.

Summary

In this chapter an overview of the analyzed data, which was taken during the first year of the complete ICECUBE detector (IC86-I), was given. First, the stability of the experimental data was checked and confirmed. The clean data sample has a *livedtime* of 28253988 s or 327 days and was measured between the 13th of May in 2011 and the 15th of May in 2012.

In a second step the simulations that will be used in the analysis presented in this thesis, were described. These simulations consist of atmospheric muons, atmospheric neutrinos and neutrinos which are produced in the decay of annihilation products from Earth WIMPs. The first two make up the background of this analysis and the latter is the signal. A detailed understanding of the background is important, as the signal would show up as a zenith dependent mismatch between the experimental data and the background simulation. Therefore all the effects that occur during the generation, propagation and detection of these particles are simulated as accurately as possible.

*Once you have commitment, you need the discipline
and hard work to get you there.*

Haile Gebrselassie

7

Event Processing and Selection

In its full 86 string configuration, ICECUBE triggers at a rate of roughly 4 kHz ($\mathcal{O}(10^{11})/\text{year}$). Most of these triggers are due to atmospheric muons and detector noise. The trigger rate of atmospheric neutrinos is only about 25 mHz ($\mathcal{O}(10^5)/\text{year}$), or 5 orders of magnitude lower. The expected WIMP-induced muon flux for the work presented in this thesis is at most at the order of a few μHz ($\mathcal{O}(10^3)/\text{km}^2/\text{year}$), i.e. 8 orders of magnitude lower than the trigger rate of ICECUBE. As the expected signal is hidden in such an overwhelming background, a dedicated event selection is needed.

In this chapter an overview is given of the selection methods, or filters, which were used in this analysis to remove the noise and atmospheric particles that trigger the detector, but at the same time keep as much of the triggered signal events as possible. The event selection is performed in several steps, as indicated in Fig. 7.1, and at each step new reconstructions and variables are used to further reduce the background. As the data rate decreases at each step, the introduced reconstructions and variables can become more time-consuming and thus precise at each of the steps. This process goes on until the event sample is dominated by signal-like atmospheric neutrino events.

This final event sample will then be used for a directional search in which the observed number of events from the direction of the the center of the Earth is compared to the background-only hypothesis.

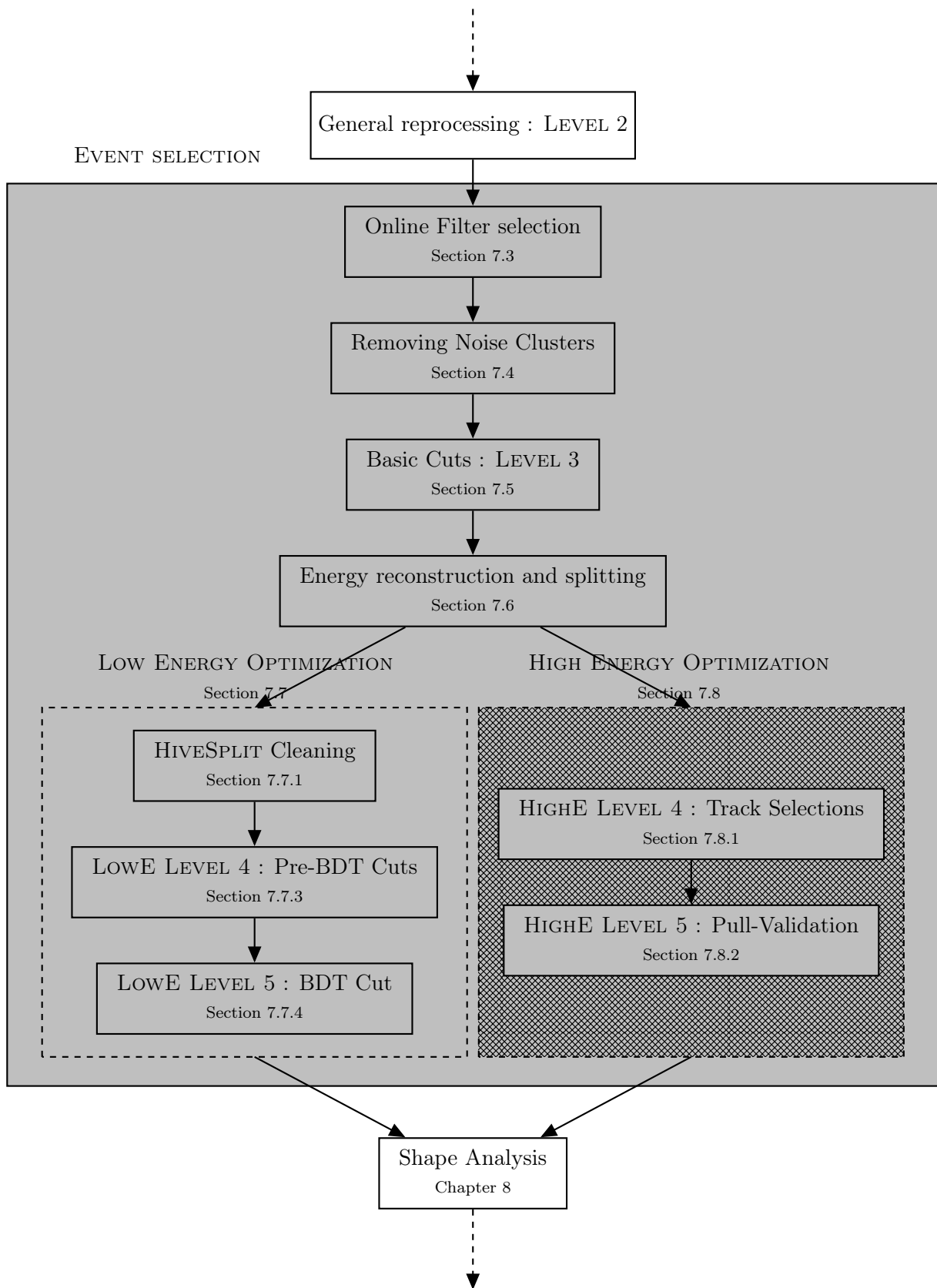


Figure 7.1: Overview of the different steps in the event selection presented in this chapter.

7.1 Overview

The rate at which Earth WIMP-induced muon neutrinos could possibly trigger ICECUBE is at most a few μHz ($\mathcal{O}(10^3)/\text{km}^2/\text{year}$), as obtained from extrapolation of the 90% Confidence Level (CL) upper-limits set by the AMANDA neutrino telescope [71, 77, 160]. The signal rate is thus roughly 8 orders of magnitude lower than the 4 kHz ($\mathcal{O}(10^{11})/\text{year}$) trigger rate of the detector. As it is not possible to detect such a small signal in this enormous background, a dedicated event selection, of which the overview is shown in Fig. 7.1, has been developed to reduce the background rate.

An event selection is optimized for a certain type of signal and it is thus crucial to have a clear signal definition, which is not straightforward in the case of Dark Matter searches as there are many candidates (Section 2.3). As described in Section 7.2.1, the work presented here will focus on WIMPs with a mass of 50 GeV, annihilating into $\tau\bar{\tau}$. To increase the sensitivity for high mass WIMPs, an independent analysis has been developed, which will be performed on a statistically independent sample, focusing on 1 TeV WIMPs annihilating into W^+W^- .

Besides having a good definition of the signal, it is also necessary to have a clear view on what the background consists of. ICECUBE has a zenith dependent efficiency, and hence the *off-source* regions are not equivalent to the source region (different acceptance and effective volume) in the analysis presented here, as described in Section 7.2.2. Therefore the background is calculated from simulations, which are checked against a fraction of the experimental data sample, the burnsample, at every step in the event selection. The reader is referred to Chapter 6 for a description of the experimental data and the simulated data which are used in the analysis presented in this thesis.

The event selection is done in several steps and continues until the data are dominated by signal-like atmospheric neutrino events, which form an irreducible background. At every step of the event selection, the data rate is reduced, and better, more time-consuming reconstructions and variables can be calculated for each event. The first step consists of a selection of online filters, together with the removal of noise clusters, as described in Section 7.3. In the second step linear cuts, based on distributions of event multiplicities and observables from signal and background simulations, are made to reduce the content of atmospheric muon events by about an order of magnitude to roughly 3 Hz (Section 7.5). Once the data rate is below 3 Hz, the data are reprocessed using more precise (and more time-consuming) reconstructions. One of the reconstructions is an energy reconstruction that is used to split the data into two statistically independent data sets (Section 7.6). These two samples, a low and high energy sample, are then further cleaned to search for respectively low ($10 \text{ GeV} < m_\chi < 250 \text{ GeV}$) and high mass ($250 \text{ GeV} < m_\chi < 5 \text{ TeV}$) WIMPs. Both independent analyses use boosted decision trees (BDTs, Section 7.7.2) to reduce the background until the data samples are dominated by an irreducible background of signal-like atmospheric neutrino events. The cuts on the BDT score are chosen such that the sensitivities of the analyses are optimal. These sensitivities are calculated with a likelihood ratio hypothesis test based on the values

of the reconstructed zenith. This is done with the use of the Feldman-Cousins unified approach, as described in Chapter 8.

7.2 Signal and background

7.2.1 The signal definition

The neutrino flux produced by annihilating WIMPs in the center of the Earth scales linearly with the annihilation rate of these WIMPs, which on itself scales linearly with the capture rate of WIMPs, as explained in Section 2.6. If the WIMP mass is nearly identical to that of one of the nuclear species in the Earth, the capture rate, and thus the neutrino flux in ICECUBE, will increase considerably, as is shown in Fig. 7.2¹

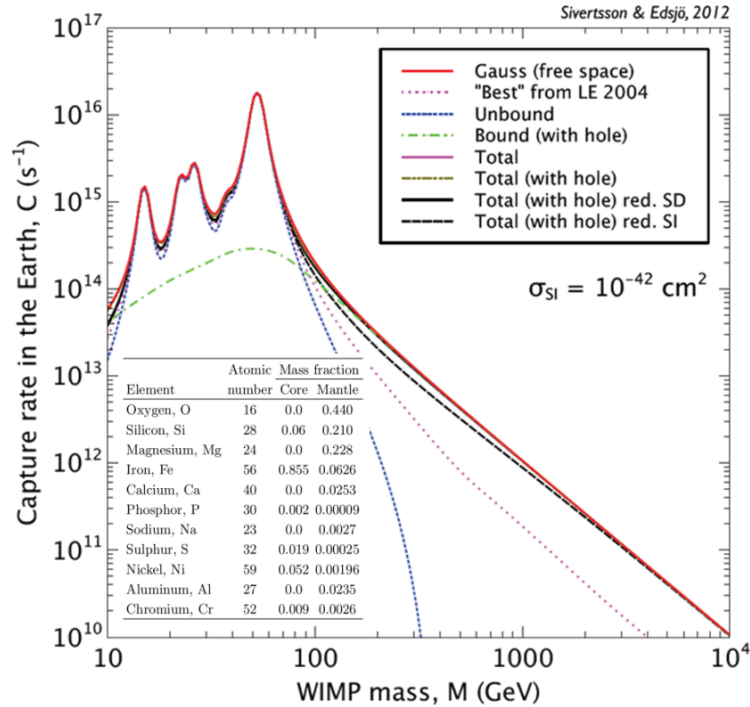


Figure 7.2: This figure shows the rate at which dark matter particles are captured to the interior of the Earth, for a scattering cross-section of $\sigma = 10^{-42} \text{ cm}^2$. The peaks correspond to resonant capture on the most abundant elements (listed in the table, abundances are given in weight %) considered in the Earth model [75], ^{16}O , ^{24}Mg , ^{28}Si and ^{56}Fe and their isotopes. A dark matter halo density of $\rho_X = 0.3 \text{ GeV cm}^{-3}$ is assumed [74].

As the capture is most efficient for WIMPs with a mass close to the mass of the most

¹It should be noted that recent direct detection limits [35] exclude cross-sections larger than $\sigma_p^{SI} = 10^{-43} \text{ cm}^2$ over a wide range of WIMP masses. This implies that the normalization in Fig. 7.2 should be corrected downward by about an order of magnitude, as the cross-section that is assumed in the calculation for the capture rate is $\sigma = 10^{-42} \text{ cm}^2$ [74], but this does not affect the overall shape.

abundant element Iron, the analysis described in this thesis will be optimized for WIMPs with a mass $m_\chi = 50$ GeV that annihilate into $\tau\bar{\tau}$. In this annihilation channel, a hard neutrino energy spectrum is produced. In Fig. 7.3a, the expected neutrino spectrum (solid line) and the neutrino-induced muon spectrum (dashed line) at trigger level of 50 GeV WIMPs annihilating into $\tau\bar{\tau}$, are shown. As the expected muon energy for this channel is lower than 50 GeV, the DEEPCORE detector will be crucial in a search for such a signal.

To be sensitive to a wide range of WIMP masses, a complementary analysis has been developed in parallel which is optimized on 1 TeV WIMPs annihilating into W^+W^- . The expected neutrino spectrum and the neutrino-induced muon spectrum of these WIMPs at TRIGGER LEVEL are shown in Fig. 7.3b.

Fig. 7.4 shows the expected zenith angle distributions, at trigger level, of the WIMP-induced neutrinos (black) and the daughter muons (green) for 50 GeV WIMPs annihilating into $\tau\bar{\tau}$ (a) and 1 TeV WIMPs annihilating into W^+W^- (b). The shape of the sharply peaking muon distribution around 180° is a consequence of the zenith dependent trigger efficiency of ICECUBE. The more vertical the muon track, the more efficient ICECUBE will be, as the vertical distance between DOMs is much smaller than the horizontal distance. Therefore ICECUBE is only triggering on near-vertical Earth WIMP-induced events, especially in the case of low energetic tracks, with low light output. The shape of the neutrino distribution is a consequence of the space angle effect on one hand and of the distribution of the WIMPs in the Earth, of which the size is inversely proportional to the mass WIMPs [28], on the other hand.

The neutrino distribution and the muon distribution differ in shape as there is an energy dependent kinematic angle between the incoming neutrino and its daughter muon (Eq. (3.16)). Note the different scales on the x-axes in Fig. 7.4a and Fig. 7.4b.

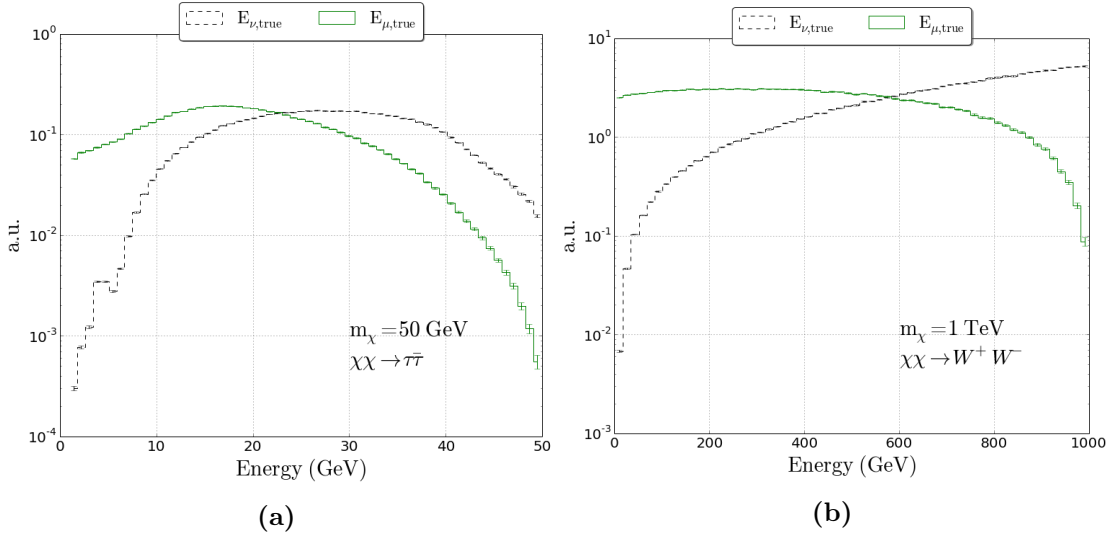


Figure 7.3: The normalized energy distributions for WIMP-induced signal neutrinos and muons induced by signal neutrinos at trigger level, for a WIMP mass of 50 GeV (a) and 1 TeV (b).

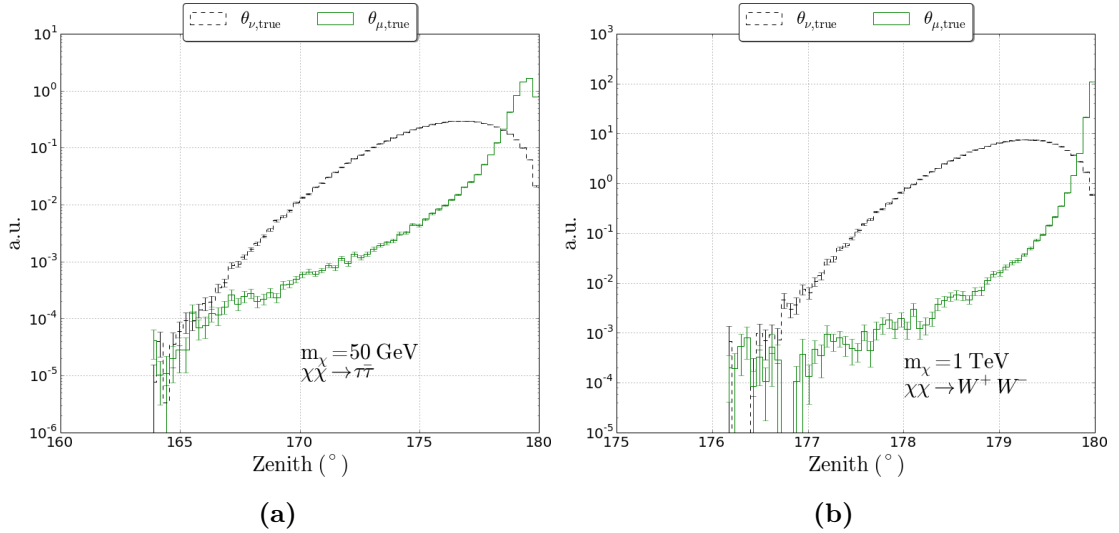


Figure 7.4: The normalized zenith angle distributions for WIMP-induced signal neutrinos (black dashed lines) and muons induced by signal neutrinos (green solid lines) at TRIGGER LEVEL, for a WIMP mass of 50 GeV (a) and 1 TeV (b).

The two analyses use different data samples and are thus statistically independent as explained in Section 7.6.

7.2.2 Estimation of the background

In most ICECUBE analyses the expected background is calculated in a data driven way, by observing an *off-source region* in the sky. The signal contribution from the source is then calculated by observing on-source and subtracting the expected background. This approach is possible if an off-source region can be defined which has the same characteristics as the on-source region and for which the detector has the same acceptance. As ICECUBE has a zenith dependent efficiency, this off-source region is usually picked by looking in a region with the same zenith angle as the source, but with a different azimuth angle. Because of this zenith dependence of the detector, it is not possible to define an off-source region if the source is located in the center of the Earth, as is the case for the analysis described here. Therefore this analysis has to rely on simulations to estimate the background and it is thus of great importance that the simulation of the atmospheric muon and atmospheric neutrino data is correct.

As the signal rate is only of the order of a few μHz at most, the possible WIMP signal will not be visible in the experimental data sample until the very last step of the event selection. There is thus no danger in using the burnsample (10% of the data) to validate the background during the event selection and to compare the background simulation to this fraction of the data.

In the statistical analysis that is performed at the very last step (Chapter 8), the background will be estimated by simulations.

The absolute number of events in each simulation sample at LEVEL 2 is given in Table 7.1.

Table 7.1: Amount of events of two WIMP models and of the different simulated background sets at LEVEL 2.

	absolute number of events at LEVEL 2
WIMPs $m_\chi = 50$ GeV	923290
WIMPs $m_\chi = 1$ TeV	601151
atmospheric μ	$\sim 2.6 \times 10^8$
atmospheric $\bar{\nu}_\mu$ (NuGen)	9044752
atmospheric $\bar{\nu}_e$ (NuGen)	7872009
atmospheric $\bar{\nu}_\mu$ (GENIE)	11505986
atmospheric $\bar{\nu}_e$ (GENIE)	3023948
atmospheric $\bar{\nu}_\tau$ (GENIE)	1683104

7.3 Online filter selection

As presented in Section 4.6.2, all events passing one of the online filters are sent from the South Pole to the data warehouse in the University of Wisconsin, where they are stored. The first step of the event selection is to select online filters which are tagging events that are of interest for this analysis. In this selection, a compromise has to be found between low background rate and high signal efficiency, where efficiency is defined as

$$\text{efficiency} = \frac{\text{event rate after the filter selection}}{\text{event rate before the filter selection}} \quad (7.1)$$

The four filters that are tagging potentially interesting events are the *Vertical Event Filter (VEF)*, the *LowUp Filter*, the *Muon Filter* and the *DEEPCORE Filter (DC)*, which were described in detail in Section 4.6.2. To have a high signal efficiency for all considered WIMP masses and annihilation channels, every event that is tagged by at least one of the four considered filters is selected. As can be seen in Fig. 7.5, this selection has a signal efficiency based on different WIMP models of $\sim 85\%$ or higher. Note that the *Vertical Event Filter* has a large contribution for the 50 GeV WIMPs, annihilating into $\tau^+\tau^-$.

The background rates and signal efficiencies after the selection of these four filters, are presented in Table 7.2.

7.4 Removing Noise Clusters

A fraction of the events that are tagged by the online filters consists mainly of correlated noise. As explained in Section 5.3, these events are most probably due to luminescence,

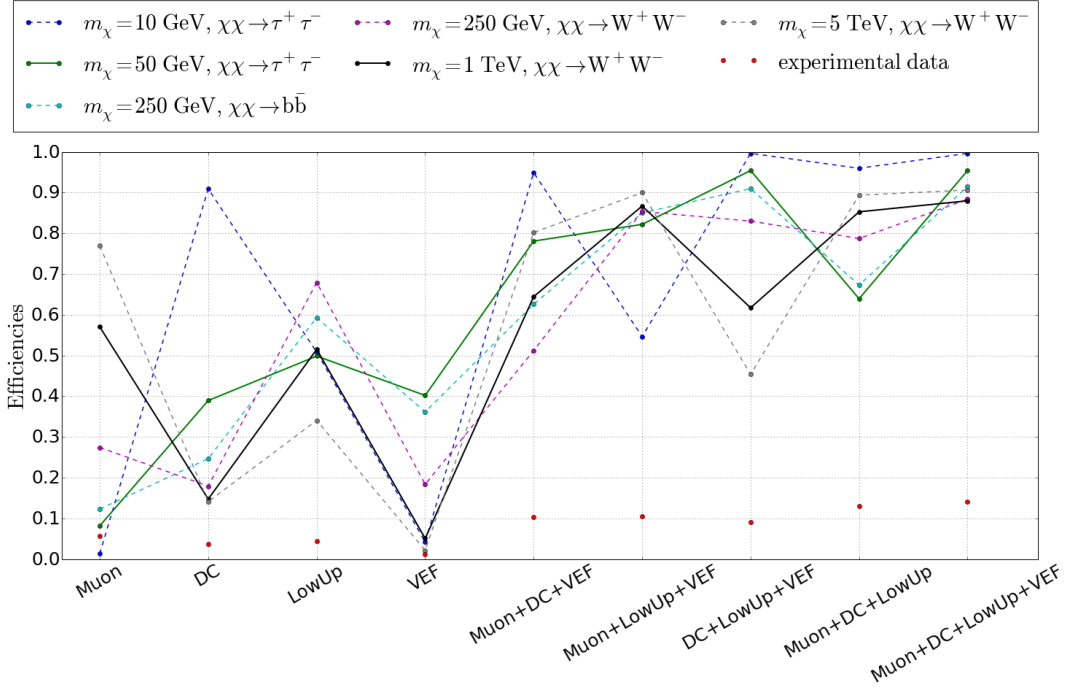


Figure 7.5: Efficiencies (Eq. (7.1)) of individual online filters and combinations of these filters. These efficiencies are shown for different WIMP masses and annihilation channels (full and dashed lines), as well as for experimental data (red dots). The full lines show the efficiencies for the WIMP models that will be used for the low (green line) and the high (black line) energy optimization.

which is caused by radioactive decay of elements like Thorium and Uranium in the glass of the DOM. The majority of these noise clusters occur in the DEEPCORE subdetector, as there the DOMs are closer to each other and have a higher quantum efficiency. Therefore the NOISEENGINE algorithm is used to evaluate all events passing the DEEPCORE Filter, and to remove the events that are tagged as correlated noise.

As discussed in Section 6.2.3, the correlated noise is not well simulated in the atmospheric muon simulation used in this analysis, so while this step reduces the experimental data rate from 91 Hz to 85 Hz, the rate of the simulated atmospheric muons is unaffected by this cleaning and stays at 81 Hz, as indicated in Table 7.2. The data rate is thus underestimated by the simulation at a level of about 10%. More investigations on this will follow at later stages of the event selection.

Table 7.2: Percentages of the amount of simulated signal (w.r.t. LEVEL 2) for two WIMP models and rates of the simulated background and burnsample data at different selection levels. The total simulated background consists of atmospheric muons (μ_{atm}) and atmospheric neutrinos of all flavors ($\nu_{\mu,\text{atm}}$, $\nu_{e,\text{atm}}$ and $\nu_{\tau,\text{atm}}$)

	# WIMP (%)		Simulated Background (Hz)			Data (Hz)
	$m_\chi = 50 \text{ GeV}$	$m_\chi = 1 \text{ TeV}$	ν_{atm}	μ_{atm}	total	
Level 2	100.0	100.0	27×10^{-3}	650	650	670
Filter Selection	95.4	88.0	25×10^{-3}	81	81	91
Noise Cleaning	92.5	87.9	24×10^{-3}	81	81	85

7.5 Reducing the data rate to a few Hz

At this stage, the data are still strongly dominated by atmospheric muons (see Table 7.2). To reduce the contribution of these atmospheric muon events to a few Hz, linear cuts based on distributions of event multiplicities and observables from signal and background are made. This step in the event selection is referred to as the LEVEL 3 selection.

In the remaining of this chapter, all histograms show the distributions for 4 data samples

- The IC86-I burnsample, i.e. 10% of the experimental data: red dots with error-bars.
- Atmospheric muons simulated with CORSIKA: blue histogram.
- The total sample of atmospheric neutrinos of all flavors simulated with NuGen and GENIE (combined as described in Section 6.2.1), including oscillation effects in the Earth: magenta histogram.
- Signal muon neutrinos, produced by 50 GeV WIMPs annihilating into $\tau\bar{\tau}$ simulated with WimpSim: green histogram.

The simulation of the atmospheric muons and atmospheric neutrinos are weighted such that they represent the true rates in the detector, and can directly be compared to the burnsample data. The distribution of the simulated signal is scaled up, in order to be visible. So contrary to the other distributions, the absolute value of the bin heights have no meaning in case of the signal.

The sum of the simulated atmospheric muons and neutrinos is shown as a gray band, of which the width represents one standard deviation (statistical) uncertainty on that sum. At the bottom of each histogram the ratio of the experimental data over the total background simulation is shown, again with one standard deviation uncertainty.

7.5.1 The LEVEL 3 cut variables

The aim of the LEVEL 3 filter is to achieve a comparable efficiency for low and high mass WIMP neutrinos, as the data sample has not been split yet. Therefore the variables that are chosen, are not based on energy, but rather on the direction and the starting point of the tracks. Remind that the reconstructions which are used in this chapter were described in detail in Chapter 5.

SPEFIT Zenith Angle

One very straightforward selection to make is a cut on the reconstructed zenith angle. The angular resolution of all the reconstructions which are available at this stage were checked and the Single Photo-Electron Fit (SPEFIT) turned out to be the reconstruction with the best angular resolution for signal neutrinos at this stage. Therefore, the zenith angle of this reconstruction is used. In Fig. 7.6 the distributions of the reconstructed zenith angle are shown for the different background and signal components. The cut on this zenith angle must not be too strict, since no off-source region can be defined in this analysis (see Section 7.2.2). A signal free control region is thus needed in which the background simulation can be compared to the data.

Based on these considerations, the zenith angle cut is chosen such that all events with a reconstructed zenith angle < 2.0 rad ($\sim 120^\circ$) are removed.

FINITERECO Vertex Point

Signal neutrino-induced muons and atmospheric muons do not only differ in direction, but also the visible starting point of the muon tracks are expected to be different. The atmospheric muons always start outside the detector, more precisely in the atmosphere, whereas muons from neutrino interactions can start in the detector. The position of the starting point of a muon track may thus be used as a cut variable. The starting points are reconstructed using the simple version of the FINITERECO algorithm, as the data rate is still too high to run the more complicated and time-consuming version of this algorithm.

The position of these reconstructed vertices are shown in Figs. 7.7 and 7.8. In Fig. 7.7 the position in the xy -plane (left) and rz -plane (right) are shown for background (top) and signal (bottom), where $r = \sqrt{x^2 + y^2}$, hence the distance to the central axis of the detector in the xy -plane. Fig. 7.8 shows the distributions of the reconstructed r -coordinate (left) and z -coordinate (right). Note that these values are calculated with respect to the center of the detector, in which the (x,y,z) coordinates are chosen to be $(0,0,0)$.

From Figs. 7.7 and 7.8 it is clear that the reconstructed starting point of the muon track is mainly concentrated in the lower central part, hence DEEPCORE, for signal events, while atmospheric muons mainly have a reconstructed starting point at the top and side of the detector. This is because the signal neutrinos have low energies (see

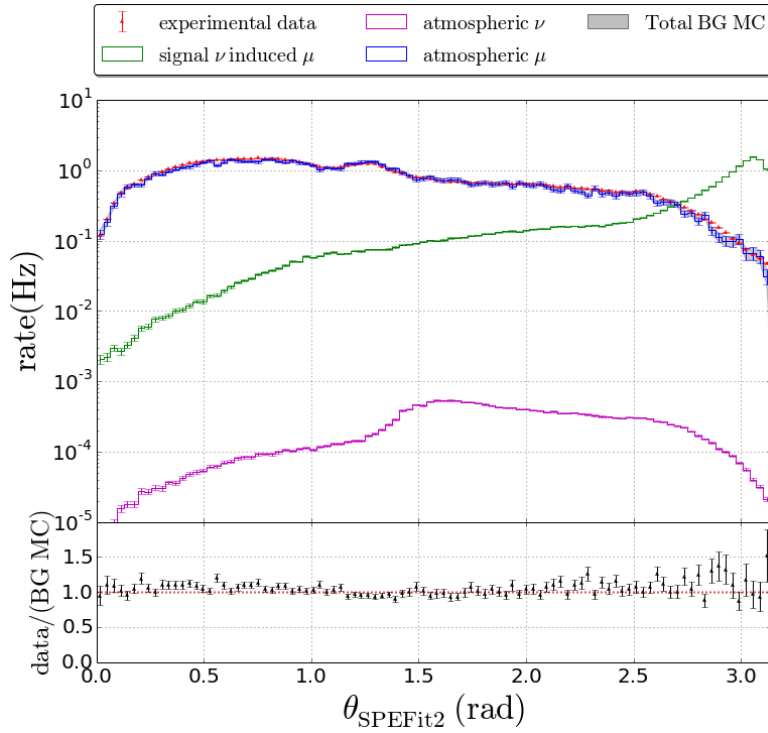


Figure 7.6: The zenith angle distributions for experimental data, simulated background muons and neutrinos and simulated signal neutrinos, before applying any of the LEVEL 3 cuts.

Fig. 7.3a) and will thus mainly be detected by the DEEPCORE sub-detector, located in the center-bottom part of the ICECUBE detector.

Events with a track that has a reconstructed starting point inside the ICECUBE volume but well outside the DEEPCORE volume, either to the side ($r_{\text{vertex}} > 490$ m) or above ($z_{\text{vertex}} > 180$ m), are removed.

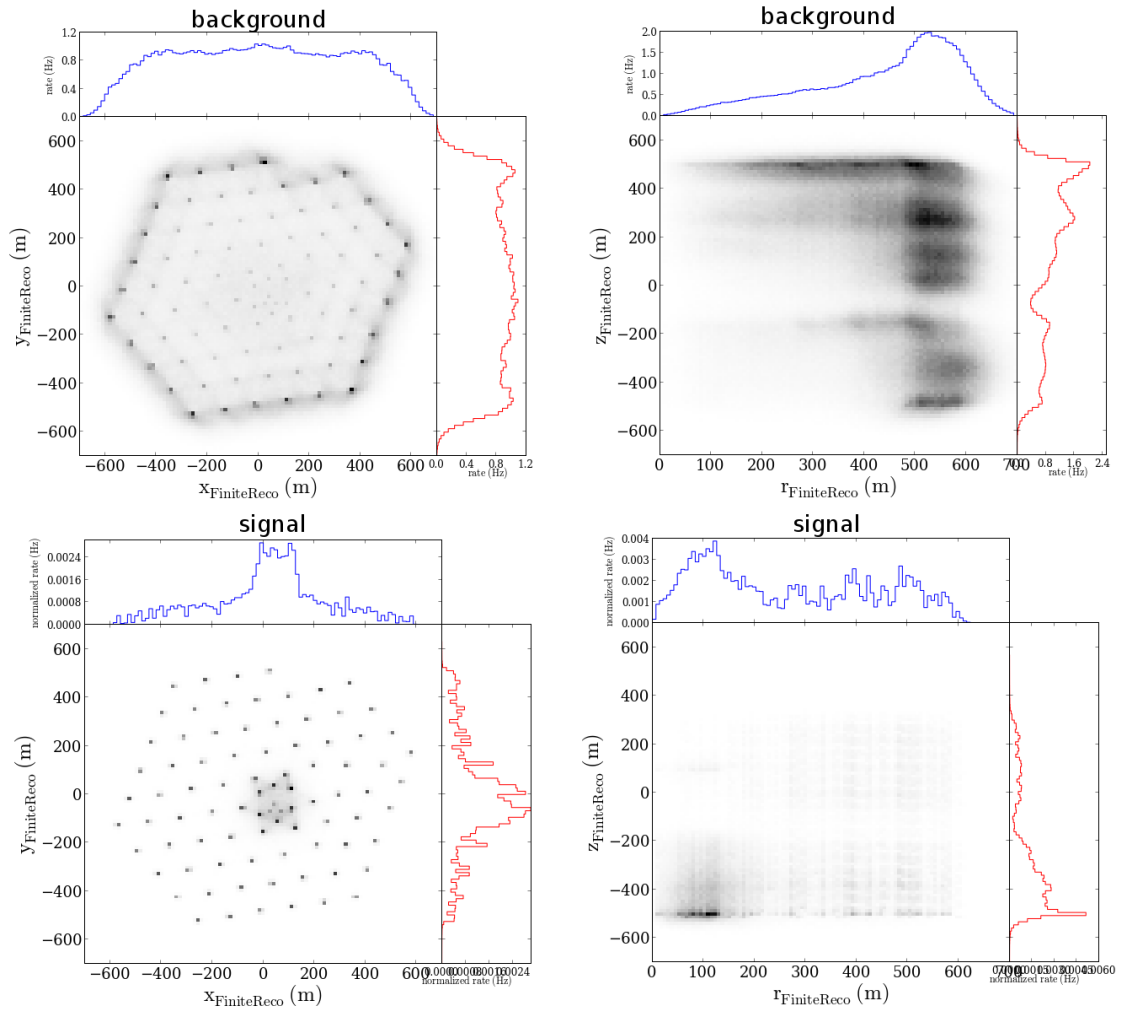
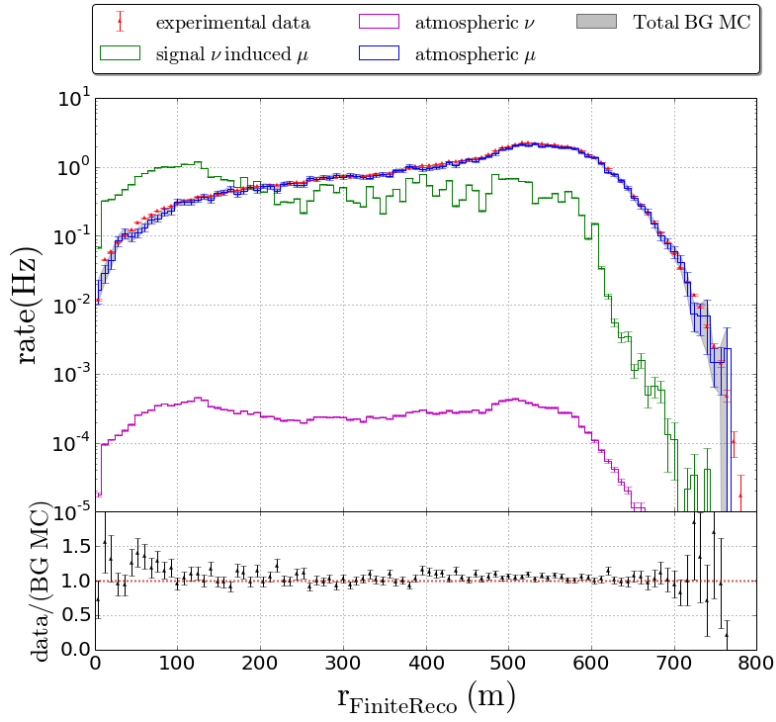
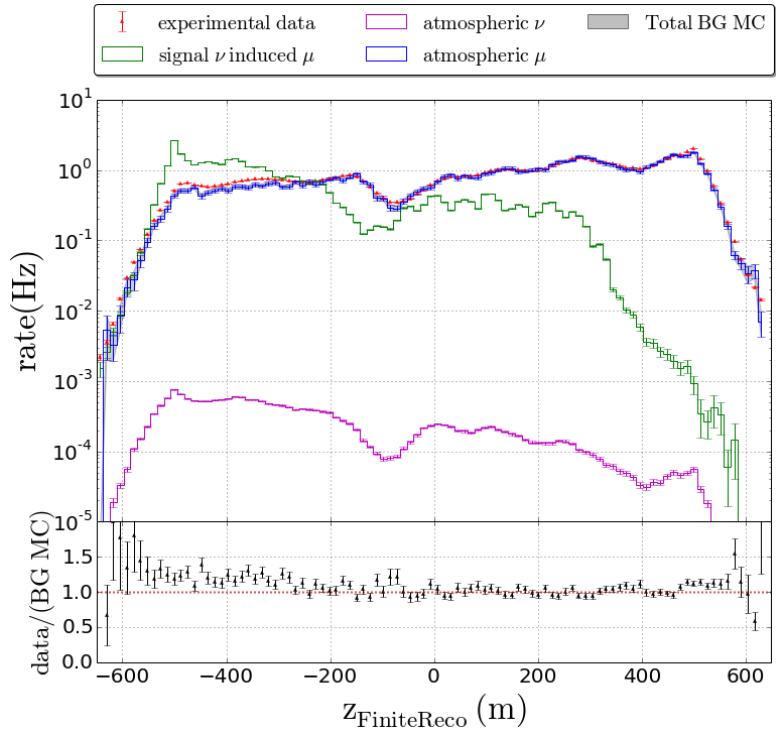


Figure 7.7: The reconstructed starting point projected in the xy -plane (left) rz -plane (right) of the detector for background events (top) and signal events (bottom), before applying any of the LEVEL 3 cuts. The point density indicates the event rate.



(a)



(b)

Figure 7.8: Distributions of the r -coordinate (a) and z -coordinate (b) of the reconstructed interaction vertex, before applying any of the LEVEL 3 cuts.

Average drift of hits in the vertical direction

The last variable that is used at this LEVEL is z_{travel} . This is the average drift of hits in the vertical (z) direction

$$z_{\text{travel}} = \sum_{i=1}^n \frac{z_i - \langle z_{\text{quartile},1} \rangle}{n}, \quad (7.2)$$

where n is the number of fired DOMs, z_i is the z position of the i^{th} hit DOM and $\langle z_{\text{quartile},1} \rangle$ is the mean z coordinate of the first quartile of hits in time. This should be negative for down-going tracks, i.e. background, and positive for up-going tracks, i.e. signal (see Fig. 7.9).

Events with $z_{\text{travel}} < 10$ m are removed.

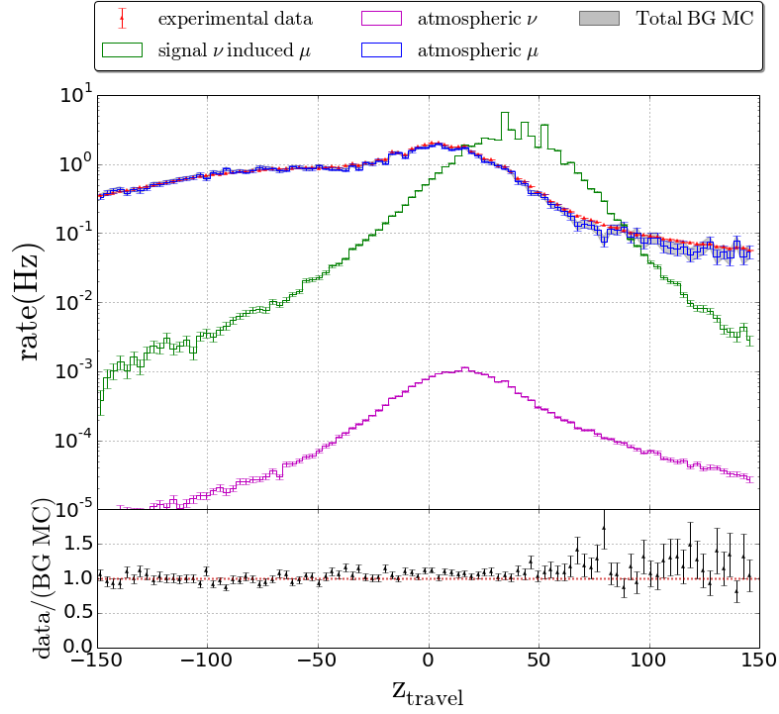


Figure 7.9: Distributions of z_{travel} , before applying any of the LEVEL 3 cuts.

7.5.2 Selecting the cut values.

The cut values mentioned in the previous section (except the cut on the zenith angle) are chosen by looping over all possible combinations of values of the variables described above and checking which combination brings down the background rate below 3 Hz, while removing as little signal as possible.

To check which combination suits these criteria best, all cut combinations are plotted on a background rate versus signal efficiency scatter plot, as shown in Fig. 7.10, where signal efficiency is calculated as :

$$\epsilon_S = \frac{\text{event rate after the linear cuts}}{\text{event rate at LEVEL 2}} \quad (7.3)$$

The combination that brings down the rate to ~ 3 Hz and has the highest signal efficiency is picked. The values obtained for the cuts are summarized in Table 7.3.

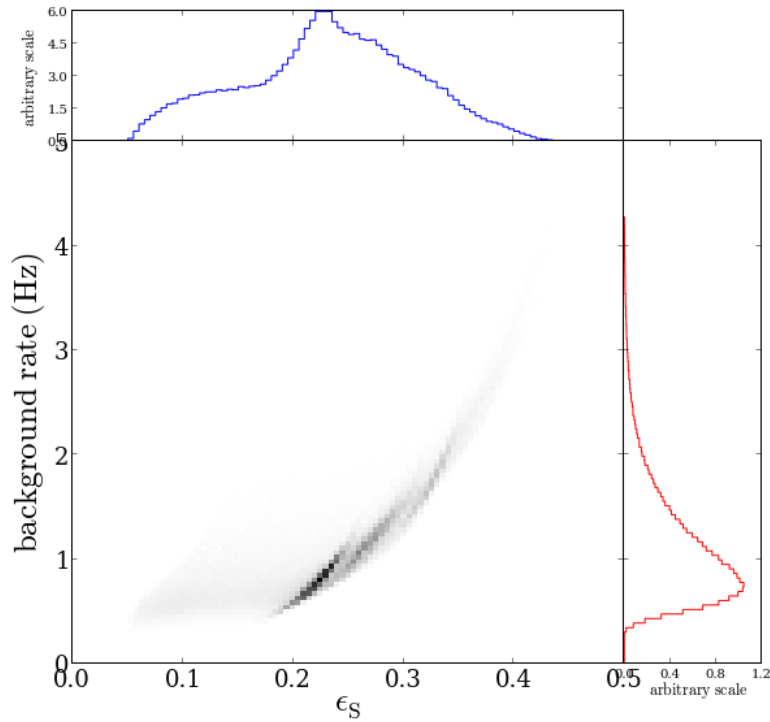


Figure 7.10: Background rate versus signal efficiency scatter plot for all combinations of cut values of the four variables (except the cut on the reconstructed zenith angle, which is fixed at 2 radians) described in Section 7.5.1. Each dot on the plot represents a combination of cuts.

Table 7.3: Cut values of the LEVEL 3 filter.

	part of the phase space that is removed
θ_{SPEFIT}	< 2 radians
r_{FR}	> 490 m
z_{FR}	> 180 m
z_{travel}	< 10 m

After these cuts, the signal ($m_\chi = 50$ GeV) efficiency ϵ_S is 41.7% and the background rate (based on experimental data) is 2.96 Hz. An overview of the signal efficiencies and of the rate of the different background components after these cuts is given in Table 7.4. Note that the experimental data rate is still underestimated by the background simulation. Further investigations on this underestimation, as well as a reduction of this disagreement, are discussed in Section 7.7.3 of this chapter.

Also note that this step of the event selection is similarly efficient for WIMPs with masses $m_\chi = 50$ GeV and $m_\chi = 1$ TeV, as was intended.

Table 7.4: Percentages of the amount of simulated signal (w.r.t. LEVEL 2) and rates of the simulated background and data events at different selection levels.

	# WIMP (%)		Simulated Background (Hz)			Data (Hz)
	$m_\chi = 50$ GeV	$m_\chi = 1$ TeV	ν_{atm}	μ_{atm}	total	
LEVEL 2	100.0	100.0	27×10^{-3}	650	650	670
LEVEL 3	41.7	53.4	5.3×10^{-3}	2.32	2.32	2.96

7.6 Splitting the data sample

To make the Earth WIMP analysis efficient for both low and high WIMP masses, the analysis is split in 2 parts, a low and a high energy analysis. The splitting of the samples is done based on reconstructed energy.

The algorithm that is used for the neutrino energy reconstruction has been optimized for 10-80 GeV muon neutrinos, and has been developed for an ICECUBE analysis that measured the neutrino oscillation parameters from atmospheric muon neutrino disappearance [88]. This algorithm is based on the fact that the total energy of a muon neutrino in a charged current interaction can be estimated as the sum of the energy of the hadronic cascade E_{shower} at the interaction point and the energy of the muon E_μ .

$$E_{\nu_\mu} = E_{\text{shower}} + E_\mu \quad (7.4)$$

First, the energy of the muon E_μ is reconstructed (Fig. 7.11 b)). This is done by reconstructing its track-length, using the precise version of the FINITERECO reconstruction. From the length of the muon track L , its energy E_μ can be estimated using the following relation [161]

$$E_\mu(L) \approx \frac{a}{b} \left(e^{bL} - 1 \right), \quad (7.5)$$

where $a \approx 0.2$ GeV·m⁻¹ and $b \approx 3.4 \cdot 10^{-4}$ m⁻¹ in the case of water/ice. The length L of the muon track is calculated with the extended FINITERECO algorithm, which can be included at this point, as the data rate is now low enough to reconstruct each event with this time-consuming algorithm in a realistic time span.

Before reconstructing the energy of the hadronic cascade E_{shower} , the track light has to be removed from the event, to avoid double counting of pulses. The expected amount

of photons that are created by a muon track and arrive at a DOM can be calculated in the following way [162]

$$\gamma_\mu = 28400 \cdot \frac{r_d^2}{2d \cdot \sin \theta_C} \cdot \epsilon \cdot \exp\left(-\frac{d}{l_{\text{att}} \cdot \sin \theta_C}\right), \quad (7.6)$$

where r_d is the radius of a DOM, θ_C is a Cherenkov angle, $\epsilon=0.33$ is the overall efficiency of DOMs in DEEPCORE, d is the distance from the DOM to the track and $l_{\text{att}} \approx 35$ m is the effective attenuation length (including both the absorption and the scattering in the ice).

The light that is expected from the muon, can thus be calculated using Eq. (7.6). After removing the hits that are associated to this light, only the cascade charge is left (Fig. 7.11 d). The energy of the hadronic cascade is reconstructed with the MONOPOD cascade reconstruction algorithm [162], based on the remaining pulses. The MONOPOD reconstruction uses the fact that for an electromagnetic cascade, the charge recorded by a DOM scales linearly with the number of photons that arrive to it, given that it does not reach saturation. The reconstruction looks for the most likely value of the energy of the electromagnetic cascade E_{EM} , given the overconstrained system of linear equations

$$Q_i = B_i E_{EM}, \quad (7.7)$$

where Q_i is the observed charge (PEs) in the i th DOM and B_i is the predicted photon distribution from an electromagnetic cascade of energy E_{EM} . As the reconstruction uses a parametrization of an electromagnetic cascade to maximize Eq. (7.7), a correction factor needs to be introduced to convert this result to the energy of the hadronic cascade. It has been found empirically that the reconstructed energy needs to be multiplied by a factor 1.4 to correspond to the true energy of the hadronic cascade [97].

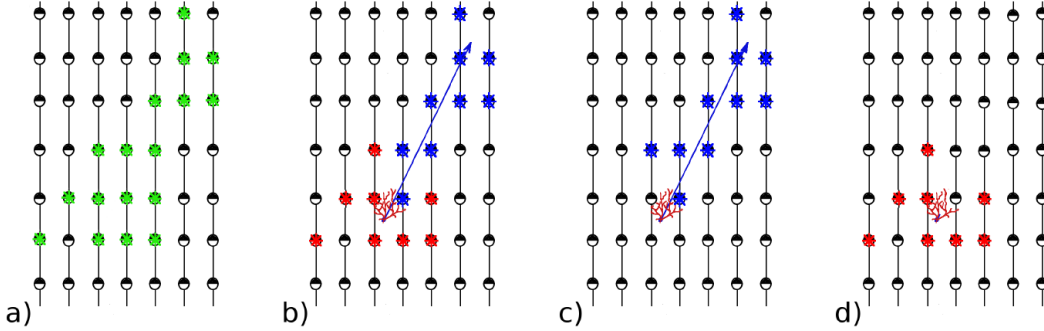


Figure 7.11: Procedure of the energy reconstruction algorithm: a) all hits in the event; b) reconstructed track through the hits; c) hits associated to the reconstructed track; d) hits that are not associated to the track and thus belong to the hadronic cascade. Figure from [161].

The energy reconstruction is performing well for low energy neutrinos, for which it has been optimized. For the neutrinos produced by the 50 GeV WIMPs, the true neutrino

energy is slightly underestimated by the reconstruction, as can be seen in Fig. 7.12. When fitting a gaussian distribution to the difference between the true $E_{\nu,\text{true}}$ and the reconstructed energies E_{reco} , a mean (μ) and standard deviation (σ) of respectively -4.00 GeV and 11.08 GeV are found. This underestimation is also visible in Fig. 7.13, where a scatter plot of the reconstructed vs. the true neutrino energy is shown.

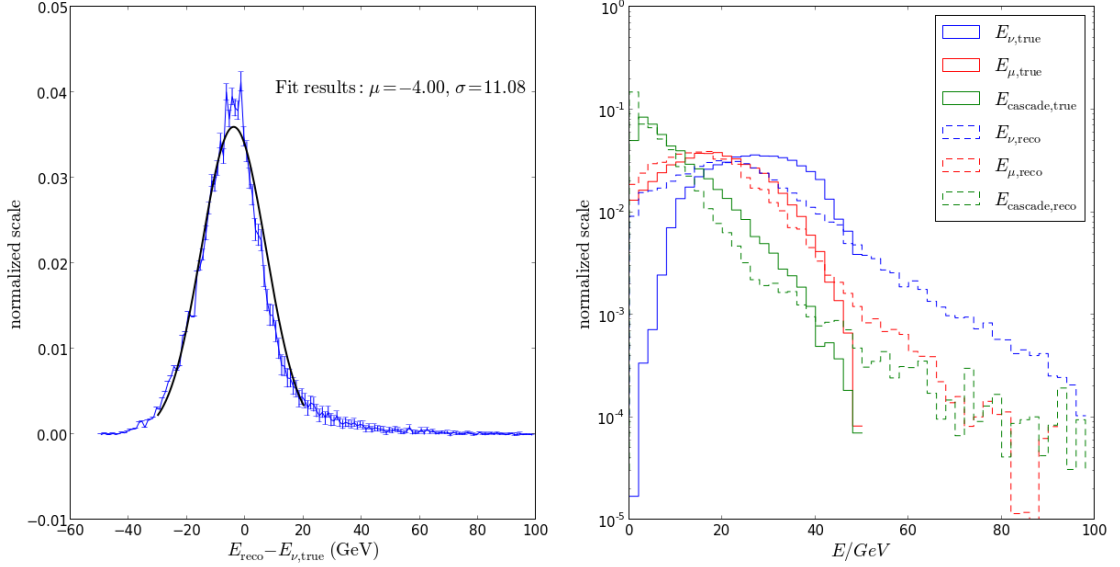


Figure 7.12: The left panel shows the difference between the true and the reconstructed energies of a sample of neutrinos originating from 50 GeV WIMP annihilations (blue histogram), as well as a fitted gaussian distribution (black line) through the [-30 GeV,25 GeV] energy range of this histogram. In the right panel, the true (solid lines) and reconstructed (dashed lines) energies are shown for the neutrino (blue), the muon (red) and the hadronic cascade (green).

Fig. 7.14 shows the reconstructed neutrino energy distributions for neutrinos induced by 50 GeV WIMPs (green) and 1 TeV WIMPs (black). Note that the 1 TeV WIMP-induced neutrinos mainly have reconstructed energies below 500 GeV, and the reconstruction algorithm thus underestimates the energy of the neutrinos in the case of this WIMP model (compare to Fig. 7.3b in Section 7.2.1 of this chapter). This is because the energy reconstruction performs best on events with contained muon tracks and hadronic cascades, preferably within the dense DEEPCORE sub-detector, whereas many of the 1 TeV WIMP-induced neutrinos interact outside the detector, and only part of the Cherenkov photons emitted by the muon and the hadronic cascade are recorded by the ICECUBE and DEEPCORE DOMs. Another notable feature in the E_{reco} distribution, is the peak at 748.95 GeV. This energy corresponds to an artificial muon track length of 2 km (eq. (7.5)), which is the length that is set by the FINITERECO reconstruction if the starting or ending point of the track cannot be estimated (i.e. long tracks).

As the main focus of this analysis lies on the 50 GeV WIMPs, it is important that the analysis is as optimal as possible for this WIMP mass, so the value at which the

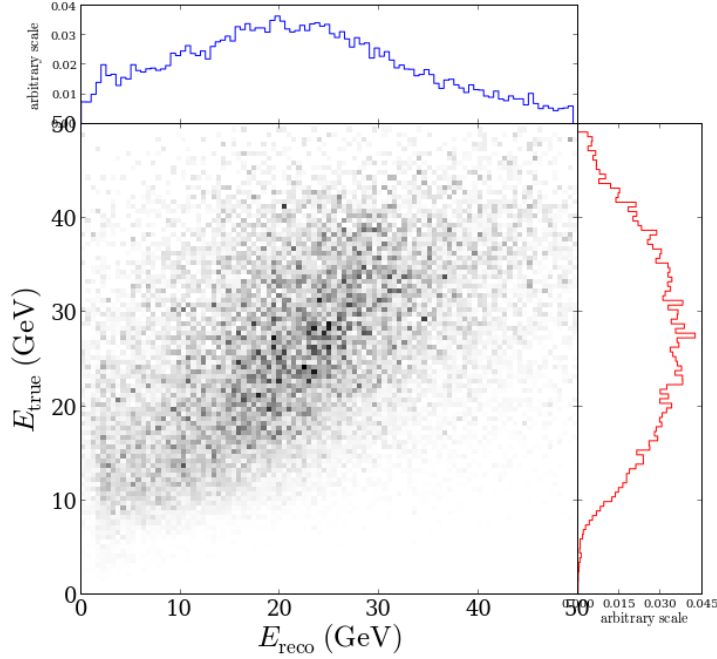


Figure 7.13: Scatterplot of the true neutrino energy vs. the reconstructed energy, both shown in the energy range [0 GeV, 50 GeV].

reconstructed energy is split should be such that it keeps most of the 50 GeV WIMP neutrinos in the low energy sample. Based on the distributions of this reconstructed energies, shown in Fig. 7.14, it was decided to split the sample as:

1. $E_{\nu, \text{reco}} \leq 100 \text{ GeV} \rightarrow \text{low energy sample.}$

Events in this LOWE sample will be used in the part of the analysis that is optimized on 50 GeV WIMPs that annihilate into $\tau^+\tau^-$. This analysis is the core of the present thesis.

2. $E_{\nu, \text{reco}} > 100 \text{ GeV} \rightarrow \text{high energy sample.}$

Events in this HIGH sample will be used in the part of the analysis that is optimized on 1 TeV WIMPs that annihilate into W^+W^- .

The numbers of the signal and background data sets after the splitting, are given in Table 7.5.

After the splitting, further reduction of the background is done independently for the two samples. The aim of the analysis presented in this thesis, is to search for neutrinos induced by 50 GeV WIMPs. Therefore the optimization of the low energy sample will be presented in full detail in the next sections. The optimization of the high energy sample was first done by Isabelle Anseau [163] and in a later stage further optimized by Jan Lünemann [164], in close collaboration with the author. The detailed discussion of the

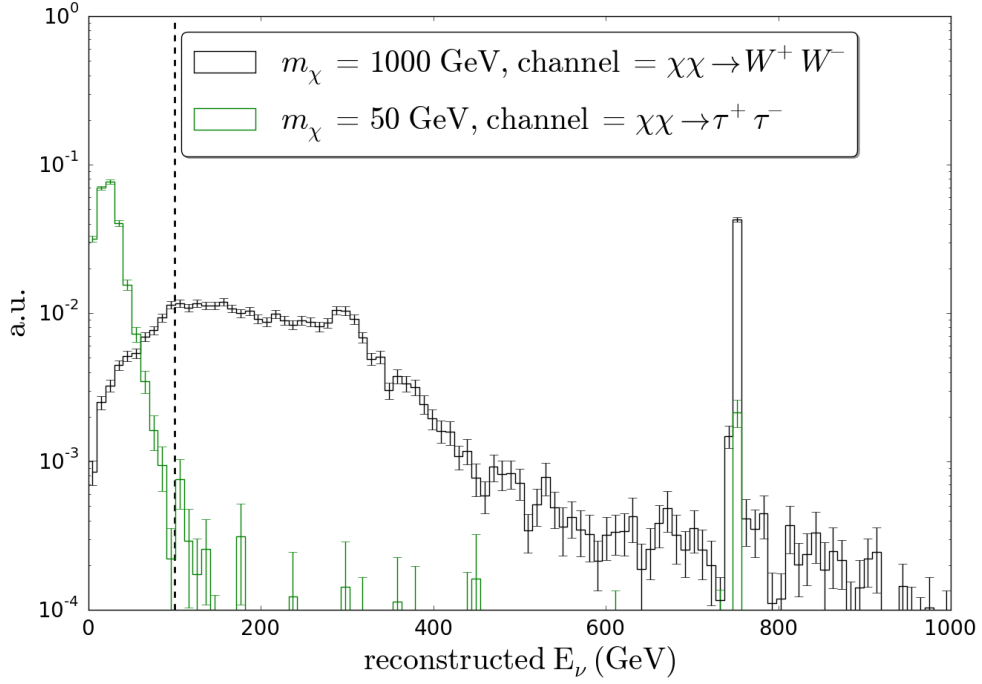


Figure 7.14: The reconstructed energy distributions for neutrinos induced by 50 GeV and 1 TeV Earth WIMPs. The vertical dashed line shows where the data sets are split. The peak at ~ 750 GeV comes from tracks with an artificially reconstructed length of 2 km, which is the value that is set by the algorithm when the length of the muon track cannot be reconstructed (e.g. when it is not contained in the detector). As these events are generally bright events, it is a good feature that they end up in the high energy sample.

Table 7.5: Percentages of the amount of simulated signal (w.r.t. LEVEL 2) and rates of the simulated background and data events at different selection levels.

	# WIMP (%)		Simulated Background (Hz)			Data (Hz)
	$m_\chi = 50$ GeV	$m_\chi = 1$ TeV	ν_{atm}	μ_{atm}	total	
LEVEL 2	100.0	100.0	27×10^{-3}	650	650	670
LEVEL 3	41.7	53.4	5.3×10^{-3}	2.32	2.32	2.96
LOWE LEVEL 3	40.84	8.19	2.5×10^{-3}	1.03	1.03	1.39
HIGHE LEVEL 3	0.82	45.24	2.8×10^{-3}	1.29	1.29	1.57

optimization of the low energy sample is given in Section 7.7, and a short overview of the high energy analysis is given in Section 7.8.

7.7 The low energy optimization

The data rate in the low energy (LOWE) sample is about one Hz ($\mathcal{O}(10^8)$ /year), hence at least 5 orders of magnitude higher than the expected signal rate, which is at most a few μHz ($\mathcal{O}(10^3)/\text{km}^2/\text{year}$). Also, the data are still dominated by atmospheric muons, so more events have to be removed before being at the scale of the irreducible atmospheric neutrino background. To get parameters which provide a good separation between WIMP-induced signal neutrinos and atmospheric background events, the remaining events are reprocessed using the sophisticated HIVESPLIT cleaning, and (new) reconstructions and variables are calculated using these pulses, as explained in Section 7.7.1. These variables, as well as previously calculated variables, are then used to train *Boosted Decision Trees (BDTs)*. As described in Section 7.7.2, a BDT is a machine learning algorithm which is a very powerful tool to separate signal from background. To get a high separation power, the algorithm needs to be *trained* (the trees are *grown*) on subsamples of the signal and background data.

Before training the BDT, one has to be sure that the simulation is representing the experimental data in a correct way. For this reason additional linear cuts are made prior to the BDT training in order to increase the agreement between data and simulation (Section 7.7.3). After this step, the experimental data rates are on the order of 100 mHz, and the data are still dominated by atmospheric muons. The BDTs are then trained on variables that are not too correlated, and that have good data-simulation agreement (Section 7.7.4).

The cut on the BDT output is then chosen such that the sensitivity of the analysis is optimal. The sensitivity is calculated with a likelihood ratio hypothesis test based on the values of the reconstructed zenith. This is done by using the Feldman-Cousins unified approach, as explained in detail in Chapter 8. The sensitivity will be calculated by using the zenith distribution of the WimpSim simulation as signal sample and as there is no off-source region, the background sample will be estimated from the zenith distributions of the remaining simulated atmospheric muons and neutrinos. Having a good data-MC agreement is thus of great importance, and this agreement will thus be checked in great detail in each of the following filter levels.

As the events in this part of the analysis have energies in the $\mathcal{O}(10 - 100)$ GeV range, several challenges have to be faced. First, the ICECUBE detector was not built to look for events with these low energies, so it is not trivial to detect and reconstruct these events. The DEEPCORE sub-detector will have an important contribution in the detection and reconstruction of these events.

Another aspect is that noise has a drastic impact on events with these low energies, as the events themselves only contain few hits and a small contribution from noise can thus lead to a different direction reconstruction and event topology.

Also the simulation of atmospheric neutrinos needs to be done carefully as in this

energy range the largest fraction of atmospheric neutrino events will come from the Genie simulation, but there will still be a fraction coming from NuGen and the two samples are combined as explained in Section 6.2. Neutrinos of these energies crossing the earth will oscillate, so their oscillation probabilities are taken into account as also described in Section 6.2.

Lastly the systematic effects like e.g. the simulation of the hole ice, ice properties, DOM efficiency are crucial for these low energy events, as their light output is very limited. Therefore, the systematic uncertainty on this part of the analysis will be larger than that of the high energy analysis.

7.7.1 HIVESPLIT Cleaning

Now that the data rate has been reduced to a bit more than 1 Hz (Table 7.5), the data are reprocessed with the more sophisticated HIVESPLIT pulse cleaning and splitting algorithm, which was discussed in detail in Section 5.1.2. During this reprocessing also more sophisticated reconstructions as e.g. MUX (Section 5.2.4) are added to the events, and every variable is calculated for both the TWSRT pulses and the HIVESPLIT pulses.

The reconstructions are performing better when the HIVESPLIT pulses are used, as can be seen in Figs. 7.15 and 7.16. In Fig. 7.15, the HIVESPLIT (left panel) and TWSRT (right panel) cleaned pulses are shown for the same event, with the true atmospheric muon track indicated in green, and the MUX4MPE reconstructed muon track in red. For this particular event, the TWSRT cleaning is harsher than the HIVESPLIT cleaning, resulting in the false removal of physics hits in the case of TWSRT cleaning.

A quantitative proof of the better performance of the HIVESPLITTER algorithm is given in Fig. 7.16, which shows the distributions of the zenith angle reconstructed by the MUX4MPE reconstruction algorithm after running the reconstruction on the HIVESPLIT pulses (Fig. 7.16a) and on the TWSRT pulses (Fig. 7.16b). When using HIVESPLIT pulses, most of the atmospheric muons are correctly reconstructed as down-going, i.e. $\theta_{\text{MUX4MPE}} < \pi/2$, while this is not the case when using the TWSRT pulses. The performance of the reconstruction on the signal and on the atmospheric neutrinos is comparable for both types of pulse-series.

It should be noted that not all variables have a better separation power between signal and background when the HIVESPLIT pulses are used. For some variables, the TWSRT pulses are still providing a better separation power. In the next step, *Boosted Decision Trees* (BDTs, Section 7.7.2) will be used to clean the sample. As was mentioned in the introduction of this section, a BDT is a machine learning algorithm which is *trained* (the trees are *grown*) on subsamples of the signal and background data, to get a high separation power. All the variables using both HIVESPLIT and TWSRT pulses will be used in the training of the BDT and the variables that have the largest contribution in the construction of the tree will be kept.

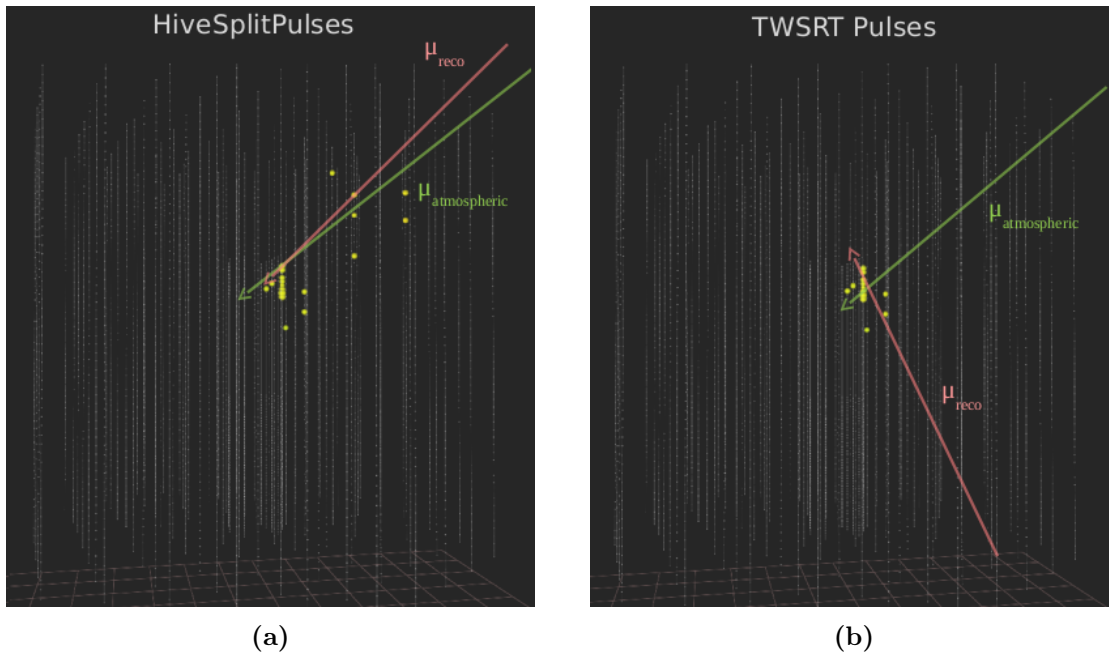
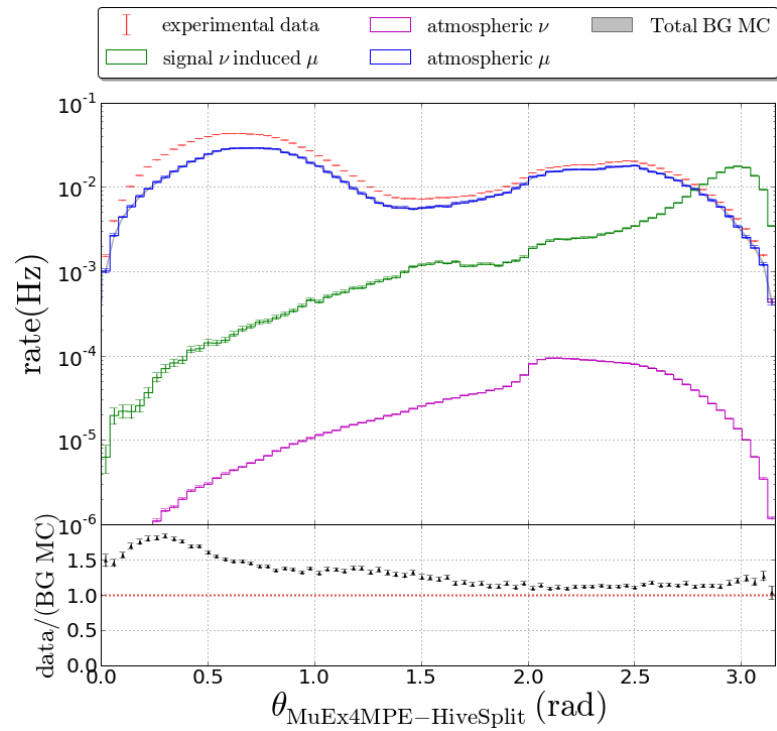
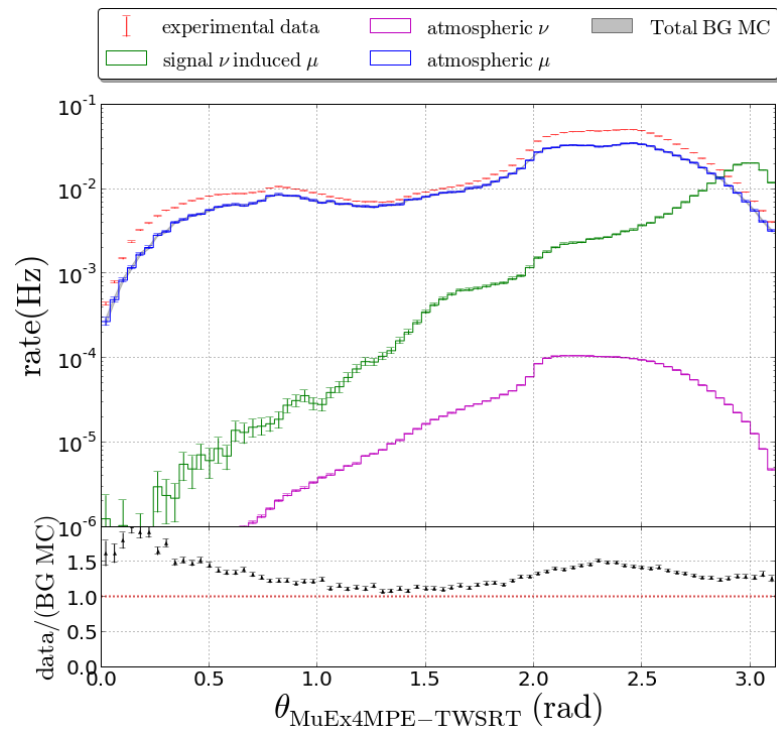


Figure 7.15: HIVESPLIT pulses (a) and TWSRT pulses (b) of an muon track event, of which the true direction is indicated in green. The resulting MUEX4MPE reconstruction, based on the clean pulses, is indicated by the red arrow.



(a)



(b)

Figure 7.16: Reconstructed zenith angle distributions of the MuEx4MPE reconstruction based on the HIVESPLIT pulses (a) and the TWSRT pulses (b).

7.7.2 Introducing Boosted Decision Trees

At this point, the data are still dominated by atmospheric muons (Table 7.5 and Fig. 7.16) by several orders of magnitude. To remove most of these muons in an efficient way without removing too much signal, a more sophisticated method is needed. As the data rate has been reduced to roughly 1 Hz, machine learning algorithms like *Boosted Decision Trees* (BDTs) can be used to remove (most of the) remaining atmospheric muon background. In a first step, the trees are *grown* by using a subsample, the *training sample*, of the signal and background data. This growing of the tree, referred to as *training*, is done such that the separation power of the tree is optimal, as described below. After the trees have been trained, the BDT algorithm is applied on a statistically independent subsample, the testing sample, to check whether the BDT is giving similar results for the training and the testing sample. If this is true, the BDT is trustworthy, if not, the BDT has been *overtrained* and needs to be retrained with different parameter settings.

Within the ICECUBE framework, a tool called PYBDT [165] has been developed, which is an algorithm that is comparable to the BDT algorithm provided by ROOT-TMVA [166].

Decision Trees (DTs) are well known classifiers that allow a straightforward interpretation as they can be visualized by a simple two-dimensional tree structure (see Fig. 7.17). The DTs can be used to look for the ideal cuts to make on a set of parameters in order to separate the signal from the background. A DT consists of several *nodes*, and at each node, starting with the root node, a cut on a specific parameter is made, after which the node is split into two child nodes. This split is determined by finding the parameter and its corresponding cut value that provides the best separation between signal and background, as explained below. Once certain criteria are satisfied (as discussed below), child nodes are no further split and the final nodes are referred to as *leaves*. A leaf is called a *signal leaf* or a *background leaf* (respectively indicated as **S** and **B** in Fig. 7.17) according to the class the majority of events in the leaf belongs to.

Events can then be categorized as either signal or background by tracing their path through the DT.

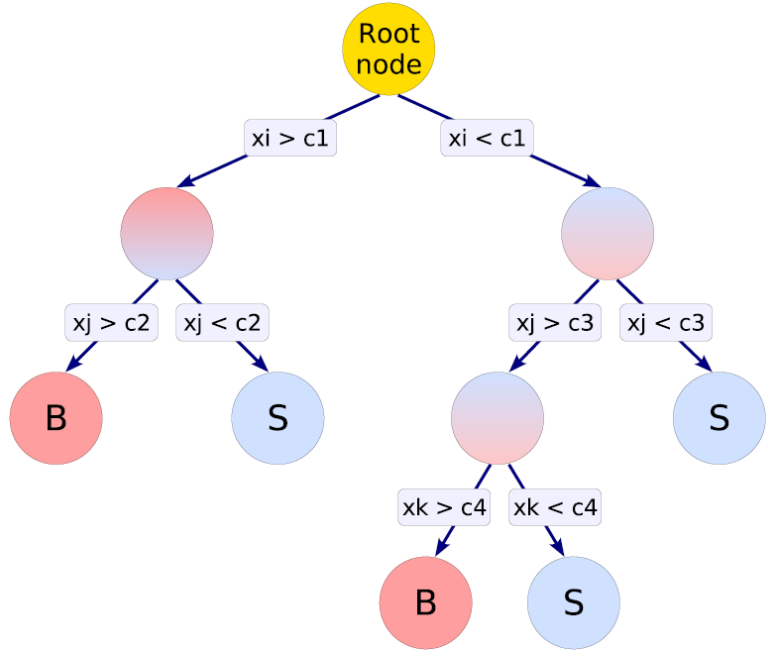
The node splitting can be done in different ways of which one, the one used in this work, is described below. The reader is referred to [166] for an overview of other methods.

The quality of the separation between signal and background can be checked by looking at the purity p .

$$p = \frac{\sum_s w_s}{\sum_s w_s + \sum_b w_b} \quad (7.8)$$

where $w_{s(b)}$ is the signal (background) event weight and the sums are taken over the signal (s) and background (b) events.

Figure 7.17: Scheme of a decision tree. Picture from [166].



It follows that

- $p = 0.5$ when the samples are purely mixed,
- $p > 0.5$ for *signal-leaves*,
- $p < 0.5$ for *background-leaves*.

The cuts should be chosen in such a way that they separate background and signal as well as possible. This means that they should create *pure* leaves:

- $p \rightarrow 1$ for signal-leaves,
- $p \rightarrow 0$ for background-leaves.

In order to get this good result, an impurity measure has to be defined. In this analysis, the *Gini Index* g is used

$$g \equiv \left(\sum_{i=1}^n w_i \right) \cdot p \cdot (1 - p), \quad (7.9)$$

where n is the number of events on that branch.

Using g , the separation gain ΔS is calculated for each cut considered

$$\Delta S = g_{\text{parent}} - (g_{\text{daughter, left}} + g_{\text{daughter, right}}) \quad (7.10)$$

The cut that maximizes the separation gain ΔS will be selected.

In principle, a perfect discrimination between signal and background could be reached, by continuing the splitting until leaves would be pure background and pure signal like. This would however lead to decision trees which are fine-tuned on statistical fluctuations (or atypical events) in the training sample, leading to a performance of the tree on the unknown test sample which is inconsistent with its performance on the training sample, a phenomenon referred to as *overtraining*. To avoid this overtraining, the splitting stops whenever one of the following criteria is met:

- A maximum tree depth is reached (set to 3 in this analysis).
- A minimum number of events in a node is reached.
- A node has either only signal or only background training events remaining.

Depending on whether an event falls in a signal or a background leaf, an event gets a discrete *score* s of respectively $+1$ or -1 .

Another useful tool to reduce or eliminate overtraining is *Pruning*. Pruning is defined as the process of cutting back a tree from the bottom up after it has been built to its maximum size [166]. Its purpose is to remove statistically insignificant nodes and thus reduce the overtraining of the tree. Pruning a decision tree thus consists of identifying splits that are less important by some metric, and converting those split nodes into leaf nodes. There are several ways to introduce the pruning process. In this analysis *CostComplexity pruning* is used. This is a process in which subtrees that add more leaves but not much separation are identified. The algorithm defines a pruning sequence, where the first step prunes the most expendable subtree, and the last step would leave only the root node. The pruning sequence is calculated by pruning a copy of the tree until the root is reached, noting the node at which each prune operation takes place in the copy. Afterwards, the desired percentage (set to 35% in this analysis) of the prune sequence is executed on the original tree.

To see what is the gain of adding extra nodes, the weighted separation gain ΔS , defined in Eq. (7.10), is calculated for each node. The cost complexity for this node is defined as

$$\rho = \frac{\Delta S}{n_{\text{leaves}} - 1}, \quad (7.11)$$

where n_{leaves} refers to the number of leaves in the subtree below this split node. By recursively pruning away the nodes with the smallest value of ρ , the problem of overtraining is avoided.

Another problem about decision trees is that they are very unstable with respect to statistical fluctuations in the training sample from which the tree is derived. This problem can however be overcome by constructing a forest of decision trees and classifying an event on a majority vote of the classifications done by each tree in the forest. In the forest, each tree is derived from the same training ensemble, but the events in this ensemble are reweighted for the growing of every tree. The reweighting of events is called *boosting*,

as it *boosts* the weights of misclassified training events, as explained below. The output of all the individual trees is then combined into a single classifier which is given by a (weighted) average of the individual decision trees.

The boosting method that was used in this analysis is *AdaBoost*. In this method, the scores s_i of each event in training sample are compared with the true identities y_i of the training sample after a tree is trained. Next a function $I(s, y)$ is used to indicate whether an event is classified correctly or incorrectly :

- $I(s, y) = 0$ if $s = y$, so the event is classified correctly
- $I(s, y) = 1$ if $s \neq y$, so the event is classified incorrectly

These values are then used to calculate the error rate e and the boost factor α for the tree:

$$e = \frac{\sum_i w_i \cdot I(s_i, y_i)}{\sum_i w_i} \quad (7.12)$$

$$\alpha = \beta \cdot \ln\left(\frac{1 - e}{e}\right), \quad (7.13)$$

where β is the boost strength, set to 0.7 in this analysis. The weights are then adjusted to

$$w_i \rightarrow w_i \cdot \exp(\alpha \cdot I(s_i, y_i)) \quad (7.14)$$

Finally, the weights are renormalized so that $\sum_i w_i = 1$. The new weights are used to train the next tree. After that, the weights are boosted again and this process continues until the desired number of trees m have been trained ($m = 400$ in this analysis).

At the end of this training, each event has a score s_i that is calculated as:

$$s_i = \frac{\sum_m \alpha_m(s_i)_m}{\sum_m \alpha_m}, \quad (7.15)$$

which is a number between -1 and +1, where

- -1 = most probably a background event,
- +1 = most probably a signal event.

The BDT score distributions can be used to separate the background and the signal in an efficient way.

Once the BDT has been trained, the score distributions of the training sample are compared with the score distributions of the testing samples. This comparison can be done by e.g. doing a Kolmogorov-Smirnov test, which is a goodness of fit test that compares the cumulative distributions of the two samples [167]. It returns a *p-value* which represents how probable it is that two samples are identical, hence this value is close to one in case of no overtraining.

7.7.3 Cuts prior to the BDT

Before training the BDT, one has to be sure that the simulation is representing the experimental data in a correct way. Discrepancies between the data and the simulation, from now on referred to as data-MC discrepancies, should be removed prior to training the BDT. This is because in this analysis, the background sample in the BDT is taken from experimental data (50% of the burnsample), while the signal training sample is (of course) a simulated WIMP sample. An error, referred to as data-MC overtraining, could be introduced, if the BDT trains on differences between data and simulations, rather than on differences between signal and background. This type of overtraining is more subtle than the standard overtraining, as it will not be detected by standard overtraining checks as the Kolmogorov-Smirnov test.

One of the main sources for the data-MC discrepancies is coming from the incorrect/insufficient simulation of detector noise in the MC datasets, as described in Section 6.2.3. So to remove the data-MC discrepancy, one has to look for variables in which the noise can be caught, i.e. the noise shows up in an isolated region of the parameter value distribution, rather than being smeared out over the whole distribution.

Four cuts have been made to reduce the data-MC discrepancy in combination with reducing the data rate prior to the BDT training. This selection level is referred to as the LOWE LEVEL 4.

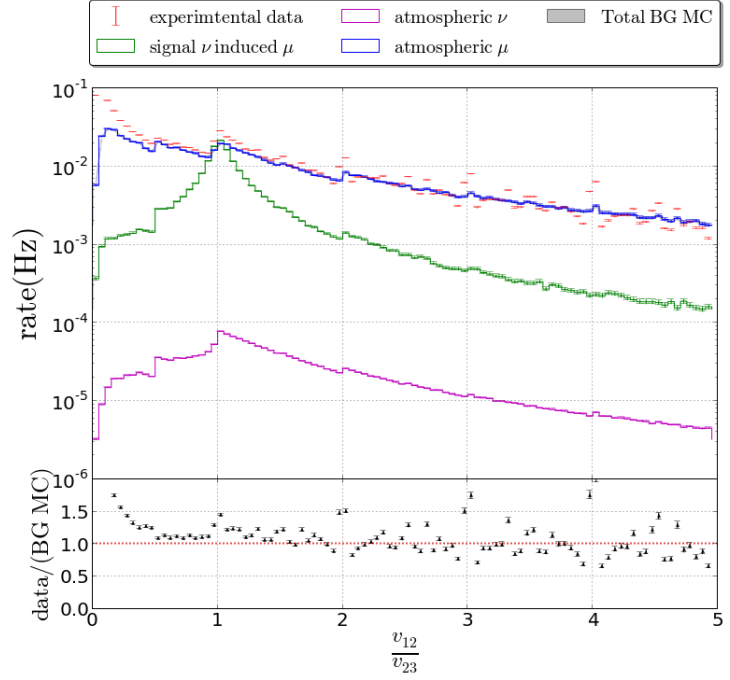
Distribution of the first 3 HLC hits.

A first way to isolate the wrongly simulated or unsimulated detector noise which could induce the data-MC discrepancy, is by looking at the distribution of the first three Hard Local Coincidence (HLC, see Section 4.3) hits in an event. More specifically, by looking into the ratio of the hypothetical speeds of the signal between the first two HLC hits and between the first and the third HLC hit

$$\frac{v_{12}}{v_{13}} = \frac{d(\text{HLC}_1, \text{HLC}_2)/\Delta t(\text{HLC}_1, \text{HLC}_2)}{d(\text{HLC}_1, \text{HLC}_3)/\Delta t(\text{HLC}_1, \text{HLC}_3)}, \quad (7.16)$$

where $d(\text{HLC}_i, \text{HLC}_j)$ is the distance between the DOMs which recorded the i th and the j th HLC hits, and $t(\text{HLC}_1, \text{HLC}_2)$ is the time difference between the i th and the j th HLC hit. If the HLC hits are produced by the Cherenkov photons of a muon, this value will be close to one. This should hold especially in the case of vertically up-going tracks, for which the distance between two neighboring DOMs is small, and hence not a lot of scattering is expected. The distribution for this variable is shown in Fig. 7.18. As expected, the distribution of the signal neutrinos peaks nicely around a value of one, just as the distribution of the atmospheric neutrinos. The experimental data, however, has a first peak around zero, which does not show up in the simulated muons or neutrinos. This peak around zero can be explained by noise hits, that are present in the experimental data, but not in the simulation.

Figure 7.18: $\frac{v_{12}}{v_{13}}$ distribution for the Low Energy sample.



Part of the data which is not reproduced properly by the atmospheric muon simulations, can thus be removed by cutting away events with $\frac{v_{12}}{v_{13}} < 0.5$.

Distribution of the number of direct hits N_{dir} .

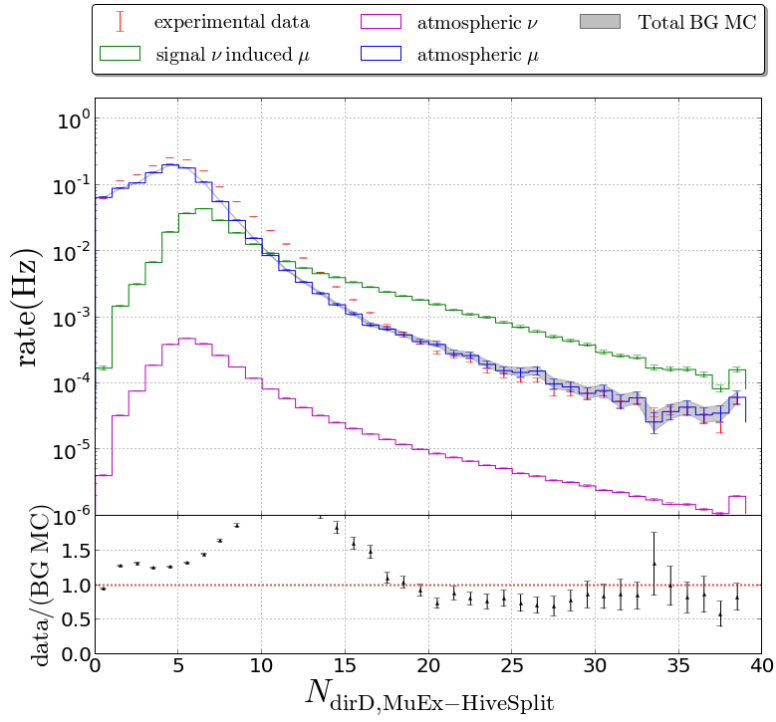
Another method to catch badly simulated events, is by looking at the number of *direct hits*. A hit is considered direct when the time residual t_{res} falls within a specified time window. The time residual is defined as the observed time of a hit minus the expected time, based on a charged particle emitting unscattered light at the Cherenkov angle. In ICECUBE, four time windows are used to define direct hits:

1. Time window A : [-15 ns, 15 ns]
2. Time window B : [-15 ns, 25 ns]
3. Time window C : [-15 ns, 75 ns]
4. Time window D : [-15 ns, 125 ns]

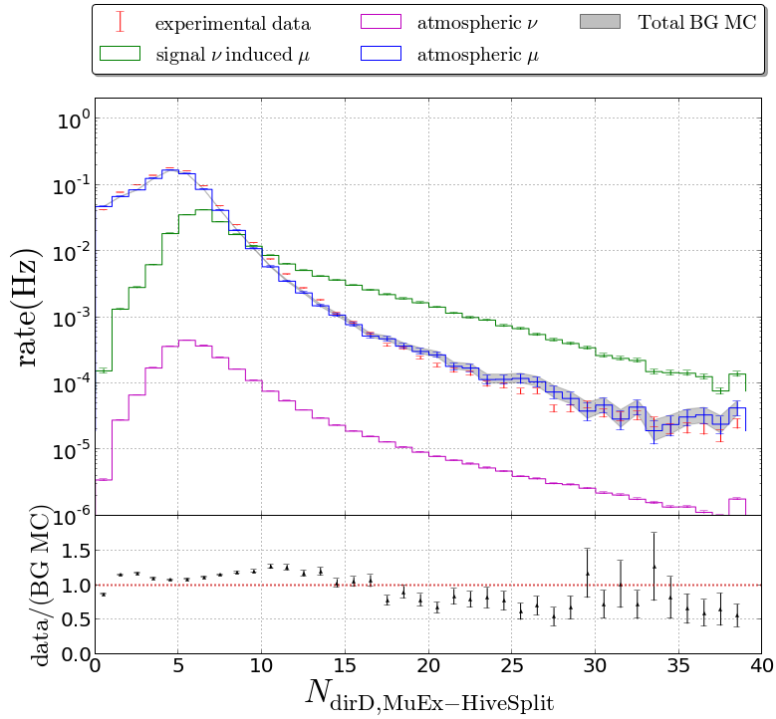
In the present analysis, the residual time between the HIVESPLIT pulses and the MUEX4MPE track reconstruction on those pulses was used.

The distributions of the direct hits within time window D are shown in Figs. 7.19a and 7.19b, respectively before and after the cut on $\frac{v_{12}}{v_{13}}$. It follows that most of the data-MC discrepancy has already been removed by the cut on $\frac{v_{12}}{v_{13}}$, but the data is still underestimated by the simulation for low values of N_{dir} , an effect that could be caused by noise.

In order not to remove too many signal events, only events with $N_{dir} < 3$ are removed.



(a)



(b)

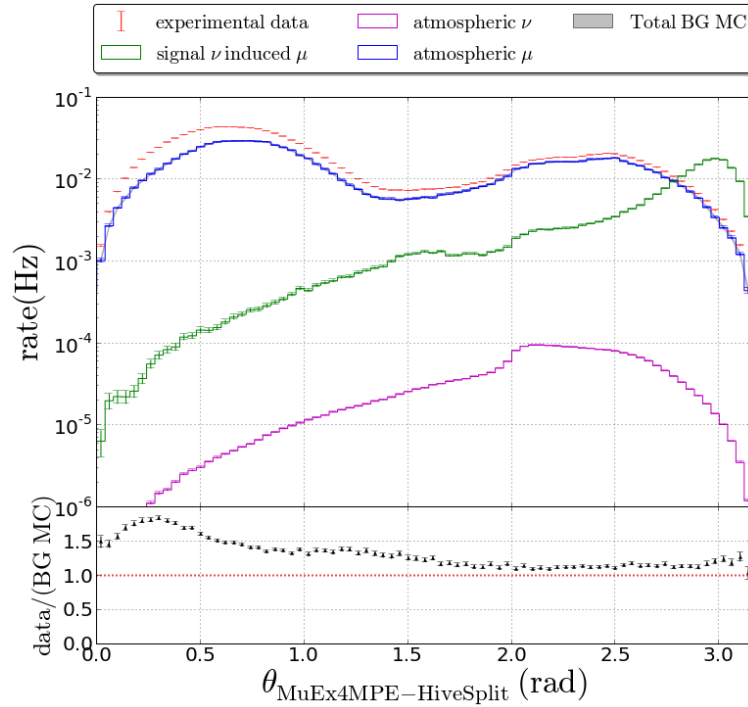
Figure 7.19: The distributions of the direct hits in time window D before (a) and after (b) the cut on $\frac{\nu_{12}}{\nu_{13}}$

Distribution of the reconstructed zenith.

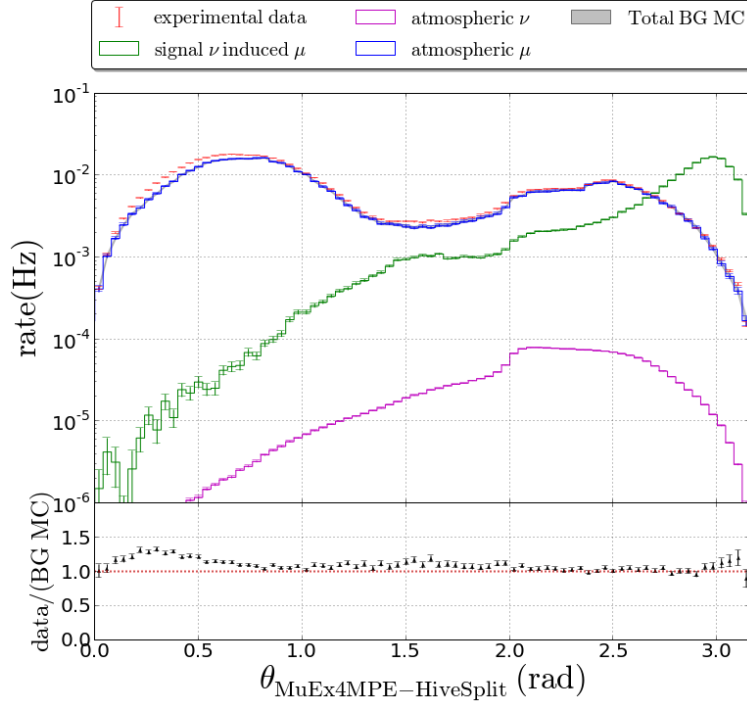
Since the signal which is sought for is coming from the center of the Earth, and thus has zenith angles close to π radians, events which have a reconstructed zenith angle far away from the center of the Earth should be removed. A cut on the reconstructed SPEFIT zenith angle has already been made as one of the LEVEL 3 cuts (Section 7.5.1). At this stage, better reconstructions like MUEX4MPE are available. Contrary to the SPE reconstruction which was performed on TWSRT pulses, the MUEX4MPE track reconstruction has also been performed on HIVESPLIT Pulses.

As was already mentioned in Section 7.5.1, the zenith angle cut can not be too strict as we aim to retain a signal free control region. Therefore only events with a MUEX4MPE reconstructed zenith angle < 2.0 rad ($\sim 120^\circ$) are removed, just as was done earlier for the SPEFIT. From Fig. 7.20b it can be seen that this cut also removes part of the data-MC discrepancy. The discrepancy shows up in the down-going region ($\theta < \pi/2$), i.e. the region in which the SPEFIT was misreconstructing these down-going events to be up-going. So for these events SPEFIT on TWSRT pulses and MUEX4MPE on HIVESPLIT pulses give very different results.

A possible explanation for this is that the HIVESPLIT pulses are on the one hand more noise free than the TWSRT pulses and on the other hand, HIVESPLIT pulses recover signal pulses which were not part of the TWSRT pulses (see Fig. 7.15).



(a)



(b)

Figure 7.20: The distributions of the MuEX4MPE reconstructed zenith angle before (a) and after (b) the cuts on $\frac{v_{12}}{v_{13}}$ and $N_{dir,D}$

Distribution of the HLC hits in the z direction.

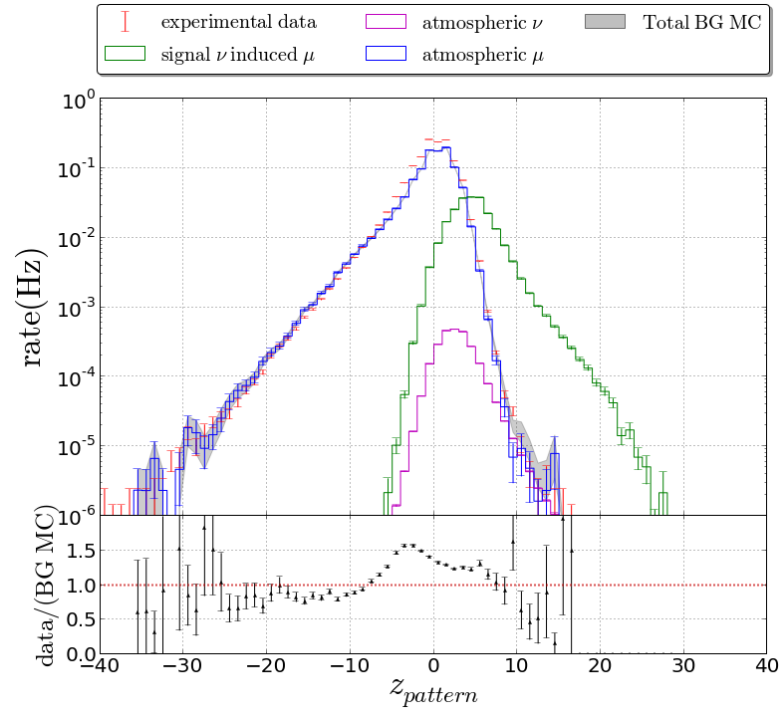
The last variable that is used to reduce the data-MC discrepancy is z_{pattern}

$$z_{\text{pattern}} = \sum_i \text{sign}((\Delta z)_i), \quad (7.17)$$

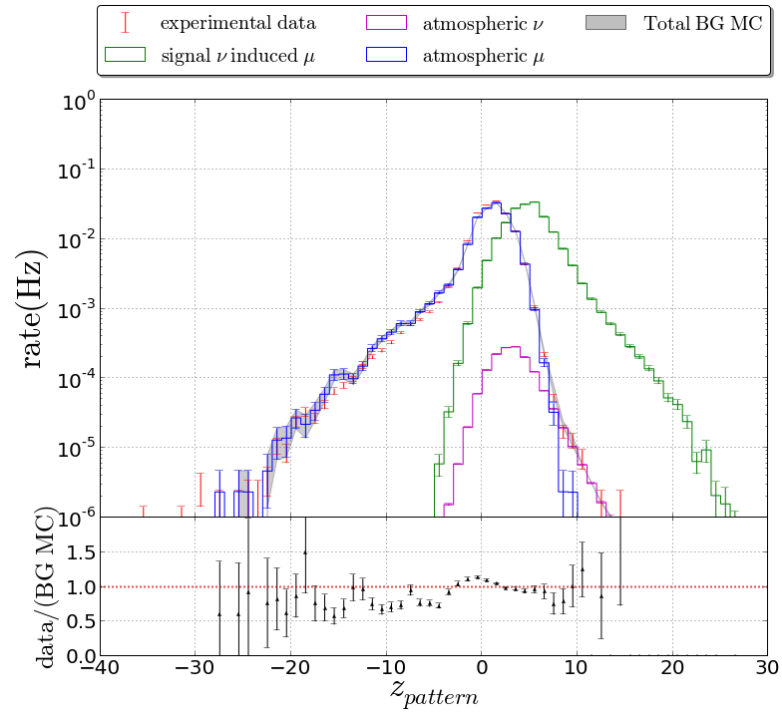
where $(\Delta z)_i$ is the difference between the z -coordinates of two temporally succeeding HLC hits. z_{pattern} will thus have positive values for up-going tracks and negative values for down-going tracks.

It can be seen from the transition from Fig. 7.21a to Fig. 7.21b that most of the data-MC discrepancy has already been removed by the previous cuts, but the data is not well described by the simulation for negative values of z_{pattern} , an effect that could again be caused by badly simulated noise.

By removing events with $z_{\text{pattern}} < 0$, the data-MC discrepancy is further decreased.



(a)



(b)

Figure 7.21: z_{pattern} distributions before (a) and after (b) the cuts on $\frac{v_{12}}{v_{13}}$, $N_{\text{dir},D}$ and $\theta_{\text{MuEx4MPE-HiveSplit}}$.

After these cuts (the LOWE LEVEL 4), which are summarized in Table 7.6, the data/MC ratio is reduced from a factor 1.345 (see e.g. Table 7.5) to a factor 1.002. The numbers of the signal and background data sets after this cuts, are given in Table 7.7. Note that the background has been reduced by a factor of about 20, while only 20% of the signal neutrinos in the low energy sample were removed in this step.

Table 7.6: Values of the pre-BDT cuts.

	part of the phase space that is removed
$\frac{v_{12}}{v_{13}}$	< 0.5
N_{dir}	< 3
θ_{MuEx}	< 2 radians
z_{pattern}	< 0

Table 7.7: Percentages of the amount of simulated signal (w.r.t. LEVEL 2) and rates of the simulated background and data events at different selection levels.

	# WIMP (%) $m_\chi = 50$ GeV	Simulated Background (Hz)			Data (Hz)
		ν_{atm}	μ_{atm}	total	
Level 2	100.0	27×10^{-3}	650	650	670
LOWE LEVEL 3	40.84	2.5×10^{-3}	1.03	1.03	1.39
LOWE LEVEL 4	31.2	1.5×10^{-3}	74.4×10^{-3}	75.9×10^{-3}	76.0×10^{-3}

7.7.4 Moving towards a neutrino pure sample: the BDT

Training the BDT

Now that the data-MC disagreement has been removed, a Boosted Decision Tree (Section 7.7.2) can be trained on the remaining signal and background samples. For the training of the BDT, half of the 50 GeV WIMP neutrino simulation ($\mathcal{O}(10^5)$ events) was used as signal sample, and half of the remaining events of the burnsample ($\mathcal{O}(10^5)$ events) were used as background sample.

The other half of these datasets are then used as testing samples, i.e. to test for overtraining, as well as in the next steps of the analysis.

In a first step, the BDT is trained on a large set of potentially good variables, which show good data-MC agreement. Some of the variables are highly (anti-)correlated and do thus not really add information to the BDT, but only increase the complexity. Whenever two variables are (anti-)correlated by (less) more than 60%, the one with the lowest importance in the BDT training process is removed. The importance of the variable in the BDT is reflected in a ranking of the variables which is returned after the BDT has

been trained. This ranking is derived by counting how often a variable is used to split decision tree nodes and by weighting each split occurrence by the separation gain-squared it has achieved and by the number of events in the node.

After the removal of correlated variables, a set of nine variables is left. An overview of these variables, together with their importance in the BDT, is given in Table 7.8. The distributions of these variables are shown in Figs. 7.22a till 7.22i, where the order of the figures corresponds to their importance in the BDT². The correlations between the variables are shown in Figs. 7.23a and 7.23b for the background and the signal respectively.

Note that the reconstructed zenith angles of high quality reconstructions as MUEX, the SPEFIT or the MPEFIT are not used in the BDT training, as these would remove the signal free control region that has been conserved up to this point and will be important to check the data-MC agreement after the cut on the BDT-score distribution.

Table 7.8: Overview of the variables used for the BDT training, with a brief explanation of each variable and its importance in the BDT training.

variable	brief explanation	BDT importance
$z_{\text{pattern,HLC}}$	Eq. (7.17) calculated with the HLC pulses	0.29
$r_{\text{first 5 hits}}$	r -coordinate of the center of gravity of the first five HIVESPLIT pulses	0.23
$\sigma(\text{MUEX4MPE})$	σ -parameter of the MUEX reconstruction on HIVESPLIT pulses (see Section 5.2.4)	0.15
z_{travel}	Eq. (7.2) calculated with the HIVESPLIT pulses	0.11
$z_{\text{first 5 hits}}$	z -coordinate of the center of gravity of the first five HIVESPLIT pulses	0.08
$N_{\text{HIVESPLIT EVENTS}}$	the amount of splits the HIVESPLIT algorithm proposes for an event.	0.08
smoothness	measure of how the charge in the HIVESPLIT hits is distributed along the MUEX reconstructed track	0.05
θ_{LINEFIT}	zenith of the LINEFIT reconstruction on HIVESPLIT pulses	0.02
v_{LINEFIT}	particle speed from the LINEFIT reconstruction on TWSRT hits (see Section 5.2.1)	0.01

The sum of the simulated atmospheric muons and neutrinos is shown as a gray band, of which the width represents the one standard deviation (statistical) uncertainty on that sum. At the bottom of each histogram the ratio of the experimental data over the total background simulation is shown, again with one standard deviation uncertainty.

²The same distributions are shown in Appendix A, where they are shown on a larger scale.

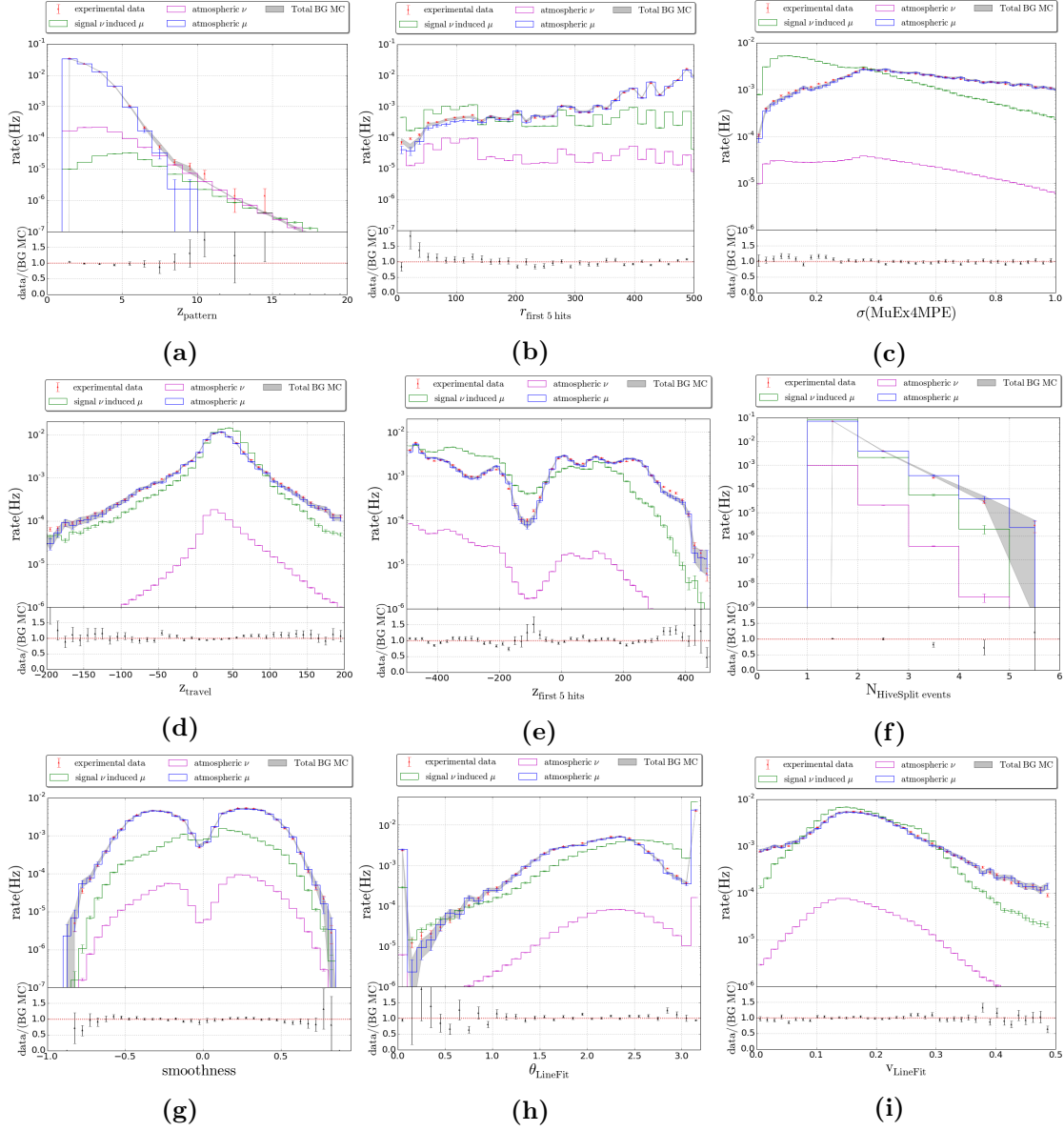
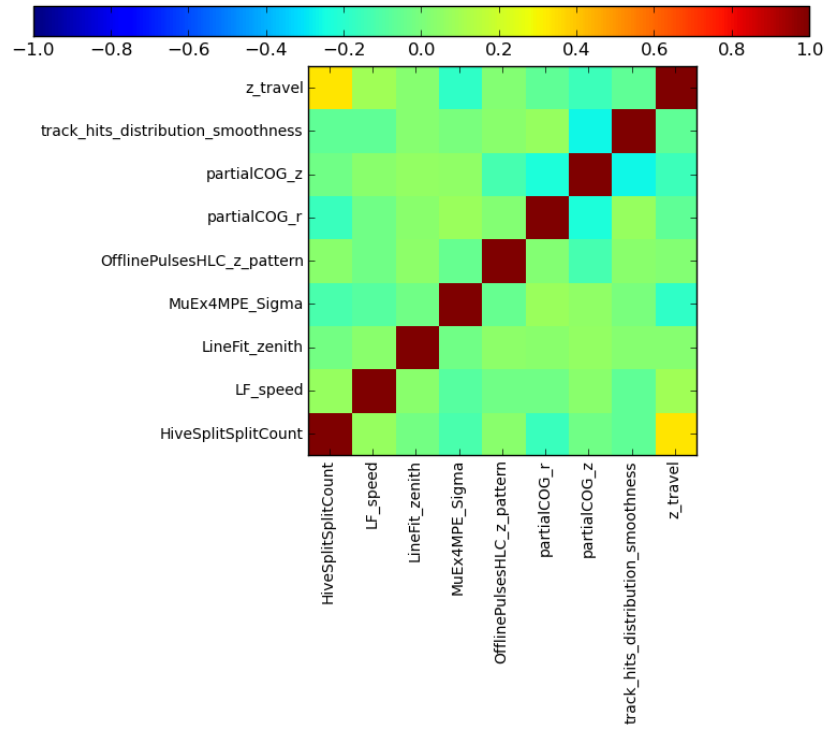
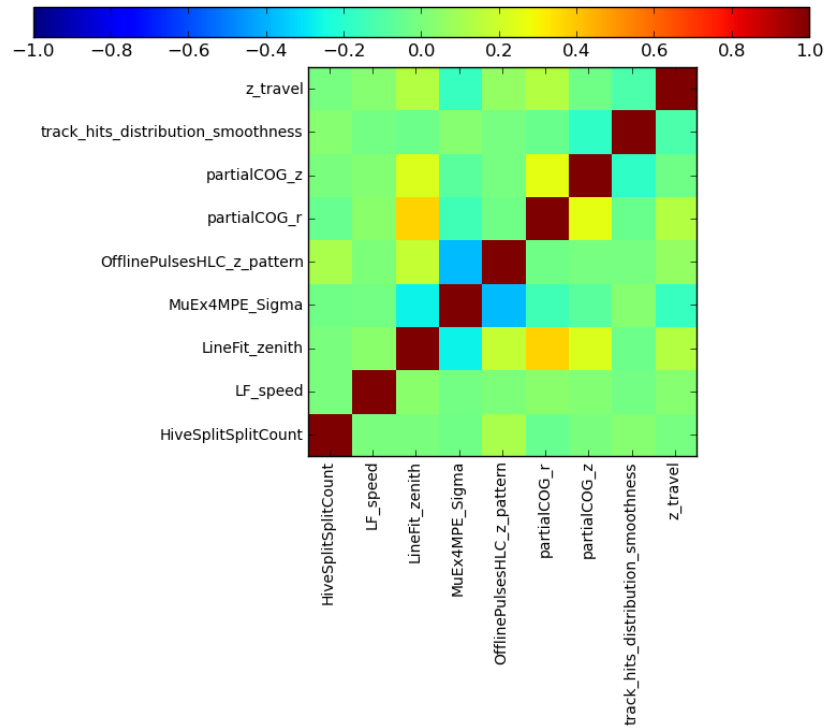


Figure 7.22: Distributions of the variables used for the BDT training after the BDT precuts, ordered by their importance in the BDT training. The plots show the rates in Hz of the experimental data (red error-bars), atmospheric μ (blue line), atmospheric ν (magenta line), the total atmospheric background (gray) and signal-induced muon neutrinos (green) as a function of the considered variable, as well as the ratio of the experimental data over the total background simulation. A brief explanation of the variables is given in Table 7.8.



(a)



(b)

Figure 7.23: Correlation matrices showing the correlation between the variables used in the BDT for background (a) and signal (b), after the BDT precuts.

Verifying the BDT-output

The output BDT score distributions and the integrated rates are shown respectively in Fig. 7.24a and Fig. 7.24b. An overtraining check using the Kolmogorov-Smirnov (KS) test was done, by comparing the BDT score output of the training sample to that of the testing sample, as shown in Fig. 7.25. From this figure, and from the KS p-values which are close to one, it can be concluded that there is negligible or no overtraining.

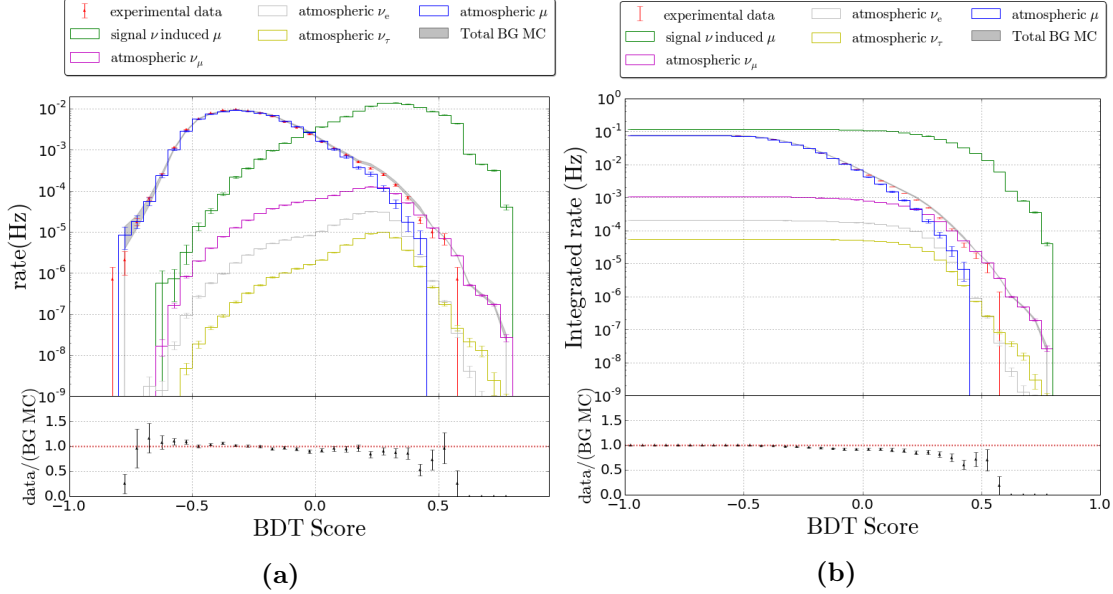


Figure 7.24: The BDT score distributions (a) and the integrated rate (b), where in the latter figure, the integral is calculated from the indicated BDT score to a BDT score value of +1. In these figures, the distribution of the atmospheric neutrinos is decomposed into the individuals distribution of each flavor ν_μ (magenta), ν_e (gray) and ν_τ (yellow). This is done to visualize the contribution of each neutrino flavor.

Figs. 7.24a and 7.24b show that there is a good data-MC agreement in the region where the BDT scores are negative and hence the background atmospheric muons dominate, but that the simulation is overestimating the experimental data in the positive part of the score distribution. As this is the interesting region, in which the events are more signal-like, steps have to be taken to understand and reduce this disagreement.

The disagreement gets larger when the data gets more neutrino-dominated (larger BDT scores), so the most likely explanation is that the neutrino simulation is still slightly off. The neutrino simulation for example does not take into account events in which the atmospheric neutrino is in coincidence with an atmospheric muon, as mentioned in Section 6.2.1. As explained in Section 5.1.2, about 10% of the events triggered by ICECUBE are coincident events. If events which contain both an atmospheric neutrino and an atmospheric muon are rejected by the event selection, this could lead to a disagreement

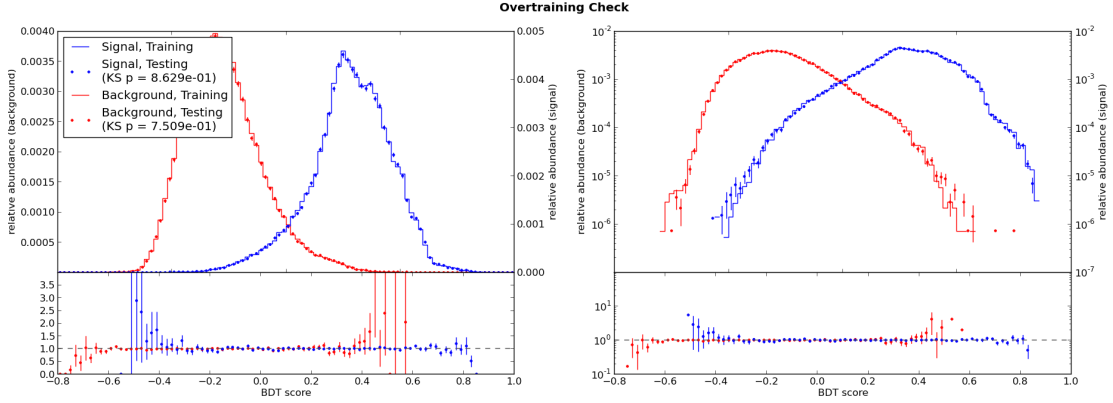


Figure 7.25: Comparison of the BDT score distributions of the training (solid line) and the testing (dots) samples for signal (blue) and background (red). The left plot shows the comparison in linear scale, and the right plot shows it in logarithmic scale. A KS test is performed on these samples, and the returned p-value is indicated in the legend.

between the data and neutrino simulation of at least 10%. This 10% factor is an overall factor, so as ICECUBE is detecting more low energy events, this factor is higher for event samples which are dominated by low energetic events, as is the case for the LOWE sample. As will be discussed later, the non-simulation of coincident atmospheric muons is probably the (main) reason for the disagreement between the data and the simulated atmospheric neutrinos.

Other factors could come from the predicted atmospheric neutrino flux used in the simulation, which has different values for different models (see Section 4.5), or wrongly simulated detector effects, such as e.g. the ice model, the hole ice or the DOM efficiency.

All of the above mentioned effects are taken into account in the systematic uncertainties, which are presented in more detail in Section 9.1, and for now the atmospheric neutrino simulation is rescaled such that it matches the experimental data.

Scaling the simulation sets

To overcome the disagreement between data and simulation of a factor of roughly 0.7 in the neutrino-pure region, the simulation sets are scaled to match the burnsample data. This scaling is done on the BDT-score distribution, as in this variable, there is a muon-dominated region (negative score values) and a neutrino dominated region (positive score values), such that both samples can be scaled independently and in the correct way. It is of course important that the background simulation is fit to the data in a signal-free (off-source) region, as otherwise the signal would be hidden by fitting the background to the data. therefore, only events with $\theta_{\text{MuEx4SPE}} < 2.3$ rad are used to do the fit, as in this way only 5% of signal could be contaminating the experimental data, as

indicated in Fig. 7.26a. The reason why θ_{MuEx4SPE} is used, is because MuEx4SPE is the reconstruction with the best resolution at this level of the analysis.

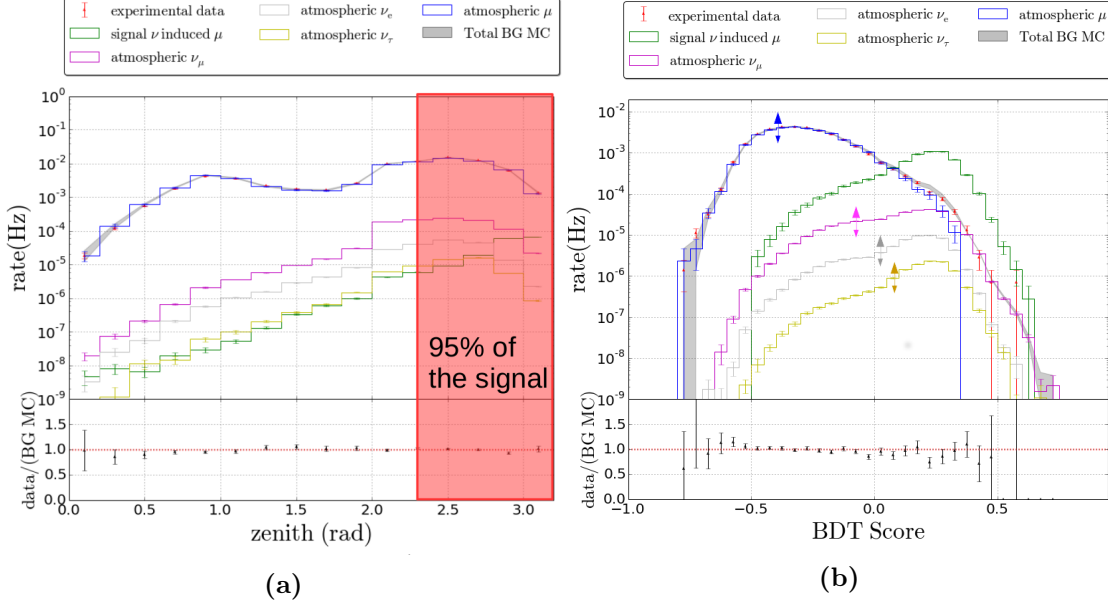


Figure 7.26: In panel (a), the distribution of the MuEx4SPE reconstructed zenith angle is shown. The red box on this plot indicates the region from which events are excluded to make the fit. The BDT score distributions of the remaining events ($\theta_{\text{MuEx4SPE}} < 2.3$ rad) are shown in panel (b). The arrows indicate schematically that all the different datasets are corrected with an individual scaling factor.

A scaling factor ω_i is then introduced for every component of the atmospheric background simulation i , i.e. atmospheric muons μ , atmospheric muon-neutrinos ν_μ , atmospheric electron-neutrinos ν_e and atmospheric tau-neutrinos ν_τ . Each set is rescaled such that the BDT score distribution of the sum of the simulation matches the BDT score distribution of the burnsample for all events with $\theta_{\text{MuEx4SPE}} < 2.3$ rad, as illustrated in Fig. 7.26b. The scaling factors are calculated by fitting the bin heights of the weighted sum of the background simulation samples to the bin heights of the experimental data $N_{\text{exp. data}}$

$$N_{\text{exp. data}}(\text{bin}_i) = \sum_{k \in \{\mu, \nu_\mu, \nu_e, \nu_\tau\}} N_k(\text{bin}_i) \cdot \omega_k \quad (7.18)$$

The algorithm then checks which combination of scaling parameters gives the best result for all considered bins.

The resulting scaling factors are summarized in Table 7.9. Note that the atmospheric muons are not rescaled ($\omega_\mu = 1.00$), which was expected, as there is no data-MC disagreements at low BDT score values; and that the largest effect of the rescaling is in the atmospheric muon neutrino sample ($\omega_{\nu_\mu} = 0.68$), which is the dominating sample at high BDT score values.

Table 7.9: Scaling factors of the simulation sets.

scaling factor	value
$\omega_{\nu\mu}$	0.68
$\omega_{\nu e}$	0.94
$\omega_{\nu\tau}$	0.99
ω_{μ}	1.00

When applying these factors on the whole dataset (all zenith angles), the BDT score distribution and integrated rate have a much better data-MC agreement over the whole range, as can be seen in Fig. 7.27.

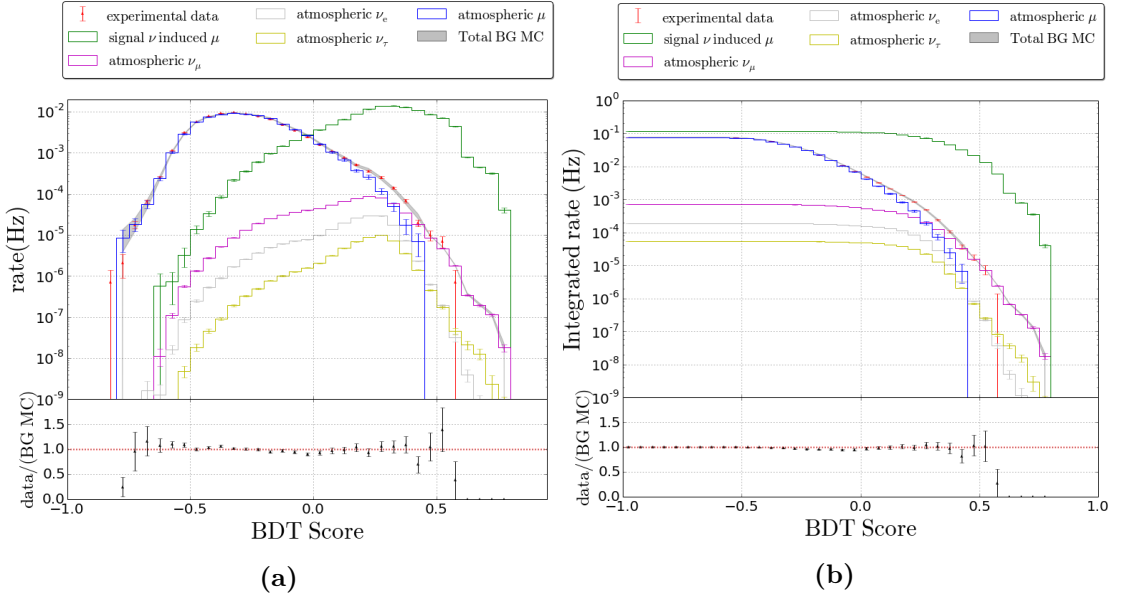


Figure 7.27: The BDT score distributions (a) and the integrated rate (b) after applying the scaling factors given in Table 7.9.

These scaling factors are applied in the remainder of this thesis, so for the calculation of the final numbers (presented below), of the sensitivity (Chapter 8) and the result (Chapter 9). Now that there is a good data-MC agreement, a cut on the BDT score value can be defined. The cut is chosen such that it optimizes the sensitivity of the analysis to the *volumetric flux* $\Gamma_{\nu\rightarrow\mu}$. $\Gamma_{\nu\rightarrow\mu}$ is a quantity which represents how many signal-like neutrinos μ_s would convert into ν muons during a certain time t_{live} , in a detector with an effective volume V_{eff}

$$\Gamma_{\nu\rightarrow\mu} = \frac{\mu_s}{t_{\text{live}} \times V_{\text{eff}}} \quad (7.19)$$

The best sensitivity of the analysis is achieved by minimizing this quantity in the

background-only scenario, as discussed in Section 8.3. This sensitivity is a balance between having a low background rate and a high signal efficiency. Both these measures go down when one starts cutting harder on the BDT-score distributions, and the optimal cut value is given by the cut which minimizes Eq. 7.19. The sensitivity is calculated with a likelihood ratio hypothesis test based on the values of the reconstructed zenith, using the Feldman-Cousins unified approach, as explained in detail in Chapter 8.

The best sensitivity is obtained when events with a BDT score distribution < 0.28 are removed.

7.7.5 Rates, efficiencies and angular resolution of the FINAL LOWE sample

LOWE FINAL LEVEL

An overview of the rates and efficiencies of events after the cut is given in Table 7.10. Note that roughly 2/3rd of the experimental data are atmospheric neutrinos and 1/3rd are atmospheric muons, hence the data is 68% neutrino pure. The distributions after the BDT cut of the variables that were used in the BDT training are shown in Fig. 7.28³.

After the BDT-cut, a very last selection is made based on the zenith angle. The zenith angle distribution which will be used to calculate the sensitivity of the present analysis, is the MPEFIT based on the HIVESPLIT pulses. Depending on the energy of the primary neutrino, either this MPEFIT or the MUEX4SPE reconstruction has the best angular resolution of the available reconstructions at the final level, as indicated in Fig. 7.30. Note that in the present analysis, the angular resolution is calculated as the median of the difference in zenith between the true incoming neutrino and the reconstructed muon track. Only the zenith angle is thus considered in the calculation of the angular resolution, as this is the only directional information which matters in this particular analysis. The angular resolution in Fig. 7.30 is calculated using all the simulated atmospheric neutrinos (of all flavors) which are left after the LOWE BDT cut.

The MPEFIT reconstruction has the advantage that the remaining simulated atmospheric muons are spread over the whole considered zenith range, as shown in Fig. 7.29b, while for the MUEX4SPE reconstruction many of the atmospheric muons are reconstructed in the signal region, as can be seen in Fig. 7.29a. As there are only very few simulated muons left (a total of 37 simulated events, as indicated in Table 7.11), the distribution of these muons suffers from very large statistical fluctuations. Therefore, the simulated atmospheric muon distribution is smoothened using Kernel Density Estimation (KDE) [168, 169], which is a method that smoothenes each observed data point over a local neighborhood of that data point, as presented in Section 8.1.

The results of the smoothening of the simulated atmospheric muon distribution and the total simulated background distribution is indicated by the dashed lines in Figs. 7.29a

³The same distributions are shown in Appendix A, where they are shown on a larger scale.

and 7.29b respectively for the MUEX4SPE reconstruction and the MPEFIT reconstruction. From these figures it is clear that even the smoothed histograms predict a background sample with a high atmospheric muon contribution in the signal region in the case of the MUEX4SPE reconstruction, while the atmospheric muons are spread out evenly when using the MPEFIT reconstruction. Therefore, the MPEFIT reconstruction is used for the statistical analysis of the final sample. Only events with a reconstructed zenith angle $\theta_{\text{MPEFIT_HIVESPLIT}} > 2.3$ rad (132 degrees) are considered for the final fit, such that the region which is considered for the statistical analysis is concentrated around the signal region and contains roughly 95% of the simulated WIMP-induced neutrino signal.

The efficiencies and rates at this LOWE FINAL LEVEL are presented in the last row of Table 7.10 and the absolute amount of events of simulated signal-induced neutrinos and of the different simulated backgrounds are summarized in Table 7.11. The effective volume V_{eff} of the detector (Section 6.2.1) and the angular resolution of the LOWE FINAL sample for different WIMP models are presented in Table 7.12. In this table, the median of the difference in zenith between the true incoming neutrino and the reconstructed muon track, as well as the median of the difference in zenith between the true zenith angle of the neutrino induced muon and the reconstructed muon track. At these low energies, the kinematic angle between the incoming muon neutrino and the induced muon is quite large, as discussed in Section 3.4. This is the reason for the difference between the values of $\text{median}(\theta_{\nu_{\text{true}}} - \theta_{\mu_{\text{reco}}})$ and $\text{median}(\theta_{\mu_{\text{true}}} - \theta_{\mu_{\text{reco}}})$ in Table 7.12.

For the calculation of these numbers, the scaling factors, presented in Table 7.9, are taken into account. The effective volume is rescaled by the same factor as the atmospheric muon neutrinos, $\omega_{\nu_{\mu}} = 0.68$, as this rescaling is most probably due to unsimulated coincident muon events.

Table 7.10: Percentages of the amount of simulated signal (w.r.t. LEVEL 2) and rates of the simulated background and data events at different selection levels.

	# WIMP (%) $m_{\chi} = 50$ GeV	Simulated Background (Hz)			Data (Hz)
		ν_{atm}	μ_{atm}	total	
LEVEL 2	100.0	27×10^{-3}	650	650	670
LOWE LEVEL 3	40.84	2.5×10^{-3}	1.03	1.03	1.39
LOWE BDT	17.3	0.26×10^{-3}	0.12×10^{-3}	0.38×10^{-3}	0.39×10^{-3}
LOWE FINAL	15.6	0.20×10^{-3}	0.08×10^{-3}	0.28×10^{-3}	0.28×10^{-3}

7.7. THE LOW ENERGY OPTIMIZATION

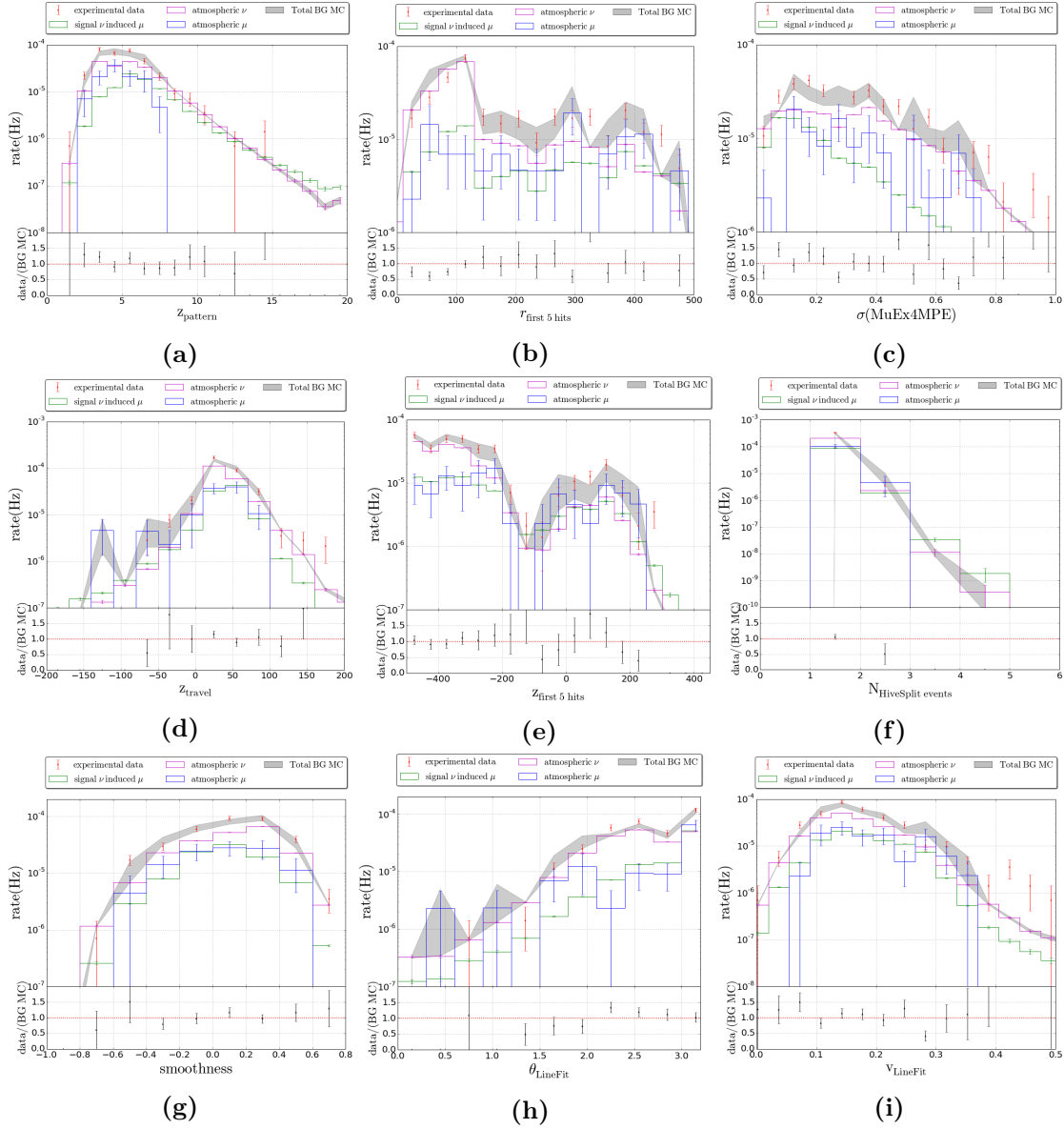


Figure 7.28: Distributions of the variables used for the BDT training, after applying a cut on the BDT score distribution of 0.28. A brief explanation of the variables is given in Table 7.8.

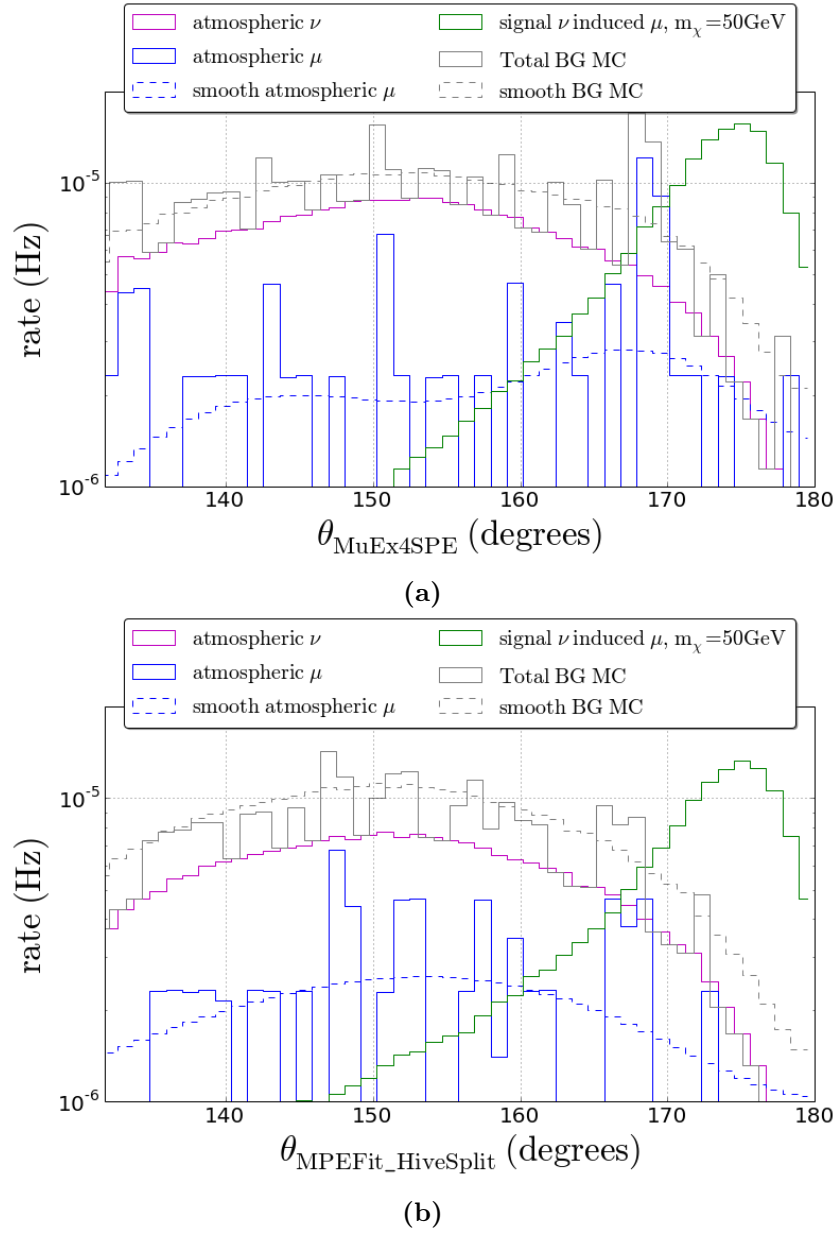


Figure 7.29: The MuEx4SPE (top) and MPEFIT (bottom) reconstructed zenith angle distribution for the signal and atmospheric background samples. The solid lines indicate the histograms, and the dashed lines represent the smoothed (KDE) atmospheric muon simulation (blue) and the smoothed total atmospheric background simulation (gray).

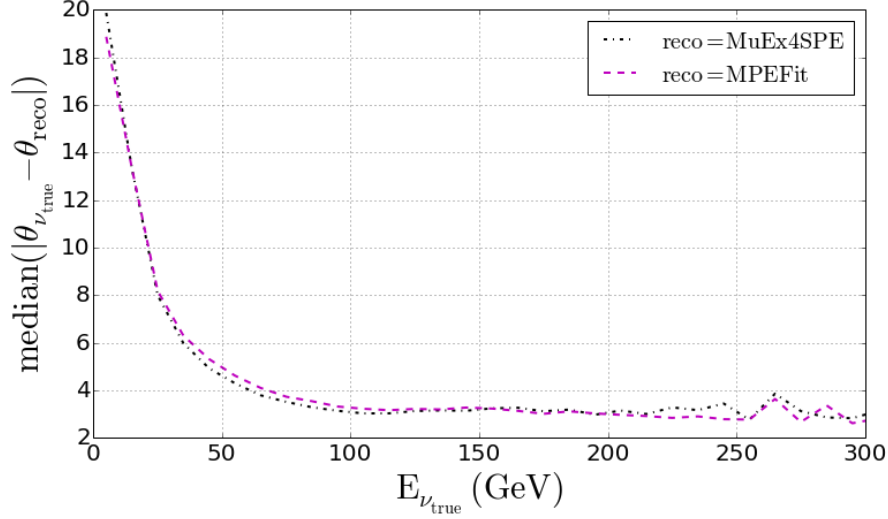


Figure 7.30: Angular resolution (considering only the zenith angle) of the MUEX4SPE reconstruction on the TWSRT pulses (dashed-dotted black line) and the MPEFIT reconstruction on the HIVESPLIT pulses (dashed magenta line). This is calculated using all the simulated atmospheric neutrinos (of all flavors) which are left after the LOWE BDT cut.

Table 7.11: Amount of events of signal-induced neutrinos and of the different simulated backgrounds in the FINAL LOWE sample.

	absolute number of events in the FINAL LOWE sample
WIMPs $m_\chi = 50$ GeV	122376
atmospheric μ	37
atmospheric $\bar{\nu}_\mu$ (NuGen)	126548
atmospheric $\bar{\nu}_e$ (NuGen)	36810
atmospheric $\bar{\nu}_\mu$ (GENIE)	269326
atmospheric $\bar{\nu}_e$ (GENIE)	50301
atmospheric $\bar{\nu}_\tau$ (GENIE)	21983

Table 7.12: Angular resolutions and effective volume of the detector for all considered WIMP models in the FINAL LOWE sample.

WIMP model		median($\theta_{\nu_{\text{true}}} - \theta_{\mu_{\text{reco}}}$)	median($\theta_{\mu_{\text{true}}} - \theta_{\mu_{\text{reco}}}$)	Effective Volume (km ³)
$m_\chi = 10$ GeV	$\chi\chi \rightarrow \tau^+\tau^-$	20.8°	15.8°	4.5×10^{-4}
$m_\chi = 20$ GeV	$\chi\chi \rightarrow \tau^+\tau^-$	16.2°	12.5°	1.5×10^{-3}
$m_\chi = 35$ GeV	$\chi\chi \rightarrow \tau^+\tau^-$	9.5°	7.1°	3.5×10^{-3}
	$\chi\chi \rightarrow b\bar{b}$	22.1°	15.8°	0.7×10^{-3}
$m_\chi = 50$ GeV	$\chi\chi \rightarrow \tau^+\tau^-$	6.7°	4.8°	5.8×10^{-3}
	$\chi\chi \rightarrow b\bar{b}$	17.0°	11.8°	1.5×10^{-3}
$m_\chi = 100$ GeV	$\chi\chi \rightarrow W^+W^-$	3.3°	1.9°	2.1×10^{-2}
	$\chi\chi \rightarrow b\bar{b}$	6.7°	4.5°	6.6×10^{-3}
$m_\chi = 250$ GeV	$\chi\chi \rightarrow W^+W^-$	3.1°	1.7°	3.3×10^{-2}
	$\chi\chi \rightarrow b\bar{b}$	4.1°	2.3°	2.1×10^{-2}
$m_\chi = 500$ GeV	$\chi\chi \rightarrow W^+W^-$	3.3°	1.8°	2.6×10^{-2}
	$\chi\chi \rightarrow b\bar{b}$	3.8°	2.0°	2.8×10^{-2}
$m_\chi = 1$ TeV	$\chi\chi \rightarrow W^+W^-$	3.3°	1.8°	1.8×10^{-2}
	$\chi\chi \rightarrow b\bar{b}$	3.8°	1.9°	3.1×10^{-2}
$m_\chi = 3$ TeV	$\chi\chi \rightarrow W^+W^-$	3.4°	1.9°	1.4×10^{-2}
	$\chi\chi \rightarrow b\bar{b}$	3.9°	1.9°	2.4×10^{-2}
$m_\chi = 5$ TeV	$\chi\chi \rightarrow W^+W^-$	3.5°	1.9°	1.5×10^{-2}
	$\chi\chi \rightarrow b\bar{b}$	3.9°	1.9°	2.2×10^{-2}

7.8 The high energy optimization

An optimization for the more energetic WIMPs was done in parallel to the low energy optimization by other analyzers. This analysis starts with the HIGHE LEVEL 3 sample (see Table 7.5), which contains the events with a reconstructed neutrino energy greater than 100 GeV, as explained in Section 7.6 of this chapter. The HIGHE part of the analysis is optimized on a WIMP model in which the WIMPs have a mass of 1 TeV and annihilate 100% into W^+W^- (the hard channel).

A first optimization was done by Isabelle Anseau [163] and this was further optimized by Jan Lünemann [164], both in close collaboration with the author. The latter optimization is summarized below, and the sensitivities and results based on these final event samples will be combined with the sensitivities and results of the low energy analysis, as explained in Chapter 8 and Chapter 9.

Note that the HIGHE part of the analysis is less sensitive to noise and systematic detector effects, as the events in the TeV energy range are much brighter. It also benefits from the fact that the ICECUBE detector is better adapted to events in this energy range.

Contrary to the LOWE part, the atmospheric neutrino background in this energy range can be estimated completely by NuGen simulations (same NuGen datasets as in the LOWE part), and neutrino oscillations in Earth are negligible. The atmospheric muon background is calculated with the same simulated datasets as were used in the LOWE analysis, and the burnsample data which is used for verification of the simulation is coming from the same 10% of experimental data as in the LOWE analysis.

7.8.1 Selecting up-going tracks

The first step of this part, the HIGHE LEVEL 4, of the selection consists of selecting up-going, track like, events. This selection is based on a common filter in ICECUBE, called the *Offline Muon Filter*, which is described in detail in [170]. The Offline Muon Filter is used in many ICECUBE analyses, as it is optimized to search for neutrino-induced muon tracks from the full sky, with energies in the TeV to PeV range.

Only events which pass the Offline Muon Filter and are reconstructed as up-going are kept, since down-going events are of no interest in this analysis. The rates of the different background components, as well as the signal efficiency after this selection level, are summarized in Table 7.13.

7.8.2 Pull-Validation

To get to neutrino level, the *Pull-Validation* method [164, 171] is used. In this method several BDTs (200 in the case of the present analysis) are trained on small subsets that are randomly resampled from the complete dataset. The variation of the BDT output between the different training sets can be interpreted as a probability density function

(PDF) for each event. This PDF can be used to calculate a weight w_{PV} (see Eq. 7.20) that is applied to each event instead of making a binary cut decision. Prior to the BDT training, additional linear cuts are made to reduce the data-MC disagreement, similar to the low energy optimization.

Using the Pull-Validation method, the BDT score distributions, shown in Fig. 7.31a for a single BDT, are smoothed and broadened, as can be seen in Fig. 7.31b. Not only the BDT score distributions are smoothed, but also the variable distributions. In particular the reconstructed zenith distributions which will be used to calculate the sensitivity (Chapter 8) are smooth, as events that would be removed when using a single BDT could now be kept, albeit with a smaller weight.

In analogy to the LOWE analysis, the cut on the BDT score is chosen such that the sensitivity of the analysis is optimal for the benchmark model, namely 1 TeV WIMPs annihilating 100% into W^+W^- . The value for this cut is 0.16. After this cut, all the events are reweighted by a Pull-Validation weight w_{PV} , which reflects how many of the 200 BDT scores of the event are above the cut threshold

$$w_{PV} = \frac{\# \text{ scores above cut threshold}}{200}. \quad (7.20)$$

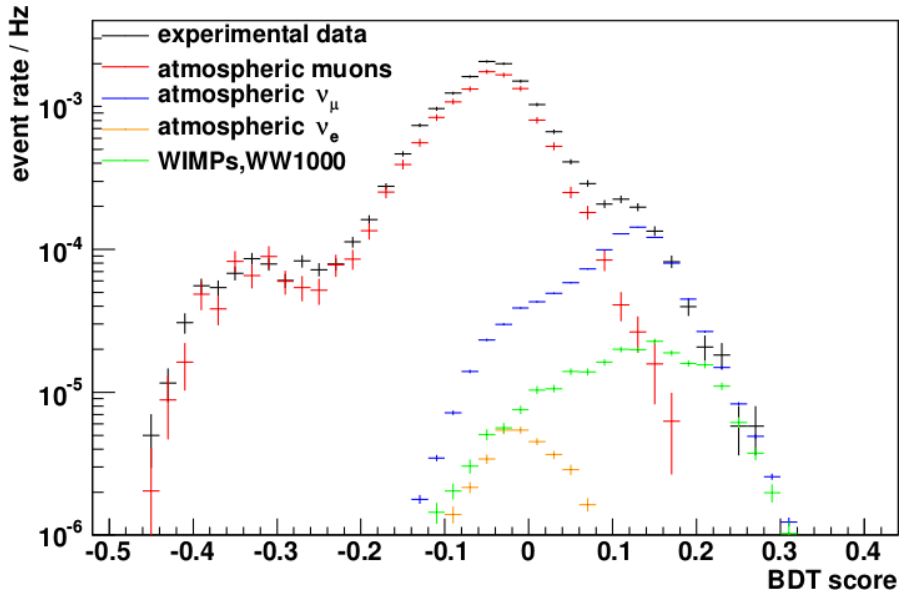
The rates of the background and efficiencies of the signal after applying this weight to the events, are summarized in Table 7.13. Note that about 90% of the events in the FINAL HIGHE sample are atmospheric neutrinos, so this sample has a very high neutrino purity. The absolute amount of events of simulated signal-induced neutrinos and of the different simulated backgrounds in the FINAL HIGHE sample are summarized in Table 7.14. These numbers represent all the event with $w_{PV} > 0$.

Table 7.13: Percentages of the amount of simulated signal (w.r.t. LEVEL 2) and rates of the simulated background and data events at different selection levels.

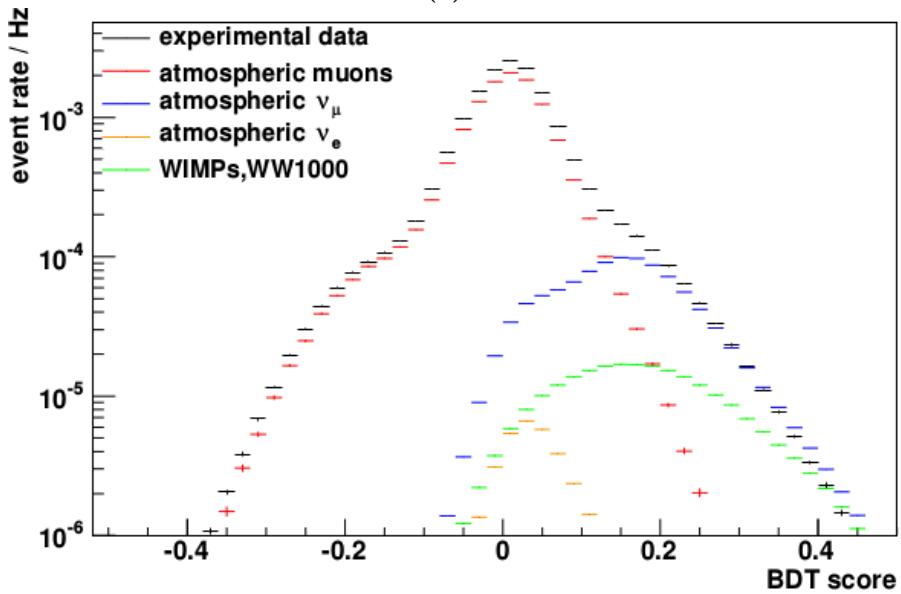
	# WIMP (%)	Simulated Background (Hz)			Data (Hz)
	$m_\chi = 1 \text{ TeV}$	ν_{atm}	μ_{atm}	total	
LEVEL 2	100.0	27×10^{-3}	650	650	670
HIGHE LEVEL 3	45.2	2.5×10^{-3}	1.03	1.03	1.39
HIGHE LEVEL 4	32.1	1.05×10^{-3}	12.0×10^{-3}	13.1×10^{-3}	15.2×10^{-3}
Pull-Validation cut	17.0	0.46×10^{-3}	0.06×10^{-3}	0.52×10^{-3}	0.56×10^{-3}

The effective volume V_{eff} of the detector and the angular resolution of the HIGHE FINAL sample for different WIMP models are presented in Table 7.15. As there are (almost) no WIMP-induced events from WIMPs with masses below 100 GeV in the FINAL HIGHE sample, the effective volumes for these WIMP models are negligible and thus not presented here. Most, or even all, of the events from WIMPs with these low masses, will be in the LOWE sample, making the two analyses very complementary.

In Fig. 7.32, the effective volumes V_{eff} of the final LowE and final HighE samples are shown for the hard channel and soft channel.



(a)



(b)

Figure 7.31: Panel (a) shows the score distribution for a single BDT, trained on a complete dataset available for training. In the panel (b), the sum of 200 BDT score distributions, each trained on 10% of the training data, is shown. Figures taken from [171].

Table 7.14: Amount of events of signal-induced neutrinos and of the different simulated backgrounds in the FINAL HIGHE sample.

	absolute number of events in the FINAL HIGHE sample
WIMPs $m_\chi = 1$ TeV	135342
atmospheric μ	487
atmospheric $\bar{\nu}_\mu$ (NuGen)	273183
atmospheric $\bar{\nu}_e$ (NuGen)	36064

Table 7.15: Angular resolutions and effective volume of the detector for all considered WIMP models in the FINAL HIGHE sample.

WIMP model		median($\theta_{\nu_{\text{true}}} - \theta_{\mu_{\text{reco}}}$)	median($\theta_{\mu_{\text{true}}} - \theta_{\mu_{\text{reco}}}$)	Effective Volume (km ³)
$m_\chi = 100$ GeV	$\chi\chi \rightarrow W^+W^-$	4.67°	3.91°	4.2×10^{-4}
	$\chi\chi \rightarrow b\bar{b}$	4.53°	4.83°	2.4×10^{-5}
$m_\chi = 250$ GeV	$\chi\chi \rightarrow W^+W^-$	2.51°	2.25°	3.7×10^{-2}
	$\chi\chi \rightarrow b\bar{b}$	3.03°	2.75°	1.5×10^{-3}
$m_\chi = 500$ GeV	$\chi\chi \rightarrow W^+W^-$	2.11°	1.85°	9.7×10^{-2}
	$\chi\chi \rightarrow b\bar{b}$	2.39°	2.11°	1.3×10^{-2}
$m_\chi = 1$ TeV	$\chi\chi \rightarrow W^+W^-$	1.63°	1.45°	1.7×10^{-1}
	$\chi\chi \rightarrow b\bar{b}$	1.97°	1.73°	4.1×10^{-2}
$m_\chi = 3$ TeV	$\chi\chi \rightarrow W^+W^-$	1.17°	1.09°	3.1×10^{-1}
	$\chi\chi \rightarrow b\bar{b}$	1.57°	1.37°	1.1×10^{-1}
$m_\chi = 5$ TeV	$\chi\chi \rightarrow W^+W^-$	1.09°	1.03°	5.0×10^{-1}
	$\chi\chi \rightarrow b\bar{b}$	1.43°	1.25°	1.5×10^{-1}
$m_\chi = 10$ TeV	$\chi\chi \rightarrow W^+W^-$	0.89°	0.87°	5.0×10^{-1}
	$\chi\chi \rightarrow b\bar{b}$	1.25°	1.13°	1.5×10^{-1}

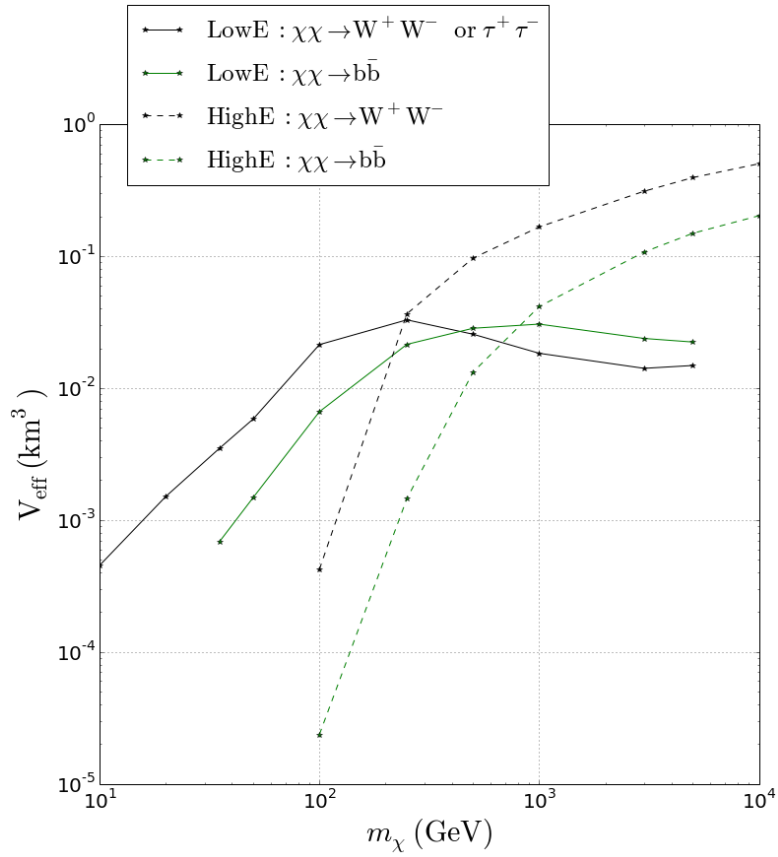


Figure 7.32: The effective volumes V_{eff} of the final LowE (solid) and final HighE (dashed) samples for the hard channel (black) and soft channel (green).

Summary

In this chapter an overview was presented which shows how the data is reduced from a few kHz ($\mathcal{O}(10^{11})$ /year) to less than a mHz ($\mathcal{O}(10^4)$ /year). A schematic overview of this event selection is shown in Fig. 7.1.

The first step in the process consisted of selecting which online filters are of interest for this analysis. Next a noise filter was used to remove noise clusters which mainly show up in the DEEPCORE event stream. The data rate was further reduced to roughly 3 Hz by applying linear cuts on the direction and starting point of the event. After this step, the sample was split in two statistically independent data sets, based on the reconstructed energy of the event. The data rate of each of the samples was consequently further reduced in two independent event selections, a low energy event selection and a high energy event selection, optimized for signal neutrinos from 50 GeV WIMPs and 1 TeV WIMPs respectively.

Both analyses made use of Boosted Decision Trees (BDT), which is a machine learning technique that is designed to optimally separate signal from background by assigning a score between -1 (background-like) and +1 (signal-like) to each event. Before training the BDT, one has to be sure that the simulation is representing the experimental data in a correct way. For this reason additional linear cuts were made prior to the BDT training in order to get good agreement between data and simulation. While the low energy optimization only used one single BDT, the high energy part used the Pull-Validation method, in which 200 BDTs are trained and applied to each event. The cut on the BDT score distributions were selected such that the best sensitivities for the WIMP signals were achieved. The final numbers are summarized in Table 7.16.

Table 7.16: Percentages of the amount of simulated signal (w.r.t. LEVEL 2) and rates of the simulated background and data events at LEVEL 2 and at the final level.

	# WIMP (%)		Simulated Background (Hz)			Data (Hz)
	$m_\chi = 50 \text{ GeV}$	$m_\chi = 1 \text{ TeV}$	ν_{atm}	μ_{atm}	total	
LEVEL 2	100.0	100.0	27×10^{-3}	650	650	670
final LOWE sample	15.6	-	0.20×10^{-3}	0.08×10^{-3}	0.28×10^{-3}	0.28×10^{-3}
final HIGH E sample	-	17.0	0.46×10^{-3}	0.06×10^{-3}	0.52×10^{-3}	0.56×10^{-3}

These final event samples will be used for a directional search in which the observed number of events from the direction of the center of the Earth is compared to the background-only hypothesis, in order to estimate the sensitivity of ICECUBE to Earth WIMPs in the range $10 \text{ GeV} < m_\chi < 10 \text{ TeV}$. This will be explained in the following chapter.

*It is a capital mistake to theorize before one has data.
Insensibly one begins to twist facts to suit theories,
instead of theories to suit facts.*

Sir Arthur Conan Doyle

8

Estimation of the Sensitivities

In the previous chapter the data was reduced by roughly seven orders of magnitude, leading to two independent final event samples, the LOWE and the HIGHE samples, each containing roughly $\mathcal{O}(10^4)$ events/year, dominated by atmospheric neutrinos. These samples can now be analyzed to look for a contribution of muons from Earth WIMP-induced neutrinos (at most $\mathcal{O}(10^3)/\text{km}^2/\text{year}$) on top of the atmospheric background. Recall that the LOWE sample was optimized on neutrinos induced by 50 GeV WIMPs, annihilating purely into $\tau^+\tau^-$, and that in this sample the background consists of low energetic atmospheric neutrinos ($\sim 70\%$) and muons ($\sim 30\%$). The HIGHE sample was optimized on WIMPs with a mass of 1 TeV, which annihilate 100% into W^+W^- , and in this sample the background consists of higher energy atmospheric neutrinos ($\sim 90\%$) and some atmospheric muons ($\sim 10\%$).

The analysis method presented below, uses the reconstructed zenith angle distributions (θ) of the signal and background as Probability Density Functions (PDFs, Section 8.1) to test hypotheses with μ_s signal events in the final dataset. This method is explained in Section 8.2 and has already been used successfully in several ICECUBE analyses [172, 66, 55].

In Section 8.3, the sensitivity of the analysis for one year of data is calculated by testing the background-only hypothesis, based on background simulations.

In the next chapter, the full sample of the IC86-I data will then be analyzed, to see which signal hypothesis fits the data best.

8.1 Probability densities

The reconstructed zenith angle distributions are used as Probability Density Functions (PDFs) in this analysis. For the signal, the zenith angle distribution at each WIMP mass is calculated with WimpSim and for the background the zenith angle distributions of the remaining simulated atmospheric muons and neutrinos are used¹. These distributions are shown in Fig. 8.1a and Fig. 8.1b for the low and high energy sample respectively. The reconstructions that are used here are MPEFIT² for the LOWE sample and SPLINEMPE³ for the HIGHE sample, as these yield the best angular resolution and provide an evenly distributed atmospheric muon background at this level of the analysis (see the discussion in Section 7.7.5).

While the signal and background PDFs of the HIGHE sample are smooth, this is not the case for the PDFs in the LOWE sample, at least not for the background PDF of that sample. The background PDF is a combination of simulated atmospheric muons and atmospheric neutrinos, of which the individual PDFs for the LOWE sample are shown in Fig. 8.2. In the final LOWE sample there are only 37 simulated atmospheric muon (CORSIKA) events left.

The high energy sample does not suffer from the problem of low statistics, as it used the Pull-Validation method, which artificially increases the statistics (Section 7.8.2).

Remind that the neutrino purities, \mathcal{P} , of the final LOWE and HIGHE samples are respectively 71% and 88% (Table 7.16), where \mathcal{P} is defined as

$$\mathcal{P} = \frac{\text{atmospheric } \nu \text{ rate}}{\text{atmospheric } \mu \text{ rate} + \text{atmospheric } \nu \text{ rate}}, \quad (8.1)$$

and is estimated from simulations. The high purity of the samples is the reason for the low number of simulated atmospheric muons left in the final samples.

In the LOWE analysis, special measures are taken to deal with the low number of simulated atmospheric muon events. Large statistical fluctuations in the PDF might have consequences on the shape analysis, therefore the reconstructed zenith angle distribution of the simulated atmospheric muons, in the LOWE sample, is smoothed using Kernel Density Estimation (KDE) [168, 169], which is a method that smoothens each observed data point over a local neighborhood of that data point, as described hereafter.

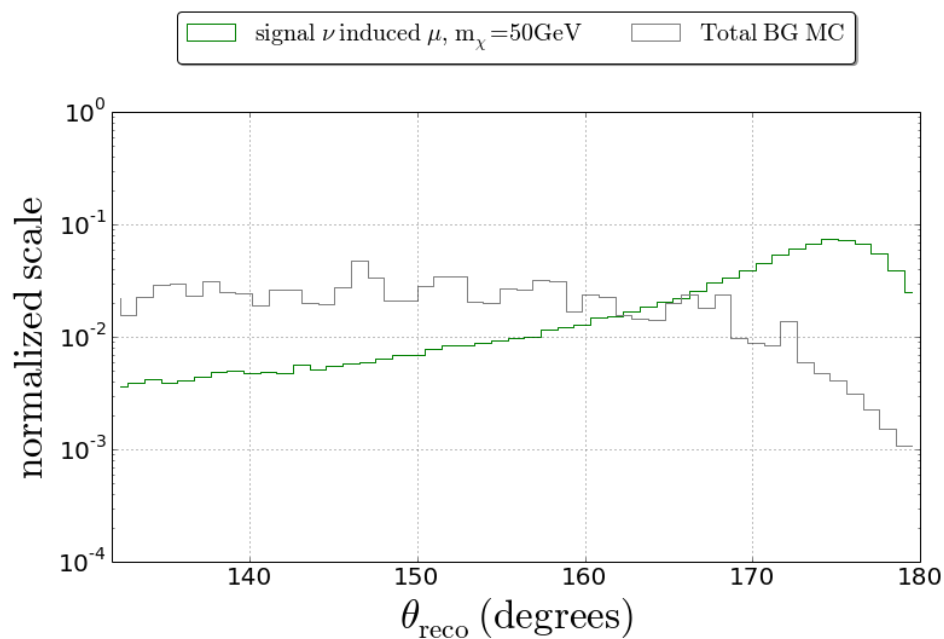
Assume a set of n measurements $\{X_1, X_2, \dots, X_n\}$ of a random variable with density f . The kernel density estimate of f at a point x is given by

$$\hat{f}_h(x) = \frac{1}{nh} \sum_{i=1}^n K\left(\frac{x - X_i}{h}\right), \quad (8.2)$$

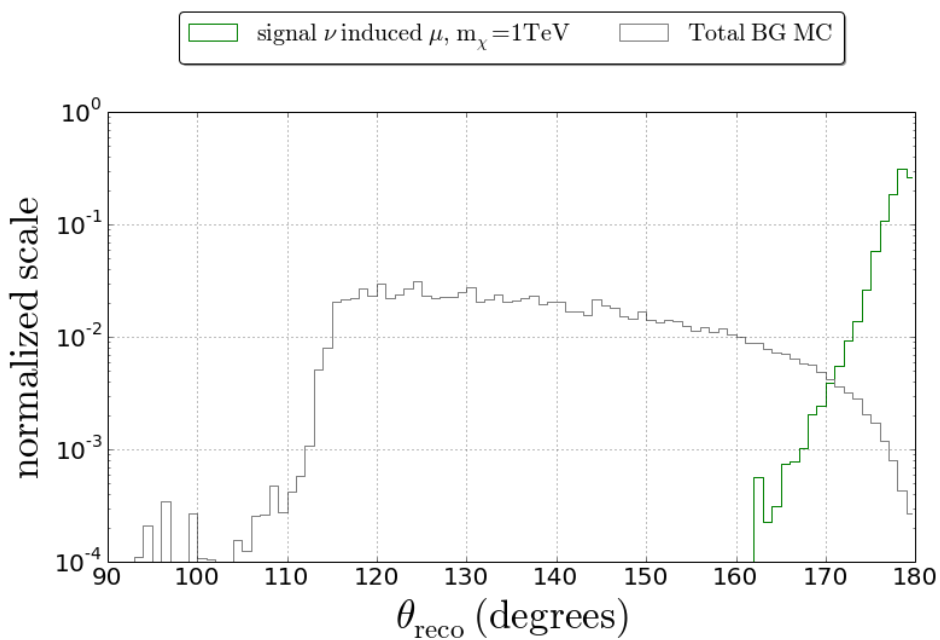
¹Both the signal and background simulations were described in detail in Chapter 6.

²This reconstruction was described in Section 5.2.2.

³The SPLINEMPE reconstruction, is just like the SPEFIT or MPEFIT reconstruction, a likelihood fit, which uses tabulated and parametrized light yields for the computation of the most probable track.



(a)



(b)

Figure 8.1: The normalized signal (green) and background (gray) distributions of the reconstructed zenith for the LOWE sample (top) and the HIGHE sample (bottom).

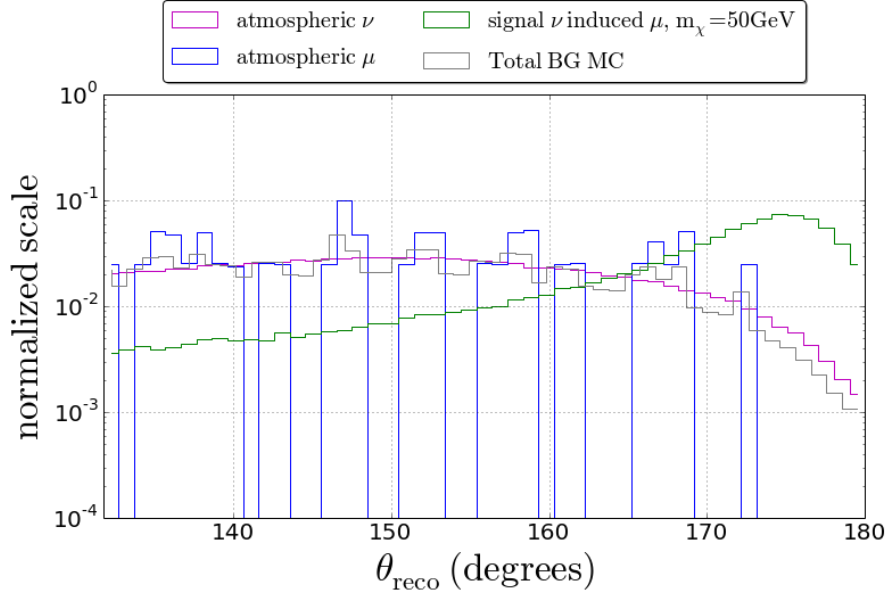


Figure 8.2: The normalized distributions of the reconstructed zenith angle for the signal (green), atmospheric muon background (blue), atmospheric neutrino background (magenta) and total background (gray) in the LOWE sample.

where K is the kernel, satisfying $\int K(x)dx = 1$, and h is the smoothing parameter, also referred to as the *bandwidth*. In this analysis, the most popular choice for K is considered [173], namely the Gaussian kernel around zero, with standard deviation $\sigma = 1$

$$K(x) = \frac{1}{\sqrt{2\pi}} \exp\left(-\frac{x^2}{2}\right). \quad (8.3)$$

Silverman showed that in the case of this Gaussian kernel, the optimal choice for the bandwidth h is given by [173]

$$h = \frac{1.06 \cdot \sigma(X)}{n^{1/5}}, \quad (8.4)$$

where n is the number of measurements $\{X_i\}$ and $\sigma(X)$ is the standard deviation of the sample. Contrary to histograms, in which a distribution of parameter f is described by bins with a certain height that depends on the amount of measurements in that bin (left panel of Fig. 8.3), this method smears out the measurements and describes the distribution of f by the sum of these smeared out points (right panel of Fig. 8.3).

The background PDF $f_{BG}(\theta)$ of the low energy sample is smoothed using the described KDE method. In order to save computing time, only the atmospheric muon distribution is smoothed, and this smooth muon PDF $f_\mu(\theta)$ is then added to the already smooth atmospheric neutrino background PDF $f_\nu(\theta)$, by weighting each sample

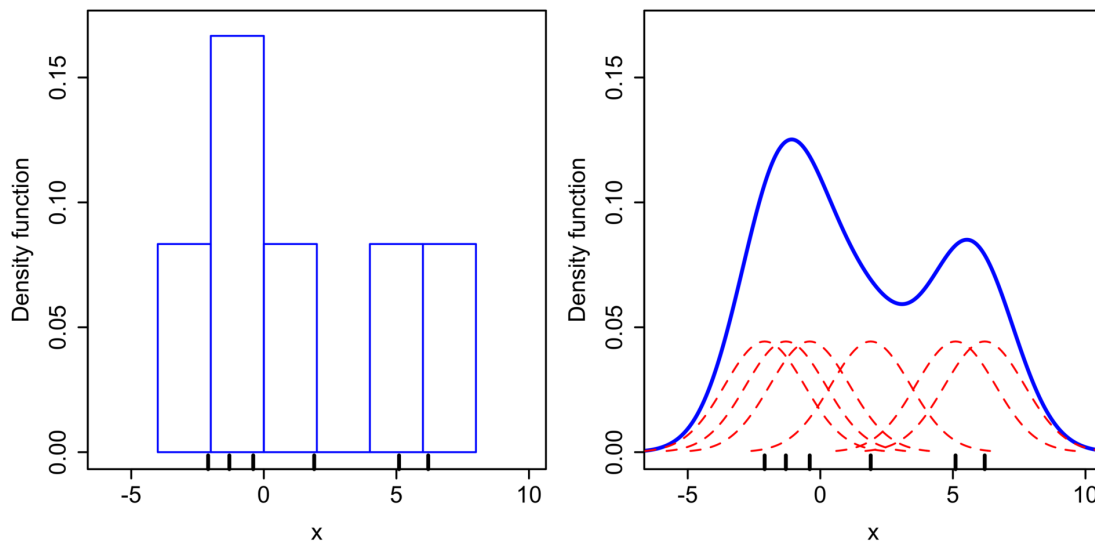


Figure 8.3: Comparison of the histogram (left) and kernel density estimate (right) constructed from the same dataset. The six individual kernels are represented by the red dashed curves and their sum, i.e. the kernel density estimate, by the blue curve. The data points are indicated by vertical bars on the horizontal axis. Figure from https://en.wikipedia.org/wiki/Kernel_density_estimation.

according to their relative contribution n_μ and n_ν respectively

$$f_{BG}(\theta) = \frac{n_\mu(\theta) \cdot f_\mu + n_\nu \cdot f_\nu(\theta)}{n_\mu + n_\nu}. \quad (8.5)$$

The resulting, smooth background PDF $f_{BG}(\theta)$, shown in Fig. 8.4, will be used in the shape analysis.

Events which are reconstructed with high zenith angle values (vertically up-going events) have to be treated properly, as the individual kernels might continue outside the physical region ($\theta > 180^\circ$), a phenomenon referred to as overflow. As events are no longer represented by points, but rather by a kernel with a certain width, it can happen that part of the kernel is outside the physically allowed space, so greater than 180° in case of the reconstructed zenith angle. Whenever this happens, the overflow part is reflected and summed with corresponding values of the physically allowed space. For the reconstructed zenith angle, this means that values $y > 180^\circ$ are reflected as follows

$$y = 180^\circ + x \rightarrow y' = 180^\circ - x, \quad (8.6)$$

for $x \in [0, 180^\circ]$. This method is just one of the possible solutions to the problem, other solutions are e.g. the use of non-symmetrical kernels or the re-norming of kernels [173, 174], but these were not considered in this work.

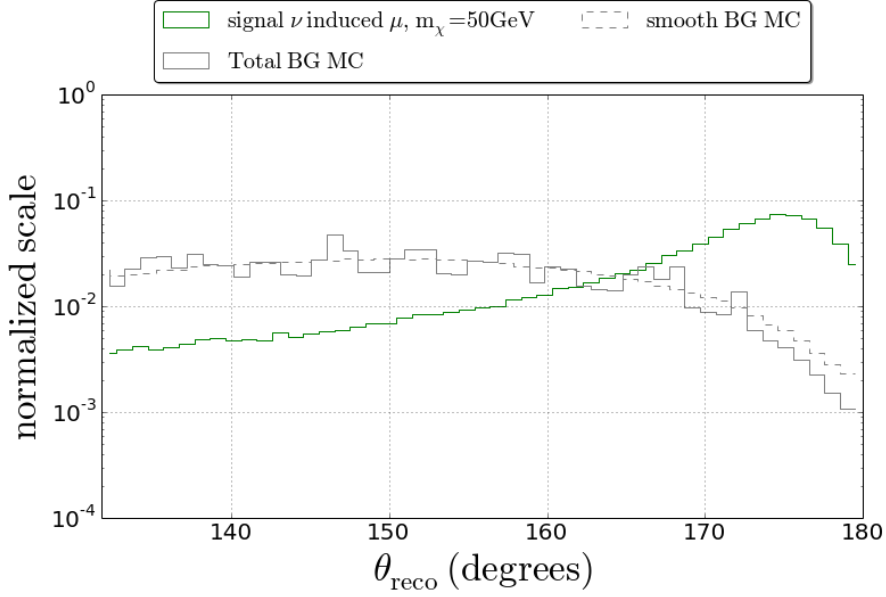


Figure 8.4: The normalized distributions of the reconstructed zenith angle for the signal (green) and total background (gray), as well as the kernel density estimate of the background (gray-dashed) in the low energy sample.

8.2 Shape analysis

In the present analysis, the sensitivity of the detector is estimated as the median upper-limit at 90% confidence level (CL) on the amount of signal events, $\bar{\mu}_s^{90\%}$, in a background only scenario (i.e. absence of signal, indicated by the bar ($\bar{\quad}$) above the quantity in the remainder of this chapter), divided by the effective volume, V_{eff} , and the livetime, t_{live}

$$\bar{\Gamma}_{\nu \rightarrow \mu}^{90\%} = \frac{\bar{\mu}_s^{90\%}}{t_{\text{live}} \times V_{\text{eff}}}. \quad (8.7)$$

$\Gamma_{\nu \rightarrow \mu}$ is thus a quantity which represents how many signal-induced neutrinos would convert into muons, μ_s , during a certain time t_{live} , in a detector with an effective volume V_{eff} . This quantity is referred to as the volumetric flux.

The lower the median upper-limit on the amount of signal events, $\bar{\mu}_s^{90\%}$, and the higher the effective volume, V_{eff} , the better the sensitivity of the analysis on the volumetric flux. Therefore, for each cut on the BDT score (see Chapter 7), $\bar{\mu}_s^{90\%}$ and V_{eff} are calculated for the remaining sample, and the cut value for which the combination of these quantities minimizes $\bar{\Gamma}_{\nu \rightarrow \mu}^{90\%}$ is selected as final cut. The effective volume of each sample is calculated as explained in detail in Section 6.2.1 and the $\bar{\mu}_s^{90\%}$ is estimated with 10000 pseudo-experiments, as described hereafter.

To derive the amount of signal events μ_s^α compatible with the observed data sample at a certain confidence level α , the PDFs, described in Section 8.1, are used. The probability

to observe an event with a reconstructed zenith angle θ_i , when μ_s signal events are present among a total number of observed events, n_{obs} , is given by

$$f(\theta_i|\mu_s) = \frac{\mu_s}{n_{\text{obs}}} f_S(\theta_i) + \left(1 - \frac{\mu_s}{n_{\text{obs}}}\right) f_{BG}(\theta_i), \quad (8.8)$$

where $f_S(\theta_i)$ and $f_{BG}(\theta_i)$ are respectively the signal and the background PDF. The likelihood of the presence of μ_s signal events in an experiment that observed n_{obs} events with an ensemble of zenith angles $\{\theta_i\}$, is given by the product of all individual event probabilities

$$\mathcal{L}(\mu_s) = \prod_{i=1}^{n_{\text{obs}}} f(\theta_i|\mu_s). \quad (8.9)$$

This likelihood, $\mathcal{L}(\mu)$, can be used in the likelihood-ratio test statistic, suggested by Feldmann and Cousins (FC) [175]

$$\mathcal{R}(\mu_s) = \frac{\mathcal{L}(\mu_s)}{\mathcal{L}(\hat{\mu}_s)}, \quad (8.10)$$

where $\hat{\mu}_s$ is the result of the best fit to the observed ensemble of zenith angles, maximizing the likelihood $\mathcal{L}(\mu_s)$. So $\mathcal{R}(\mu_s) \leq 1$ for all physical values of $\mu_s \in [0, n_{\text{obs}}]$.

Feldmann and Cousins used this likelihood-ratio, $\mathcal{R}(\mu_s)$, as a *rank*, since starting at high values, it ranks the experimental results in order of inclusion in the acceptance interval. In this method, the parameter μ_s is bound to physical values, so $\mu_s \in [0, n_{\text{obs}}]$, while in the *standard* χ^2 frequentist approach, non-physical best fits ($\mu_s \notin [0, n_{\text{obs}}]$) could arise at the boundaries of the interval.

The acceptance intervals in this approach at the desired α confidence level are

$$[\mathcal{R}_{\text{crit}}^\alpha(\mu_s), 1], \quad (8.11)$$

where $\mathcal{R}_{\text{crit}}^\alpha(\mu_s)$ is defined such that the acceptance interval contains a fraction α of the $\mathcal{R}(\mu_s)$ -values.

Once this $\mathcal{R}_{\text{crit}}^\alpha(\mu_s)$ value is known, the confidence interval $[\mu_{s,\text{low}}^\alpha, \mu_{s,\text{up}}^\alpha]$ for a certain number of signal events μ_s can be calculated

$$[\mu_{s,\text{low}}^\alpha, \mu_{s,\text{up}}^\alpha] = \{\mu_s | \ln \mathcal{R}(\mu_s) \geq \ln \mathcal{R}_{\text{crit}}^\alpha(\mu_s)\}. \quad (8.12)$$

To calculate this confidence interval, the $\mathcal{R}(\mu_s)$ distribution needs to be known. The procedure to get this $\mathcal{R}(\mu_s)$ distribution has been used in many IceCube/AMANDA WIMP searches [172, 66, 55], and goes as follows:

For each value of $\mu_s \in [0, 400]^4$, with step-size $\Delta\mu_s = 1$

1. for each pseudo-experiment $k = 1, \dots, 10000$
 - (a) sample a set of n_{obs} zenith angles, $\{\theta_i\}_k$, from Eq. (8.8), with μ_s signal events, and $n_{\text{obs}} - \mu_s$ background events,
 - (b) calculate the likelihood $\mathcal{L}_k(\mu_s)$ with Eq. (8.9),
 - (c) find which value of $\hat{\mu}_{s_k}$ maximizes the likelihood $\mathcal{L}_k(\hat{\mu}_{s_k})$ as in Eq. (8.9),
 - (d) calculate $\ln \mathcal{R}_k(\mu)$ as in Eq. (8.10),
2. find the critical value $\ln \mathcal{R}_{\text{crit}}^\alpha(\mu_s)$ following the FC ordering principle (Eq. (8.11)).

The output of the procedure is shown in Fig. 8.5, which shows $-\ln \mathcal{R}(\mu_s)$ as a function of the simulated amount of signal μ_s . This output is calculated for the FINAL LOWE sample, with the zenith angle distribution of muons induced by neutrinos from 50 GeV WIMPs annihilating into $\tau^+\tau^-$ as signal PDF and the smoothened zenith angle distribution of the simulated atmospheric background as background PDF, and with $n_{\text{obs}} = 7911$, i.e. the expected amount of events in the final LOWE sample IC86-I sample (311 days, see Chapter 9), extrapolated from the burnsample (see Table 7.16). The solid red line in this figure indicates the critical value at 90% confidence level, $-\ln \mathcal{R}_{\text{crit}}^{0.9}(\mu_s)$, as a function of μ_s . Hence, 90% of all pseudo-experiments have $-\ln \mathcal{R}(\mu_s)$ values above this line. The dashed red line shows the χ^2 approximation to this function. Wilks' Theorem [176] states that $-2 \ln \mathcal{R}$ becomes χ^2 distributed in a Gaussian scenario ($n_{\text{obs}} \rightarrow \infty$). In this case, where there is one degree of freedom, this theorem states that⁵

$$-2 \ln \mathcal{R}_{\text{crit}}^\alpha(\mu_s) = \chi^2(\alpha, 1) \quad (8.13)$$

This approximation is valid once μ is far enough from the physical boundary region. In the case of Fig. 8.5, Eq. (8.13) is valid for $\mu_s \gtrsim 50$, where $\ln \mathcal{R}_{\text{crit}}^{0.9}(\mu) = -0.5 \cdot \chi^2(0.9, 1) = -1.35$.

Also shown in this figure are the output of two example pseudo-experiments, one with $\mu_{s,\text{true}} = 0$ and the other $\mu_{s,\text{true}} = 200$, both indicated by the blue dashed lines. As described by Eq. (8.12), the 90% CL intervals of these experiments are given by the region where $\ln \mathcal{R}(\mu_s) \geq \ln \mathcal{R}_{\text{crit}}^{90\%}(\mu_s)$, so $[\mu_{s,\text{low}}^{90\%}, \mu_{s,\text{up}}^{90\%}] = [0, 69]$ in the case of $\mu_{s,\text{true}} = 0$ and $[\mu_{s,\text{low}}^{90\%}, \mu_{s,\text{up}}^{90\%}] = [146, 291]$ for $\mu_{s,\text{true}} = 200$. Note that in the example of $\mu_{s,\text{true}} = 200$ the *best fit value* (the value which maximizes the likelihood), $\hat{\mu}_k$, does not exactly correspond to its simulated value, but the 90% CL interval contains the true value.

⁴a maximum of 400 signal muons in the final sample is thus considered.

⁵This form of Wilks theorem is for the case of no assumed physical boundary of the scanned parameter, in this case μ_s . When a boundary is imposed, dedicated methods exist to deal with this boundary [177].

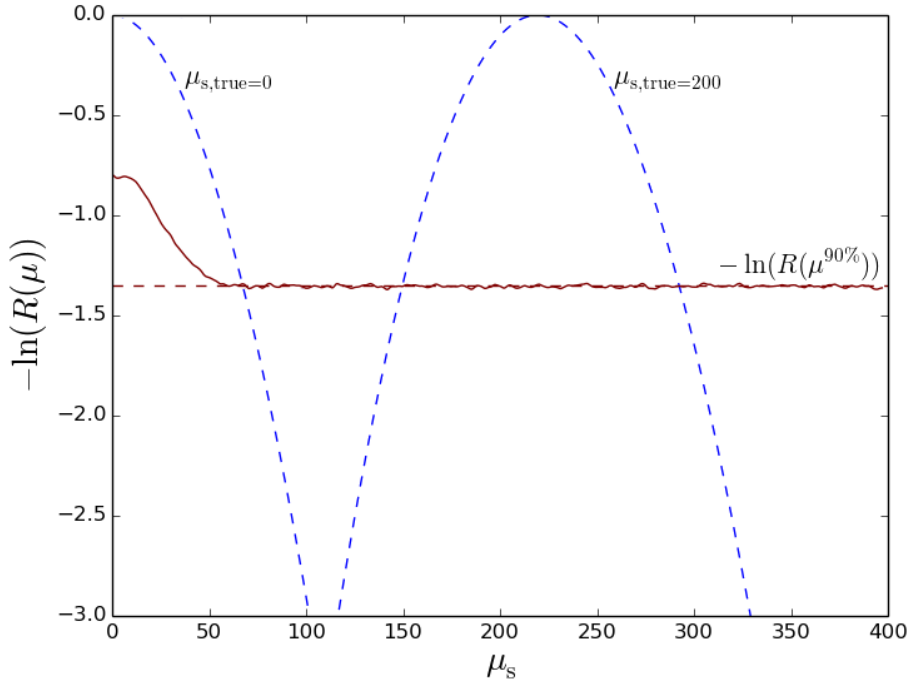


Figure 8.5: Output of the procedure described in the text, resulting in a $-\ln \mathcal{R}(\mu_s)$ as a function of the simulated amount of signal μ_s . The solid red line indicates the critical value $\ln \mathcal{R}_{\text{crit}}^{0.9}(\mu_s)$ at 90% confidence level and the dashed red line shows the χ^2 approximation. The output of two example pseudo-experiments, one with $\mu_{s,\text{true}} = 0$ and the other $\mu_{s,\text{true}} = 200$, are indicated by the blue dashed lines. This figure is made using the final samples of the LOWE analysis, using the zenith angle distribution of neutrinos from 50 GeV WIMPs annihilating into $\tau^+\tau^-$ as signal PDF and the smoothened zenith angle distribution of the simulated atmospheric background as background PDF.

As mentioned before, $\bar{\mu}^{90}$ is defined as the 90% CL median upper-limit on the number of signal events in a background only scenario. This is thus given by the median value of the upper endpoint of the confidence interval, $\mu_{s,\text{up}}^{90\%}$ in Eq. (8.12), of 10000 pseudo-experiments, generated with $\mu_{s,\text{true}} = 0$. The resulting lower and upper endpoints of the confidence intervals of the 10000 background-only pseudo-experiments, are shown in Fig. 8.6. In this plot, the blue and the red histograms show the distributions of respectively the lower endpoint, $\mu_{s,\text{low}}^{90\%}$, and the upper endpoint, $\mu_{s,\text{up}}^{90\%}$. The vertical solid line represents the value of $\bar{\mu}_s^{90\%}$, and the dashed lines indicate the one standard deviations (statistical) uncertainties on $\bar{\mu}_s^{90\%}$.

The 90% CL median upper-limit on the number of signal events in a background only scenario, $\bar{\mu}^{90\%}$, of the final LOWE sample, for the 50 GeV WIMPs annihilating into

$\tau^+\tau^-$ signal scenario, in the final IC86-I sample (311 days), is expected to be

$$\bar{\mu}^{90\%} = 65_{-33}^{+41} \text{ events}, \quad (8.14)$$

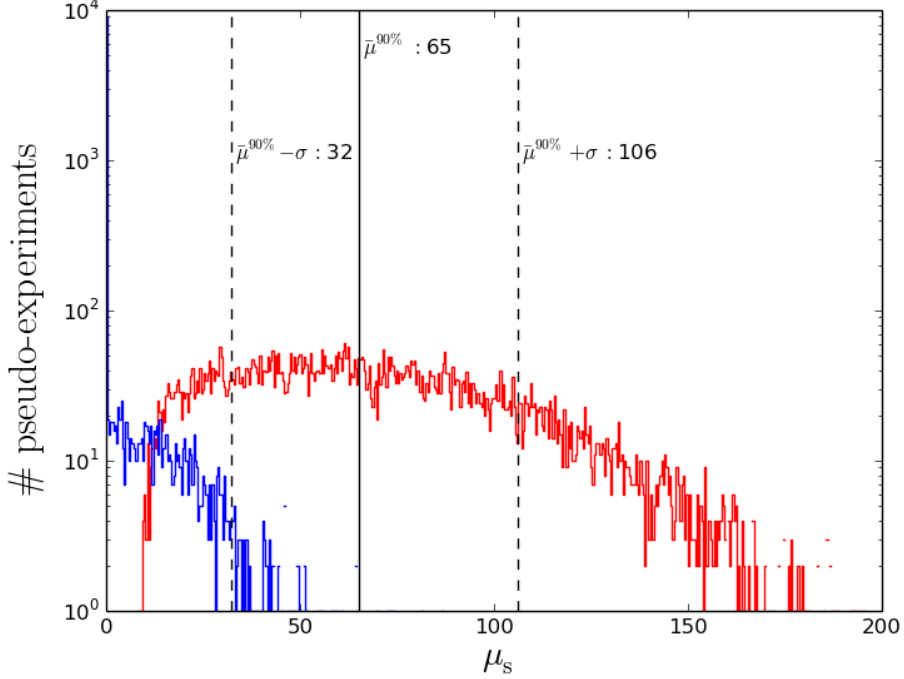


Figure 8.6: Distributions of the lower (blue) and upper (red) endpoints of the 90% CL intervals of $[\mu_{s,\text{low}}^{90\%}, \mu_{s,\text{up}}^{90\%}]$ of 10000 background-only pseudo-experiments. This output is calculated for the FINAL LOWE sample, with the zenith angle distribution of neutrinos from 50 GeV WIMPs annihilating into $\tau^+\tau^-$ as signal PDF and the smoothed zenith angle distribution of the simulated atmospheric background as background PDF, for one year of IceCube data. The vertical lines indicate the 90% CL median upper-limit on the number of signal events in a background only scenario, $\bar{\mu}^{90\%}$ (solid line), and its 68% standard deviations (dashed lines).

8.3 Sensitivity

With the above information, the sensitivity of the analysis can be calculated. As mentioned at the beginning of the previous section, the cut value on the BDT score is chosen such that it minimizes the value of the volumetric flux in the background-only scenario, $\bar{\Gamma}_{\nu \rightarrow \mu}^{90\%}$, given by Eq. (8.7).

In Fig. 8.7a and 8.7b the value of $\bar{\Gamma}_{\nu \rightarrow \mu}^{90\%}$ as a function of the value of the cut on the BDT scores are shown for the LOWE sample and the HIGHE sample respectively.

In Fig. 8.7a, two distributions are shown, showing the effect of the scale factors in the LOWE analysis on the sensitivity. In the lower (red) distribution, no rescalings (see Section 7.7.4) have been taken into account for the background or the signal samples, while in the upper (gray) distribution, the rescaling factors of Table 7.9 were used for the background, and a rescaling of 0.68 was used for the signal. As in the present analysis, the rescaling factor of the background atmospheric muon neutrinos is assigned to the lack of coincident muon events, a similar scaling factor should indeed be introduced for the signal muon neutrinos. The same would be true in the case that the factor would be due to wrongly simulated detector effects, which would affect the signal-induced neutrinos in a similar way as the atmospheric neutrinos. If, on the other hand, the rescaling of the background atmospheric muon neutrinos is coming from a wrong normalization of the assumed flux model, no rescaling is needed for the signal-induced muon neutrinos. Note that the rescaling of the signal corresponds linearly to a rescaling of the effective volume, V_{eff} , which is inversely proportional with the resulting sensitivity of $\Gamma_{\nu \rightarrow \mu}$ (Eq. 8.7). Assuming a rescaling of 0.68 for the signal is thus the most conservative case, so this scaling factor will be used in the calculation of the sensitivities and results (Chapter 9) of the LOWE sample.

As can be seen from those plots, the minima are not really explicit, but in both cases there is a region in which the cut is optimal.

For the LOWE sample, this region is between 0.23 and 0.35, independent of whether or not the samples are rescaled, hence the rescaling has no effect on the choice of the cut value. The sudden *jumps* in the distribution are due to the removal of simulated atmospheric muon events with high weights. For high cut values on the BDT score (>0.35), only very few events are left in the samples, so those results might be sensitive to statistical fluctuations.

For the HIGH E sample, the optimal cut value lies in the range between 0.14 and 0.20.

To have a final sample with high enough statistics, the low energy sample is cut in the middle of the region of the minima, hence at a BDT score value of 0.28, whereas the cut on the high energy sample was selected at the true minimum of the distribution, thus at 0.16.

Now that the cut values are fixed, the $\bar{\Gamma}_{\nu \rightarrow \mu}^{90\%}$ factor can be calculated for a range of different WIMP masses and channels, for both the low and the high energy samples. The mass range which is scanned is 10 GeV-10 TeV, as this is where the analyses described in this work have sensitivity. The calculation is performed for the most (hard) and least (soft) energetic neutrino spectrum (at generation level) for each of these masses. The softest spectrum is given by 100% annihilation into $b\bar{b}$ and the hardest spectrum is given by 100% annihilation into W^+W^- if $m_\chi > m_W$ and 100% annihilation into $\tau^+\tau^-$ in the other cases. As an example, the neutrino spectra of 50 GeV WIMPs, of the soft channel ($\chi\chi \rightarrow b\bar{b}$) and the hard channel ($\chi\chi \rightarrow \tau^+\tau^-$) were shown respectively in Fig. 3.2 and Fig. 3.3. Other choices of branching ratios are expected to have intermediate energy

spectra and would thus provide intermediate sensitivities.

Fig. 8.8a shows the resulting sensitivities $\bar{\Gamma}_{\nu \rightarrow \mu}^{90\%}$ as a function of the WIMP mass of the LOWE analysis and the HIGH E analysis. For the calculation of the sensitivities of the LOWE analysis, the rescaling factors are applied to the background simulation sets, and a rescaling of 0.68 is applied to the signal-induced neutrinos, by rescaling the effective volume by this factor of 0.68, as was done in the previous chapter in Tables 7.10 and 7.12 and Fig. 7.32. The resulting values of $\bar{\mu}_s^{90\%}$ (extrapolated to a full year of data), V_{eff} and $\bar{\Gamma}_{\nu \rightarrow \mu}^{90\%}$ of the LOWE analysis for the considered WIMP models are presented in Table 8.1.

As expected, the low energy sample yields a better sensitivity for low mass WIMP models, while the high energy analysis gets more sensitive for masses of 250 GeV and higher. Finally, the analysis with the best sensitivity at each WIMP model is selected, as shown in Fig. 8.8b.

In a next step, the full IC86-I data sample is analyzed for the presence of a WIMP signal, as described in the next chapter, Chapter 9.

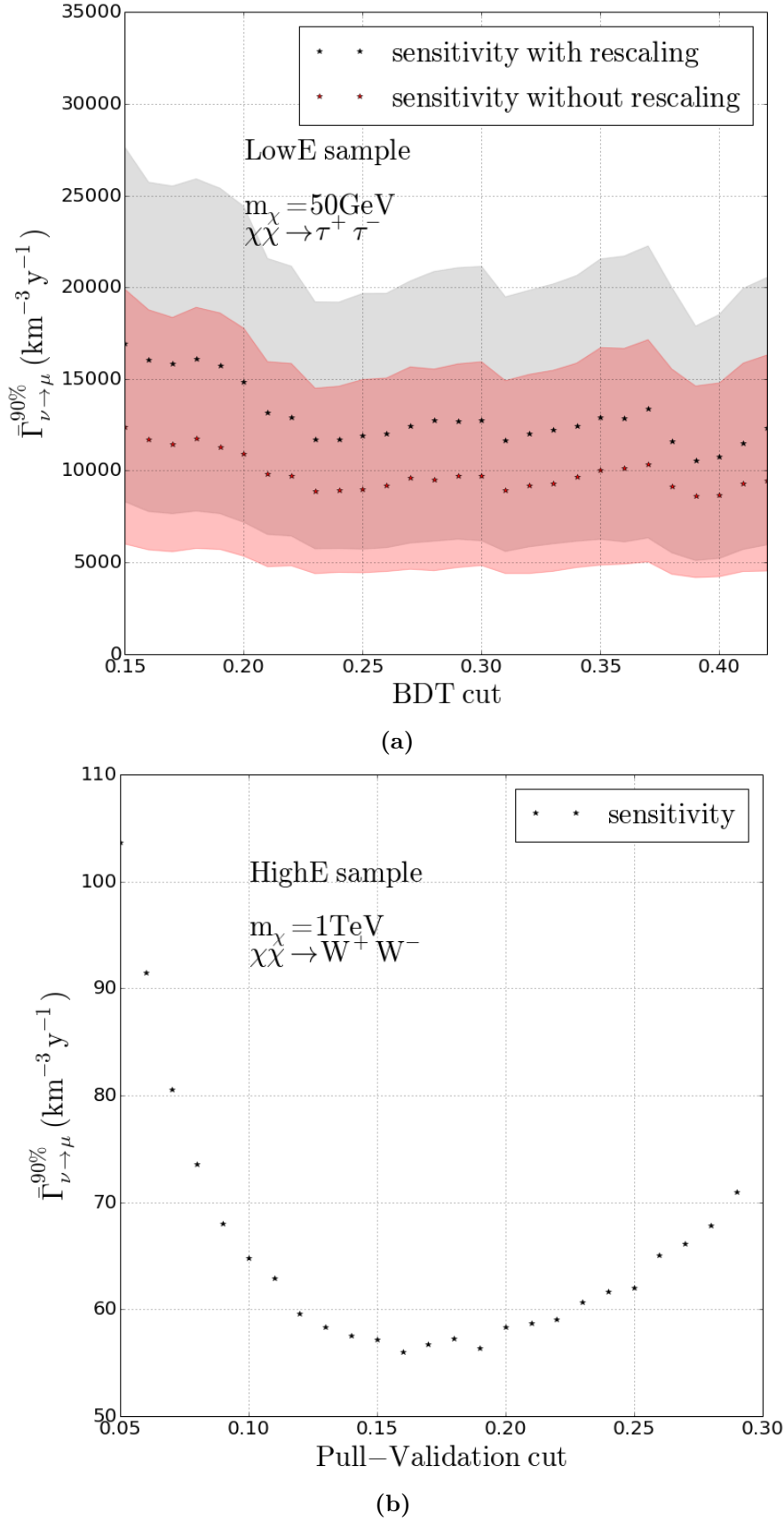
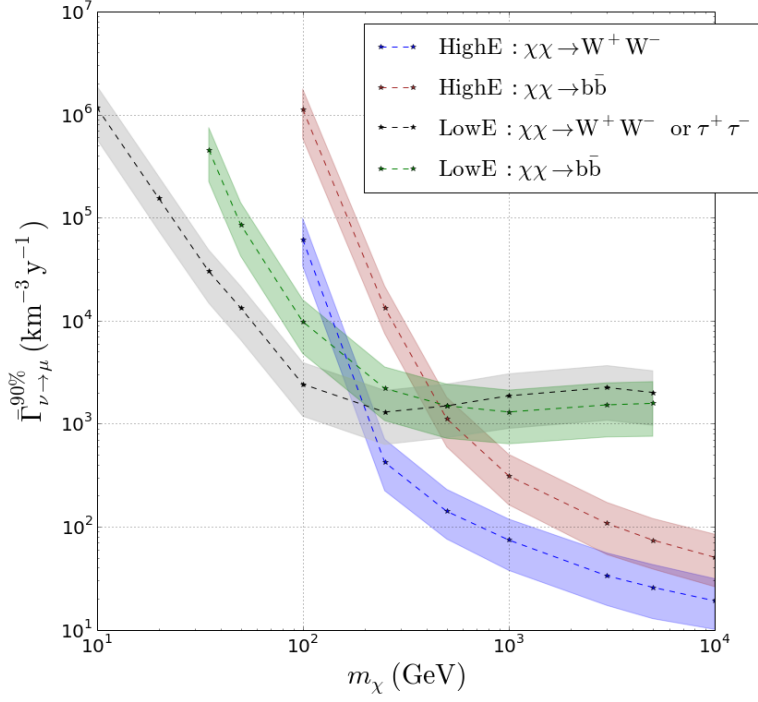


Figure 8.7: $\bar{\Gamma}_{\nu \rightarrow \mu}^{90\%}$ sensitivity (dots), as a function of the value of the cut on the BDT scores are shown for the LOWE (a) sample and the HIGH E (b) sample. In panel (a), the sensitivity is calculated with (gray) and without (red) rescaling, the one standard deviation (statistical) uncertainty is indicated by the shaded regions.

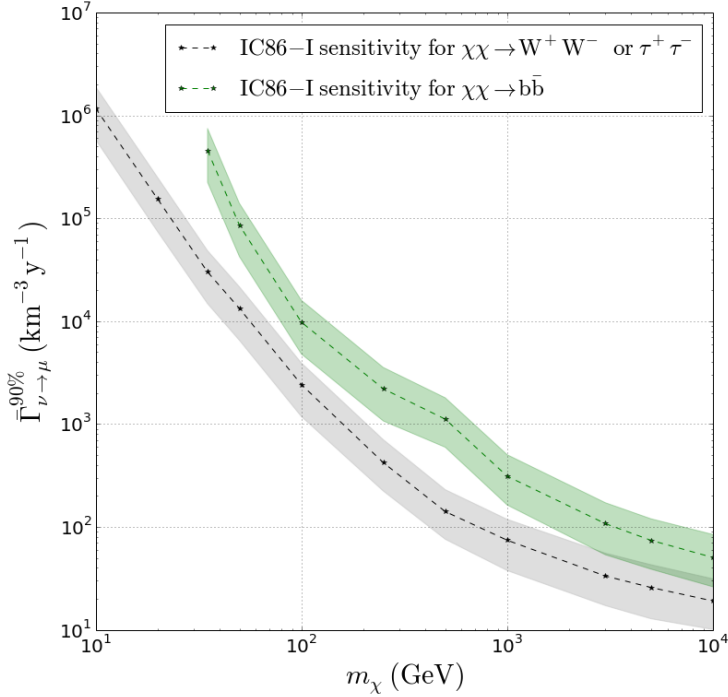
CHAPTER 8. ESTIMATION OF THE SENSITIVITIES

Table 8.1: $\bar{\mu}_s^{90\%}$, V_{eff} and $\Gamma_{\nu \rightarrow \mu}^{90\%}$ of the LOWE analysis for different WIMP models.

WIMP model		$\bar{\mu}^{90\%}$ (events/yr)	V_{eff} (km^3)	$\bar{\Gamma}_{\nu \rightarrow \mu}^{90\%}$ (events/ km^3/yr)
$m_\chi = 10 \text{ GeV}$	$\chi\chi \rightarrow \tau^+\tau^-$	532_{-268}^{+330}	4.5×10^{-4}	$1.17_{-0.59}^{+0.73} \times 10^6$
$m_\chi = 20 \text{ GeV}$	$\chi\chi \rightarrow \tau^+\tau^-$	232_{-120}^{+145}	1.5×10^{-3}	$1.54_{-0.80}^{+0.96} \times 10^5$
$m_\chi = 35 \text{ GeV}$	$\chi\chi \rightarrow \tau^+\tau^-$	104_{-53}^{+64}	3.5×10^{-3}	$3.00_{-1.52}^{+1.83} \times 10^4$
	$\chi\chi \rightarrow b\bar{b}$	310_{-158}^{+197}	0.7×10^{-3}	$4.56_{-2.32}^{+2.89} \times 10^5$
$m_\chi = 50 \text{ GeV}$	$\chi\chi \rightarrow \tau^+\tau^-$	77_{-40}^{+48}	5.8×10^{-3}	$1.33_{-0.68}^{+0.83} \times 10^4$
	$\chi\chi \rightarrow b\bar{b}$	127_{-64}^{+80}	1.5×10^{-3}	$8.55_{-4.32}^{+5.40} \times 10^4$
$m_\chi = 100 \text{ GeV}$	$\chi\chi \rightarrow W^+W^-$	52_{-26}^{+32}	2.1×10^{-2}	$2.42_{-1.23}^{+1.50} \times 10^3$
	$\chi\chi \rightarrow b\bar{b}$	65_{-33}^{+41}	6.6×10^{-3}	$9.77_{-4.98}^{+6.17} \times 10^3$
$m_\chi = 250 \text{ GeV}$	$\chi\chi \rightarrow W^+W^-$	42_{-21}^{+26}	3.3×10^{-2}	$1.29_{-0.67}^{+0.80} \times 10^3$
	$\chi\chi \rightarrow b\bar{b}$	47_{-24}^{+29}	2.1×10^{-2}	$2.20_{-1.13}^{+1.35} \times 10^3$
$m_\chi = 500 \text{ GeV}$	$\chi\chi \rightarrow W^+W^-$	38_{-19}^{+24}	2.6×10^{-2}	$1.49_{-0.75}^{+0.93} \times 10^3$
	$\chi\chi \rightarrow b\bar{b}$	42_{-22}^{+26}	2.8×10^{-2}	$1.49_{-0.77}^{+0.93} \times 10^3$
$m_\chi = 1 \text{ TeV}$	$\chi\chi \rightarrow W^+W^-$	34_{-18}^{+22}	1.8×10^{-2}	$1.86_{-0.96}^{+1.18} \times 10^3$
	$\chi\chi \rightarrow b\bar{b}$	40_{-20}^{+25}	3.1×10^{-2}	$1.30_{-0.66}^{+0.82} \times 10^3$
$m_\chi = 3 \text{ TeV}$	$\chi\chi \rightarrow W^+W^-$	32_{-16}^{+20}	1.4×10^{-2}	$2.24_{-1.16}^{+1.41} \times 10^3$
	$\chi\chi \rightarrow b\bar{b}$	36_{-18}^{+23}	2.4×10^{-2}	$1.52_{-0.78}^{+0.96} \times 10^3$
$m_\chi = 5 \text{ TeV}$	$\chi\chi \rightarrow W^+W^-$	30_{-15}^{+18}	1.5×10^{-2}	$2.00_{-1.04}^{+1.25} \times 10^3$
	$\chi\chi \rightarrow b\bar{b}$	35_{-18}^{+22}	2.2×10^{-2}	$1.57_{-0.82}^{+0.98} \times 10^3$



(a)



(b)

Figure 8.8: $\bar{\Gamma}_{\nu \to \mu}^{90\%}$ as a function of the WIMP mass of the LOWE analysis (gray and green lines) and the HIGH E analysis (blue and brown lines). In the top panel, the sensitivities of the analyses are shown individually on the soft channel (LOWE : green, HIGH E : brown) and on the hard channel (LOWE : gray, HIGH E : blue). The bottom panel shows the combined sensitivities on the soft channel (green) and on the hard channel (gray). The shaded regions indicate the one standard deviation uncertainty on the sensitivity. These sensitivities and their uncertainties are calculated without including systematic uncertainties.

Summary

In this chapter, the sensitivities of the analyses described in this work were calculated. In the present analysis, the sensitivity is defined as the median upper-limit at 90% confidence level of the volumetric flux in a background-only scenario, $\bar{\Gamma}_{\nu \rightarrow \mu}^{90\%}$.

The calculation of the sensitivities were based on the reconstructed zenith angle distributions, θ , of the simulated signal and background events, which were used as Probability Density Functions in a shape analysis. As these PDFs should be smooth, the background sample of the LOWE analysis was smoothed using a Kernel Density Estimator algorithm.

The smooth PDFs were then used to calculate the volumetric flux, $\Gamma_{\nu \rightarrow \mu}$, which depends on the final sample and thus on the cut on the BDT score described in the previous chapter. The cuts on the BDT scores were chosen such that they minimized $\bar{\Gamma}_{\nu \rightarrow \mu}^{90\%}$, to optimize the sensitivities.

The sensitivities of both the LOWE and HIGH E analysis were then calculated for different WIMP masses in the range 10 GeV-10 TeV, and were combined by selecting the analysis with the best sensitivity at each mass.

However beautiful the strategy, you should occasionally look at the results.

Winston Churchill

9

Measurement of the WIMP annihilation rate and related physical quantities

After having defined the event selection procedure and the signal search method in the two previous chapters, the zenith distribution of the complete IC86-I dataset can be analyzed to see if there is an excess from the direction of the center of the Earth. The excess is defined with respect to the expected atmospheric background, which is obtained from simulated data.

Before comparing the experimental data with the background simulation, the uncertainties on the latter distributions need to be studied, as presented in Section 9.1. The data are then compared to the simulated background, as presented in Section 9.2. All data are in agreement with the background expectation within one standard deviation uncertainty.

Finally, upper-limits on the WIMP annihilation rate and related physical quantities are calculated and compared with the upper-limits set by other experiments, as presented in Section 9.3.

Throughout this chapter, the LOWE part of the analysis will be handled in more detail than the HIGHE part, as the latter part was not the main work of the author of this thesis.

9.1 Systematic Uncertainties

Several sources of systematic uncertainties need to be taken into account, some of which act both on the signal and the background samples, while others just need to be considered in one of both samples.

A first class of uncertainties, acting in a similar way on both the signal and the background, are detector effects. These consist of limitations in the detector simulation and uncertainties in the detector calibration.

The second class of the systematic uncertainties are parametrization uncertainties on particle fluxes, cross-sections and neutrino properties. These effects will be different for the signal neutrinos and the background events.

A last class of systematics that needs to be considered are non-simulated coincident events in the atmospheric neutrino samples and the WIMP-induced signal neutrinos. As this is a lack of simulation of real physics, this is a systematic error rather than a systematic uncertainty.

All three classes will affect the simulated zenith angle distributions and need to be taken into account in the shape analysis which was described in Section 8.2. An overview of the values of the systematic uncertainties which apply for the FINAL LOWE sample is given in Table 9.1.

Detection uncertainties

These uncertainties include the actual DOM sensitivity (Section 4.3), the optical properties of the glacial ice and the propagation of the Cherenkov photons through the medium (Section 4.2). They affect all the different simulations, be it atmospheric muons, muons (and other leptons) induced by atmospheric neutrinos or muons (and other leptons) from WIMP-induced neutrinos.

The baseline atmospheric ν_μ data used in this study, are not rescaled (see Section 7.7.4). This is because the simulation sets used for the study were simulated in the same way as the baseline set, except that some particular parameters were varied. All the obtained values discussed, below and presented in Table 9.1, are thus w.r.t. the unscaled baseline set.

To estimate the dependence of the simulated zenith angle distributions on the DOM sensitivity, this sensitivity was varied with an overall shift of $\pm 10\%$ around its baseline value. This 10 % variation corresponds to the actual uncertainty on the DOM efficiency. Varying the sensitivity with $\pm 10\%$ has a $\pm 10\%$ effect on the event rate, as illustrated by the yellow band in Fig. 9.1, in which the rate of atmospheric neutrinos with energies below 190 GeV (GENIE) is shown as a function of the reconstructed zenith angle.

There are different sources of uncertainty in modeling the ice and the propagation of Cherenkov photons in it. The uncertainties on the optical properties of the ice were estimated in several ways. As described in Section 4.2, the baseline ice model that

was used in this analysis was SPICE-MIE. In that same section, an updated ice model, SPICE-LEA, was described. Recall that the SPICE-LEA ice model includes an azimuthal dependence of the light propagation properties, which is not included in the SPICE-MIE ice model.

When considering the SPICE-LEA ice-model, the expected event rate is roughly 10% lower than in the case of SPICE MIE as shown by the red distribution in Fig. 9.1. Another effect comes from the diameter of the hole ice, which was also mentioned in Section 4.2. The effect of the variation of the hole ice is adopted from the detailed study in [97], where it was shown that varying the radius of the hole ice from 0 cm to 100 cm has a $\pm 10\%$ effect on the event rates. The last considered detection uncertainty is given by the absorption and scattering coefficients of the photons in ice. The values for these uncertainties have been adopted from another, similar analysis [33], where a $\pm 10\%$ effect on the event rate was reported.

These detector uncertainties need to be considered for all different simulated data types, atmospheric muons, atmospheric neutrinos and WIMP-induced neutrinos.

Concerning the atmospheric muons, the detector uncertainties are the only effects which are considered as systematic uncertainties. As mentioned in the previous chapter, the final event sample of the LOWE analysis, only has very few (37) CORSIKA events left, and the sensitivity was calculated by smoothening the atmospheric muon events with the KDE method. In what follows, the contribution of the CORSIKA events to the total background zenith distribution is also estimated by smoothening the CORSIKA events, as presented in Figs. 9.4a and 9.4b. The total uncertainty on this smooth distribution is calculated by summing the mean of the statistical uncertainty of each bin with a systematic uncertainty of 20% (see Table 9.1) in quadrature, as shown in Eq. (9.1).

Physics uncertainties

Contrary to the detection uncertainties, physics uncertainties only apply for a certain type of events, so there are different effects for atmospheric neutrinos, atmospheric muons and WIMP-induced signal neutrinos. For the atmospheric muons, no physical uncertainties are considered.

The first uncertainty comes from the absolute scale of the atmospheric muon-neutrino flux. According to [97], this absolute scale of the atmospheric muon-neutrino flux has been measured to an accuracy of roughly 30%, in the energy range between 10 GeV and 100 GeV, which is the dominating range in the LOWE sample. An uncertainty of 30% on the atmospheric neutrino event rate is thus assumed.

In [33] the uncertainties on the ν -nucleon cross-sections $\sigma_{\nu-N}$ and on the neutrino oscillation parameters were studied and were estimated to have an overall effect on the neutrino event rate of the order of 6% each. This effect depends of course on the energy of the neutrino, but the 6% value is conservatively considered as a global uncertainty on the neutrino event rate in the present analysis. These uncertainties apply for both the

atmospheric neutrinos and the signal neutrinos.

As explained in Section 2.4, there is an uncertainty on the velocity distribution of the WIMPs in the galaxy, which has a direct impact on the capture rate of the WIMPs in the Earth and thus on the expected neutrino flux. This type of theoretical uncertainty is not taken into account in this work, and the results presented below are for a standard velocity distribution, which is shown in Fig. 2.5.

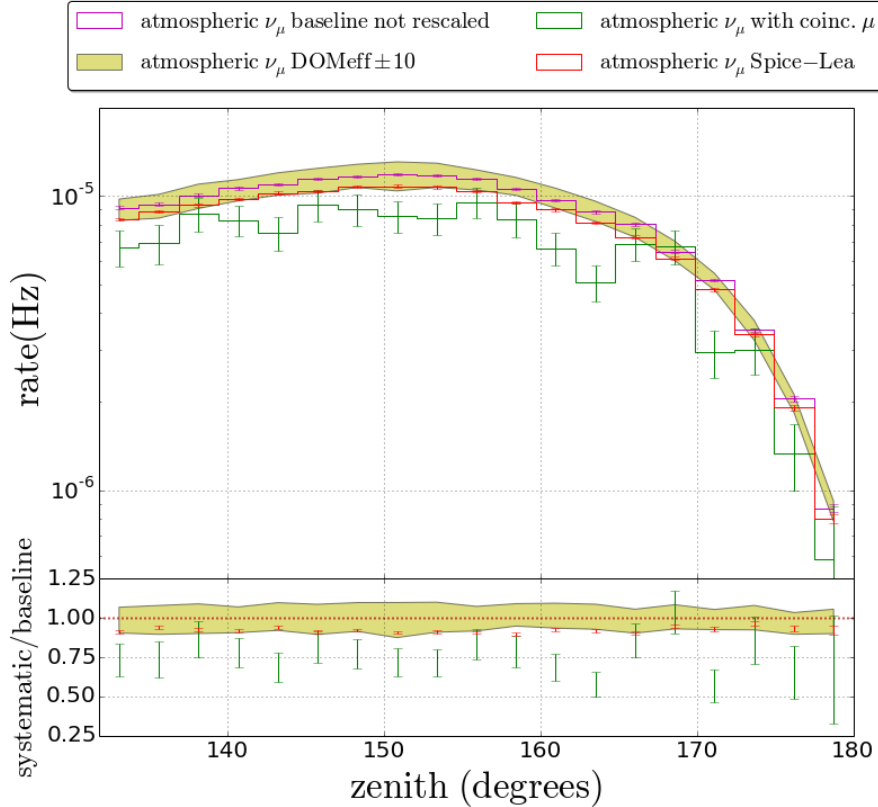


Figure 9.1: The distribution of the reconstructed zenith angles of the simulated atmospheric ν_μ events in the final LOWE sample. The magenta distribution shows the atmospheric ν_μ event rate for the baseline (GENIE) dataset used in the present analysis, the yellow area indicate the effect on the atmospheric ν_μ event rate when varying the DOM sensitivity with $\pm 10\%$, the red distribution shows the expected atmospheric ν_μ event rate when using the SPICE-LEA ice model and the green distribution shows the expected atmospheric ν_μ event rate when considering coincident atmospheric muons.

Unsimulated coincident events

As discussed in Section 7.7.3 and Section 5.1.2, about 10% of the events triggered by IceCube are coincident events. This effect is bigger for low energy event samples, as IceCube is measuring more of these low-energy events (the atmospheric neutrino flux

decreases steeply with increasing energies, as shown in Fig. 4.14.). Coincident events were not included in the neutrino simulation samples (both atmospheric and signal) that were used for this analysis, because no correct, reviewed coincident baseline samples are existing for IC86-I. Recently, simulated atmospheric neutrino samples including coincident muon events have been created, but the results of those are still preliminary, as the samples still have to be tested in more detail. These preliminary samples are used here to get an idea of the effect that atmospheric coincident muons might have.

The green distribution in Fig. 9.1 shows the effect on the reconstructed zenith distribution. This distribution shows that the event rate of the atmospheric ν_μ in the low energy sample of this analysis is lowered by 20-30% when coincident atmospheric are considered. A more detailed study on this subject is presented in Appendix B. Coincident muons were only simulated in the atmospheric muon simulation (CORSIKA), but not in the atmospheric neutrino simulation, nor in the signal neutrino simulation.

The total systematic uncertainty for each simulation sample, is then estimated by adding all of the above effects in quadrature. The total uncertainties, as well as an overview of the individual uncertainties, are given in Table 9.1.

Table 9.1: Relative systematic uncertainties on the event rates, for all the considered effects, and the total systematic uncertainties for each simulated dataset for the FINAL LOWE sample.

Uncertainty class	Source	Relative uncertainty	Affected simulation
Detector uncertainties	DOM sensitivity	$\pm 10\%$	atmospheric μ , atmospheric ν , signal ν
	ice-model	-10%	
	hole ice	$\pm 10\%$	
	γ propagation in ice	$\pm 10\%$	
Physics uncertainties	ν_{atm} flux	$\pm 30\%$	atmospheric ν
	ν oscillations	$\pm 6\%$	atmospheric, ν
	$\sigma_{\nu-N}$	$\pm 6\%$	signal ν
Unsimulated coincident events		-30%	atmospheric ν , signal ν
Total systematic uncertainty : $\sigma_{\text{syst,tot}}$		$+17\% - 20\%$	atmospheric μ
		$+19\% - 37\%$	signal ν
		$+36\% - 48\%$	atmospheric ν

As mentioned above, the values presented in Table 9.1 are w.r.t. the unscaled baseline datasets. In the LOWE part of the analysis, the datasets were rescaled, such that the simulated background matches the burnsample data in a signal-free region, as discussed in Section 7.7.4. The main effect of this rescaling was in the atmospheric ν_μ sample, which was rescaled by a factor $\omega_{\nu_\mu} = 0.68$. In Fig. 9.2, the zenith angle distributions for the rescaled (solid magenta line) and non-rescaled (dashed magenta line) baseline atmospheric ν_μ (GENIE) dataset are shown, together with the distribution of the atmospheric ν_μ dataset which contains coincident atmospheric muon events (solid green line). This figure shows that there is a good agreement (within uncertainties) between the rescaled baseline dataset and the dataset containing coincident atmospheric muons.

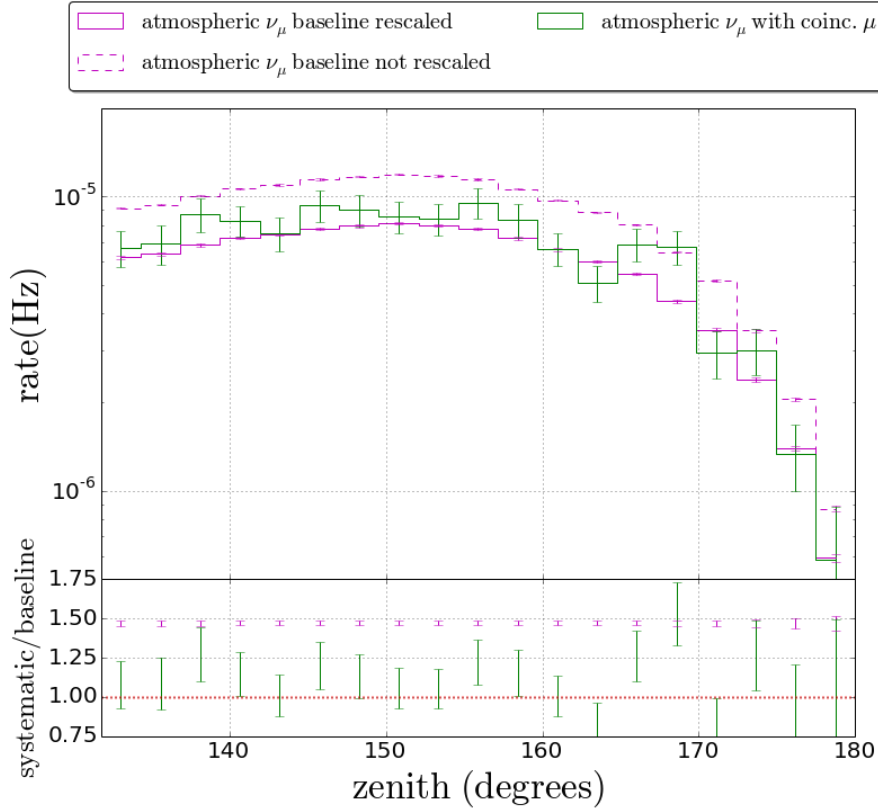


Figure 9.2: The distribution of the reconstructed zenith of the simulated atmospheric ν_μ event for the rescaled (solid magenta line) and non-rescaled (dashed-magenta line) baseline dataset used in the present analysis. The green distribution shows the expected atmospheric ν_μ event rate when considering coincident atmospheric muons.

As was mentioned before, the absence of coincident atmospheric muons in the baseline atmospheric neutrino simulation is thus a plausible explanation for the mismatch between the experimental data and the atmospheric neutrino simulation. As the neutrino datasets containing coincident events have not been reviewed and approved by the collaboration, the datasets with the coincident muons are not used in the background PDFs in the likelihood fit described in Chapter 8, but it justifies the introduced reweighting factor. A more detailed study on this subject is presented in Appendix B.

The rescaling factor is included in the systematic uncertainties on the muon neutrinos by scaling down the atmospheric ν_μ with the fitted scaling factor $\omega_{\nu_\mu} = 0.68$, and then assuming an upwards uncertainty of 47% ($=1/0.68$) on the atmospheric ν_μ event rate calculated from the rescaled baseline set. As this 47% is already a large uncertainty, which is comparable in size to the total upwards systematic uncertainty on the atmospheric ν_μ rate (see Table 9.1), it is considered that this value covers all the systematic uncertainties. The downwards systematic uncertainty on the atmospheric ν_μ rate is considered to be

37%, to take into account all the systematic uncertainties listed in Table 9.1, except the uncertainty coming from the unsimulated coincident events.

The systematic uncertainties are then added to the statistical uncertainties in quadrature to get the total uncertainty on the distribution

$$\sigma_{\text{tot}} = \sqrt{\sigma_{\text{syst,tot}}^2 + \sigma_{\text{stat}}^2}. \quad (9.1)$$

The total uncertainty is then taken into account in the shape analysis, which was explained in Section 8.2. As explained in that section, the pseudo-experiments are sampled according to the signal and background PDFs. To include the uncertainty in the calculation, the height of these PDFs is smeared with a gaussian with a width that corresponds to the uncertainty. This method is based on the method described by Conrad et al, who worked this out for the case of a cut-and-count approach in [178].

The effect of the value of the assumed uncertainty on the sensitivity of the LowE sample, is shown in Fig. 9.3.

For the HIGHE sample, no in-depth study on the systematic uncertainties has been done yet. The assumed values for this sample are based on the obtained values of the systematic uncertainties of the LOWE, and on the uncertainties quoted in [33], and are summarized in Table 9.2. Note that the uncertainty of coincident events is not considered for the HIGHE sample. This is because for this sample, no rescaling was needed, so the effect of the coincident events is probably much smaller than for the LOWE sample.

The preliminary values of Table 9.2 will be used in the remainder of this chapter, for the calculation of the sensitivities and upper-limits set by the HIGHE part of the analysis.

Table 9.2: Relative systematic uncertainties on the event rates, for all the considered effects, and the total systematic uncertainties for each simulated dataset for the FINAL HIGHE sample. These values are preliminary, as an in-depth study still needs to be done.

Uncertainty class	Source	Relative uncertainty	Affected simulation
Detector uncertainties	DOM sensitivity	$\pm 10\%$	atmospheric μ , atmospheric ν , signal ν
	ice-model	-10%	
	hole ice	$\pm 10\%$	
	γ propagation in ice	$\pm 5\%$	
Physics uncertainties	ν_{atm} flux	$\pm 30\%$	atmospheric ν
	$\sigma_{\nu-N}$	$\pm 3\%$	atmospheric, ν signal ν
Total systematic uncertainty : $\sigma_{\text{syst,tot}}$		$+15\% - 18\%$	atmospheric μ
		$+15\% - 18\%$	signal ν
		$+34\% - 35\%$	atmospheric ν

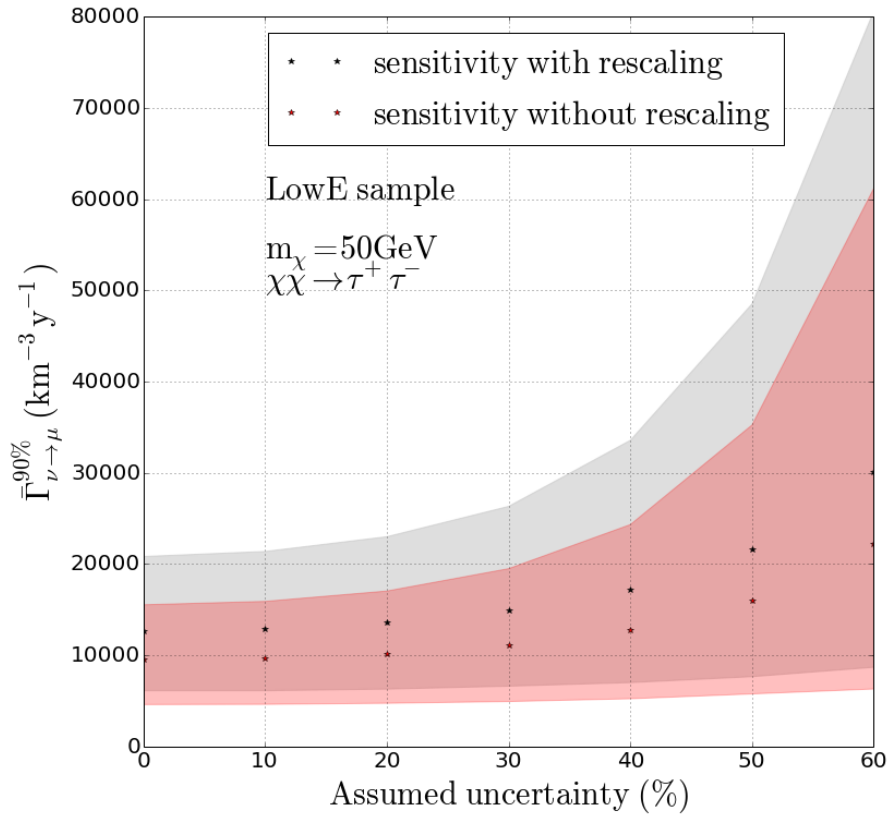


Figure 9.3: Effect of the value of the assumed uncertainty on the sensitivity. In this figure, the values of the sensitivity on $\Gamma_{\nu \rightarrow \mu}$ for 50 GeV WIMPs annihilating into $\tau^+ \tau^-$ are calculated for the LOWE sample. The gray points (with one standard deviation uncertainties indicated by the gray region) indicate the sensitivities in the case of rescaling, and the red points (with one standard deviation uncertainties indicated by the red region) are calculated assuming no rescaling.

9.2 The Unblinded Zenith Angle Distributions

Up to this point, only the burnsample (10% of the experimental data) was used in the event selection part (Chapter 7). This was done to check the simulated background samples. The sensitivities were calculated using simulations (Chapter 8). After approval of this analysis by the ICECUBE Collaboration, the full IC86-I sample was unblinded. The zenith distribution of this unblinded IC86-I data sample can now be compared to the simulated background distribution, to check for an excess from the direction of the center of the Earth. The full IC86-I sample has a livetime, t_{live} , of 28253988 s (or 327 days), and from this sample the part of the burnsample that was used for the BDT training (half of the burnsample, or roughly 5% of the total set) is removed, resulting in a final sample with a livetime of 26883324 s or roughly 311 days.

The final zenith angle distributions of the LOWE and HIGHE samples are shown respectively in Fig. 9.4 and Fig. 9.5. In the top panels in these figures, only the statistical uncertainty of the simulated background samples is considered, while in the bottom panels, also the systematic uncertainties on the simulated background samples, discussed in Section 9.1, are taken into account.

As can be seen from these plots, both the LOWE and HIGHE final unblinded samples are in agreement with the simulated background samples within less than one standard deviation, over the whole zenith range, when considering the systematic uncertainties.

The shape analysis, described in Section 8.2, is then performed on the zenith distribution of the unblinded data sample, and the resulting best fit for the amount of signals in the final sample, $\hat{\mu}_s^{90\%}$, is compared to the median upper-limit on this quantity $\bar{\mu}_s^{90\%}$. This is repeated for all considered WIMP models (masses and channels). As described in the previous chapter, the mass range which is scanned is 10 GeV-10 TeV and the shape analysis is done for the hardest (100% annihilation into W^+W^- if $m_\chi > m_W$ and 100% annihilation into $\tau^+\tau^-$ for the other cases) and softest (100% annihilation into $b\bar{b}$) energy spectrum for each of these masses.

The total uncertainty which is taken into account on the PDFs in the likelihood calculation, is 40% for the LOWE sample and 35% for the HIGHE sample. This assumed value of the uncertainty corresponds to the (conservatively rounded) mean total uncertainty on the total atmospheric background in each bin. All values presented below (in the tables and in the figures) are thus calculated assuming this 40%. Considering these uncertainties in the shape analysis scales up the sensitivities and the limits by roughly 30% for the LOWE sample and roughly 25% for the HIGHE sample, as can be seen in Fig. 9.3.

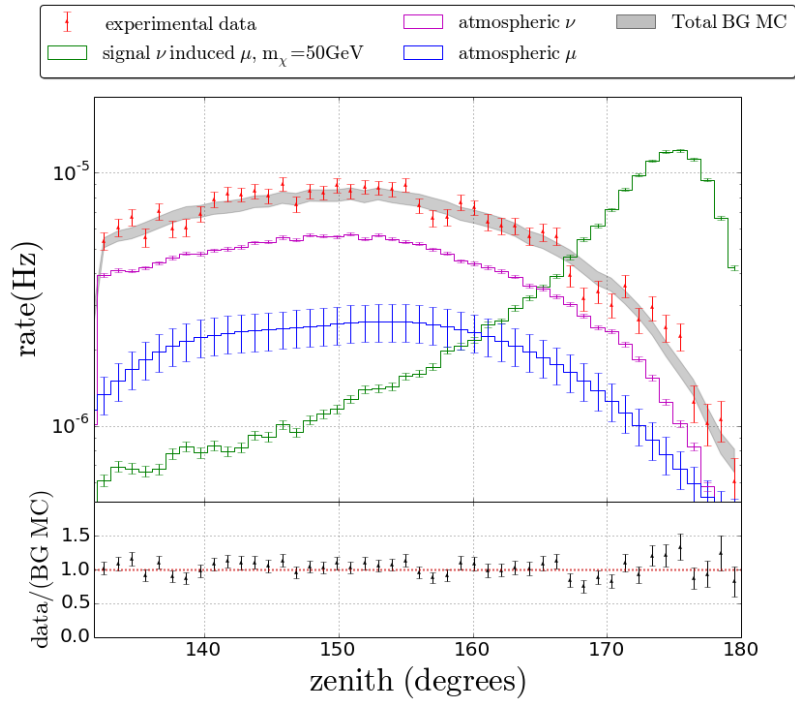
It is found that for each model, the result of the fit, $\hat{\mu}_s^{90\%}$, is in agreement with the background-only scenario, $\bar{\mu}_s^{90\%}$, within two standard deviations, and most of the models even within one standard deviation uncertainty. The results of the LOWE sample

CHAPTER 9. MEASUREMENT OF THE WIMP ANNIHILATION RATE AND RELATED PHYSICAL QUANTITIES

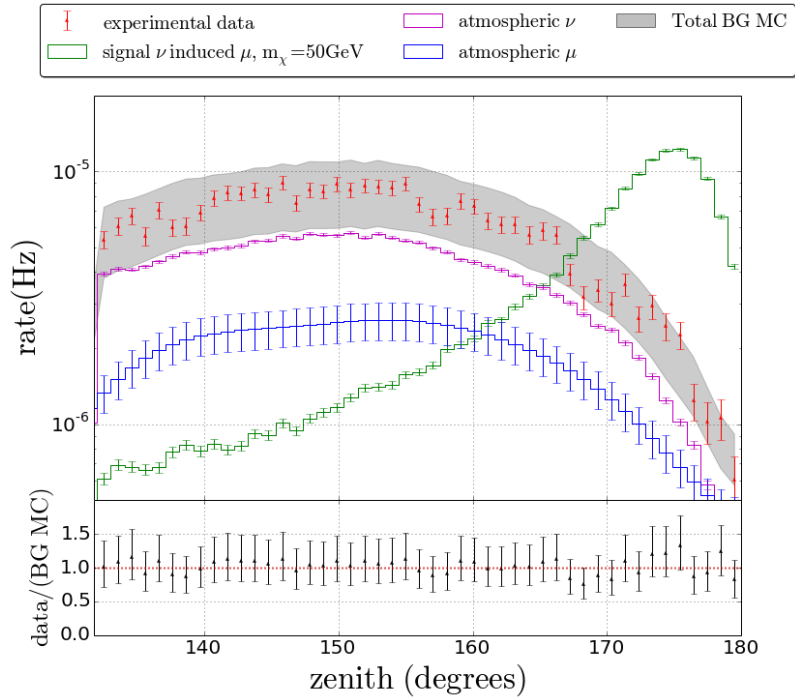
are presented in Fig. 9.6 and Table 9.3. Note that the quantities are presented as the limits on the amount of signal events per year, $\bar{\mu}_s^{90\%}/t_{\text{live}}$, hence they were obtained by extrapolation of the livetime of the final sample ($t_{\text{live}} = 311$ days) to a full year ($t_{\text{live}} = 365$ days). The results of the HIGH-E sample are not presented in detail here, but are included in Figs. 9.7 till 9.11.

Table 9.3: $\bar{\mu}_s^{90\%}$, $\hat{\mu}_s^{90\%}$, $\bar{\Gamma}_{\nu \rightarrow \mu}^{90\%}$ and $\hat{\Gamma}_{\nu \rightarrow \mu}^{90\%}$ of the LOW-E analysis for different WIMP models, assuming an uncertainty of 40% on the signal and background PDFs in the likelihood fit.

WIMP model		$\bar{\mu}_s^{90\%}$ (events/yr)	$\hat{\mu}_s^{90\%}$ (events/yr)	$\bar{\Gamma}_{\nu \rightarrow \mu}^{90\%}$ (events/km ³ /yr)	$\hat{\Gamma}_{\nu \rightarrow \mu}^{90\%}$ (events/km ³ /yr)
$m_\chi = 10$ GeV	$\chi\chi \rightarrow \tau^+\tau^-$	657_{-359}^{+326}	586	$1.45_{-0.79}^{+0.72} \times 10^6$	1.29×10^6
$m_\chi = 20$ GeV	$\chi\chi \rightarrow \tau^+\tau^-$	308_{-182}^{+287}	209	$2.04_{-1.21}^{+1.90} \times 10^5$	1.39×10^5
$m_\chi = 35$ GeV	$\chi\chi \rightarrow \tau^+\tau^-$	135_{-78}^{+129}	202	$3.89_{-2.25}^{+3.71} \times 10^4$	5.81×10^4
	$\chi\chi \rightarrow b\bar{b}$	415_{-242}^{+272}	405	$6.10_{-3.56}^{+4.01} \times 10^5$	5.59×10^5
$m_\chi = 50$ GeV	$\chi\chi \rightarrow \tau^+\tau^-$	100_{-57}^{+98}	189	$1.71_{-0.98}^{+1.68} \times 10^4$	3.25×10^4
	$\chi\chi \rightarrow b\bar{b}$	167_{-95}^{+160}	253	$1.12_{-0.64}^{+1.08} \times 10^5$	1.71×10^4
$m_\chi = 100$ GeV	$\chi\chi \rightarrow W^+W^-$	67_{-39}^{+64}	148	$3.16_{-1.83}^{+3.00} \times 10^3$	6.96×10^3
	$\chi\chi \rightarrow b\bar{b}$	85_{-49}^{+79}	172	$1.28_{-0.75}^{+1.20} \times 10^4$	2.60×10^4
$m_\chi = 250$ GeV	$\chi\chi \rightarrow W^+W^-$	55_{-32}^{+52}	116	$1.69_{-0.97}^{+1.57} \times 10^3$	3.53×10^3
	$\chi\chi \rightarrow b\bar{b}$	61_{-35}^{+56}	128	$2.85_{-1.63}^{+2.62} \times 10^3$	5.99×10^3
$m_\chi = 500$ GeV	$\chi\chi \rightarrow W^+W^-$	50_{-29}^{+45}	96	$1.94_{-1.12}^{+1.77} \times 10^3$	3.78×10^3
	$\chi\chi \rightarrow b\bar{b}$	55_{-32}^{+51}	111	$1.94_{-1.12}^{+1.79} \times 10^3$	3.93×10^3
$m_\chi = 1$ TeV	$\chi\chi \rightarrow W^+W^-$	44_{-25}^{+40}	78	$2.42_{-1.40}^{+2.18} \times 10^3$	4.28×10^3
	$\chi\chi \rightarrow b\bar{b}$	51_{-29}^{+48}	101	$1.68_{-0.96}^{+1.56} \times 10^3$	3.32×10^3
$m_\chi = 3$ TeV	$\chi\chi \rightarrow W^+W^-$	41_{-24}^{+37}	70	$2.92_{-1.68}^{+2.66} \times 10^3$	4.93×10^3
	$\chi\chi \rightarrow b\bar{b}$	47_{-27}^{+43}	87	$1.99_{-1.15}^{+1.82} \times 10^3$	3.67×10^3
$m_\chi = 5$ TeV	$\chi\chi \rightarrow W^+W^-$	39_{-22}^{+35}	62	$2.62_{-1.51}^{+2.34} \times 10^3$	4.15×10^3
	$\chi\chi \rightarrow b\bar{b}$	46_{-26}^{+42}	83	$2.04_{-1.18}^{+1.87} \times 10^3$	3.71×10^3



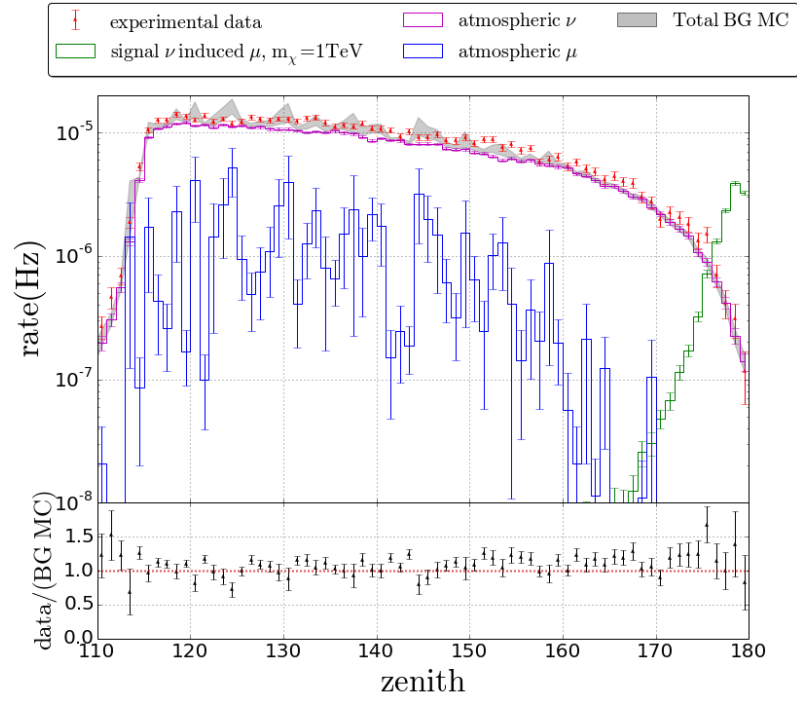
(a)



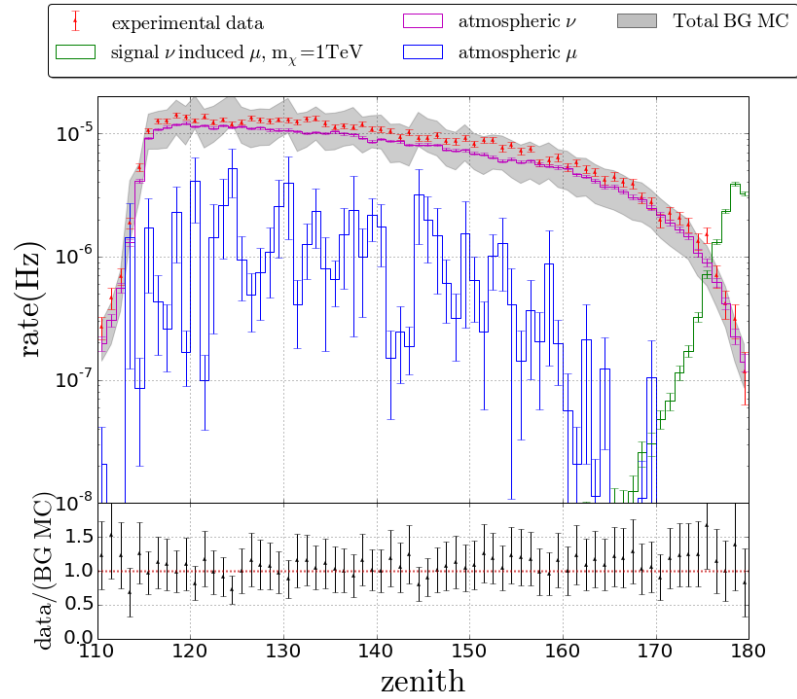
(b)

Figure 9.4: Distributions of the reconstructed zenith angles of the final LOWE samples. The gray band represents the one standard deviation uncertainty on the background simulation, calculated by only assuming the statistical uncertainties in the top panel, and also the systematic uncertainties in the bottom panel.

CHAPTER 9. MEASUREMENT OF THE WIMP ANNIHILATION RATE AND RELATED PHYSICAL QUANTITIES

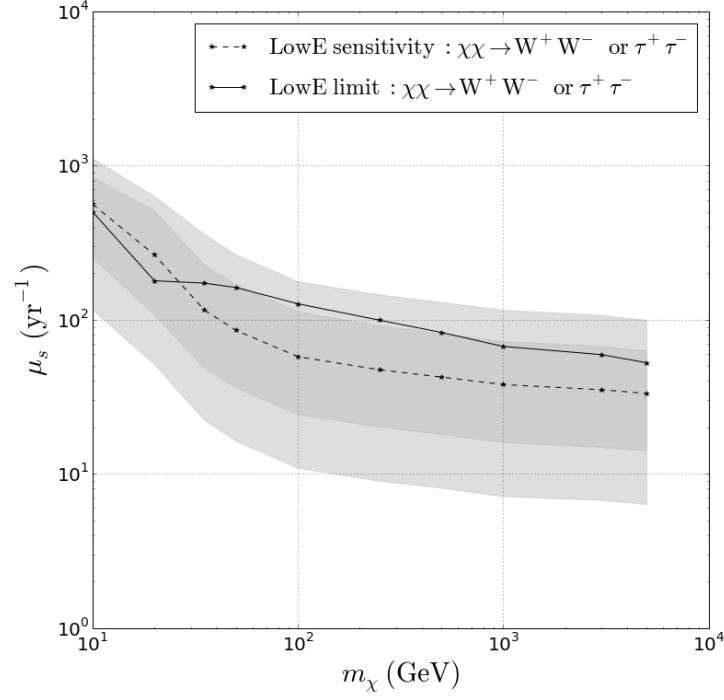


(a)

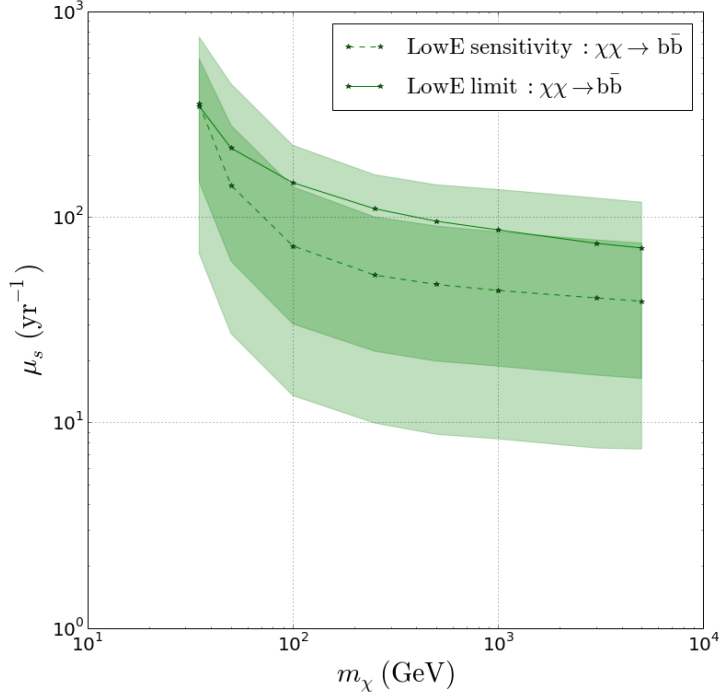


(b)

Figure 9.5: Distributions of the reconstructed zenith angles of the final HIGHE samples. The gray band represents the one standard deviation uncertainty on the background simulation, calculated by only assuming the statistical uncertainties in the top panel, and also the systematic uncertainties in the bottom panel.



(a)



(b)

Figure 9.6: Sensitivities (dashed line) and 90% CL upper-limits (solid line) of the LOWE analysis on $\mu_s^{90\%}/t_{\text{live}}$ as a function of the WIMP mass, for the hard (top) and soft (bottom) annihilation spectra. The shaded regions indicate the one (darker band) and two (lighter band) standard deviation uncertainties on the sensitivity. These results have been calculated considering a 40% uncertainty on the signal and background PDFs.

9.3 Flux Limits

As no excess has been found, 90% CL upper-limits on the volumetric flux, $\Gamma_{\nu \rightarrow \mu}$, and related physical quantities can be calculated. As discussed in Section 8.3, rescaling factors (Section 7.7.4) are applied in the LOWE analysis to calculate the sensitivities and the limits. This is done by rescaling the background simulation sets according to the values presented in Table 7.9 and rescaling the effective volume by a factor of 0.68, to account for the rescaling of the signal.

In the figures which are presented below, the sensitivities and limits, respectively indicated by the dashed lines and solid lines, are shown for the LOWE and HIGHE analysis. The shaded regions in the figures indicate the one standard deviation uncertainties on the sensitivities.

9.3.1 Upper-Limit on the Volumetric Flux

First, an upper-limit on the volumetric flux, $\Gamma_{\nu \rightarrow \mu}$, is calculated and compared to the sensitivity. Recall that the volumetric flux is a quantity that represents how many signal-induced neutrinos would convert into muons, μ_s , in a detector with a livetime t_{live} and an effective volume V_{eff} ,

$$\Gamma_{\nu \rightarrow \mu} = \frac{\mu_s}{t_{\text{live}} \times V_{\text{eff}}}. \quad (9.2)$$

Both the HIGHE and LOWE event selections were optimized to minimize this quantity.

The 90% CL upper-limit on the volumetric flux, $\Gamma_{\nu \rightarrow \mu}^{90\%}$, thus directly follows from the limit on the number of signal events per year, $\hat{\mu}_s^{90\%}/t_{\text{live}}$, presented in Fig. 9.6 and Table 9.3.

The 90% CL upper-limits of the LOWE analysis and HIGHE analysis on $\Gamma_{\nu \rightarrow \mu}$ as a function of the WIMP model are shown in Fig. 9.7. An overview of the values obtained for the LOWE analysis is given in Table 9.3.

9.3.2 Upper-Limit on the Annihilation Rate

The upper-limit on $\Gamma_{\nu \rightarrow \mu}$ can be converted to an upper-limit on the WIMP annihilation rate in the center of the Earth Γ_A , since [28]

$$\Gamma_{\nu \rightarrow \mu} = \frac{\Gamma_A}{4\pi D^2} \int_0^\infty dE_\nu \cdot \sigma_{\nu N}(E_\mu > E_{thr}|E_\nu) \cdot \rho_N \cdot \sum_X B_X \left(\frac{dN}{dE_\nu} \right)_X, \quad (9.3)$$

where D is the distance between the WIMP population and the detector, hence the radius of the Earth, $\sigma_{\nu N}$ is the neutrino-nucleon cross-section, ρ_N is the nucleon density at the detector, E_{thr} is the muon energy threshold of the simulation (this is 1 GeV in the simulation), and B_X is the branching ratio for the annihilation channel X with associated neutrino spectrum $\left(\frac{dN}{dE_\nu} \right)_X$.

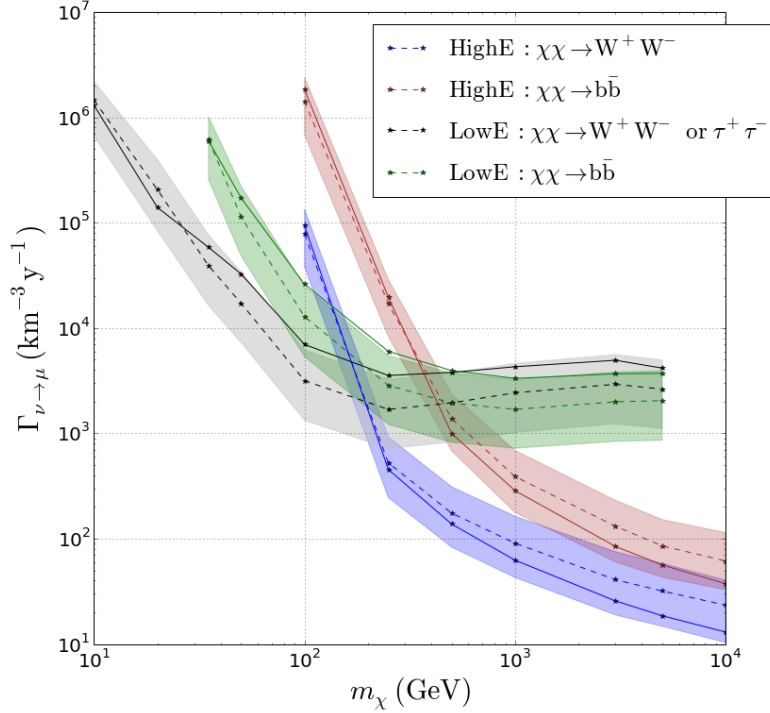


Figure 9.7: Sensitivities (dashed lines) and 90% CL upper-limits (solid lines) on $\Gamma_{\nu \rightarrow \mu}$ as a function of the WIMP mass of the LOWE analysis (gray and green lines) and the HIGHE analysis (blue and brown lines). The sensitivities and limits of the analyses are shown individually for the soft channel (LOWE : green, HIGHE : brown) and for the hard channel (LOWE : gray, HIGHE : blue). The shaded regions indicate the total one standard deviation uncertainty on the sensitivity. For the calculation of all the presented curves, both systematic and statistical uncertainties on the background and signal PDFs were taken into account.

The total neutrino spectrum dN_ν/dE_ν is given by

$$\left(\frac{dN_\nu}{dE_\nu}\right) = \sum_X B_X \left(\frac{dN}{dE_\nu}\right)_X. \quad (9.4)$$

This spectrum depends on the WIMP mass and composition. In this calculation, the same WIMP models (masses and channels) as before, listed in e.g. Table 9.3, are considered.

The sensitivities, $\bar{\Gamma}_A$, and 90% CL upper-limits, $\hat{\Gamma}_A$, on Γ_A as a function of the WIMP model are presented in Fig. 9.8a and Table 9.4. The 90% CL upper-limits of the LOWE analysis and HIGHE analysis on Γ_A as a function of the WIMP model are shown in Fig. 9.8. In Fig. 9.8a, the results of the LOWE analysis and HIGHE analysis are shown individually. An overview of the values obtained for the LOWE analysis is given in Table 9.4.

Note that the detector efficiency and energy threshold are taken into account in the calculation of the annihilation rate, Γ_A (Eq. (9.3)). Therefore, the upper-limits on the annihilation rate of Earth WIMPs, can be directly compared to previously published results. The most recent, still preliminary, limit comes from ANTARES [70], and prior to this result, one has to go back to AMANDA analyses [71, 179]. As the ANTARES limit is still preliminary, it is not included in Fig. 9.8b, but the results presented in [70] indicate that the ANTARES Earth WIMP search, based on 5 years of data, has similar sensitivities than the IC86-I (1 year) analysis presented in this thesis.

The combined result of the LOWE and HIGHE analyses on the hard channel is shown in Fig. 9.8b, where it is compared to the AMANDA limit [71, 179]. The presented AMANDA limit is a combination of two analyses, of which one is optimized for low mass ($50 \text{ GeV} < m_\chi < 250 \text{ GeV}$) WIMPs and based on three years of data [179] and the other analysis is optimized on a broad WIMP mass spectrum and used one year of data [71]. In the following figures, the AMANDA analysis with the best limit is picked for each WIMP mass for comparison to the IC86-I result.

The 90% CL upper-limit of the present analysis is about an order of magnitude lower than the AMANDA limit over the whole mass range, except for $m_\chi = 100 \text{ GeV}$. The smaller difference between the limits in this point is due to the combination of an underfluctuation in the AMANDA result [179] and an overfluctuation in the IC86-I result for this WIMP model.

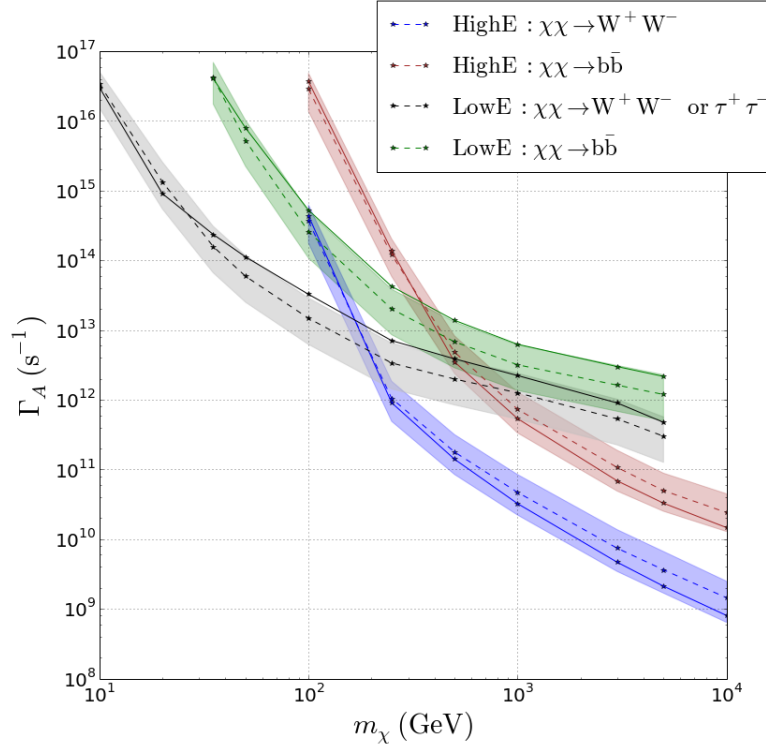
9.3.3 Upper-Limit on the Muon Flux

Once the limit on the WIMP annihilation rate is known, the upper-limit on the muon flux, caused by WIMP-induced neutrinos, can be calculated [28]

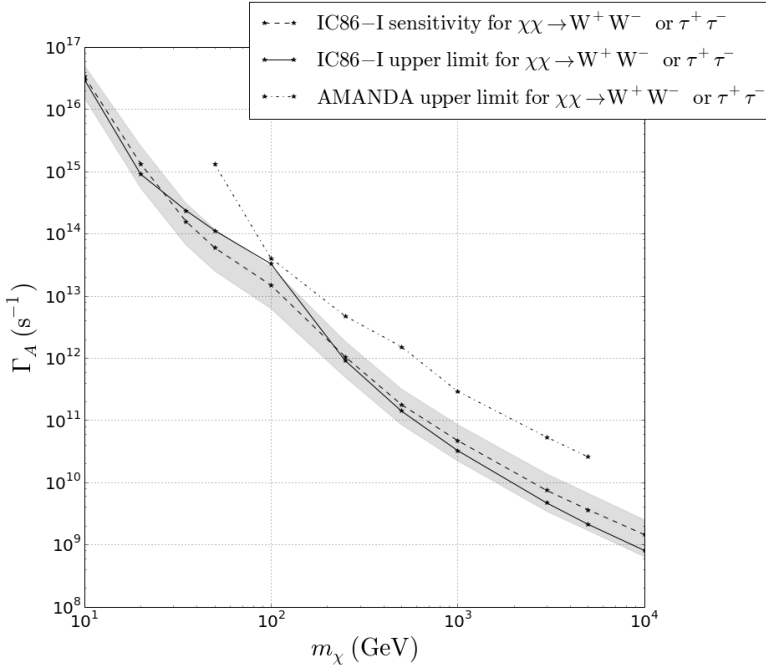
$$\Phi_\mu(E_\mu > E_{thr}) = \frac{\Gamma_A}{4\pi D^2} \int_{E_{thr}}^{\infty} dE_\mu \frac{dN_\mu}{dE_\mu}, \quad (9.5)$$

where $\frac{dN_\mu}{dE_\mu}$ is the neutrino-induced muon energy spectrum at the detector, and E_{thr} is the considered muon energy threshold. For the calculation of the presented limits, this threshold is set to a “standard” value of $E_{thr} = 1 \text{ GeV}$, such that the obtained results can be compared to the upper-limits set by other experiments. Fig. 9.9a shows the sensitivities and 90% CL upper-limits of the individual IC86-I analyses. An overview of the values obtained for the LOWE analysis is given in Table 9.4.

In Fig. 9.9b, the combined IC86-I results for the hard annihilation channel are presented, and again compared to the AMANDA 90% CL upper-limits.



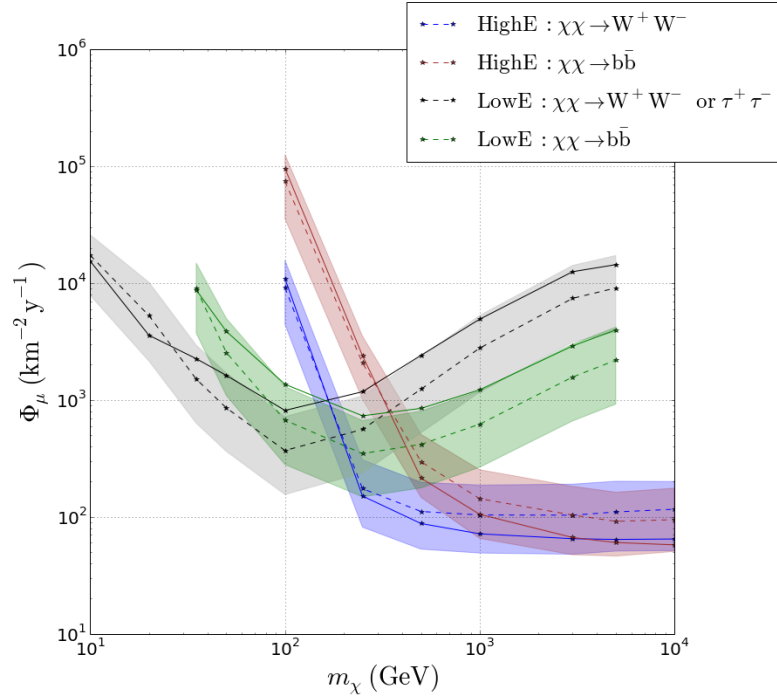
(a)



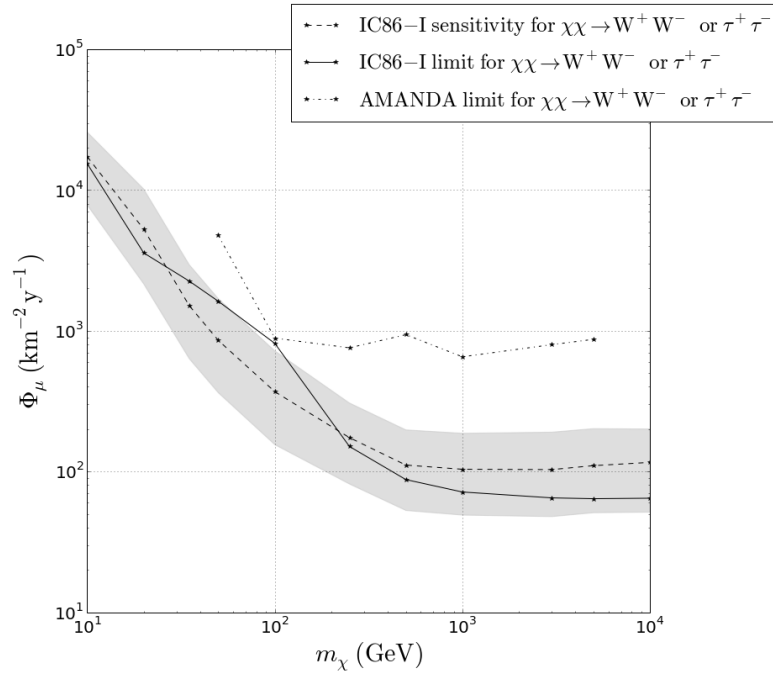
(b)

Figure 9.8: Sensitivities (dashed lines) and 90% CL upper-limits (solid lines) on Γ_A as a function of the WIMP mass. In the top panel, the individual results of the LOWE and HIGH E IC86-I analyses are shown. The bottom panel shows the combined IC86-I results on the hard channel and the most stringent 90% CL upper-limits set by AMANDA [71, 179] (dashed-dotted line). For the calculation of all the presented curves, both systematic and statistical uncertainties on the background and signal PDFs were taken into account.

CHAPTER 9. MEASUREMENT OF THE WIMP ANNIHILATION RATE AND RELATED PHYSICAL QUANTITIES



(a)



(b)

Figure 9.9: Sensitivities (dashed lines) and 90% CL upper-limits (solid lines) on Φ_μ as a function of the WIMP mass. In the top panel, the individual results of the LOWE and HIGH E IC86-I analyses are shown. The bottom panel shows the combined results of the LOWE and HIGH E IC86-I analyses on the hard channel and the most stringent 90% CL upper-limits set by AMANDA [71, 179] (dashed-dotted line). For the calculation of all the presented curves, both systematic and statistical uncertainties on the background and signal PDFs were taken into account.

Table 9.4: $\bar{\Gamma}_A^{90\%}$, $\hat{\Gamma}_A^{90\%}$, $\bar{\Phi}_\mu^{90\%}$ and $\hat{\Phi}_\mu^{90\%}$ of the LOWE analysis for different WIMP models, assuming an uncertainty of 40% on the signal and background PDFs in the likelihood fit.

WIMP model		$\bar{\Gamma}_A^{90\%}$ (ann./s)	$\hat{\Gamma}_A^{90\%}$ (ann./s)	$\bar{\Phi}_\mu^{90\%}$ (events/km ² /yr)	$\hat{\Phi}_\mu^{90\%}$ (events/km ² /yr)
$m_\chi = 10$ GeV	$\chi\chi \rightarrow \tau^+\tau^-$	$3.38_{-1.85}^{+1.68} \times 10^{16}$	3.01×10^{16}	$1.73_{-0.94}^{+0.86} \times 10^4$	1.54×10^4
$m_\chi = 20$ GeV	$\chi\chi \rightarrow \tau^+\tau^-$	$1.33_{-0.79}^{+1.24} \times 10^{15}$	0.90×10^{15}	$5.26_{-3.11}^{+4.89} \times 10^3$	3.57×10^3
$m_\chi = 35$ GeV	$\chi\chi \rightarrow \tau^+\tau^-$	$1.57_{-0.91}^{+1.50} \times 10^{14}$	2.35×10^{14}	$1.50_{-0.87}^{+1.43} \times 10^3$	2.52×10^3
	$\chi\chi \rightarrow b\bar{b}$	$4.16_{-2.42}^{+2.73} \times 10^{16}$	4.05×10^{16}	$8.92_{-5.20}^{+5.86} \times 10^3$	8.70×10^3
$m_\chi = 50$ GeV	$\chi\chi \rightarrow \tau^+\tau^-$	$5.89_{-3.39}^{+5.77} \times 10^{13}$	11.17×10^{13}	$8.52_{-4.90}^{+8.36} \times 10^2$	16.17×10^2
	$\chi\chi \rightarrow b\bar{b}$	$5.19_{-2.97}^{+4.98} \times 10^{15}$	7.88×10^{15}	$2.54_{-1.45}^{+2.43} \times 10^3$	3.85×10^3
$m_\chi = 100$ GeV	$\chi\chi \rightarrow W^+W^-$	$1.47_{-0.85}^{+1.40} \times 10^{13}$	3.25×10^{13}	$3.68_{-2.14}^{+3.50} \times 10^2$	8.12×10^2
	$\chi\chi \rightarrow b\bar{b}$	$2.58_{-1.51}^{+2.42} \times 10^{14}$	5.24×10^{14}	$6.70_{-3.90}^{+6.28} \times 10^2$	13.59×10^2
$m_\chi = 250$ GeV	$\chi\chi \rightarrow W^+W^-$	$3.36_{-1.93}^{+3.13} \times 10^{12}$	7.04×10^{12}	$5.59_{-3.22}^{+5.20} \times 10^2$	11.72×10^2
	$\chi\chi \rightarrow b\bar{b}$	$2.00_{-1.15}^{+1.84} \times 10^{13}$	4.22×10^{13}	$3.47_{-1.99}^{+3.19} \times 10^2$	7.30×10^2
$m_\chi = 500$ GeV	$\chi\chi \rightarrow W^+W^-$	$1.98_{-1.14}^{+1.81} \times 10^{12}$	3.85×10^{12}	$1.23_{-0.71}^{+1.13} \times 10^3$	2.41×10^3
	$\chi\chi \rightarrow b\bar{b}$	$6.77_{-3.90}^{+6.26} \times 10^{12}$	13.75×10^{12}	$4.16_{-2.40}^{+3.85} \times 10^2$	8.45×10^2
$m_\chi = 1$ TeV	$\chi\chi \rightarrow W^+W^-$	$1.26_{-0.73}^{+1.13} \times 10^{12}$	2.22×10^{12}	$2.77_{-1.61}^{+2.50} \times 10^3$	4.90×10^3
	$\chi\chi \rightarrow b\bar{b}$	$3.17_{-1.81}^{+2.94} \times 10^{12}$	6.25×10^{12}	$6.19_{-3.54}^{+5.74} \times 10^2$	12.18×10^2
$m_\chi = 3$ TeV	$\chi\chi \rightarrow W^+W^-$	$5.31_{-3.06}^{+4.84} \times 10^{11}$	8.98×10^{11}	$7.38_{-4.26}^{+6.73} \times 10^3$	12.48×10^3
	$\chi\chi \rightarrow b\bar{b}$	$1.62_{-0.94}^{+1.48} \times 10^{12}$	2.99×10^{12}	$1.57_{-0.91}^{+1.43} \times 10^3$	2.89×10^3
$m_\chi = 5$ TeV	$\chi\chi \rightarrow W^+W^-$	$2.99_{-1.73}^{+2.67} \times 10^{11}$	4.74×10^{11}	$9.05_{-5.23}^{+8.09} \times 10^3$	14.34×10^3
	$\chi\chi \rightarrow b\bar{b}$	$1.19_{-0.69}^{+1.09} \times 10^{12}$	2.16×10^{12}	$2.18_{-1.26}^{+2.00} \times 10^3$	3.96×10^3

9.3.4 Upper-Limit on the Spin-Independent cross-section

The previously discussed quantities can only be compared with the results of Earth WIMP searches performed by other neutrino detectors. To be able to compare these results to other direct and indirect searches, an upper-limit on the WIMP-nucleon cross-section should be calculated.

In Section 2.6, it was explained that the relation between the WIMP annihilation rate, $\Gamma_A(t)$, and the WIMP capture, C_C , at a time t , is given by

$$\Gamma_A(t) = \frac{1}{2}C_C \tanh^2 \left(t\sqrt{C_C C_A} \right), \quad (9.6)$$

where C_A is given by [28]

$$C_A = \frac{\langle \sigma_{Av} \rangle \cdot (m_\chi / (10 \text{ GeV}))^{3/2}}{2\sqrt{8} \cdot 10^{25} \text{ cm}^3}, \quad (9.7)$$

with $\langle \sigma_{Av} \rangle$ the velocity-averaged self-annihilation cross-section.

The capture rate (C_C) of WIMPs mainly depends on the WIMP-nucleon cross-section $\sigma_{\chi-N}$, the WIMP mass m_χ and the mass and distribution of the elements in the Earth, as described in detail in [28]. For capture in the Earth, the main contribution will thus come from the spin-independent component $\sigma_{\chi-N}^{SI}$ which is quadratically proportional to the atomic mass of the elements in the Earth, i.e. to A^2 .

Contrary to the Sun, there is no equilibrium between WIMP capture and annihilation in the Earth, as the effective capture volume of the Earth is too small for the establishment of such an equilibrium over the lifetime of the Earth. Therefore the Earth WIMP analysis is sensitive to both $\sigma_{\chi-N}^{SI}$ and $\langle \sigma_{Av} \rangle$, which respectively determine the capture and the annihilation rate. For a particular WIMP model (mass and channel) the 90% confidence interval upper-limits on the WIMP annihilation rate, $\bar{\Gamma}_A^{90\%}$, can be converted to a bound in the $C_A - C_C$ plane. This is obtained by scanning over a range of values of $\langle \sigma_{Av} \rangle$ (and thus C_A (Eq. 9.7)) and calculating C_C through Eq. (9.6). The obtained value of C_C can then be translated to $\sigma_{\chi-N}^{SI}$ [28], yielding a bound in the $\langle \sigma_{Av} \rangle - \sigma_{\chi-N}^{SI}$ plane.

This is shown in Fig. 9.10, where the IC86-I Earth WIMP limit is plotted for 50 GeV WIMPs annihilating into $\tau^+\tau^-$ (black solid line) and 1 TeV WIMPs annihilating into W^+W^- (green solid line). As a comparison, the limits of LUX, which are the current best limits on $\sigma_{\chi-N}^{SI}$ for the considered WIMP models (horizontal dashed lines), are shown. Note that the LUX limits are independent of $\langle \sigma_{Av} \rangle$ as LUX is not sensitive to this quantity.

As other experiments are in general only sensitive to $\langle \sigma_{Av} \rangle$ or $\sigma_{\chi-N}^{SI}$ and the present Earth WIMP analysis is sensitive to both these quantities, the results from our analysis provide a natural bridge between the different dark matter experiments.

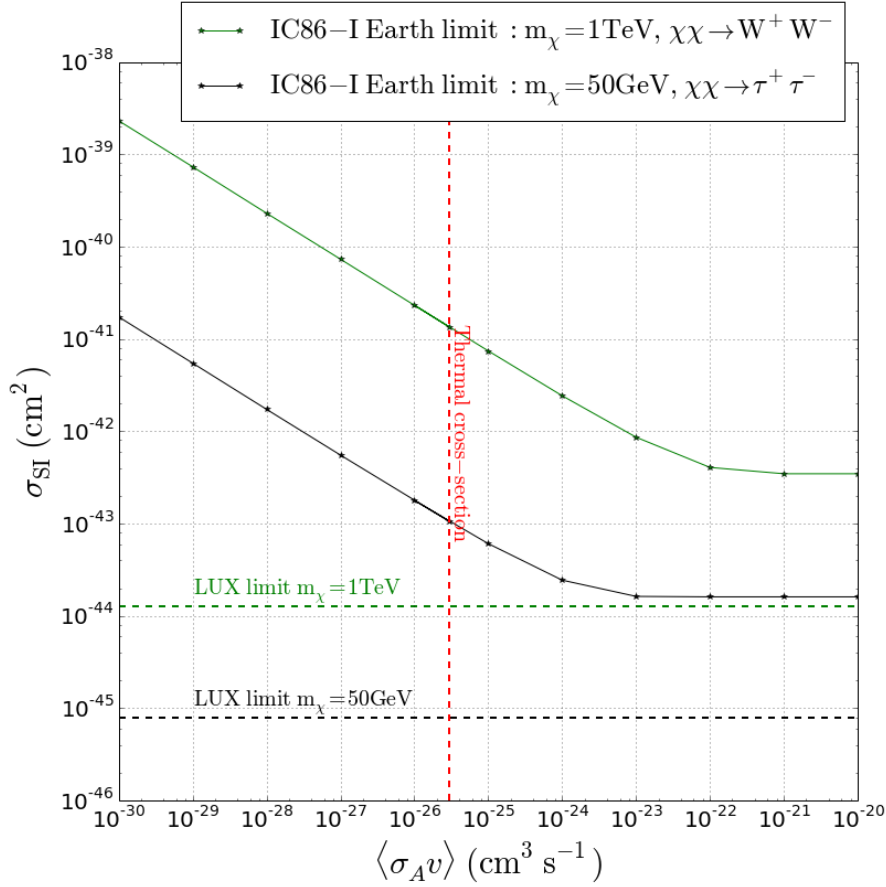


Figure 9.10: 90% CL upper-limits in the $\langle\sigma_{AV}\rangle - \sigma_{\chi-N}^{SI}$ plane for two WIMP models. The IC86-I Earth WIMP limit is plotted for 50 GeV WIMPs annihilating into $\tau^+\tau^-$ (black solid line) and 1 TeV WIMPs annihilating into W^+W^- (green solid line). As a comparison, the limits of LUX, which give the current best limits on $\sigma_{\chi-N}^{SI}$ for these WIMP models (horizontal dashed lines), are shown. The vertical red dashed line indicates the thermal annihilation cross-section $\langle\sigma_{AV}\rangle = 3 \cdot 10^{-26} \text{cm}^3 \text{s}^{-1}$.

To convert the limit on Γ_A (Fig. 9.8b) to a limit on $\sigma_{\chi-N}^{SI}$, an assumption needs to be made on the value of $\langle\sigma_{AV}\rangle$. As an example, the thermal annihilation cross-section $\langle\sigma_{AV}\rangle = 3 \cdot 10^{-26} \text{cm}^3 \text{s}^{-1}$ (indicated by the vertical dashed line in Fig. 9.10) is assumed. The resulting 90% CL upper-limit on the spin-independent cross-section $\sigma_{\chi-N}^{SI}$ of the combined IC86-I analysis is shown in Fig. 9.11. This figure also includes the current best results of direct detection experiments, as well as the preliminary results of the 5 year ANTARES Earth WIMP search and the most recent ICECUBE Solar WIMP searches [138, 180] based on 3 years of ICECUBE data. The ANTARES limit in this figure was adopted from [70], in which the preliminary result of an Earth WIMP search based on 5 years of ANTARES data is presented. This ANTARES limit is roughly a

CHAPTER 9. MEASUREMENT OF THE WIMP ANNIHILATION RATE AND RELATED PHYSICAL QUANTITIES

factor of 2-3 better than the IC86-I Earth WIMP analysis in the WIMP mass range 10 – 150 GeV. This is mainly due to the longer livetime of the considered data sample. For WIMP masses above ~ 150 GeV, the ICECUBE result is slightly better than the ANTARES result.

Note that, under the considerations made above on $\langle\sigma_A v\rangle$, the analysis presented in this thesis provides the best ICECUBE limits on $\sigma_{\chi-N}^{SI}$ for WIMP masses around 50 GeV and below 20 GeV, hence the IC86-I Earth WIMP analysis is complementary to the ICECUBE Solar WIMP analyses.

The shape of the IC86-I Earth WIMP analysis 90% CL upper-limit, reflects the A^2 dependence of $\sigma_{\chi-N}^{SI}$ and thus on the capture of WIMPs in the Earth, which was also demonstrated in Fig. 7.2.

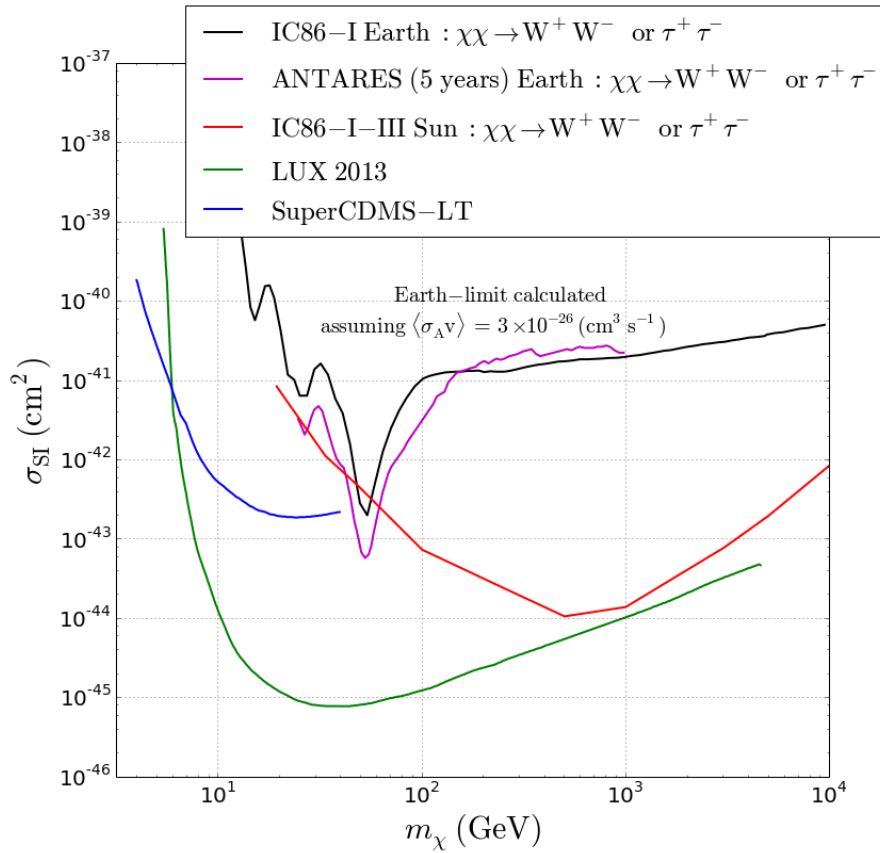


Figure 9.11: 90% CL upper-limits on $\sigma_{\chi-N}^{SI}$ as a function of the WIMP mass for several direct and indirect detection experiments. In this figure, the IC86-I Earth WIMP limit, including statistical and systematic uncertainties, is compared to the current best results of direct detection experiments, set by CDMSlite [42] and LUX [36], as well as the preliminary results of the most recent ICECUBE Solar WIMP searches [138, 180] and the preliminary result of the 5 year ANTARES Earth WIMP search [70].

Summary

In this chapter, the reconstructed zenith angle distribution of the complete IC86-I data set was compared to the background expectation. It was found that the distribution of the experimental data agrees with the background-only scenario within one standard deviation uncertainty over the whole zenith range.

The systematic uncertainties for the LOWE sample were studied in detail, and were calculated to be $+47\% - 37\%$ for the rescaled atmospheric neutrino simulation, and $+17\% - 20\%$ for the atmospheric muons. The systematic uncertainties of the simulated atmospheric muons and neutrinos in the HIGH E sample were calculated to be $+15\% - 18\%$ and $+34\% - 35\%$ respectively. In the likelihood analysis, a total uncertainty of 40% for the LOWE sample and 30% for the HIGH E sample, was considered.

As no signal was observed, 90% CL upper-limits were set on the volumetric flux, $\Gamma_{\nu \rightarrow \mu}$, the Earth WIMP annihilation rate, Γ_A , and the muon flux, Φ_μ , from WIMP-induced neutrinos at the detector. The derived upper-limits were compared to the limits set by Earth WIMP searches done with other neutrino telescopes, and were found to be comparable to the upper-limits set by a similar analysis using five years of ANTARES data and roughly a factor of ten better than the AMANDA Earth WIMP limits.

The limits were interpreted in the $\langle \sigma_{AV} \rangle - \sigma_{\chi-N}^{SI}$ phase space for hard annihilating 50 GeV and 1 TeV WIMPs. Contrary to other experiments, which in general are only sensitive to one of these quantities, the Earth WIMP analysis is sensitive to both these quantities, as there is no equilibrium between WIMP capture and annihilation in the Earth.

Finally, a 90% CL upper-limit on the spin-independent cross-section was calculated, assuming the thermal annihilation cross section $\langle \sigma_{AV} \rangle = 3 \cdot 10^{-26} \text{cm}^3 \text{s}^{-1}$. This limit was compared to the limit set by the most recent ICECUBE Solar WIMP searches, and it was found that the IC86-I Earth WIMP analysis provides better limits for WIMP masses below 100 GeV. The current best direct detection limits on this quantity are however still more than an order of magnitude better.

Life is like riding a bicycle. To keep your balance, you must keep moving.

Albert Einstein

10

Summary and Outlook

10.1 Summary

Understanding the nature of dark matter is one of the major challenges in modern physics. Many effects caused by this mysterious matter have been seen, but until today, there is no clear idea on what this dark matter is made of. The current best model to describe our Universe, the Lambda Cold Dark Matter model, naturally incorporates a dark matter component, which makes up about 27% of all the energy in the Universe and roughly 80% of all the matter.

In the most popular models, the dark matter is made up of particles, which are stable, slowly moving (cold), heavy and only interact weakly and gravitationally with ordinary baryonic matter. These particles are therefore called Weakly Interacting Massive Particles (WIMPs). An excellent candidate for the WIMP is the hypothetical neutralino, the Lightest Supersymmetric Particle (LSP), arising in supersymmetric theories beyond the Standard Model of particle physics.

A dense WIMP population is expected in the center of heavy celestial bodies such as the Earth, which arises when dark matter particles from the galactic halo become bound in the gravitational potential of the solar system as it passes through the galaxy. These particles may then scatter weakly on nuclei in the Sun or Earth and lose energy, after which they get trapped. Over time, this leads to an accumulation of dark matter in the center of the celestial body. If the accumulated dark matter density reaches a high enough value, it may self-annihilate, generating a flux of Standard Model particles which is spectrally dependent on the annihilation channel and WIMP mass. A thick dark disc in the Milky Way would enhance the WIMP capture in the Earth, which would lead to

a higher neutrino flux than expected from the Standard Halo Model.

Neutrino telescopes are the only detectors which are able to observe these signals, as neutrinos are the only Standard Model particles which can travel from the center of the Earth to the detector, with a low probability to interact on their path. Only few experiments have looked for an excess of neutrinos from WIMP annihilations in the center of the Earth. The most recent (yet unpublished) limit comes from the ANTARES neutrino telescope. Prior to this result, one has to go back to AMANDA, the predecessor of ICECUBE. The fact that there has not been a search for Earth WIMPs with ICECUBE, together with the indication of the possible existence of a dark disc, and hence an expected increase of the Earth WIMP-induced neutrino flux, were the main motivations to perform the first search for Earth WIMP-induced neutrinos with the ICECUBE neutrino detector.

In this thesis, the first Earth WIMP search with ICECUBE was presented. In the present analysis, the first year of data recorded with the full 86-string ICECUBE detector was used.

The cleaned data sample has a livetime of 327 days and was measured between the 13th of May in 2011 and the 15th of May in 2012.

The main goal of the work presented in this thesis, was to search for the presence of neutrinos induced by 50 GeV Earth WIMPs, annihilating to a $\tau^+\tau^-$ pair. This WIMP mass was chosen, as for this mass the WIMP capture in the Earth is most efficient, due to the high Iron abundance in the Earth. To be sensitive to a wider range of WIMP masses, a statistically independent analysis, optimized on 1 TeV WIMPs annihilating into W^+W^- , was done in parallel by Isabelle Anseau and Jan Lünemann.

Both analyses searched for an excess of neutrinos from the center of the Earth above the expected atmospheric background, hence this was an indirect search for dark matter.

ICECUBE triggers on atmospheric particles and detector noise at a rate of roughly 4 kHz ($\mathcal{O}(10^{11})$ /year), while the expected WIMP-induced muon flux is at most at the order of a few μHz ($\mathcal{O}(10^3)$ /km²/year). To reduce the overwhelming background, a dedicated and sophisticated event selection was necessary.

Due to the zenith dependent acceptance of the detector, it was not possible to define an off-source dataset for the Earth WIMP analysis. Therefore this analysis had to rely on simulations to estimate the background and it was thus of great importance that the simulation of the atmospheric muon and atmospheric neutrino data was correct. To check if the background simulation was correctly describing the experimental data, 10% of the data were used, and at each step of the event selection the simulated background was compared to these data. A lot of effort went into the reduction of the disagreement between data and the background simulation, here referred to as data-MC disagreement.

In a first step, the data rate is reduced from $\mathcal{O}(4)$ kHz to $\mathcal{O}(1)$ kHz by removing obvious noise triggers and bad, low quality events. The “cleaned” data are then sent to the data warehouse in Madison, where they are stored and reprocessed. Dedicated analyses, such as the present analysis, start from this level, referred to as LEVEL 2,

onwards.

The Earth WIMP event selection process started by selecting online filters and removing correlated detector noise clusters. The data rate was further reduced to roughly 3 Hz by applying linear cuts on the direction and starting point of the event. After this step, the sample was split in two statistically independent data sets, based on the reconstructed energy of the event. The data rate of each of the samples was consequently further reduced in two independent event selections, a low energy event selection and a high energy event selection, optimized for signal neutrinos from 50 GeV WIMPs and 1 TeV WIMPs respectively.

Both analyses made use of Boosted Decision Trees (BDT), which is a machine learning technique that is designed to optimally separate signal from background by assigning a score between -1 (background-like) and +1 (signal-like) to each event. Before training the BDT, one has to be sure that the simulation is representing the experimental data in a correct way. For this reason additional linear cuts were made prior to the BDT training in order to get good agreement between data and simulation. While the low energy optimization only used one single BDT, the high energy part used the Pull-Validation method, in which 200 BDTs are trained and applied to each event. The cuts on the BDT scores were selected such that the best sensitivities for the WIMP signals were achieved. The final numbers in each sample are summarized in Table 10.1.

Table 10.1: Efficiencies in selecting the simulated signal (w.r.t. LEVEL 2) and rates of the simulated background and data events at LEVEL 2 and at the final level.

	# WIMP (%)		Simulated Background (Hz)			Data (Hz)
	$m_\chi = 50 \text{ GeV}$	$m_\chi = 1 \text{ TeV}$	ν_{atm}	μ_{atm}	total	
LEVEL 2	100.0	100.0	27×10^{-3}	650	650	670
final LOWE sample	15.6	-	0.20×10^{-3}	0.08×10^{-3}	0.28×10^{-3}	0.28×10^{-3}
final HIGHE sample	-	17.0	0.46×10^{-3}	0.06×10^{-3}	0.52×10^{-3}	0.56×10^{-3}

After reducing the data samples to roughly $\mathcal{O}(10^4)$ events/year, the sensitivities of the final samples for a contribution of muons from Earth-WIMP-induced neutrinos on top of the atmospheric background, were calculated. As it was not possible to define an off-source dataset, the background was calculated from simulated atmospheric muons and neutrinos. In the present analysis, the sensitivity was defined as the median upper-limit at 90% confidence level of the volumetric flux in a background-only scenario, $\bar{\Gamma}_{\nu \rightarrow \mu}^{90\%}$.

The calculation of the sensitivities was based on the reconstructed zenith angle distributions, θ , of the simulated signal and background events, which were used as Probability Density Functions (PDFs) in a shape analysis. The PDFs were then used to calculate the volumetric flux, $\Gamma_{\nu \rightarrow \mu}$, which depends on the final sample and thus on the cut on the BDT score. The cuts on the BDT scores were chosen such that they minimized $\bar{\Gamma}_{\nu \rightarrow \mu}^{90\%}$, to optimize the sensitivities.

The sensitivities of both the LOWE and HIGHE analysis were then calculated for different WIMP masses in the range 10 GeV-10 TeV, and were combined by selecting the

analysis with the best sensitivity at each mass.

In the final chapter, the reconstructed zenith angle distribution of the complete IC86-I data set was compared to the background expectation. It was found that the distribution of the experimental data agrees with the background-only scenario within one standard deviation uncertainty over the whole zenith range.

The systematic uncertainties were studied, and were calculated to be of the order of $+50\% - 37\%$ for the rescaled atmospheric neutrino simulation. The main source of this systematic uncertainty is caused by the non-simulation of coincident atmospheric muons in the available atmospheric neutrino simulation. The effects of these coincident muons were absorbed in a scaling factor which was applied to both the atmospheric neutrinos as well as the signal neutrinos, and lead to a large systematic uncertainty.

Based on the studies of the systematic uncertainties on the atmospheric neutrinos, a systematic uncertainty of 20% was assumed for the atmospheric muon background. In the likelihood analysis, a total uncertainty of 40% was used, containing both the statistical and the systematic uncertainty

As no signal was observed, 90% CL upper-limits were set on the volumetric flux, the WIMP annihilation rate and the muon flux from WIMP-induced neutrinos at the detector. The derived upper-limits were compared to the limits set by Earth WIMP searches performed by other neutrino telescopes, and were found to be comparable to the upper-limits set by a similar analysis using five years of ANTARES data and roughly a factor of ten better than the AMANDA Earth WIMP limits.

The limits were interpreted in the $\langle\sigma_{AV}\rangle - \sigma_{\chi-N}^{SI}$ phase space for hard annihilating 50 GeV and 1 TeV WIMPs. Contrary to other experiments, which in general are only sensitive to one of these quantities, the Earth WIMP analysis is sensitive to both these quantities, as there is no equilibrium between WIMP capture and annihilation in the Earth. This way, the obtained results from this analysis provide a natural bridge between the different dark matter experiments.

Finally, 90% CL upper-limit on the spin-independent cross-section was calculated, assuming the thermal annihilation cross section $\langle\sigma_{AV}\rangle = 3 \cdot 10^{-26} \text{cm}^3 \text{s}^{-1}$. This limit was compared to the limit set by the most recent ICECUBE Solar WIMP searches, and it was found that the IC86-I Earth WIMP analysis provides better limits for WIMP masses around 50 GeV and is sensitive to WIMP masses down to 10 GeV, hence these analyses are very complementary.

10.2 Outlook

The present analysis was the first Earth WIMP analysis with ICECUBE. Even though this analysis gives very competing limits, there is still room for improvement.

The main improvement would come from better simulations of both the WIMP-induced neutrinos and the atmospheric background muons and neutrinos. The WIMP-

induced neutrino simulation as well as the atmospheric neutrino simulation should contain coincident atmospheric muon events, as it became clear in this thesis, that these coincident particles have a big impact on the final samples. Including coincident particles in the simulation, would give more correct results, and thus no need of rescaling and a much lower systematic uncertainty on the final samples.

Another improvement would come from an accurate simulation of correlated detector noise in the atmospheric muon sample. As this correlated noise was not well simulated, there was a large data-MC disagreement in the low levels of the present analysis, mainly in the LOWE part of the analysis, where the noise has a high impact. Special efforts had to be put in the reduction of this disagreement, and during this reduction, the signal rate was also reduced, leading to a less efficient final sample.

Finally, this type of analysis needs more atmospheric muon statistics, as this analysis has to rely on simulations to estimate the background. In the present analysis, special methods were used to smoothen the simulated atmospheric muon distributions, but these methods would not be necessary if more statistics would be available.

Improvements in the simulation would thus provide better sensitivities and limits, as more signal could be kept in the event selection, and the systematic uncertainty would be reduced.

The sensitivity of the present analysis would also improve, if more data were used. This analysis is based on one year of ICECUBE data, but in the meanwhile, the full 86-string ICECUBE detector already recorded over four years of data. The addition of more years to the analysis would improve the sensitivity, and thus either point to a WIMP signal, or improve the upper-limits.

Another point on which people can focus in the (near) future is the interpretation of the results of the analysis presented in this thesis. It was discussed several times that a dark disc would boost the expected muon flux. Hence, as the set limits are the current best upper-limits on the Earth WIMP-induced muon flux, one can verify what the consequences of these limits are on the features of a possible dark disc.

Appendices



Distributions of the Variables used in the BDT

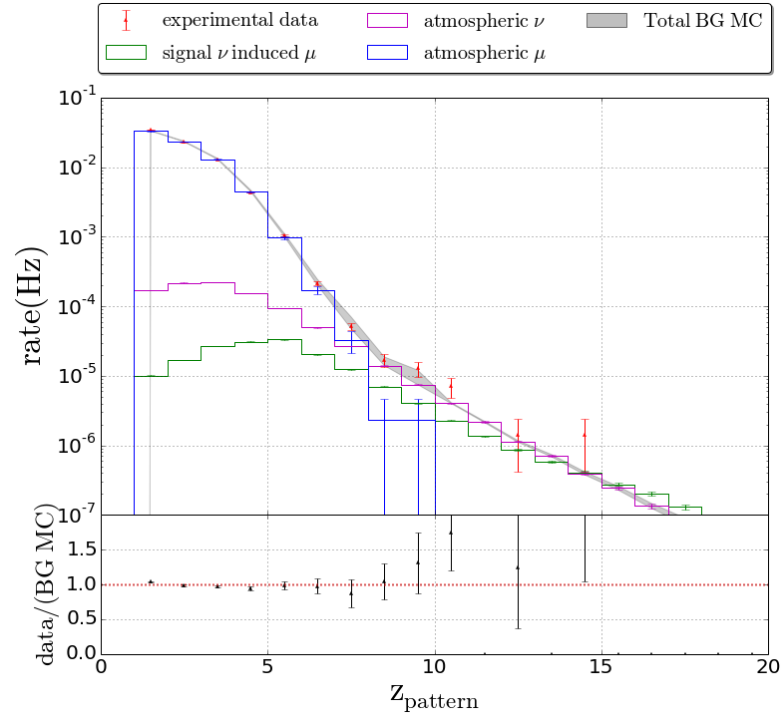
The histograms in this appendix show the distributions of the variables used for the BDT training in the LOWE analysis (Section 7.7.4), before (a) and after (b) the BDT cut. In each figure, 4 data samples are shown

- The IC86-I burnsample, i.e. 10% of the experimental data: red dots with error-bars.
- Atmospheric muons simulated with CORSIKA: blue histogram.
- The total sample of atmospheric neutrinos of all flavors simulated with NuGen and GENIE (combined as described in Section 6.2.1), including oscillation effects in the Earth: magenta histogram.
- Signal muon neutrinos, produced by 50 GeV WIMPs annihilating into $\tau\bar{\tau}$ simulated with WimpSim: green histogram.

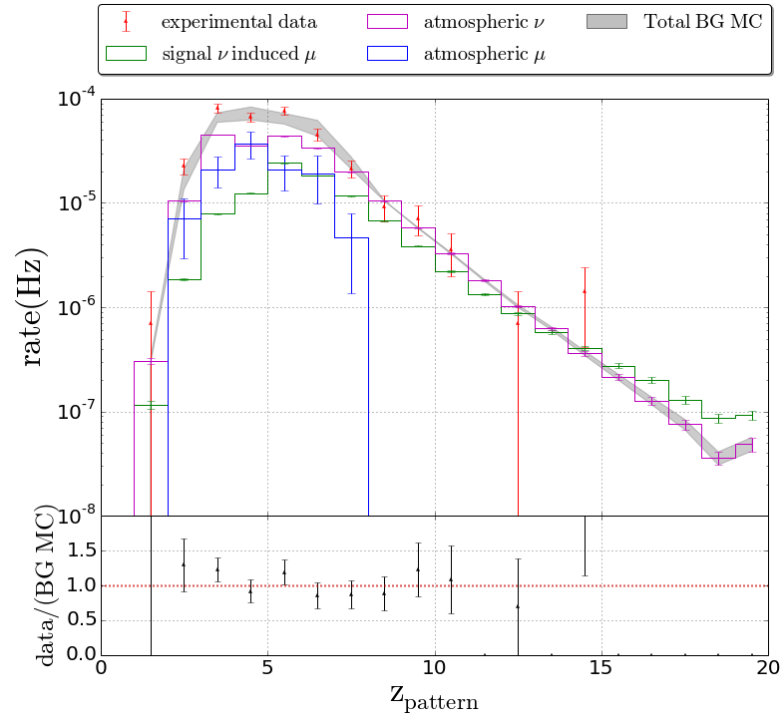
The simulation of the atmospheric muons and atmospheric neutrinos are weighted such that they represent the true rates in the detector, and can directly be compared to the burnsample data. The distribution of the simulated signal is scaled up, in order to be visible. So contrary to the other distributions, the absolute value of the bin heights have no meaning in case of the signal.

The sum of the simulated atmospheric muons and neutrinos is shown as a gray band, of which the width represents one standard deviation (statistical) uncertainty on that sum. At the bottom of each histogram the ratio of the experimental data over the total background simulation is shown, again with one standard deviation uncertainty.

APPENDIX A. DISTRIBUTIONS OF THE VARIABLES USED IN THE BDT

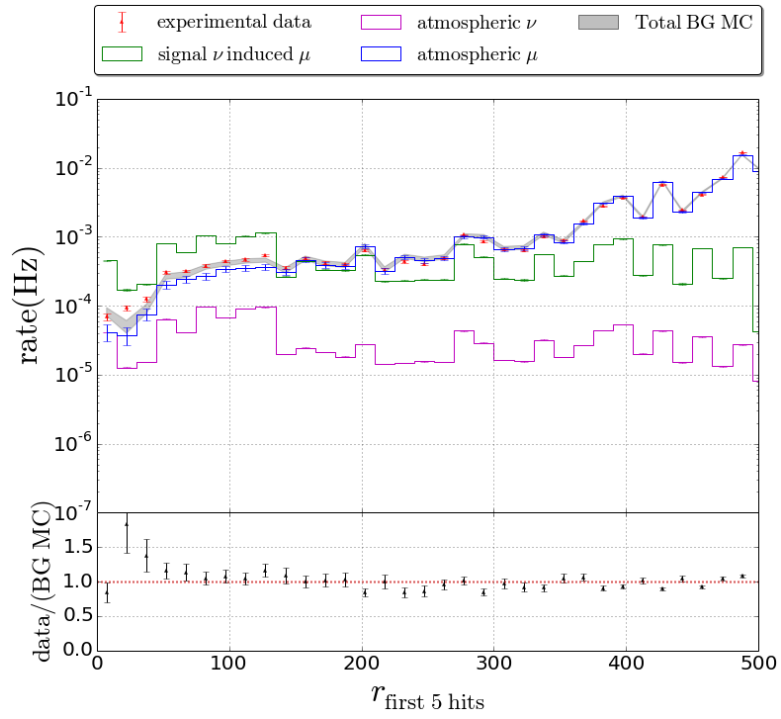


(a)

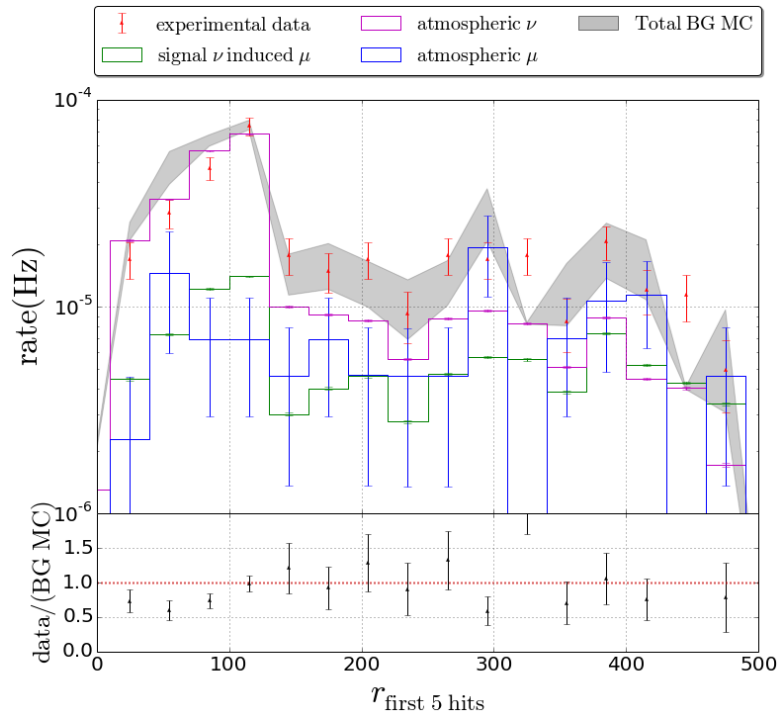


(b)

Figure A.1: z_{pattern} distributions before (a) and after (b) the BDT cut.

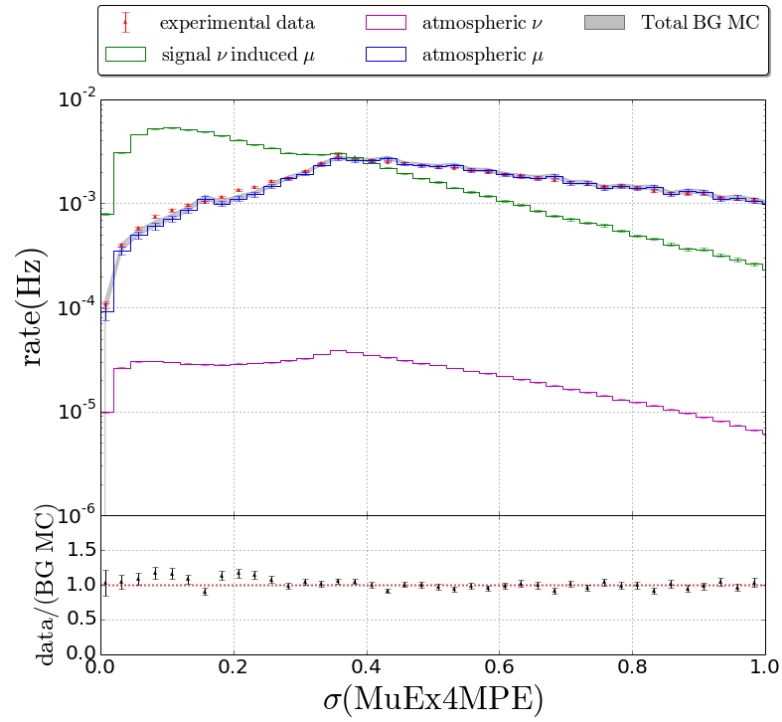


(a)

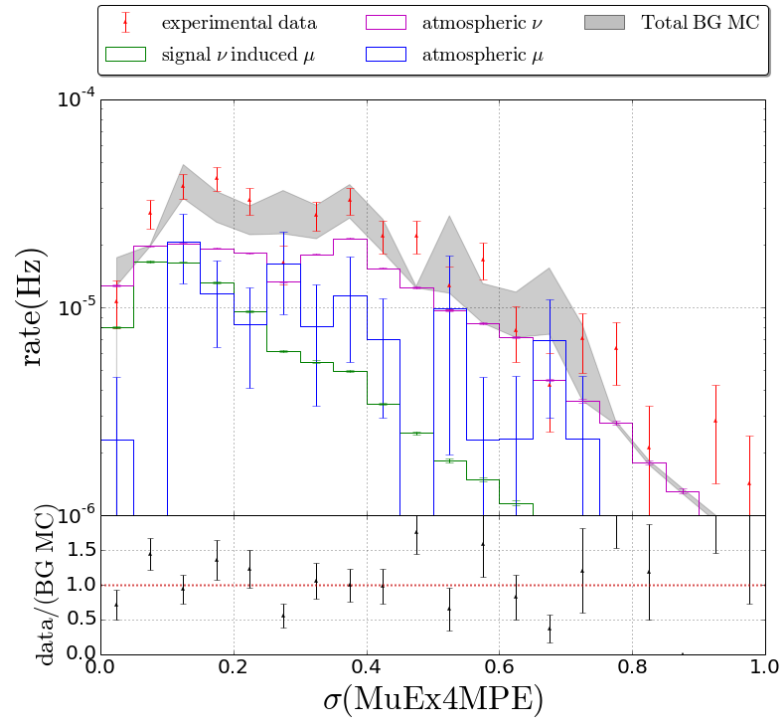


(b)

Figure A.2: $r_{\text{first 5 hits}}$ distributions before (a) and after (b) the BDT cut.

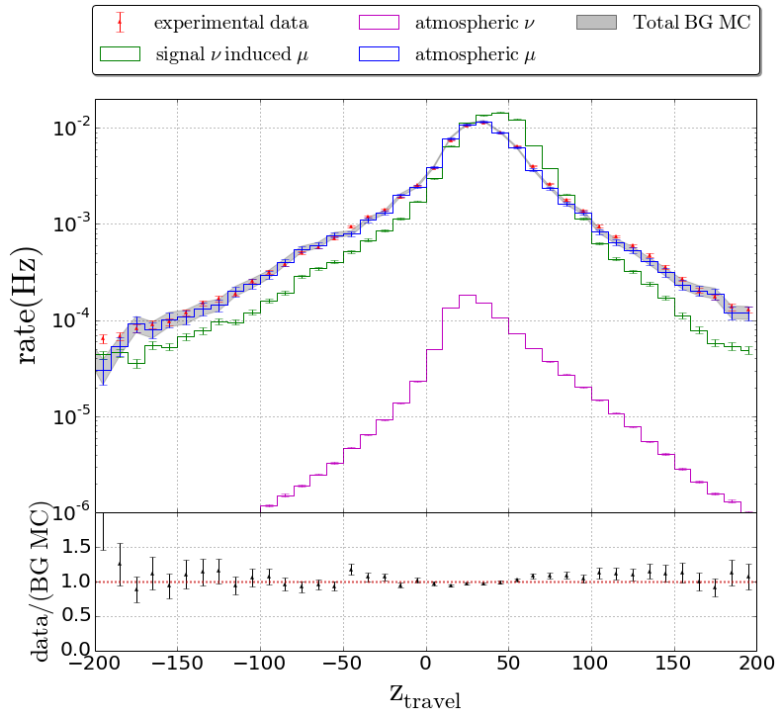


(a)

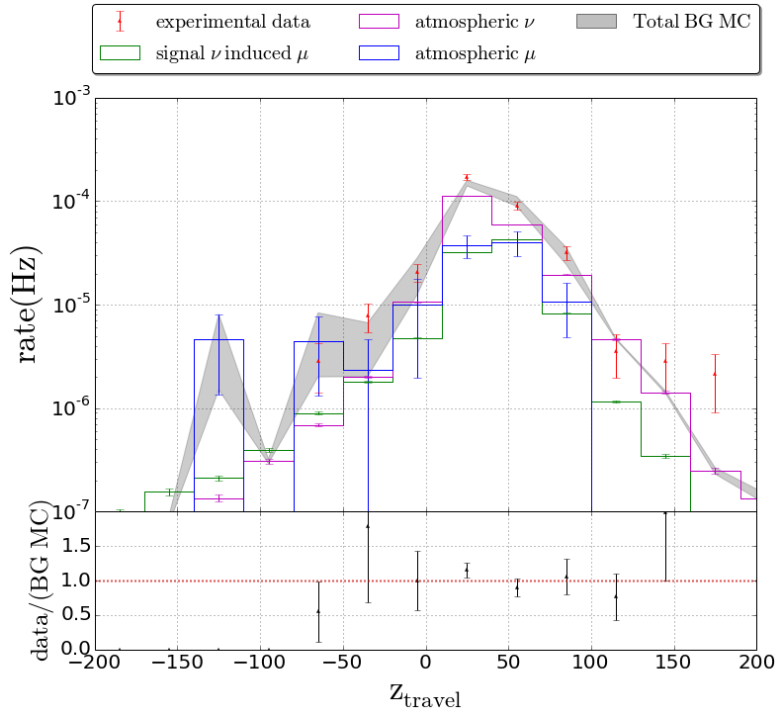


(b)

Figure A.3: $\sigma(\text{MuEx4MPE})$ distributions before (a) and after (b) the BDT cut.

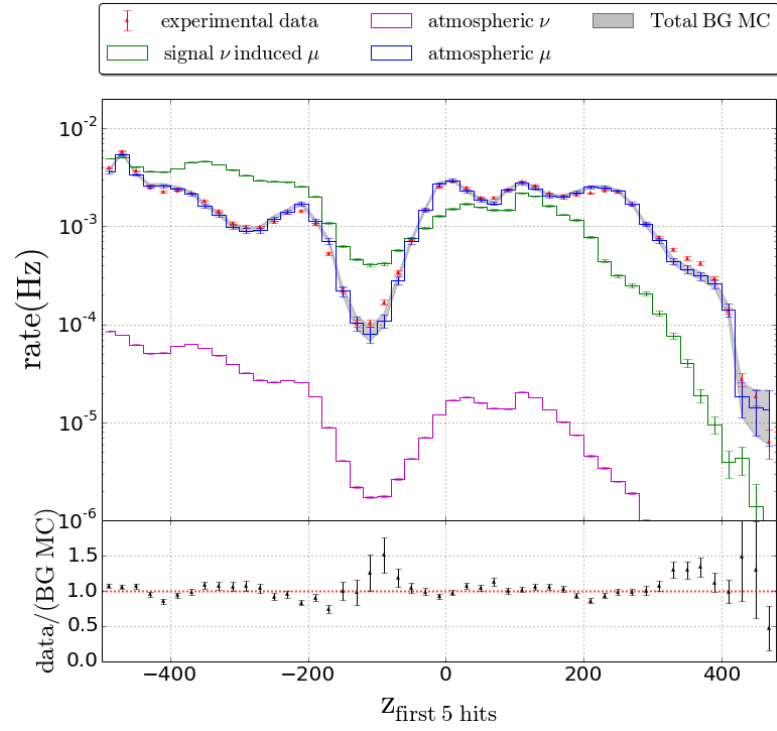


(a)

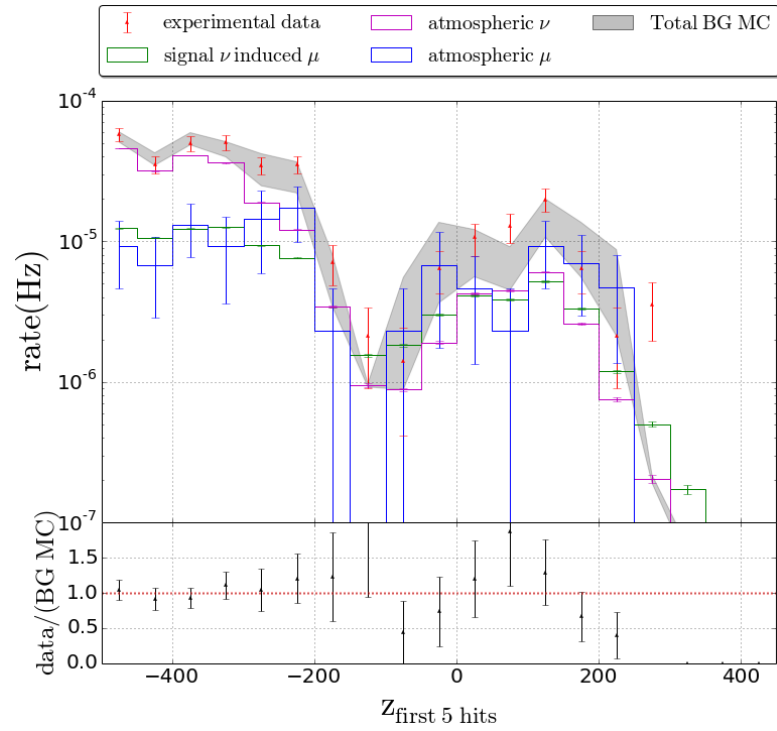


(b)

Figure A.4: z_{travel} distributions before (a) and after (b) the BDT cut.

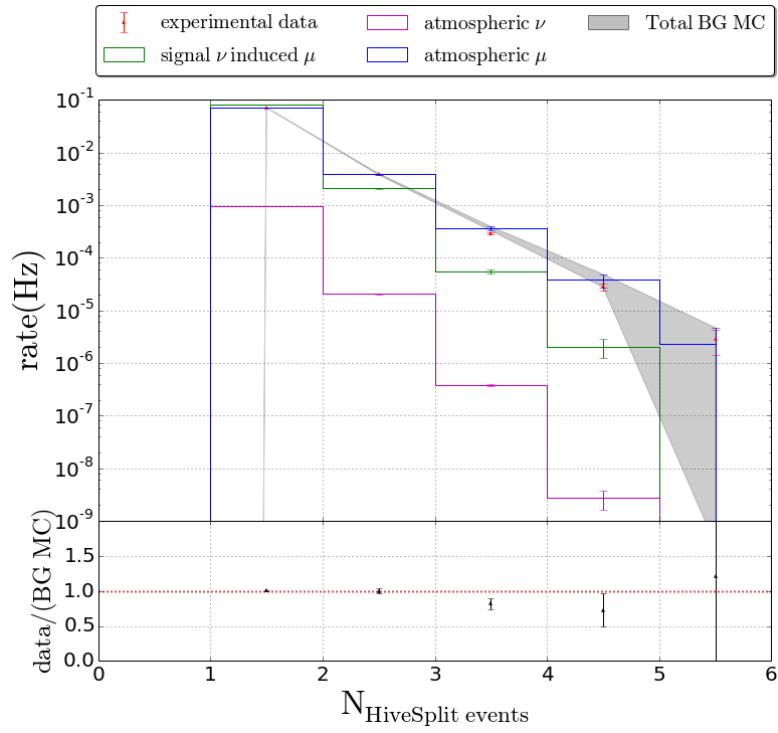


(a)

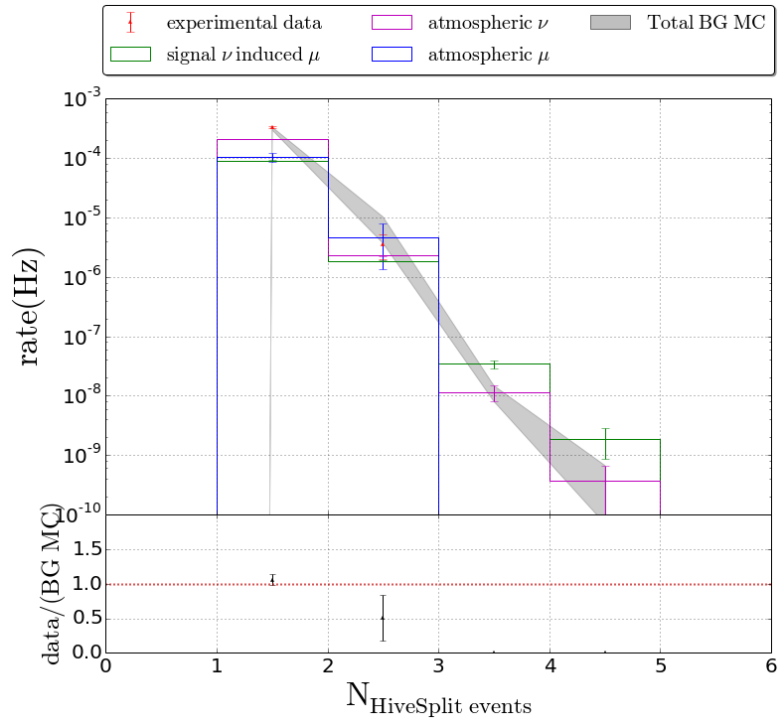


(b)

Figure A.5: $z_{\text{first 5 hits}}$ distributions before (a) and after (b) the BDT cut.

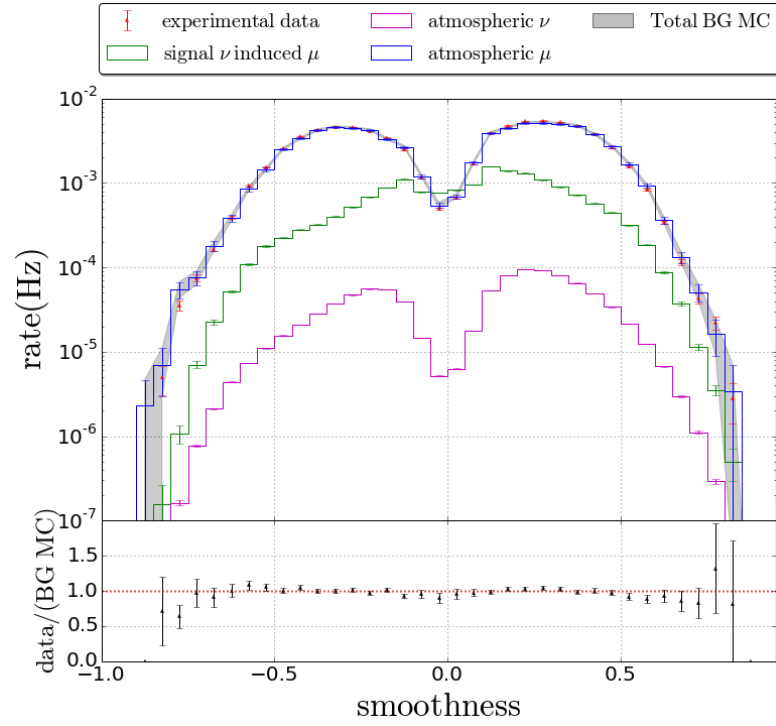


(a)

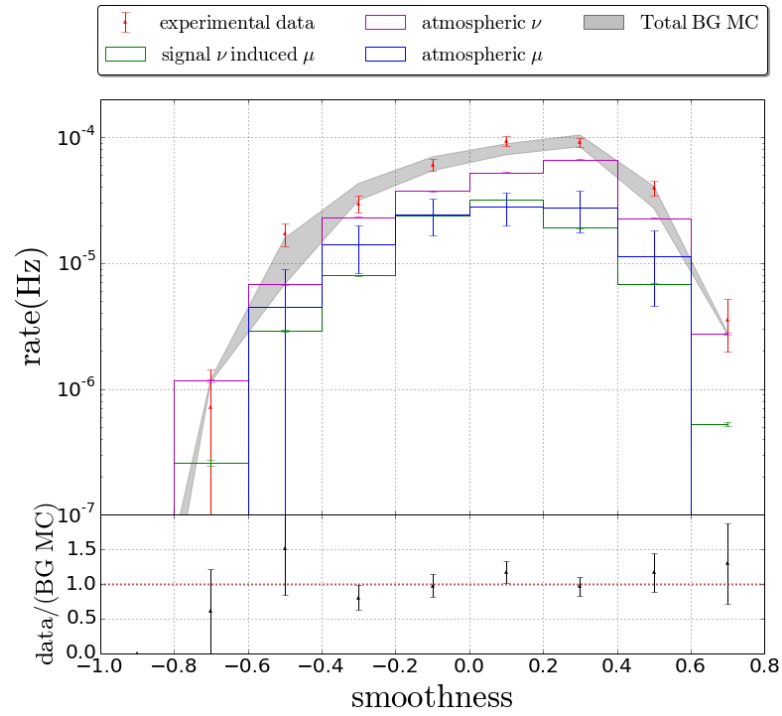


(b)

Figure A.6: $N_{\text{HiveSplit}}$ events distributions before (a) and after (b) the BDT cut.

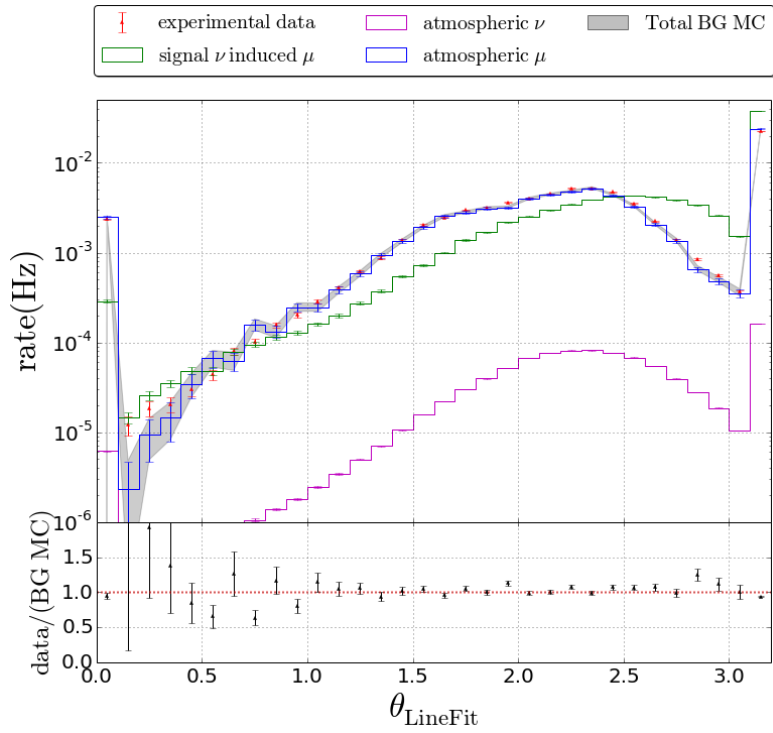


(a)

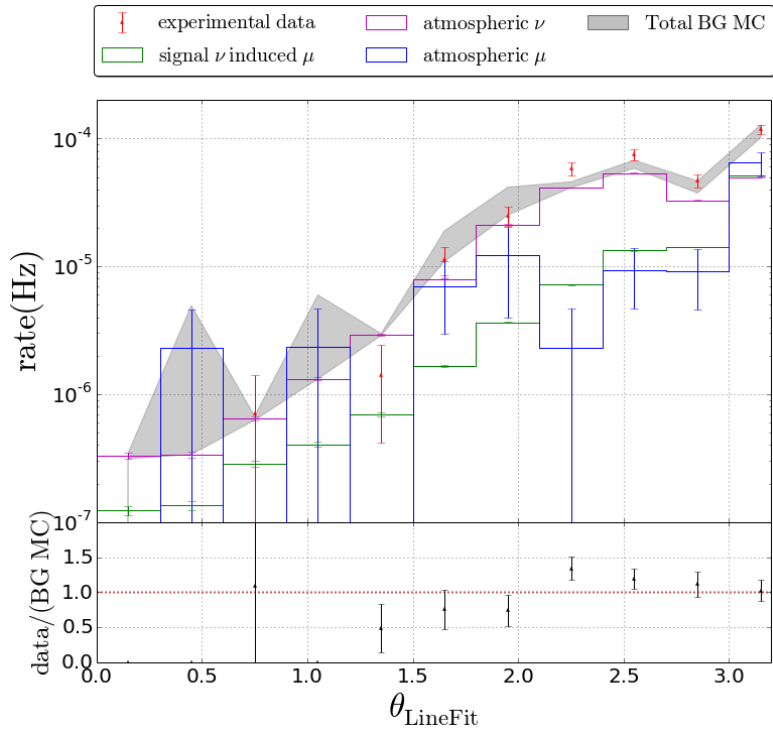


(b)

Figure A.7: Smoothness distributions before (a) and after (b) the BDT cut.

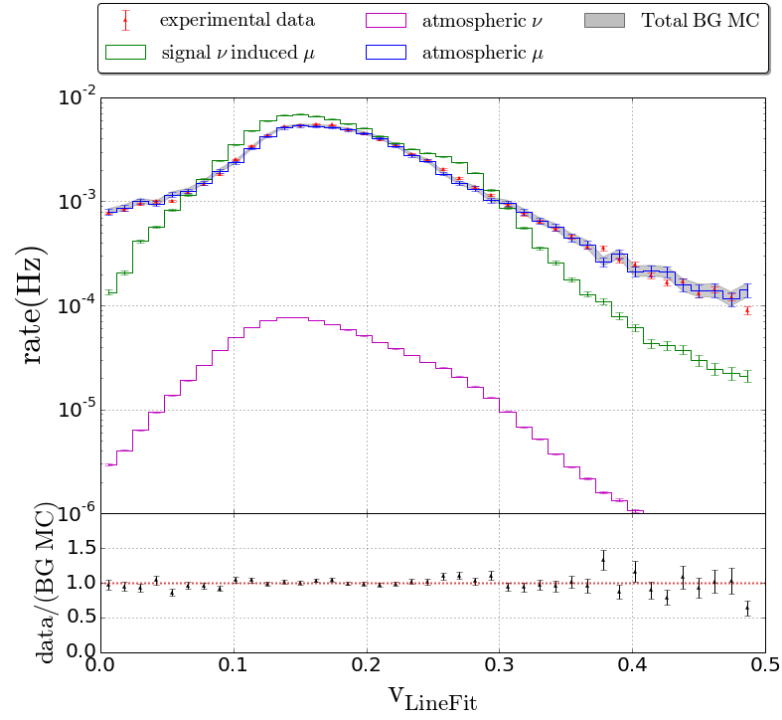


(a)

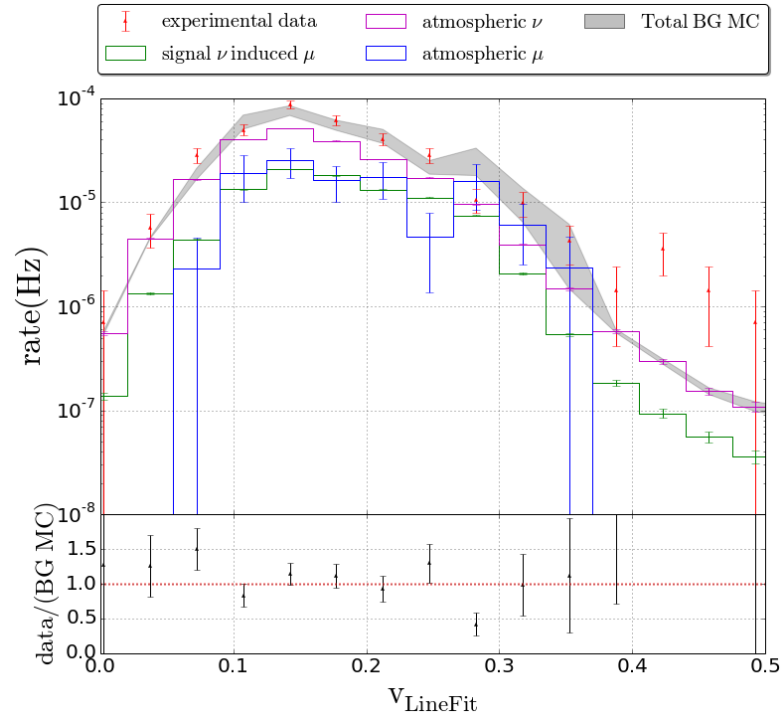


(b)

Figure A.8: θ_{LineFit} distributions before (a) and after (b) the BDT cut.



(a)



(b)

Figure A.9: v_{LineFit} distributions before (a) and after (b) the BDT cut.

B

The effect of coincident events on the neutrino flux

As described in Section 9.1 of Chapter 9 coincident events were missing in the baseline neutrino simulation sets used in the presented analysis. Roughly 10% of all the events detected by IceCube are coincident events. This factor increases when only the more abundant low energetic events are considered as is the case in the work described in this thesis.

In this appendix, the baseline atmospheric neutrino simulation sample (Genie) used in this work is compared to a sample which was simulated (Genie) with the inclusion of coincident events. The latter sample was not used as baseline in this work, as it has not been reviewed and tested by the IceCube collaboration and could thus contain errors. For this reason, the effect of coincident events is considered as a systematic error.

The true energy spectra after the online filter selection of the baseline set and the coincident set are shown in Fig. B.1 in magenta and green respectively. Note that the overall offset between the distributions is about 10 %, but is increasing with decreasing energies.

Low energetic neutrinos only produce a small amount of light in the detector, so if there is a coincident muon and the event is not properly split, the hit cleaning might remove the hits produced by the neutrino and the reconstructions will give more weight to the muon track and thus wrongly reconstruct the event as down-going. These events are then removed in the online filter selection step (Section 7.3), causing the effect seen in Fig. B.1.

The effect of coincident events gets even bigger after the LEVEL 3 filter (Section 7.5.1), yielding the distributions of the variables (defined in Chapter 7) shown in Fig. B.2. The reason for this is the cut on the z -position of the reconstructed vertex of the event, which removes more atmospheric neutrinos if coincident muons are present, as shown in

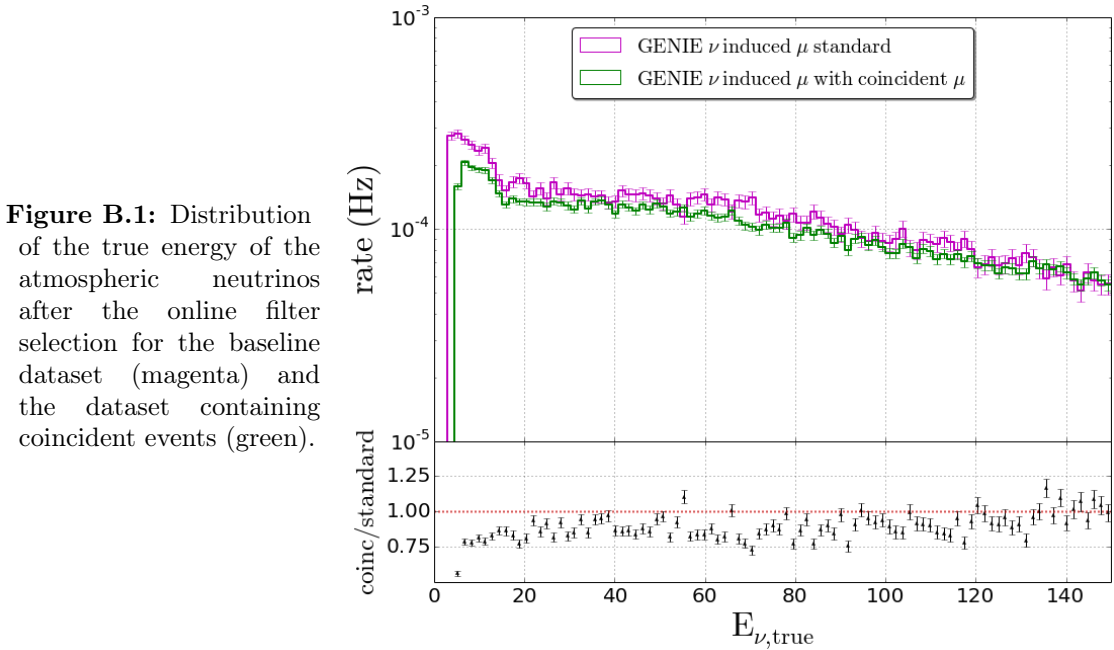


Figure B.1: Distribution of the true energy of the atmospheric neutrinos after the online filter selection for the baseline dataset (magenta) and the dataset containing coincident events (green).

Fig. B.2c. This effect can again be explained by the reconstruction giving more weight to the muon track than to the low energetic atmospheric neutrino if these particles are not split.

The final step of the low energy event selection was a cut on the BDT score distribution. In this distribution the experimental data were overestimated by a factor of roughly 1.5 ($=1/0.7$) in the neutrino dominated part of the distribution (high BDT scores), and rescaling factors were introduced to get data-MC agreement (Section 7.7.4 of Chapter 7). The inclusion of coincident events explains part of the offset. In Fig. B.3 the BDT score distribution of the different data samples with (dashed) and without (solid) coincident muons are shown. The data-MC ratios are calculated with the baseline neutrino datasets in Fig. B.3a and with the coincident neutrino data sample in Fig. B.3b. The latter shows a better data-MC agreement.

The reconstructed zenith angle distributions of the final samples also show a better data-MC agreement if the coincident events are taken into account, as can be seen in Fig. B.4 where the baseline dataset (without rescaling factors) is used for the atmospheric neutrinos in Fig. B.4a and the coincident sample in Fig. B.4b.

To conclude, it is important that future IceCube simulations contain coincident muon events.

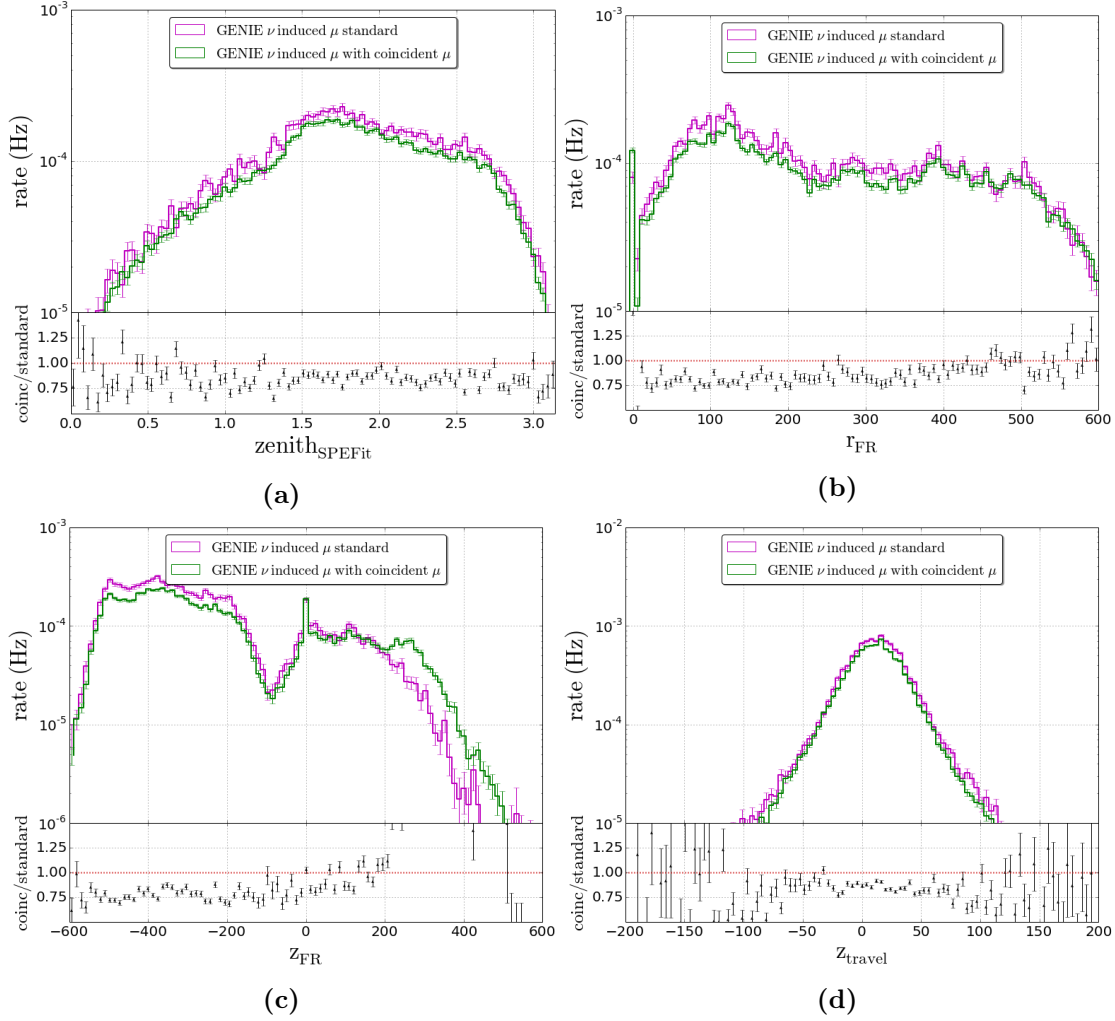
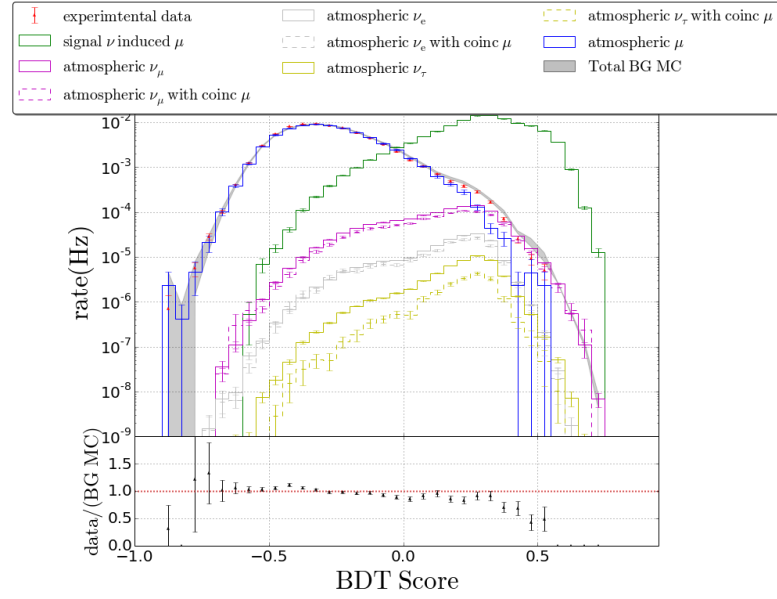
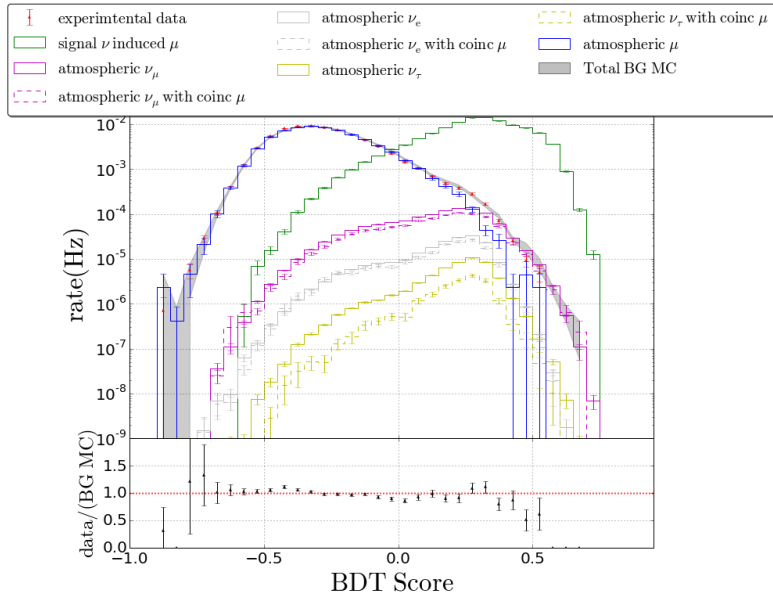


Figure B.2: Atmospheric neutrino distributions of the variables used for the LEVEL 3 selection for simulations with (green) and without (magenta) coincident atmospheric muons.

APPENDIX B. THE EFFECT OF COINCIDENT EVENTS ON THE NEUTRINO FLUX



(a)



(b)

Figure B.3: BDT score distribution of the different data samples with (dashed) and without (solid) coincident muons. The data-MC ratios are calculated with the baseline neutrino datasets in (a) and with the coincident neutrino data sample in (b).

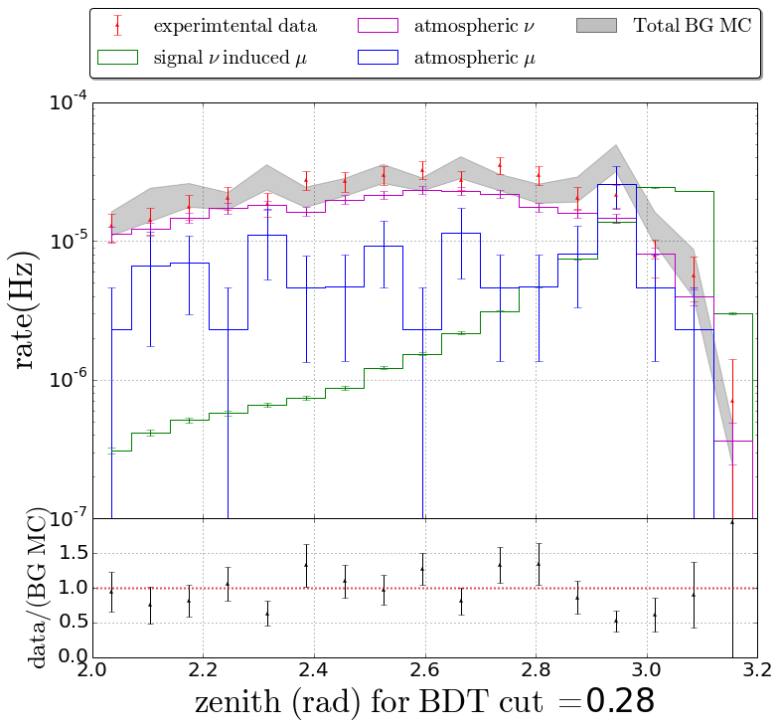
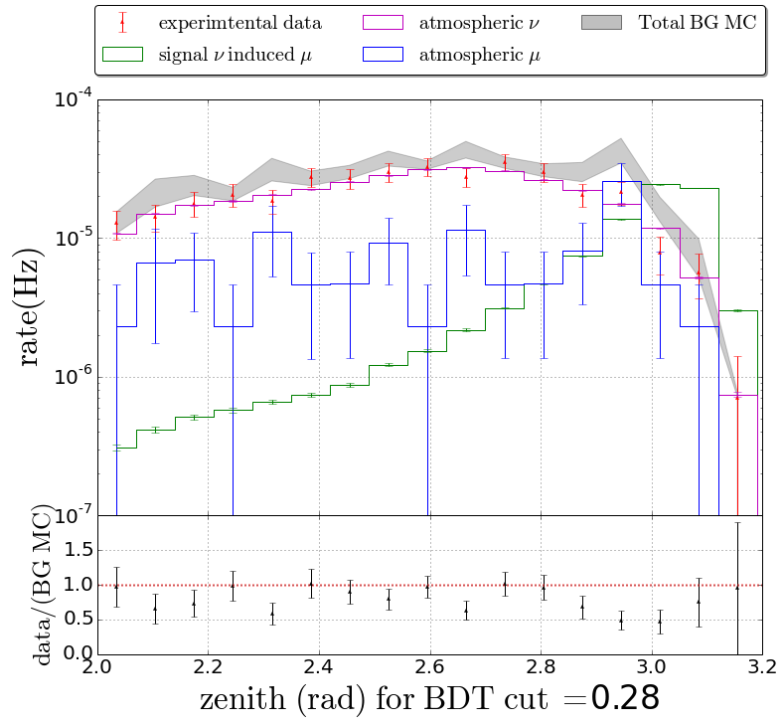


Figure B.4: Reconstructed (MuEx4SPE) zenith angle distribution of the different data samples without (a) and with (b) coincident muons.

Index

- $N_{\text{HIVESPLIT EVENTS}}$, 127
- $\sigma(\text{MUEX4MPE})$, 127
- θ_{LINEFIT} , 127
- e^+e^- pair production, 41
- $r_{\text{first 5 hits}}$, 127
- v_{LINEFIT} , 127
- $z_{\text{first 5 hits}}$, 127
- z_{pattern} , 124, 127
- z_{travel} , 105, 127
- FINITERECO, 78
- FINITERECO Vertex Point, 102
- HIGH LEVEL 4, 140
- HIGH LEVEL 5, 140
- HIGH optimization, 140
- HIGH sample, 110
- HIVESPLIT cleaning, 73, 113
- ICECUBE Run, 84
- ICECUBE online filters, 63
- ICECUBE triggers, 62
- ICECUBE zenith convention, 50
- LEVEL 1, 61
- LEVEL 2, 67
- LEVEL 3, 100
- LINEFIT, 76
- LOWE LEVEL 4, 119
- LOWE LEVEL 5, 126
- LOWE optimization, 112
- LOWE sample, 110
- MUEX reconstruction, 80
- SPEFIT Zenith Angle, 101
- SPICE-LEA ice model, 53
- SPICE-MIE ice model, 52
- TIME-WINDOW-SEEDED-RADIAL-TIME (TWSRT)
 - cleaning, 73
- Analog Transient Waveform Digitizer (ATWD)
 - 56
- Angular resolution, 135
- Atmospheric background, 98
- Atmospheric Muons, 59, 87
- Atmospheric Neutrinos, 60, 87
- Austral Summer, 84
- Baryonic matter, 12
- Blindness, 86
- Boosted Decision Trees (BDTs), 116, 126
- Bremsstrahlung, 41
- Burnsample, 86
- Cascades, 57
- Charged Current (CC) neutrino interaction,
 - 33
- Cherenkov radiation, 43
- Coincident events, 73, 88, 130
- Collider Experiments, 22
- Correlated noise clusters, 81
- CORSIKA, 87
- Dark Disc, 15
- Dark Matter, 8
- Dark matter density distribution, 14
- Dark matter velocity distribution, 15
- Dark Noise in ICECUBE, 57
- Data-MC discrepancies, 119, 131
- dCORSIKA, 87
- Detector livetime/uptime, 84
- Digital Optical Modules (DOMs), 54
- Direct detection experiments, 17
- Direct hits, 120
- Earth WIMP equilibrium, 25
- Earth-WIMP signal, 96
- Effective volume, V_{eff} , 89, 135
- Energy Splitting, 107

-
- Fast Analog to Digital Converter (fADC), 55
- Feldmann and Cousins (FC) likelihood-ratio test statistic, 153
- Generated Volume, 89
- GENIE, 87
- Hard Local Coincidence (HLC), 55
- Hard WIMP annihilation : $\chi\chi \rightarrow \tau^+\tau^-$ or W^+W^- , 31
- Hit, 72
- Hit Processing and Cleaning, 72
- Hole ice, 54
- IC86-I, 84
- Indirect detection experiments, 21
- Individual Active Volume (IAV), 73
- Ionization, 40
- Kernel Density Estimation (KDE), 148
- Kolmogorov-Smirnov (KS) test, 130
- Kolmogorov-Smirnov test, 119
- Lambda Cold Dark Matter model (Λ CDM), 9
- Lightest Supersymmetric Particle (LSP), 13
- Minimal Supersymmetric Standard Model (MSSM), 13
- MPEFit, 78
- Muon Monte Carlo (MMC), 91
- Neutral Current (NC) neutrino interaction, 33
- Neutralino, 12
- Neutrino detection in ice, 40
- Neutrino oscillation parameters, 37
- Neutrino oscillations, 34
- Neutrino scattering cross-section, 34
- NoiseEngine, 81
- NuGen, 87
- Oscillation Parameters, 87
- Pandel Function, 78
- Photo-Electron (PE), 54
- Photo-nuclear interactions, 41
- Photomultiplier Tube (PMT), 54
- Photon Propagation Code (PPC), 91
- Photon scattering and absorption in the ice, 52
- Probability Density Functions (PDFs), 148
- Pull-Validation, 140
- Pulse, 72
- R-parity conservation, 13
- Scaling factors, 131, 133
- Sensitivity, 152, 156
- Shape analysis, 152
- smoothness, 127
- Soft Local Coincidence (SLC), 55
- Soft WIMP annihilation : $\chi\chi \rightarrow b\bar{b}$, 31
- SPEFit, 78
- Spin-Independent cross-section, $\sigma_{\chi-N}^{SI}$, 182
- Standard Halo Model (SHM), 15
- Standard Model of Particle Physics, 33
- Supersymmetry (SUSY), 12
- The DEEPCORE detector, 49
- The ICECUBE neutrino detector, 49
- The ICETOP detector, 49
- Time residual, 74
- Tracks, 57
- Volumetric Flux, $\Gamma_{\nu \rightarrow \mu}$, 133, 152, 176
- Vuvuzela, 91
- Waveform, 72
- Weakly Interacting Massive Particles (WIMPs), 13
- WIMP annihilation rate, Γ_A , 25, 176
- WIMP capture, 21
- WIMP capture C_C , 24
- WIMP population in the center of the Earth, 23
- WIMP-induced Muon Flux Φ_μ , 178
- WIMP-induced neutrino flux, 31
- WimpSim, 89

Bibliography

- [1] F. Zwicky. “On the Masses of Nebulae and of Clusters of Nebulae”. In: *Astrophysical Journal* 86 (1937), p. 217. DOI: 10.1086/143864.
- [2] G. Bertone, D. Hooper, and J. Silk. “Particle dark matter: Evidence, candidates and constraints”. In: *Phys. Rept.* 405 (2005), pp. 279–390. DOI: 10.1016/j.physrep.2004.08.031. arXiv: hep-ph/0404175 [hep-ph].
- [3] D. Scott. “The standard cosmological model”. In: *Can. J. Phys.* 84 (2006), pp. 419–435. DOI: 10.1139/P06-066. arXiv: astro-ph/0510731 [astro-ph].
- [4] E. Hubble. “A Relation between Distance and Radial Velocity among Extra-Galactic Nebulae”. In: *Proceedings of the National Academy of Science*. Vol. 15. Mar. 1929, pp. 168–173.
- [5] P. A. R. Ade et al. “Planck 2015 results. XIII. Cosmological parameters”. In: (2015). arXiv: 1502.01589 [astro-ph.CO].
- [6] S. Carroll. *Spacetime and Geometry: An Introduction to General Relativity*. Addison Wesley, 2004. ISBN: 9780805387322. URL: <https://books.google.be/books?id=1SKFQgAACAAJ>.
- [7] D. Perkins. *Particle Astrophysics, Second Edition*. Oxford Master Series in Physics. OUP Oxford, 2008. ISBN: 9780199545452. URL: <https://books.google.be/books?id=fBNzZF7kLz4C>.
- [8] T. Treu and R. S. Ellis. “Gravitational Lensing - Einstein’s Unfinished Symphony”. In: (2014). arXiv: 1412.6916 [astro-ph.CO].
- [9] E. L. Lokas. “Velocity dispersions of dwarf spheroidal galaxies: dark matter versus *mond*”. In: *Mon. Not. Roy. Astron. Soc.* 327 (2001), p. L21. DOI: 10.1046/j.1365-8711.2001.04953.x. arXiv: astro-ph/0107479 [astro-ph].
- [10] N. Polonsky. “Supersymmetry: Structure and phenomena. Extensions of the standard model”. In: *Lect. Notes Phys.* M68 (2001), pp. 1–169. arXiv: hep-ph/0108236 [hep-ph].
- [11] S. P. Martin. “A Supersymmetry primer”. In: (1997). [Adv. Ser. Direct. High Energy Phys.18,1(1998)]. DOI: 10.1142/9789812839657_0001, 10.1142/9789814307505_0001. arXiv: hep-ph/9709356 [hep-ph].
- [12] L. O’Raifeartaigh and N. Straumann. “Early history of gauge theories and Kaluza-Klein theories”. In: (1998). arXiv: hep-ph/9810524 [hep-ph].

- [13] S. Hannestad. “Neutrino physics from Cosmology”. In: *Nuovo Cim.* C037.03 (2014), pp. 111–116. DOI: 10.1393/ncc/i2014-11771-9. arXiv: 1311.0623 [astro-ph.CO].
- [14] L. D. Duffy and K. van Bibber. “Axions as Dark Matter Particles”. In: *New J. Phys.* 11 (2009), p. 105008. DOI: 10.1088/1367-2630/11/10/105008. arXiv: 0904.3346 [hep-ph].
- [15] J. M. Cornell, S. Profumo, and W. Shepherd. “Dark matter in minimal universal extra dimensions with a stable vacuum and the “right” Higgs boson”. In: *Phys. Rev. D* 89.5 (2014), p. 056005. DOI: 10.1103/PhysRevD.89.056005. arXiv: 1401.7050 [hep-ph].
- [16] M. Kuhlen, M. Vogelsberger, and R. Angulo. “Numerical simulations of the dark universe: State of the art and the next decade”. In: *Physics of the Dark Universe* 1 (Nov. 2012), pp. 50–93. DOI: 10.1016/j.dark.2012.10.002. arXiv: 1209.5745 [astro-ph.CO].
- [17] V. Springel, C. S. Frenk, and S. D. M. White. “The large-scale structure of the Universe”. In: *Nature* 440 (2006), p. 1137. DOI: 10.1038/nature04805. arXiv: astro-ph/0604561 [astro-ph].
- [18] E. Corbelli and P. Salucci. “The Extended Rotation Curve and the Dark Matter Halo of M33”. In: *Mon. Not. Roy. Astron. Soc.* 311 (2000), pp. 441–447. DOI: 10.1046/j.1365-8711.2000.03075.x. arXiv: astro-ph/9909252 [astro-ph].
- [19] N. Okabe et al. “LoCuSS: The Mass Density Profile of Massive Galaxy Clusters at $z = 0.2$ ”. In: *The Astrophysical Journal Letters* 769.2 (2013), p. L35. URL: <http://stacks.iop.org/2041-8205/769/i=2/a=L35>.
- [20] A. Pillepich et al. “The Distribution of Dark Matter in the Milky Way’s Disk”. In: *The Astrophysical Journal* 784, 161 (Apr. 2014), p. 161. DOI: 10.1088/0004-637X/784/2/161. arXiv: 1308.1703.
- [21] J. I. Read. “The local dark matter density”. In: *Journal of Physics G Nuclear Physics* 41.6, 063101 (June 2014), p. 063101. DOI: 10.1088/0954-3899/41/6/063101. arXiv: 1404.1938.
- [22] J. F. Navarro, C. S. Frenk, and S. D. M. White. “The Structure of cold dark matter halos”. In: *Astrophys. J.* 462 (1996), pp. 563–575. DOI: 10.1086/177173. arXiv: astro-ph/9508025 [astro-ph].
- [23] A. Burkert. “The Structure of dark matter halos in dwarf galaxies”. In: *IAU Symp.* 171 (1996). [Astrophys. J.447,L25(1995)], p. 175. DOI: 10.1086/309560. arXiv: astro-ph/9504041 [astro-ph].
- [24] H. Yuksel et al. “Neutrino Constraints on the Dark Matter Total Annihilation Cross Section”. In: *Phys. Rev. D* 76 (2007), p. 123506. DOI: 10.1103/PhysRevD.76.123506. arXiv: 0707.0196 [astro-ph].
- [25] F. Nesti and P. Salucci. “The Dark Matter halo of the Milky Way, AD 2013”. In: *JCAP* 7, 016 (July 2013), p. 16. DOI: 10.1088/1475-7516/2013/07/016. arXiv: 1304.5127.

-
- [26] M. Wolf. “Indirect Searches for Galactic Dark Matter with IceCube-DeepCore and PINGU”. Licentiate Thesis. Stockholm University, 2014.
- [27] G. R. Knapp, S. D. Tremaine, and J. E. Gunn. “The global properties of the Galaxy. I - The H I distribution outside the solar circle”. In: *Astronomical Journal* 83 (Dec. 1978), pp. 1585–1593. DOI: 10.1086/112367.
- [28] G. Jungman, M. Kamionkowski, and K. Griest. “Supersymmetric dark matter”. In: *Phys. Rept.* 267 (1996), pp. 195–373. DOI: 10.1016/0370-1573(95)00058-5. arXiv: hep-ph/9506380 [hep-ph].
- [29] G. Lake. “Must the disk and halo dark matter be different?” In: *Astronomical Journal* 98 (Nov. 1989), pp. 1554–1556. DOI: 10.1086/115238.
- [30] J. I. Read et al. “A Dark Matter Disc in the Milky Way”. In: *American Institute of Physics Conference Series*. Ed. by V. P. Debattista and C. C. Popescu. Vol. 1240. American Institute of Physics Conference Series. June 2010, pp. 391–394. DOI: 10.1063/1.3458542. arXiv: 0901.2938.
- [31] J. I. Read et al. “A dark matter disc in three cosmological simulations of Milky Way mass galaxies”. In: *MNRAS* 397 (July 2009), pp. 44–51. DOI: 10.1111/j.1365-2966.2009.14757.x. arXiv: 0902.0009.
- [32] K. Choi, C. Rott, and Y. Itow. “Impact of the dark matter velocity distribution on capture rates in the Sun”. In: *JCAP* 1405 (2014), p. 049. DOI: 10.1088/1475-7516/2014/05/049. arXiv: 1312.0273 [astro-ph.HE].
- [33] M. Daninger. “Searches for Dark Matter with IceCube and DeepCore”. PhD thesis. Stockholm University, 2013.
- [34] T. Saab. “An Introduction to Dark Matter Direct Detection Searches Techniques”. In: *The Dark Secrets of the Terascale (TASI 2011) - Proceedings of the 2011 Theoretical Advanced Study Institute in Elementary Particle Physics*. Ed. by K. Matchev and et al. Dec. 2013, pp. 711–738. DOI: 10.1142/9789814390163_0011. arXiv: 1203.2566 [physics.ins-det].
- [35] E. Aprile et al. “Dark Matter Results from 225 Live Days of XENON100 Data”. In: *Phys. Rev. Lett.* 109 (2012), p. 181301. DOI: 10.1103/PhysRevLett.109.181301. arXiv: 1207.5988 [astro-ph.CO].
- [36] D. S. Akerib et al. “The Large Underground Xenon (LUX) experiment”. In: *Nuclear Instruments and Methods in Physics Research A* 704 (Mar. 2013), pp. 111–126. DOI: 10.1016/j.nima.2012.11.135. arXiv: 1211.3788 [physics.ins-det].
- [37] R. Agnese et al. “Maximum Likelihood Analysis of Low Energy CDMS II Germanium Data”. In: *Phys. Rev. D* (2014). [Phys. Rev.D91,052021(2015)]. DOI: 10.1103/PhysRevD.91.052021. arXiv: 1410.1003 [astro-ph.CO].
- [38] G. Angloher et al. “Results on light dark matter particles with a low-threshold CRESST-II detector”. In: (2015). arXiv: 1509.01515 [astro-ph.CO].

- [39] R. Bernabei et al. “New Results from DAMA/LIBRA: Final Model-Independent Results of Dama/Libra-Phase1 and Perspectives of Phase2”. In: *Frascati Phys. Ser.* 58 (2014), p. 41.
- [40] J. Li. “Directional dark matter by polar angle direct detection and application of columnar recombination”. In: *Phys. Rev. D* 92.4 (2015), p. 043523. DOI: 10.1103/PhysRevD.92.043523. arXiv: 1503.07320 [hep-ph].
- [41] R. Bernabei et al. “Particle Dark Matter in DAMA/LIBRA”. In: *ArXiv e-prints* (July 2010). arXiv: 1007.0595 [astro-ph.CO].
- [42] R. Agnese et al. “Search for Low-Mass Weakly Interacting Massive Particles Using Voltage-Assisted Calorimetric Ionization Detection in the SuperCDMS Experiment”. In: *Phys. Rev. Lett.* 112.4 (2014), p. 041302. DOI: 10.1103/PhysRevLett.112.041302. arXiv: 1309.3259 [physics.ins-det].
- [43] J. Kopp, T. Schwetz, and J. Zupan. “Light Dark Matter in the light of CRESST-IP”. In: *JCAP* 1203 (2012), p. 001. DOI: 10.1088/1475-7516/2012/03/001. arXiv: 1110.2721 [hep-ph].
- [44] C. E. Aalseth et al. “Results from a Search for Light-Mass Dark Matter with a p-Type Point Contact Germanium Detector”. In: *Physical Review Letters* 106.13, 131301 (Apr. 2011), p. 131301. DOI: 10.1103/PhysRevLett.106.131301. arXiv: 1002.4703 [astro-ph.CO].
- [45] R. Agnese et al. “Silicon Detector Dark Matter Results from the Final Exposure of CDMS II”. In: *Phys. Rev. Lett.* 111.25 (2013), p. 251301. DOI: 10.1103/PhysRevLett.111.251301. arXiv: 1304.4279 [hep-ex].
- [46] J. Billard, L. Strigari, and E. Figueroa-Feliciano. “Implication of neutrino backgrounds on the reach of next generation dark matter direct detection experiments”. In: *Phys. Rev. D* 89.2 (2014), p. 023524. DOI: 10.1103/PhysRevD.89.023524. arXiv: 1307.5458 [hep-ph].
- [47] P. Grothaus, M. Fairbairn, and J. Monroe. “Directional Dark Matter Detection Beyond the Neutrino Bound”. In: *Phys. Rev. D* 90.5 (2014), p. 055018. DOI: 10.1103/PhysRevD.90.055018. arXiv: 1406.5047 [hep-ph].
- [48] M. Ackermann et al. “Limits on Dark Matter Annihilation Signals from the Fermi LAT 4-year Measurement of the Isotropic Gamma-Ray Background”. In: *JCAP* 1509.09 (2015), p. 008. DOI: 10.1088/1475-7516/2015/09/008. arXiv: 1501.05464 [astro-ph.CO].
- [49] A. Abramowski et al. “Search for dark matter annihilation signatures in H.E.S.S. observations of Dwarf Spheroidal Galaxies”. In: *Phys. Rev. D* 90 (2014), p. 112012. DOI: 10.1103/PhysRevD.90.112012. arXiv: 1410.2589 [astro-ph.HE].
- [50] J. Aleksić et al. “Optimized dark matter searches in deep observations of Segue 1 with MAGIC”. In: *JCAP* 1402 (2014), p. 008. DOI: 10.1088/1475-7516/2014/02/008. arXiv: 1312.1535 [hep-ph].

-
- [51] B. Zitzer. “The VERITAS Dark Matter Program”. In: *Fifth International Fermi Symposium Nagoya, Japan, October 20-24, 2014*. 2015. arXiv: 1503.00743 [astro-ph.HE]. URL: <http://inspirehep.net/record/1347106/files/arXiv:1503.00743.pdf>.
- [52] M. Boezio et al. “PAMELA and indirect dark matter searches”. In: *New J. Phys.* 11 (2009), p. 105023. DOI: 10.1088/1367-2630/11/10/105023.
- [53] M. Aguilar et al. “First Result from the Alpha Magnetic Spectrometer on the International Space Station: Precision Measurement of the Positron Fraction in Primary Cosmic Rays of 0.5350 GeV”. In: *Phys. Rev. Lett.* 110 (14 Apr. 2013), p. 141102. DOI: 10.1103/PhysRevLett.110.141102. URL: <http://link.aps.org/doi/10.1103/PhysRevLett.110.141102>.
- [54] M. G. Aartsen et al. “IceCube Search for Dark Matter Annihilation in nearby Galaxies and Galaxy Clusters”. In: *Phys. Rev. D* 88 (2013), p. 122001. DOI: 10.1103/PhysRevD.88.122001. arXiv: 1307.3473 [astro-ph.HE].
- [55] M. G. Aartsen et al. “Search for Dark Matter Annihilation in the Galactic Center with IceCube-79”. In: *Eur. Phys. J. C* 75.10 (2015), p. 492. DOI: 10.1140/epjc/s10052-015-3713-1. arXiv: 1505.07259 [astro-ph.HE].
- [56] S. Adrian-Martinez et al. “Search of Dark Matter Annihilation in the Galactic Centre using the ANTARES Neutrino Telescope”. In: (2015). arXiv: 1505.04866 [astro-ph.HE].
- [57] A. D. Avrorin et al. “Sensitivity of the Baikal-GVD neutrino telescope to neutrino emission toward the center of the galactic dark matter halo”. In: *JETP Lett.* 101.5 (2015), pp. 289–294. DOI: 10.1134/S0021364015050021. arXiv: 1412.3672 [astro-ph.HE].
- [58] T. Daylan et al. “The Characterization of the Gamma-Ray Signal from the Central Milky Way: A Compelling Case for Annihilating Dark Matter”. In: (2014). arXiv: 1402.6703 [astro-ph.HE].
- [59] J. Kim, J.-C. Park, and S. C. Park. “Galactic center GeV gamma-ray excess from dark matter with gauged lepton numbers”. In: (2015). arXiv: 1505.04620 [hep-ph].
- [60] T. Mondal and T. Basak. “Galactic Center gamma-ray excess and Higgs-portal Dark Matter”. In: *21th DAE-BRNS High Energy Physics Symposium (hepbrns2014) Guwahati, India, December 8-12, 2014*. 2015. arXiv: 1507.01793 [hep-ph]. URL: <http://inspirehep.net/record/1381787/files/arXiv:1507.01793.pdf>.
- [61] R. Bartels, S. Krishnamurthy, and C. Weniger. “Strong support for the millisecond pulsar origin of the Galactic center GeV excess”. In: (2015). arXiv: 1506.05104 [astro-ph.HE].
- [62] L. Bergström, J. Edsjö, and G. Zaharijas. “Dark Matter Interpretation of Recent Electron and Positron Data”. In: *Physical Review Letters* 103.3, 031103 (July 2009), p. 031103. DOI: 10.1103/PhysRevLett.103.031103. arXiv: 0905.0333 [astro-ph.HE].

- [63] M. Ahlers, P. Mertsch, and S. Sarkar. “Cosmic ray acceleration in supernova remnants and the FERMI/PAMELA data”. In: *Phys. Rev.* 80.12, 123017 (Dec. 2009), p. 123017. DOI: 10.1103/PhysRevD.80.123017. arXiv: 0909.4060 [astro-ph.HE].
- [64] J. Feng and H.-H. Zhang. “Pulsar interpretation of the lepton spectra measured by AMS-02”. In: (2015). arXiv: 1504.03312 [hep-ph].
- [65] K. Kohri et al. “Can we explain AMS-02 antiproton and positron excesses simultaneously by nearby supernovae without pulsars nor dark matter?” In: (2015). arXiv: 1505.01236 [astro-ph.HE].
- [66] M. G. Aartsen et al. “Search for dark matter annihilations in the Sun with the 79-string IceCube detector”. In: *Phys. Rev. Lett.* 110.13 (2013), p. 131302. DOI: 10.1103/PhysRevLett.110.131302. arXiv: 1212.4097 [astro-ph.HE].
- [67] S. Adrian-Martinez et al. “First results on dark matter annihilation in the Sun using the ANTARES neutrino telescope”. In: *JCAP* 1311 (2013), p. 032. DOI: 10.1088/1475-7516/2013/11/032. arXiv: 1302.6516 [astro-ph.HE].
- [68] R. Kappl and M. W. Winkler. “New Limits on Dark Matter from Super-Kamiokande”. In: *Nucl. Phys.* B850 (2011), pp. 505–521. DOI: 10.1016/j.nuclphysb.2011.05.006. arXiv: 1104.0679 [hep-ph].
- [69] C. Pérez de los Heros. *The quest for dark matter with neutrino telescopes*. Ed. by T. Gaisser and A. Karle. Review. arXiv: 0901.2938. Forthcoming.
- [70] A. Gleixner and C. Tönnes. “Indirect search for dark matter towards the centre of the Earth with the ANTARES neutrino telescope”. In: *Proceedings, 34th International Cosmic Ray Conference (ICRC 2015)*. 2015.
- [71] J. Ahrens et al. “Limits to the muon flux from WIMP annihilation in the center of the Earth with the AMANDA detector”. In: *Phys. Rev.* D66 (2002), p. 032006. DOI: 10.1103/PhysRevD.66.032006. arXiv: astro-ph/0202370 [astro-ph].
- [72] D. Abercrombie et al. “Dark Matter Benchmark Models for Early LHC Run-2 Searches: Report of the ATLAS/CMS Dark Matter Forum”. In: (2015). arXiv: 1507.00966 [hep-ex].
- [73] S. Lowette. “Search for Dark Matter at CMS”. In: (2014). arXiv: 1410.3762 [hep-ex].
- [74] S. Sivertsson and J. Edsjo. “WIMP diffusion in the solar system including solar WIMP-nucleon scattering”. In: *Phys. Rev.* D85 (2012), p. 123514. DOI: 10.1103/PhysRevD.85.129905, 10.1103/PhysRevD.85.123514. arXiv: 1201.1895 [astro-ph.HE].
- [75] W. McDonough and S. Sun. “The composition of the Earth”. In: *Chemical Geology* 120 (1995), p. 223.
- [76] T. Bruch et al. “Dark matter disc enhanced neutrino fluxes from the Sun and Earth”. In: *Physics Letters, Section B: Nuclear, Elementary Particle and High-Energy Physics* 674.4-5 (2009), pp. 250–256. ISSN: 03702693. DOI: 10.1016/j.physletb.2009.03.042. arXiv: 0902.4001.

-
- [77] D. Hubert and A. Davour. “Search for neutralino dark matter with the AMANDA neutrino telescope”. In: *Proceedings, 30th International Cosmic Ray Conference (ICRC 2007)*. 2007.
- [78] M. Blennow, J. Edsjo, and T. Ohlsson. “Neutrinos from WIMP annihilations using a full three-flavor Monte Carlo”. In: *JCAP* 0801 (2008), p. 021. DOI: 10.1088/1475-7516/2008/01/021. arXiv: 0709.3898 [hep-ph].
- [79] M. E. Peskin and D. V. Schroeder. *An Introduction to Quantum Field Theory*. Vol. 47. September. 1995, p. 842. ISBN: 0201503972. DOI: 10.1063/1.2808409. URL: <http://www.amazon.com/dp/0201503972>.
- [80] R. Gandhi et al. “Ultrahigh-energy neutrino interactions”. In: *Astropart. Phys.* 5 (1996), pp. 81–110. DOI: 10.1016/0927-6505(96)00008-4. arXiv: hep-ph/9512364 [hep-ph].
- [81] C. Giunti and C. Kim. *Fundamentals of neutrino physics and astrophysics*. Vol. 54. 2. 2007, p. 720. ISBN: 0198508719. DOI: 10.1093/acprof:oso/9780198508717.001.0001.
- [82] K. A. Olive et al. “Review of Particle Physics”. In: *Chin. Phys.* C38 (2014), p. 090001. DOI: 10.1088/1674-1137/38/9/090001.
- [83] W.-K. Tung. “New generation of parton distributions with uncertainties from global QCD analysis”. In: *Acta Phys. Polon.* B33 (2002), pp. 2933–2938. arXiv: hep-ph/0206114 [hep-ph].
- [84] J. e. a. (D. G. Beringer. “2013 Review of Particle Physics.” In: *Phys. Rev. D* 86 (2012).
- [85] K. Abe et al. “Solar neutrino results in Super-Kamiokande-III”. In: *Phys. Rev. D* 83 (2011), p. 052010. DOI: 10.1103/PhysRevD.83.052010. arXiv: 1010.0118 [hep-ex].
- [86] Y. Fukuda et al. “Evidence for oscillation of atmospheric neutrinos”. In: *Phys. Rev. Lett.* 81 (1998), pp. 1562–1567. DOI: 10.1103/PhysRevLett.81.1562. arXiv: hep-ex/9807003 [hep-ex].
- [87] K. Abe et al. “Evidence for the Appearance of Atmospheric Tau Neutrinos in Super-Kamiokande”. In: *Phys. Rev. Lett.* 110.18 (2013), p. 181802. DOI: 10.1103/PhysRevLett.110.181802. arXiv: 1206.0328 [hep-ex].
- [88] M. G. Aartsen et al. “Determining neutrino oscillation parameters from atmospheric muon neutrino disappearance with three years of IceCube DeepCore data”. In: *Phys. Rev. D* 91.7 (2015), p. 072004. DOI: 10.1103/PhysRevD.91.072004. arXiv: 1410.7227 [hep-ex].
- [89] S.-B. Kim. “Observation of reactor electron antineutrino disappearance at RENO”. In: *Nucl. Phys. Proc. Suppl.* 235-236 (2013), pp. 24–29. DOI: 10.1016/j.nuclphysbps.2013.03.006.

- [90] N. Agafonova et al. “Observation of tau neutrino appearance in the CNGS beam with the OPERA experiment”. In: *PTEP* 2014.10 (2014), p. 101C01. DOI: 10.1093/ptep/ptu132. arXiv: 1407.3513 [hep-ex].
- [91] Z. Maki, M. Nakagawa, and S. Sakata. “Remarks on the unified model of elementary particles”. In: *Prog. Theor. Phys.* 28 (1962), pp. 870–880. DOI: 10.1143/PTP.28.870.
- [92] M. Apollonio et al. “Limits on neutrino oscillations from the CHOOZ experiment”. In: *Phys. Lett.* B466 (1999), pp. 415–430. DOI: 10.1016/S0370-2693(99)01072-2. arXiv: hep-ex/9907037 [hep-ex].
- [93] K. Abe et al. “Observation of Electron Neutrino Appearance in a Muon Neutrino Beam”. In: *Phys. Rev. Lett.* 112 (2014), p. 061802. DOI: 10.1103/PhysRevLett.112.061802. arXiv: 1311.4750 [hep-ex].
- [94] D. A. Dwyer. “The Improved Measurement of Electron-antineutrino Disappearance at Daya Bay”. In: *Nucl. Phys. Proc. Suppl.* 235-236 (2013), pp. 30–32. DOI: 10.1016/j.nuclphysbps.2013.03.007. arXiv: 1303.3863 [hep-ex].
- [95] G. L. Fogli et al. “Global analysis of neutrino masses, mixings and phases: entering the era of leptonic CP violation searches”. In: *Phys. Rev.* D86 (2012), p. 013012. DOI: 10.1103/PhysRevD.86.013012. arXiv: 1205.5254 [hep-ph].
- [96] K. Schreckenbach et al. “Determination of the anti-Neutrino Spectrum from U-235 Thermal Neutron Fission Products up to 9.5-MeV”. In: *Phys. Lett.* B160 (1985), pp. 325–330. DOI: 10.1016/0370-2693(85)91337-1.
- [97] J.-P. Yañez. “Measurement of neutrino oscillations in atmospheric neutrinos with the IceCube DeepCore detector”. PhD thesis. Humboldt-Universität zu Berlin, 2015.
- [98] L. Wolfenstein. “Neutrino Oscillations in Matter”. In: *Phys. Rev.* D17 (1978), pp. 2369–2374. DOI: 10.1103/PhysRevD.17.2369.
- [99] S. P. Mikheev and A. Yu. Smirnov. “Resonant amplification of neutrino oscillations in matter and solar neutrino spectroscopy”. In: *Nuovo Cim.* C9 (1986), pp. 17–26. DOI: 10.1007/BF02508049.
- [100] J. G. Learned and K. Mannheim. “High-energy neutrino astrophysics”. In: *Ann. Rev. Nucl. Part. Sci.* 50 (2000), pp. 679–749. DOI: 10.1146/annurev.nucl.50.1.679.
- [101] D. E. Groom, N. V. Mokhov, and S. I. Striganov. “Muon stopping power and range tables 10-MeV to 100-TeV”. In: *Atom. Data Nucl. Data Tabl.* 78 (2001), pp. 183–356. DOI: 10.1006/adnd.2001.0861.
- [102] S. R. Kelner, R. P. Kokoulin, and A. A. Petrukhin. “About cross-section for high-energy muon bremsstrahlung”. In: (1995).
- [103] S. R. Kelner, R. P. Kokoulin, and A. A. Petrukhin. “Direct production of muon pairs by high-energy muons”. In: *Phys. Atom. Nucl.* 63 (2000). [*Yad. Fiz.*63,1690(2000)], pp. 1603–1611. DOI: 10.1134/1.1312894.

-
- [104] L. B. Bezrukov and E. V. Bugaev. “Nucleon Shadowing Effects in Photon Nucleus Interaction. (In Russian)”. In: *Yad. Fiz.* 33 (1981), pp. 1195–1207.
- [105] D. Chirkin and W. Rhode. “Propagating leptons through matter with Muon Monte Carlo (MMC)”. In: February 2008 (2004). arXiv: 0407075 [hep-ph]. URL: <http://arxiv.org/abs/hep-ph/0407075>.
- [106] W. R. Leo. *Techniques for Nuclear and Particle Physics Experiments: A How to Approach*. 1987.
- [107] C. Huygens. *Traité de la lumière, où sont expliquées les causes de ce qui luy arrive dans la reflexion, et dans la refraction: et particulièrement dans l'étrange refraction du cristal d'Islande: avec un discours de la cause de la pesanteur*. Ed. by V. der Aa. Leiden, 1690.
- [108] M. G. Aartsen et al. “Evidence for High-Energy Extraterrestrial Neutrinos at the IceCube Detector”. In: *Science* 342 (2013), p. 1242856. DOI: 10.1126/science.1242856. arXiv: 1311.5238 [astro-ph.HE].
- [109] M. G. Aartsen et al. “Observation of High-Energy Astrophysical Neutrinos in Three Years of IceCube Data”. In: *Phys. Rev. Lett.* 113 (2014), p. 101101. DOI: 10.1103/PhysRevLett.113.101101. arXiv: 1405.5303 [astro-ph.HE].
- [110] R. Abbasi et al. “The Design and Performance of IceCube DeepCore”. In: *Astropart. Phys.* 35 (2012), pp. 615–624. DOI: 10.1016/j.astropartphys.2012.01.004. arXiv: 1109.6096 [astro-ph.IM].
- [111] M. G. Aartsen et al. “Measurement of Atmospheric Neutrino Oscillations with IceCube”. In: *Phys. Rev. Lett.* 111.8 (2013), p. 081801. DOI: 10.1103/PhysRevLett.111.081801. arXiv: 1305.3909 [hep-ex].
- [112] R. Abbasi et al. “IceTop: The surface component of IceCube”. In: *Nucl. Instrum. Meth. A* 700 (2013), pp. 188–220. DOI: 10.1016/j.nima.2012.10.067. arXiv: 1207.6326 [astro-ph.IM].
- [113] M. G. Aartsen et al. “Measurement of the cosmic ray energy spectrum with IceTop-73”. In: *Phys. Rev. D* 88.4 (2013), p. 042004. DOI: 10.1103/PhysRevD.88.042004. arXiv: 1307.3795 [astro-ph.HE].
- [114] M. G. Aartsen et al. “Measurement of South Pole ice transparency with the IceCube LED calibration system”. In: *Nucl. Instrum. Meth. A* 711 (2013), pp. 73–89. DOI: 10.1016/j.nima.2013.01.054. arXiv: 1301.5361 [astro-ph.IM].
- [115] P. Liu. “A new phase function approximating to Mie scattering for radiative transport equations”. In: *Physics in Medicine and Biology* 39.6 (1994), p. 1025. URL: <http://stacks.iop.org/0031-9155/39/i=6/a=008>.
- [116] D. Chirkin. “Evidence of optical anisotropy of the South Pole ice”. In: *Proceedings, 33rd International Cosmic Ray Conference (ICRC 2013)*. 2013.
- [117] M. Ackermann et al. “Optical properties of deep glacial ice at the South Pole”. In: *J. Geophys. Res.* 111.D13 (2006), p. D13203. DOI: 10.1029/2005JD006687.

- [118] M. G. Aartsen et al. “South Pole glacial climate reconstruction from multi-borehole laser particulate stratigraphy”. In: *Journal of Glaciology* 59.218 (2013), pp. 1117–1128. DOI: 10.3189/2013JoG13J068.
- [119] J. Lundberg et al. “Light tracking for glaciers and oceans: Scattering and absorption in heterogeneous media with Photonics”. In: *Nucl. Instrum. Meth.* A581 (2007), pp. 619–631. DOI: 10.1016/j.nima.2007.07.143. arXiv: astro-ph/0702108 [ASTRO-PH].
- [120] R. Abbasi et al. “Calibration and Characterization of the IceCube Photomultiplier Tube”. In: *Nucl. Instrum. Meth.* A618 (2010), pp. 139–152. DOI: 10.1016/j.nima.2010.03.102. arXiv: 1002.2442 [astro-ph.IM].
- [121] S. Euler. “Observation of oscillations of atmospheric neutrinos with the IceCube Neutrino Observatory”. PhD thesis. RWTH Aachen, 2014.
- [122] D. Xu. “Search for Astrophysical Tau Neutrinos in Three Years of IceCube Data”. PhD thesis. University of Alabama, 2015.
- [123] R. Enberg, M. H. Reno, and I. Sarcevic. “Prompt neutrino fluxes from atmospheric charm”. In: *Phys. Rev.* D78 (2008), p. 043005. DOI: 10.1103/PhysRevD.78.043005. arXiv: 0806.0418 [hep-ph].
- [124] M. C. Gonzalez-Garcia, M. Maltoni, and J. Rojo. “Determination of the atmospheric neutrino fluxes from atmospheric neutrino data”. In: *JHEP* 10 (2006), p. 075. DOI: 10.1088/1126-6708/2006/10/075. arXiv: hep-ph/0607324 [hep-ph].
- [125] K. Daum et al. “Determination of the atmospheric neutrino spectra with the Frejus detector”. In: *Z. Phys.* C66 (1995), pp. 417–428. DOI: 10.1007/BF01556368.
- [126] R. Abbasi et al. “Determination of the Atmospheric Neutrino Flux and Searches for New Physics with AMANDA-IF”. In: *Phys. Rev.* D79 (2009), p. 102005. DOI: 10.1103/PhysRevD.79.102005. arXiv: 0902.0675 [astro-ph.HE].
- [127] R. Abbasi et al. “Measurement of the atmospheric neutrino energy spectrum from 100 GeV to 400 TeV with IceCube”. In: *Phys. Rev.* D83 (2011), p. 012001. DOI: 10.1103/PhysRevD.83.012001. arXiv: 1010.3980 [astro-ph.HE].
- [128] R. Abbasi et al. “A Search for a Diffuse Flux of Astrophysical Muon Neutrinos with the IceCube 40-String Detector”. In: *Phys. Rev.* D84 (2011), p. 082001. DOI: 10.1103/PhysRevD.84.082001. arXiv: 1104.5187 [astro-ph.HE].
- [129] M. G. Aartsen et al. “Measurement of the Atmospheric ν_e flux in IceCube”. In: *Phys. Rev. Lett.* 110.15 (2013), p. 151105. DOI: 10.1103/PhysRevLett.110.151105. arXiv: 1212.4760 [hep-ex].
- [130] J. L. Kelley. “Event triggering in the IceCube data acquisition system”. In: *Proceedings, 6th Very Large Volume Neutrino Telescope Workshop (VLVnT13)*. Vol. 1630. 2014, pp. 154–157. DOI: 10.1063/1.4902795.
- [131] J. Van Santen. “Neutrino Interactions in IceCube above 1 TeV”. PhD thesis. University of Wisconsin-Madison, 2014.

-
- [132] M. G. Aartsen et al. “Probing the origin of cosmic rays with extremely high energy neutrinos using the IceCube Observatory”. In: *Phys. Rev. D* 88 (2013), p. 112008. DOI: 10.1103/PhysRevD.88.112008. arXiv: 1310.5477 [astro-ph.HE].
- [133] J. Davis. *Vertical Events Filter Proposal 2011*. Tech. rep. 2010.
- [134] J. Kunnen. *Request for Online Vertical Event Filter (VEF)*. Tech. rep. 2011.
- [135] M. Danninger. *LowUp Filter, Online Filter Proposal for the 2011 Season*. Tech. rep. 2010.
- [136] N. Kurahashi. *IceCube Muon Filter for 2011 Pole Season*. Tech. rep. 2010.
- [137] N. Whitehorn. “A Search for High-Energy Neutrino Emission from Gamma-Ray Bursts.” PhD thesis. University of Wisconsin-Madison, 2012.
- [138] M. C. R. Zoll. “Improved methods for solar Dark Matter searches with the IceCube neutrino telescope”. In: *Proceedings, 34th International Cosmic Ray Conference (ICRC 2015)*. 2015.
- [139] M. C. R. Zoll. “Preparations for the next solar WIMP Analysis with IceCube”. Licentiate Thesis. 2014.
- [140] J. Ahrens et al. “Muon track reconstruction and data selection techniques in AMANDA”. In: *Nucl. Instrum. Meth.* A524 (2004), pp. 169–194. DOI: 10.1016/j.nima.2004.01.065. arXiv: astro-ph/0407044 [astro-ph].
- [141] M. G. Aartsen et al. “Improvement in Fast Particle Track Reconstruction with Robust Statistics”. In: *Nucl. Instrum. Meth.* A736 (2014), pp. 143–149. DOI: 10.1016/j.nima.2013.10.074. arXiv: 1308.5501 [astro-ph.IM].
- [142] N. van Eijndhoven, O. Fadiran, and G. Japaridze. “Implementation of a Gauss convoluted Pandel PDF for track reconstruction in Neutrino Telescopes”. In: *Astropart. Phys.* 28 (2007), pp. 456–462. DOI: 10.1016/j.astropartphys.2007.09.001. arXiv: 0704.1706 [astro-ph].
- [143] D. Heereman. “HitSpooling : An Improvement for the Supernova Neutrino Detection System in IceCube”. PhD thesis. Université Libre de Bruxelles, 2015.
- [144] M. J. Larson. *Simulation and identification of non-poissonian noise triggers in the IceCube neutrino detector*. Tech. rep. 2013.
- [145] D. Boersma. *Filter Proposal for Moon & Sun Shadow Analysis IC86*. Tech. rep. 2010.
- [146] R. Abbasi et al. “Observation of Anisotropy in the Arrival Directions of Galactic Cosmic Rays at Multiple Angular Scales with IceCube”. In: *The Astrophysical Journal* 740, 16 (Oct. 2011), p. 16. DOI: 10.1088/0004-637X/740/1/16. arXiv: 1105.2326 [astro-ph.HE].
- [147] P. Desiati and T. K. Gaisser. “Seasonal variation of atmospheric leptons as a probe of charm”. In: *Phys. Rev. Lett.* 105 (2010), p. 121102. DOI: 10.1103/PhysRevLett.105.121102. arXiv: 1008.2211 [astro-ph.HE].

- [148] D. Heck et al. *CORSIKA : A Monte Carlo Code to Simulate Extensive Air Showers*. Tech. rep. 1998, p. 98.
- [149] D. Chirkin. “Cosmic Ray Energy Spectrum Measurement with the Antarctic Muon and Neutrino Detector Array (AMANDA)”. PhD thesis. University of California at Berkeley, 2003.
- [150] J. R. Hoerandel. “Models of the knee in the energy spectrum of cosmic rays”. In: *Astropart. Phys.* 21 (2004), pp. 241–265. DOI: 10.1016/j.astropartphys.2004.01.004. arXiv: astro-ph/0402356 [astro-ph].
- [151] C. Andreopoulos et al. “The GENIE Neutrino Monte Carlo Generator”. In: *Nucl. Instrum. Meth. A* 614 (2010), pp. 87–104. DOI: 10.1016/j.nima.2009.12.009. arXiv: 0905.2517 [hep-ph].
- [152] A. Gazizov and M. P. Kowalski. “ANIS: High energy neutrino generator for neutrino telescopes”. In: *Comput. Phys. Commun.* 172 (2005), pp. 203–213. DOI: 10.1016/j.cpc.2005.03.113. arXiv: astro-ph/0406439 [astro-ph].
- [153] M. Honda et al. “Calculation of atmospheric neutrino flux using the interaction model calibrated with atmospheric muon data”. In: *Phys. Rev. D* 75 (2007), p. 043006. DOI: 10.1103/PhysRevD.75.043006. arXiv: astro-ph/0611418 [astro-ph].
- [154] M. Wallraff and C. Wiebusch. “Calculation of oscillation probabilities of atmospheric neutrinos using nuCraft”. In: *ArXiv e-prints* (Sept. 2014). arXiv: 1409.1387 [astro-ph.IM].
- [155] S. Kretzer et al. “Cteq6 parton distributions with heavy quark mass effects”. In: *Phys. Rev. D* 69 (2004), p. 114005. DOI: 10.1103/PhysRevD.69.114005. arXiv: hep-ph/0307022 [hep-ph].
- [156] L. Fields et al. “Measurement of Muon Antineutrino Quasielastic Scattering on a Hydrocarbon Target at $E_\nu \sim 3.5$ GeV”. In: *Phys. Rev. Lett.* 111.2 (2013), p. 022501. DOI: 10.1103/PhysRevLett.111.022501. arXiv: 1305.2234 [hep-ex].
- [157] K. Abe et al. “Measurement of the inclusive ν_μ charged current cross section on carbon in the near detector of the T2K experiment”. In: *Phys. Rev. D* 87.9 (2013), p. 092003. DOI: 10.1103/PhysRevD.87.092003. arXiv: 1302.4908 [hep-ex].
- [158] P. Gondolo et al. “DarkSUSY: Computing supersymmetric dark matter properties numerically”. In: *JCAP* 0407 (2004), p. 008. DOI: 10.1088/1475-7516/2004/07/008. arXiv: astro-ph/0406204 [astro-ph].
- [159] D. Hubert. “Search with the AMANDA detector for neutralino dark matter in the sun”. PhD thesis. Vrije Universiteit Brussel, 2009. URL: <http://w3.iihe.ac.be/Publications/Thesis/hubert.pdf>.
- [160] O. Phillipe. “The Search for Neutralino Dark Matter with the AMANDA-B10 Detector”. PhD thesis. Vrije Universiteit Brussel, 2004.
- [161] R. Nahnauer, A. Terliuk, and J. P. Yanez. *Energy reconstruction of ν_μ events in DeepCore*. Tech. rep. 2013.

-
- [162] M. G. Aartsen et al. “Energy Reconstruction Methods in the IceCube Neutrino Telescope”. In: *JINST* 9 (2014), P03009. DOI: 10.1088/1748-0221/9/03/P03009. arXiv: 1311.4767 [physics.ins-det].
- [163] I. Ansseau. “Search for neutrinos from TeV mass Dark Matter annihilation in the centre of the Earth with the IceCube detector”. Master Thesis. Université de Mons, June 2015.
- [164] J. Kunnen and J. Lünemann. “A Search for Dark Matter in the Center of the Earth with the IceCube Neutrino Detector”. In: *Proceedings, 34th International Cosmic Ray Conference (ICRC 2015)*. 2015.
- [165] M. Richman. “A Search for Muon Neutrinos Coincident with Northern Gamma-Ray Bursts Using IceCube”. PhD thesis. University of Maryland, 2015.
- [166] J. Therhaag. “TMVA - Toolkit for multivariate data analysis”. In: *AIP Conference Proceedings*. Vol. 1504. 2012, pp. 1013–1016. ISBN: 9780735411227. DOI: 10.1063/1.4771869. arXiv: 0703039 [physics].
- [167] F. James. *Statistical Methods in Experimental Physics: 2nd Edition*. 2nd. World Scientific Publishing Company, Nov. 2006. ISBN: 9789812705273. URL: <http://amazon.com/o/ASIN/9812705279/>.
- [168] M. Rosenblatt. “Remarks on some nonparametric estimates of a density function”. In: *Annals of Mathematical Statistics* 27 (1956), pp. 832–837.
- [169] E. Parzen. “On Estimation of a Probability Density Function and Mode”. In: *Ann. Math. Statist.* 33.3 (Sept. 1962), pp. 1065–1076. DOI: 10.1214/aoms/1177704472. URL: <http://dx.doi.org/10.1214/aoms/1177704472>.
- [170] J. Feintzeig. “Searches for Point-like Sources of Astrophysical Neutrinos with the IceCube Neutrino Observatory”. PhD thesis. University of Wisconsin-Madison, 2014.
- [171] J. Kunnen et al. “Pull-validation: A resampling method to improve the usage of low-statistics datasets”. In: *Proceedings, 34th International Cosmic Ray Conference (ICRC 2015)*. 2015.
- [172] R. Abbasi et al. “Multi-year search for dark matter annihilations in the Sun with the AMANDA-II and IceCube detectors”. In: *Phys. Rev. D* 85 (2012), p. 042002. DOI: 10.1103/PhysRevD.85.042002. arXiv: 1112.1840 [astro-ph.HE].
- [173] B. W. Silverman. *Density Estimation for Statistics and Data Analysis*. London: Chapman & Hall, 1986.
- [174] R. Karunamuni and T. Alberts. “On boundary correction in kernel density estimation”. In: *Statistical Methodology* 2.3 (2005), pp. 191–212. ISSN: 1572-3127. DOI: <http://dx.doi.org/10.1016/j.stamet.2005.04.001>. URL: <http://www.sciencedirect.com/science/article/pii/S1572312705000195>.

BIBLIOGRAPHY

- [175] G. J. Feldman and R. D. Cousins. “Unified approach to the classical statistical analysis of small signals”. In: *Phys. Rev. D* 57.7 (1998), pp. 3873–3889. ISSN: 0556-2821. DOI: 10.1103/PhysRevD.57.3873. arXiv: 9711021 [physics]. URL: <http://link.aps.org/doi/10.1103/PhysRevD.57.3873>.
- [176] S. S. Wilks. *Mathematical statistics*. A Wiley publication in mathematical statistics. An early version of some of the material was issued in 1943. New York: John Wiley, cop. 1962, 1963. ISBN: 0-471-94644-3. URL: <http://opac.inria.fr/record=b1081414>.
- [177] W. Hoeffding. “Probability Inequalities for Sums of Bounded Random Variables”. In: *Journal of the American Statistical Association* 58.301 (1963), pp. 13–30. DOI: 10.1080/01621459.1963.10500830. eprint: <http://www.tandfonline.com/doi/pdf/10.1080/01621459.1963.10500830>. URL: <http://www.tandfonline.com/doi/abs/10.1080/01621459.1963.10500830>.
- [178] J. Conrad et al. “Including systematic uncertainties in confidence interval construction for Poisson statistics”. In: *Phys. Rev. D* 67 (2003), p. 012002. DOI: 10.1103/PhysRevD.67.012002. arXiv: hep-ex/0202013 [hep-ex].
- [179] A. Davour. “Search for low mass WIMPs with the AMANDA neutrino telescope”. PhD thesis. Uppsala Universitet, 2007.
- [180] M. Rameez. “Search for Dark Matter annihilations in the Sun using the completed IceCube neutrino telescope.” In: *Proceedings, 34th International Cosmic Ray Conference (ICRC 2015)*. 2015.